



National Library
of Canada

Bibliothèque nationale
du Canada

Canadian Theses Service

Services des thèses canadiennes

Ottawa, Canada
K1A 0N4

CANADIAN THESES

THÈSES CANADIENNES

NOTICE

The quality of this microfiche is heavily dependent upon the quality of the original thesis submitted for microfilming. Every effort has been made to ensure the highest quality of reproduction possible.

If pages are missing, contact the university which granted the degree.

Some pages may have indistinct print especially if the original pages were typed with a poor typewriter ribbon or if the university sent us an inferior photocopy.

Previously copyrighted materials (journal articles, published tests, etc.) are not filmed.

Reproduction in full or in part of this film is governed by the Canadian Copyright Act, R.S.C. 1970, c. C-30.

**THIS DISSERTATION
HAS BEEN MICROFILMED
EXACTLY AS RECEIVED**

AVIS

La qualité de cette microfiche dépend grandement de la qualité de la thèse soumise au microfilmage. Nous avons tout fait pour assurer une qualité supérieure de reproduction.

S'il manque des pages, veuillez communiquer avec l'université qui a conféré le grade.

La qualité d'impression de certaines pages peut laisser à désirer, surtout si les pages originales ont été dactylographiées à l'aide d'un ruban usé ou si l'université nous a fait parvenir une photocopie de qualité inférieure.

Les documents qui font déjà l'objet d'un droit d'auteur (articles de revue, examens publiés, etc.) ne sont pas microfilmés.

La reproduction, même partielle, de ce microfilm est soumise à la Loi canadienne sur le droit d'auteur, SRC 1970, c. C-30.

**LA THÈSE A ÉTÉ
MICROFILMÉE TELLE QUE
NOUS L'AVONS REÇUE**

**Advances in Wire-Grid Modelling of Antennas
and Auxiliary Computer Graphics Systems
with the CP-140 Case Study**

Colin Lionel Larose

A Thesis

in

The Department

of

Electrical Engineering

**Presented in Partial Fulfillment of the Requirements
for the Degree of Master of Engineering at
Concordia University
Montréal, Québec, Canada**

July 1986

© Colin Lionel Larose, 1986

Permission has been granted to the National Library of Canada to microfilm this thesis and to lend or sell copies of the film.

The author (copyright owner) has reserved other publication rights, and neither the thesis nor extensive extracts from it may be printed or otherwise reproduced without his/her written permission.

L'autorisation a été accordée à la Bibliothèque nationale du Canada de microfilmer cette thèse et de prêter ou de vendre des exemplaires du film.

L'auteur (titulaire du droit d'auteur) se réserve les autres droits de publication; ni la thèse ni de longs extraits de celle-ci ne doivent être imprimés ou autrement reproduits sans son autorisation écrite.

ISBN 0-315-32267-5

ABSTRACT

Advances in Wire-Grid Modelling of Antennas
and Auxiliary Computer Graphics Systems
with the CP-140 Case Study

Colin Lionel Larose

The time and cost involved in physical testing of aircraft antennas makes computer simulation attractive. In this thesis, the method of moments with wire-grid modelling is used to simulate HF antennas on the CP-140/Aurora airframe. Optimal use is made of the Numerical Electromagnetics Code (NEC) through the EMC Laboratory's new wire-grid modelling program and computerized checking against established modelling guidelines. The mini-computer version, MININEC, is integrated to the existing laboratory software, and comparisons with NEC are started. Graphics programs are written for improved display of input impedance, radiated fields, and induced wire currents.

Two different antenna configurations are modelled with simple or complex models progressively optimized for agreement with measured results over the HF band. Simple stick models are seen to reproduce the main pattern characteristics over an extensive frequency range, whereas complex models, at the expense of additional computing time, produce the degree of agreement suitable for system range calculations. Accurate impedance curves are reproduced, which can be used to assess the tuning of antenna couplers.

ACKNOWLEDGMENTS

I wish to thank Dr. S. J. Kubina for the four exciting years spent under his supervision. I appreciate the challenging goals he has set before me, and his confidence in my fulfilling them. The excellence of his character has been an inspiration to me and other lab members.

I wish to thank Defence Research Establishment Ottawa for funding the work described in this thesis. I must also thank Dr. C. W. Trueman for the time he has wholeheartedly devoted in discussing with me the more difficult concepts that have enriched this work. I am grateful to Mike Marak and David Gaudine for their expert advice in text processing and output. Special thanks to David for enlivening the atmosphere of the laboratory with a unique sense of humor. The assistance of Miss Iona Farrell with the multiwriter was especially welcome. I want to thank also my good friend Sergio Prestipino, who assisted in the last stages of the CP-140 project and left a clear situation behind him when leaving for Northern Telecom.

My thanks to fellow workers Nguyen Lu Ba Lan, Benita Rosenzweig, and Michael Wong, who assisted me in other projects this summer, for their occasional help in preparing figures for this work. I fully appreciated their patience and respect during my busiest periods when I was less avail-

able for help or advice.

Ironically, the greatest contributors to this thesis are the less educated. I must thank my parents for their interest and support during my period of studies, but especially the time they have devoted to me in my early years. I vividly remember the private guidance and instruction I have received while my mind was most malleable. I must emphasize that this has strongly contributed to the intellect and character required in the completion of a project of this scope. Let this be a tribute to the family institution, which is fast disintegrating in this "evolving" society. I therefore dedicate this work to my parents.

TABLE OF CONTENTS

LIST OF ILLUSTRATIONS	viii
LIST OF TABLES	xii
LIST OF SYMBOLS	xiii
INTRODUCTION	1

PART ONE

ADVANCES IN WIRE-GRID MODELLING TOOLS

CHAPTER I. THE NUMERICAL ELECTROMAGNETICS CODE	7
Structure Geometry Input Format	7
Program Control Lines	10
Boundary Conditions and the Method of Moments	12
Current Expansion on Wires	15
Example: Current on Isolated Segment	21
The Solution Procedure	23
The Output Format	26
Validation of Models	29
Modelling Guidelines	29
Program CHECK	31
CHAPTER II. THE MINI-NUMERICAL ELECTROMAGNETICS CODE	37
The Input Format	38
Pulse Numbering	44
The Solution Procedure	47
The Output Format	51
Language Conversions	55
CHAPTER III. GRAPHICS SOFTWARE DEVELOPMENTS	57
Logarithmic Impedance Plots	57
Color Displays of Currents with SPCTRM	58
Use of Color for Current Magnitude	59
Use of Color for Current Phase	65
The User Interface	68
Displays of Radiation Patterns with MOVIE.BYU	74
The Plotting Process	77
Elemental Pattern Shapes	81

CHAPTER IV. NUMERICAL TECHNIQUES	83
Program ISOLEV	83
Radiated Power and Isotropic Level	84
The Military Standard MIL-9080 (USAF)	90
HF Aircraft Assessment Parameters	92
Program EFAR	96
Theoretical Formulation of EFAR	97
Validation of EFAR	103
Effect of Ground Plane	107

PART TWO

CP-140/AURORA HF ANTENNA CONFIGURATIONS

CHAPTER V. THE P3V-1 HF INSTALLATION	110
The Measurements	111
Model Generation	114
Thin Stick Models	116
Fat Stick Models	120
Radiation Patterns	124
Percentage of E-Theta Power	146
Impedance and Current Distribution	148
CHAPTER VI. THE CP-140 HF INSTALLATION	153
The Measurements	153
Model Generation	155
Stick Models	155
Complex Models	170
Radiation Patterns	180
Stick Models	180
Complex Models	208
Miscellaneous Tests	221
E-theta and Impedance	225
SUMMARY AND CONCLUSIONS	238
LIST OF REFERENCES	246

LIST OF ILLUSTRATIONS

1. Sample Input File for Program NEC	8
2. Tangential Cancellation of Impressed and Scattered Fields at the Surface of an Excited Segment . .	13
3. Current Basis Function Associated with a Segment .	16
4. Current Flowing unto the End Cap of a Segment with Finite Radius	18
5. Currents and Linear Charge Densities at a Junction of N Wires	19
6. Current Basis Function on Isolated Segment	23
7. Sample Solution File as Compressed by Program STRIP	28
8. Sample Output File of Program CHECK	32
9. Checking against the Seg/rad Error at a Junction of Two Segments at the Origin	35
10. Sample Run of MININEC	40
11. Procedure for Finding End Connection of Wire 1 in Program MINIGEN	43
12. Definition of MININEC Current Basis Functions in the Course of Geometry Entry	45
13. Use of Three Different MININEC Current Expansions on the Same Model, Resulting in the Same Current Distribution	48
14. Networks with Independent Loops, and Pulses Defined	49
15. SPCTRM Current Magnitude Displays with Different Resolution Indices	62
16. Distribution of the 61 Colors on the Current Magnitude Scale	63
17. Distribution of the 90 Colors around the Phase Circle	66
18. SPCTRM Displays with Modes 2 to 5	67
19. Choice of 8 Viewport Layouts in SPCTRM	69
20. SPCTRM Zooming Process in Two Stages	72
21. Effects of Freezing Current Scale	72
22. Standard Spherical Coordinate System	74
23. Comparison of Altitude Plots of Azimuth Patterns with MOVIE.BYU Plots	76
24. Derivations for MOVIE.BYU Plots of Viewing Angle and Axis Length	80
25. E-Theta, E-Phi and Power Density Patterns of a Short Dipole in Different Orientations	82
26. Statistics Computed and Inserted by ISOLEV into the Input Solution File	84
27. Use of the Z-Directed Current Element in Deriving the Far Field of a Segment of Arbitrary Location	98

28. Graph of the Sine-over-Argument Function over the Interval $(0, \pi)$	105
29. Comparison of the Normalized Far Field of a Current Element and a $.2\lambda$ Segment	106
30. Current-Carrying Segment over a Perfect Ground Plane, and Equivalent Free-Space Situation . . .	108
31. P3V-1 HF Antenna Installation	113
32. Original and Corrected PR Model	115
33. P3V-1 Stick Models T1 and T2 or T2L	119
34. P3V-1 Stick Models F1 and F2 or F2L	122
35. P3V-1 Stick Model F1'	123
36. Comparisons of Measured and Computed Principal Plane Patterns for Model T1 at 2, 4, 6, 8, 10, and 12 MHz	128
37. Comparisons of Measured and Computed Principal Plane Patterns for Model T2 at 2, 4, and 12 MHz	132
38. Comparisons of Measured and Computed Principal Plane Patterns for Model T2L at 2 and 4 MHz . . .	134
39. Principal Plane Patterns of Models T1 and T2 at 5 and 11 MHz	135
40. Comparisons of Measured and Computed Principal Plane Patterns for Model F1 at 2, 4, 6, 8, 10, and 12 MHz	137
41. Comparisons of Measured and Computed Principal Plane Patterns for Model F2 at 8 and 12 MHz . . .	141
42. Principal Plane Patterns of Models F1 and F2 at 11 MHz	143
43. Comparisons of Measured and Computed Principal Plane Patterns for Model F1' at 2 MHz	144
44. Altitude Plots at 2 MHz, Measured and Computed from Models T1, F1', and F1	145
45. Comparisons of Measured and Computed $\%E$ -Theta Curves for P3V-1 Thin and Fat Models	147
46. Comparisons of Measured and Computed Resistance and Reactance Curves for P3V-1 Thin Models	150
47. Comparisons of Measured and Computed Resistance and Reactance Curves for P3V-1 Fat Models	152
48. CP-140 HF Antenna Installation	162
49. CP-140 Stick Model S	162
50. CP-140 Stick Models SE and SE'	163
51. CP-140 Stick Models ST1, ST2, and ST3	164
52. CP-140 Stick Models S* and S*'	165
53. CP-140 Stick Models SF and SF*	166
54. Six Current Paths on the CP-140	167
55. CP-140 Stick Models SA1, SA2, and SA3	168
56. CP-140 Stick Models SA1*, SA2*, and SM	169
57. Markings on Drawings of the PR Model for Purposes of Digitization via DIDE	176
58. Choice of Wire Radii Based on Area Equivalence for a Circular Aircraft Cross-Section	176

59. CP-140 Complex Model S 177

60. Details of Antenna Connections on CP-140 Complex Models 178

61. CP-140 Complex Models CF and CD with Details of Antenna Connections 179

62. MOVIE.BYU Plots of Radiation Patterns at 2 MHz, Measured and Computed from Model S, Port and Starboard Antennas 188

63. Comparisons of Measured and Computed Principal Plane Patterns for Model S, Port Antenna, at 2, 6, 20, and 24 MHz 190

64. Comparisons of Measured and Computed Principal Plane Patterns for Model S, Starboard Antenna, at 2, 6, 20, and 24 MHz 193

65. Altitude Plots at 2 MHz, Port Antenna, Measured and Computed from CP-140 Stick Models 196

66. Altitude Plots at 2 MHz, Starboard Antenna, Measured and Computed from CP-140 Stick Models 201

67. Equivalent Ideal Dipole Orientations of Stick Models at 2 MHz, Port and Starboard Antennas 206

68. Magnitudes of Angular Errors in Equivalent Ideal Dipole Orientations of Stick Models at 2 MHz, Port and Starboard Antennas 207

69. MOVIE.BYU Plots of Radiation Patterns at 2 MHz, Measured and Computed from Model C, Port and Starboard Antennas 211

70. Comparisons of Measured and Computed Principal Plane Patterns for Model C, Port Antenna, at 2, 6, 20, and 24 MHz 213

71. Comparisons of Measured and Computed Principal Plane Patterns for Model C, Starboard Antenna, at 2, 6, 20, and 24 MHz 216

72. Equivalent Ideal Dipole Orientations of Complex Models at 2 MHz, Port and Starboard Antennas 219

73. Comparisons of Measured and Computed Principal Plane Patterns for Model CD, Port Antenna, at 24 MHz 220

74. Altitude Plots at 6 MHz, Starboard Antenna, Measured and Computed from Model S with NEC and MININEC 223

75. Altitude Plots for Model S at 6 MHz, Starboard Antenna, in Free Space and at 1 m and 30 m above Ground 224

76. Comparisons of Measured and Computed θ E-Theta Curves for Models S and C, Port and Starboard Antennas 230

77. Comparisons of Measured and Computed Impedance Curves for Model S, Port and Starboard Antennas 231

78. Impedances of CP-140 Stick Models at 2 MHz, Port and Starboard Antennas 232

79. Comparisons of Measured and Computed Impedance Curves for Model C, Port and Starboard Antennas	233
80. Comparisons of Measured Impedance Curves, Port Antenna, with Those of Model C Shunted with 15 and 30 pF	234
81. Impedance Curves for Port Antenna, 16 to 24 MHz: Comparison of Models C and CF, and Comparisons of Measurements with Model CF Shunted with 30, 40, 45, and 50 pF	235
82. Impedance Curves for Starboard Antenna, 16 to 24 MHz: Comparison of Models C and CF, and Comparisons of Measurements with Model CF Shunted with 30, 40, 45, and 50 pF	236

LIST OF TABLES

1. Sequence of 90 Colors with SETRGB Parameters	61
2. The 21 MIL-SPEC Angles and their Cosines	91
3. Comparison of CP-140 Path Lengths	159

LIST OF SYMBOLS

η_0	Intrinsic impedance of free space
λ	Wavelength
k	Phase constant (or wave number)
Δ	Segment length
a	Segment radius
s	Length-along-the-segment parameter
\hat{s}	Unit vector in reference segment direction
\hat{n}	Unit vector normal to wire surfaces
\hat{n}_c	Unit vector normal to wire end cap
V	Voltage applied to a segment
\vec{E}^i	Impressed electric field
\vec{E}^s	Scattered electric field
\vec{J}_s	Surface current density
\vec{L}	Linear operator acting on \vec{J}_s to derive \vec{E}_s
$I(s)$	Current function along a segment
$q(s)$	Linear charge density function along a segment
P	Radius dependent proportionality factor
γ	Euler's constant
X	Wire free-end constant
N	Order of solution in moment methods
$[G]$	Interaction matrix
$[L]$	Lower triangular matrix from factorization of $[G]$
$[U]$	Upper triangular matrix from factorization of $[G]$

[A]	Current basis function amplitude vector
[E]	Excitation vector
E_{θ}	Vertical component of electric far field
E_{ϕ}	Horizontal component of electric far field
S	Power density
P	Total radiated power
P_u	Useful radiated power
$P_{E_{\theta}}$	Total power radiated by E_{θ}
$P_{E_{\phi}}$	Total power radiated by E_{ϕ}
$P_{u\theta}$	Useful power radiated by E_{θ}
$P_{u\phi}$	Useful power radiated by E_{ϕ}
E_{iso}	Isotropic level
η_p	Radiation pattern efficiency
$\%E_{\theta}$	Percentage of E_{θ} power
$\%E_{\theta}^*$	Percentage of useful E_{θ} power
δ	Delta function
Sa	Sine-over-argument function

INTRODUCTION

This thesis describes research work accomplished by the author at the Electromagnetic Compatibility (EMC) Laboratory of Concordia over the past four years in relation to the CP-140 project. Being the first project undertaken by the author, it has reached a state of completion not yet attained by other projects and has been intimately connected with the major software developments described in this work.

Coverage of the HF antennas of the CP-140/Aurora aircraft is far from ideal but is typical of that obtained from wire antennas mounted on an airframe. They may radiate too little of the desired polarization, or not enough in the useful directions. Experimental pattern measurements must therefore be done in order to assess antenna performance throughout the frequency band of operation. A common measurement practice, less cumbersome than flight of the actual aircraft, is the use of a scale model. Extensive measurements are nevertheless prohibitive due to cost and time factors and are advantageously replaced by computer simulation.

The computer-aided approach requires a numerical model of the aircraft/antenna combination that can be analyzed with an electromagnetics computer code. Since validation of computer models requires comparisons of measured and computed results, the need of experimental measurements

is not completely eliminated, but validated computer models can be used afterwards to fill the gaps in the measured data. In addition, a computer model can provide additional information that is difficult or impossible to obtain by measurements, such as induced RF currents and near fields. Induced currents can give additional insight into the formation of radiation patterns, and near fields are useful for the assessment of the total electromagnetic environment and of hazards to personnel (Kubina, 1983b). A validated computer model can also be used to study the effects of changes in parameters such as position of the antenna, its length, or its spacing from the fuselage.

The computer modelling of the CP-140 antenna installation was of interest in itself for the further development of the modelling methodology. Advances were made in this area as well as in the meaningful display of electromagnetic data. Part One of the thesis is devoted to descriptions of the software that was tested, improved, or created for these purposes.

The Numerical Electromagnetics Code (NEC), developed at the Lawrence Livermore Laboratory of California, uses an integral-equation approach which is best suited for structures with dimensions up to several wavelengths (Burke and Poggio, 1980). This makes the program applicable to HF antennas on aircraft and therefore it was used throughout the

CP-140 project. In this program the modelling components are wires or patches. Wires are easier to define and wire-grid models lend themselves more naturally to interactive display programs. For these reasons and others, the wire-grid modelling technique was used exclusively. The technique is more advanced and refined in procedure than surface modelling. In surface modelling, problems of current discontinuities between patches (Bahoun, 1981) must be overcome by increasing the number of patches representing the conducting surface. This makes modelling of complicated surfaces very difficult and requires more NEC running time because of the extra computations.

The description of NEC in Chapter I serves as convenient introduction to wire-grid modelling and to the various modelling guidelines that must be followed. Descriptions of the input and output formats will identify respectively the problems of efficient model generation and meaningful interpretation of computed results. Details of the current expansion on wires are covered for purposes of critical comparison with MININEC. This code is the mini-computer version of NEC, acquired by the laboratory in 1983 and the subject of Chapter II. Its description parallels that of NEC to highlight similarities and differences. Interest in the program stems from the advantages having a smaller antenna analysis code executable on the laboratory's

own computer systems.

The vast amount of data generated by electromagnetics codes in the modelling of aircraft antennas calls for optimal display methods or data compression schemes. Chapter III describes graphics programs that were written by the author as improvements over display methods previously in use at the laboratory. Improved impedance and radiation pattern displays, in particular, were made possible with the acquisition of graphics packages DIGRAF (Warner, 1979) and MOVIE.BYU (Christiansen and Stephenson, 1985) respectively. The reader will appreciate the inclusion of impedance plots thus obtained in part two of this thesis. Plots of radiation patterns, however, are included mostly in the traditional polar plot or altitude plot forms because few improved plots had been produced for the CP-140 project at the time of writing. Chapter III closes with a description of a current color display program with photographs included to illustrate its important features. A more convenient means of color reproduction is not yet available at the laboratory, and therefore the cost and delay in producing photographs has restricted their use to this part of the thesis.

Chapter IV describes changes that are suggested or that were implemented in two programs, ISOLEV and EFAR, which exploit numerical techniques to extend the usefulness of the antenna analysis programs. Hence full theoretical

surveys of the programs are supplied. The case of ISOLEV brings in the topic of data compression via aircraft assessment parameters. Use of one of these, the percentage of E-theta power, is exploited in Part Two.

Part Two of the thesis describes the contribution of the author to one major portion of a contract from Defence Research Establishment Ottawa (DSS Contract No. 8SU82-00074): continuation of the work with the method of moments as applied to the design and analysis of HF aircraft antennas. Previous work had been directed at the CL-28/Argus aircraft because a comprehensive data set of HF antenna patterns was available only for this airframe. Studies on this phased-out aircraft type were re-assigned to one of immediate interest to the Canadian Forces, the CP-140/Aurora airframe, as soon as radiation pattern data became available. This new project was undertaken by the author in summer 1982 and has since been the subject of several reports (Kubina, 1983a, 1983b, and 1985) and appendices (Larose and Kubina, 1983; Larose, 1985) that are here merged for the first time.

PART ONE

ADVANCES IN WIRE-GRID MODELLING TOOLS

CHAPTER I

THE NUMERICAL ELECTROMAGNETICS CODE

The Numerical Electromagnetics Code (NEC) is the most advanced computer code available for the analysis of electromagnetic problems. It analyses the electromagnetic response of models that may include a combination of smooth surfaces, wires, nonradiating networks, transmission lines, perfect or imperfect conductors, lumped element loading and a ground plane that may be either a perfect or imperfect conductor (Burke and Poggio, 1980). The excitations may be either voltage sources on the structure or an incident plane wave of arbitrary polarization, and the output may include induced currents or charges, near electric or magnetic fields, and radiated (far) fields. For the purpose of this work, the description of NEC will be restricted to those aspects related to wire-grid modelling.

Structure Geometry Input Format

Figure 1 shows a small NEC input file to illustrate the input requirements. The file is divided into three major sections: the comment lines, the structure geometry input, and the program control lines. A two-character label begins each input line to identify its function.

```

CM WIRE T-ANTENNA
CM
CM OVER PERFECT GROUND PLANE
CM
CM 4 SEGMENTS
CM
CM COMPUTED
CE
GW 1 2 0.000 0.000 0.000 0.000 0.000 0.000 0.004
GW 2 1 0.000 -0.170 0.000 0.000 0.000 0.000 0.004
GW 3 1 0.000 0.170 0.000 0.000 0.000 0.000 0.004
GE 1
EX
FX 0 0 199.00
CM 1
EX 0 1 1 1.0
RP 0 10 1 0. 0. 10. 0.
RP 0 10 1 0. 90. 10. 0.
EN

```

Fig. 1. Sample input file for program NEC

Comment lines (CM) may be included to identify the run and describe its structure parameters. A CE line must in any case be included to signal the end of the comment section. Wires are specified in the geometry section by means of GW lines. These specify the following wire parameters in order: tag number, number of segments, end one coordinates (x,y,z), end two coordinates (x,y,z), and radius, all in meters. Wires are considered perfect conductors unless otherwise stated in the control lines. The distinction between ends one and two of a wire serves to define a positive reference direction for current.

The second parameter, the number of segments into which the wire will be divided, allows to quickly specify a straight chain of equal length segments. The tag number is any integer from 1 to 999 which is assigned to all the seg-

ments of the wire. It is for later use when a segment must be referenced, such as for voltage source connection or lumped loading. It is optional and may be left blank, in which case the segments of the wire cannot be referenced. The radius is assigned to all segments of the wire. If however it is zero or blank, a second line (GC) is read to set parameters to taper the radius from one end of the wire to the other. This line may also specify a parameter to taper the segment lengths.

Two wires are considered electrically connected if their connected ends have identical coordinates. If input is in units other than meters, a GS line must be used to scale the units to meters. The geometry section ends with a GE line. The integer 1 may follow the GE label to inform NEC that a ground plane will be specified in the program control section. This modifies the structure symmetry as required by the method of images.

Other useful structure geometry lines that apply to wire-grid modelling have not been used by the author and are therefore not explained here. These include in particular GF (Numerical Green's Function) and GX (reflect structure), which may be instrumental in saving computer time.

Program Control Lines

Control lines serve to set electrical parameters for the model, select options for the solution procedure, and request data computation.

EK, FR, GN and LD lines were used by the author to set electrical parameters for the models tested. The EK line is the extended thin-wire flag. It provides greater precision in computing the near fields of thick wires at the expense of additional computation time. Its use is further explained in a later section.

The FR line specifies the frequency in MHz. It can also specify a set of frequencies by providing a linear or multiplicative frequency stepping increment and the number of frequency steps. If no FR line is present, the wavelength is assumed to be 1 m, i.e. a frequency of 299.8 MHz. This causes the geometry to be in units of wavelength, which may be desirable in theoretical problems.

The GN line followed by a 1 indicates the presence of an infinite, perfectly conducting ground plane at $z=0$. Segments having one end at $z=0$ are considered connected to the ground plane. Several other types of ground planes may be specified but were not used by the author.

LD lines are used to specify the impedance loading on one or more segments. A segment is referenced by its tag number and its rank among the set of segments having this

tag number. It may also be referenced by its absolute segment number, i.e. its order of occurrence in the entire wire-grid model, but this scheme is seldom advantageous. A sequence of segments on a wire or a sequence of absolute segment numbers may also be specified on one line, and several LD lines may be grouped to achieve the desired loading. Series and parallel RLC circuits can be generated, with absolute or per-meter units. Impedance (resistance and reactance) and wire conductivity (mhos/meter) can also be specified.

Only the EX line has been used by the author to select options for the solution procedure. It was used to specify voltage sources on wire-grid models, but it can also specify an elementary current source, or a plane wave incident on the structure. The latter option makes it possible to solve receiving as well as scattering problems. Parameters specified for voltage sources are the real and imaginary parts in volts, and the segments excited in the same way as in LD lines.

RP, CP, and EN lines were used by the author to request data computation. RP lines are requests for radiation pattern (far fields) computation. Since this requires the knowledge of wire currents, program execution is initiated, causing the interaction matrix to be computed and factored, and the wire currents to be computed. The RP line supplies

a sequence of theta and phi angles, and the radiated field is computed at every combination of these theta and phi values, varying theta first. A sequence of angles is specified by the initial value, the number of values wanted and the angle increment, all in degrees.

CP lines request calculation of the maximum coupling between all pairs of up to five segments. The specified segments must be excited one at a time in the specified order and the currents computed. After this is done the couplings are computed and printed. The EN line indicates to the program the end of all execution. Other control lines of potential utility include NE (near electric field request), WG (write Numerical Green's Function file) and XQ (execute).

Boundary Conditions and the Method of Moments

The boundary condition for the electric field at the surface of a perfectly conducting body is that the tangential component vanishes to zero. Consider now a perfectly conducting wire segment of length Δ along which is impressed an axially-directed sinusoidal field of magnitude E . This may be thought of as distributing a voltage source of magnitude $V = E\Delta$ along the segment length. Surface currents will be induced on the segment in such a way as to create a scattered field whose tangential component at the

surface of the segment cancels out the impressed field, thus satisfying the boundary condition (see Figure 2).

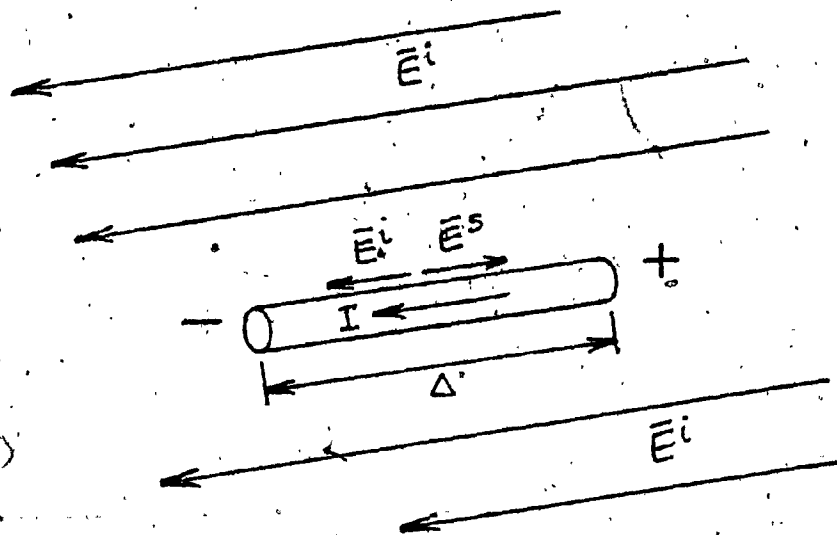


Fig. 2. Tangential cancellation of impressed and scattered fields at the surface of an excited segment

If now other segments are placed in the vicinity of the excited one, and possibly connected to it, they will be subjected to its scattered field. It follows that currents will also be induced on these segments in such a way that the electric field boundary condition is satisfied everywhere on the surface of every segment. This may be expressed mathematically as $\hat{n} \times (\vec{E}^i + \vec{E}^s) = 0$, where \hat{n} is the unit vector normal to wire surfaces, and \vec{E}^i , \vec{E}^s are the impressed and scattered fields. If we denote by \bar{L} the linear operator that generates the fields scattered by an arbitrary

surface current density function \bar{J}_s , we have $\bar{E}^s = \bar{L}(\bar{J}_s)$.
Substituting into the previous expression,

$$\hat{n} \times \bar{L}(\bar{J}_s) = -\hat{n} \times \bar{E}^i.$$

In NEC, this equation is solved for \bar{J}_s through the method of moments (Harrington, 1968). In this method, the unknown function is approximated by the weighted sum of N linearly independent expansion, or basis, functions defined in the domain of interest. The N weighting factors involved are solved for by satisfying the equality at N distinct points in the domain. A system of N equations in N unknowns is thus generated, and the coefficients are obtained by matrix algebra.

Satisfying the equality at distinct points is known as the collocation method of solution, or point matching. General solution methods call for a set of N testing, or weighting, functions defined over the domain of interest. An application of this will be seen in the solution method used by MININEC (Chapter II). For generalization purposes, note that point matching may be considered as the use of N impulses for weighting functions, located at the match points.

Current Expansion on Wires

This section describes the choice of current basis functions used in the method of moments formulation of NEC. To begin with, two approximations applicable to thin wires are made to make the solution easier:

- a) Transverse currents can be neglected relative to axial currents on the wire,
- b) The circumferential variation in the axial current can be neglected.

By condition a) we need to solve only for an axial component of current, and by condition b) this component is solely a function of axial position on the wire. Using s as a length-along-the-wire parameter, we therefore solve for $J_g(s)$, or equivalently, the total current $I(s) = 2\pi a J_g(s)$, where a is the wire radius. The boundary equation then becomes

$$\hat{n} \times \bar{L}(I(s)) = -\hat{n} \times \bar{E}^i$$

Each basis function used in NEC for the expansion of wire currents is defined over a subsection of the domain of solution, i.e. part of the segments of the model. This is called the method of subsections. In a model comprising N wire segments, there is a current basis function associated with every segment, resulting in an N th-order approximation.

Figure 3 shows the basis function associated with a given segment; it is defined not only over that segment but also extends over the m segments connected to its entrance node and the n segments connected to its exit node. This function is defined as follows over the $1+m+n$ segments involved:

$$I_1(s) = A_1 + B_1 \sin(ks) + C_1 \cos(ks),$$

$$-\Delta_i/2 < s < \Delta_i/2, \quad i = 0, 1, \dots, m, m+1, \dots, m+n,$$

where k is the phase constant ($2\pi/\lambda$) and the Δ_i 's are the lengths of the segments.

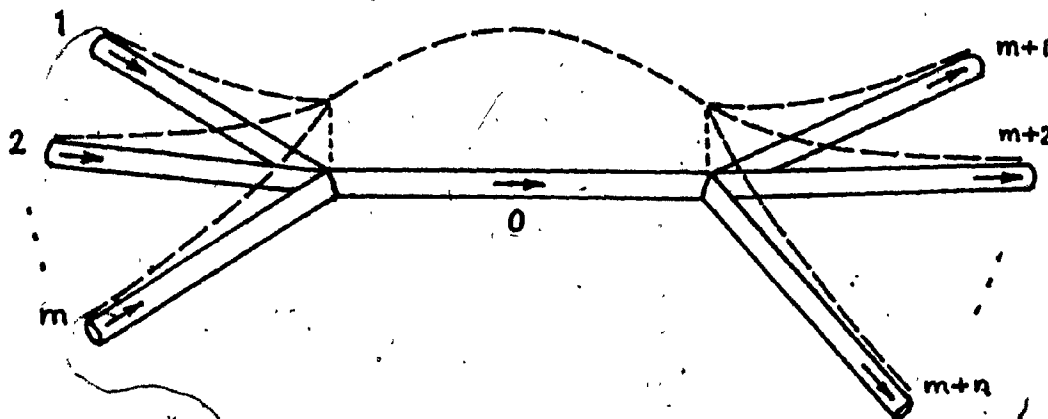


Fig. 3. Current basis function associated with segment 0, shown extending over connected segments

This function involves $3(1+m+n) = 3+3m+3n$ unknowns, of which $2+3m+3n$ must be eliminated. This defines the exact shape of the basis function and leaves one amplitude constant (in general complex) to be determined by the method of

moments, along with the $N-1$ amplitudes of the remaining basis functions. A total of $2+3m+3n$ equations involving the A's, B's and C's are obtained for this purpose from local conditions on the current.

Before giving details of these equations, two conditions on current are first described: the "free-end" current condition and the King-Wu charge density constraint.

In a study referred to by Burke and Poggio (1980) a condition relating the current at a wire end to the current derivative is derived as follows:

$$I(s) \Big|_{s \text{ at end}} = \frac{-(\hat{s} \cdot \hat{n}_c) J_1(ka)}{k J_0(ka)} I'(s) \Big|_{s \text{ at end}},$$

where J_1 and J_0 are Bessel functions of order 1 and 0 and \hat{s} is the unit vector along wires. The unit vector \hat{n}_c is normal to the end cap; hence $\hat{s} \cdot \hat{n}_c$ is -1 at the entrance end and $+1$ at the exit end. This means that on a wire of finite radius, the current can flow onto the end cap and hence be non-zero at the wire end. Figure 4 illustrates the situation and the variables involved.

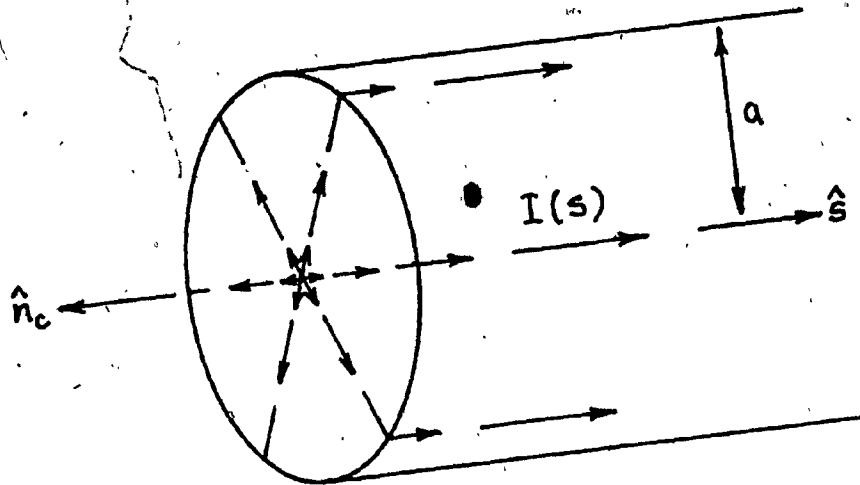


Fig. 4. Current flowing onto the end cap of a segment with finite radius

Wu and King (1976) have derived a condition relating the linear charge densities on n connected wires at the junction point:

$$P_1 q_1(s) \Big|_{s \text{ at junction}} = P_2 q_2(s) \Big|_{s \text{ at junction}} = \dots = P_n q_n(s) \Big|_{s \text{ at junction}}.$$

The P 's are radius dependent proportionality factors given as

$$P_i = \ln(2/ka_i) + \gamma,$$

where a_i is the radius of wire i and γ is Euler's constant, equal to about 0.5772. Figure 5 illustrates the situation. Noting that the equation of continuity requires $I'(s) =$

$-j\omega q(s)$, a similar relation can be obtained to relate current derivatives at a junction:

$$P_1 I_1'(s) \Big|_{s \text{ at junction}} = \dots = P_n I_n'(s) \Big|_{s \text{ at junction}}$$

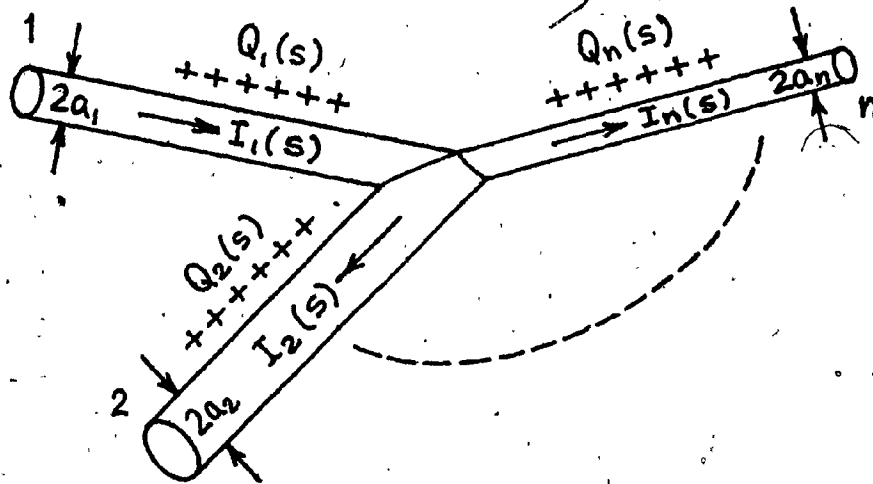


Fig. 5. Currents and linear charge densities at a junction of n wires

With the help of these relations one can begin to generate the $2+3m+3n$ equations from which a given basis function will take form. The 2 first equations are conditions on the current at each end of segment 0 (the segment associated with the basis function). Depending on whether this segment has other segments connected to its two ends, the equations will come from either the free-end condition on current or Kirchoff's law of current continuity (KCL).

Therefore, for the entrance node:

$$I_0(-\Delta_0/2) = \begin{cases} (X/k) I_0'(-\Delta_0/2) & \text{if } m = 0 \text{ (free-end cond.)} \\ \sum_{i=1}^m I_i(\Delta_i/2) & \text{if } m \neq 0 \text{ (KCL),} \end{cases}$$

where X is the free-end constant $J_1(ka_0)/J_0(ka_0)$.

Similarly, for the exit node:

$$I_0(\Delta_0/2) = \begin{cases} -(X/k) I_0'(\Delta_0/2) & \text{if } n = 0 \text{ (free-end cond.)} \\ \sum_{i=m+1}^{m+n} I_i(-\Delta_i/2) & \text{if } n \neq 0 \text{ (KCL).} \end{cases}$$

The next $3m$ equations are conditions on the current at ends of segments 1 to m (segments connected to entrance node of segment 0):

- 1) $P_i I_i'(\Delta_i/2) = P_0 I_0'(-\Delta_0/2)$ (King-Wu constraint),
 - 2) $I_i'(-\Delta_i/2) = 0$ (zero current derivative),
 - 3) $I_i(-\Delta_i/2) = 0$ (zero current),
- $i = 1, 2, \dots, m.$

Equations 2) and 3) are obvious from an observation of Figure 3.

The last $3n$ equations are similar conditions at ends of segments $m+1$ to $m+n$ (segments connected to exit node of segment 0):

- 1) $P_i I_i'(-\Delta_i/2) = P_0 I_0'(\Delta_0/2)$ (King-Wu constraint),
 - 2) $I_i'(\Delta_i/2) = 0$ (zero current derivative),
 - 3) $I_i(\Delta_i/2) = 0$ (zero current),
- $i = m+1, m+2, \dots, m+n.$

The sum of the N current basis functions on the model results in the current on each segment being represented by three terms: a constant, a sine and a cosine. This choice was made as close as possible to the actual current distribution because for finite N , the sum of the basis functions cannot exactly equal a general current distribution. This expansion has been shown to provide rapid solution convergence, and it has the added advantage that the fields of the sinusoidal currents are easily evaluated in closed form. Note finally that if individual basis functions conform to the conditions on current mentioned above, the total current distribution will also by superposition.

Example: Current on Isolated Segment

An example is now given of how the basis function is derived for a single segment in free space, i.e. $m=n=0$.

This function involves $3+3(0)+3(0) = 3$ unknowns, hence two equations are required, obtained in this case from the free-end current condition applied at both ends of the segment:

$$1) I(-\Delta/2) = (X/k) I'(-\Delta/2),$$

$$2) I(\Delta/2) = -(X/k) I'(\Delta/2).$$

Substituting $I(s) = A + B\sin(ks) + C\cos(ks)$, and hence $I'(s) = kB\cos(ks) - kC\sin(ks)$, one obtains:

$$1) A - B\sin(k\Delta/2) + C\cos(k\Delta/2) = XB\cos(k\Delta/2) + XC\sin(k\Delta/2),$$

$$2) A + B\sin(k\Delta/2) + C\cos(k\Delta/2) = -XB\cos(k\Delta/2) + XC\sin(k\Delta/2).$$

Adding the above equations, one gets $2A + 2C\cos(k\Delta/2) = 2XC\sin(k\Delta/2)$, from which

$$C = \frac{A}{X\sin(k\Delta/2) - \cos(k\Delta/2)},$$

and subtracting the two equations, one gets $B=0$.

Substituting into the original equation for $I(s)$,

$$I(s) = A \left[1 + \frac{\cos(ks)}{X\sin(k\Delta/2) - \cos(k\Delta/2)} \right],$$

where A is now the complex amplitude constant to be deter-

mined.

NEC initially sets A to -1 , from which the basis function is

$$I(s) = \frac{\cos(ks)}{\cos(k\Delta/2) - X\sin(k\Delta/2)} - 1.$$

Figure 6 shows a plot of this function on a short wire ($k\Delta/2 \ll \pi/2$). As expected the current magnitude tapers down to a finite value near the ends.

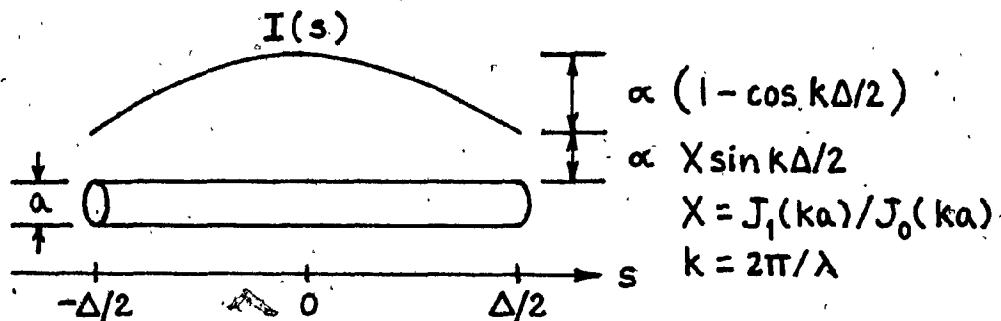


Fig. 6. Current basis function on isolated segment

The Solution Procedure

Having defined the shape of the N current basis functions on the N -segment wire-grid model, the electric field boundary condition is then enforced at N points on the surface of the model. Each segment has a sample point located on its surface half-way between its end caps. At this stage two additional thin-wire approximations are introduced

to make the solution easier:

- a) The boundary condition on the electric field need be enforced in the axial direction only,
- b) The current can be represented by a filament on the wire axis.

Condition a) reduces the boundary condition from a vector equation to the scalar equation

$$\hat{s} \cdot \bar{L}(I(s)) = -\hat{s} \cdot \bar{E}^i,$$

and condition b) simplifies the evaluation of the fields scattered by a given segment. The latter condition may appear to nullify the effects of wire radius, but this is still taken into account by the fact that match points are located on the surface of the wires. For thicker wires, the filament approximation starts to break down and for this purpose NEC provides the EK option to integrate the current over the actual surfaces.

Enforcing the boundary condition at a point creates a linear equation involving the N unknown basis function amplitudes. Doing this at every match point generates an N by N linear system of equations that can be written in matrix notation as $[G][A] = [E]$. Element G_{ij} is the axial component of the electric field scattered at the match point of segment i by the jth current basis function; hence $[G]$ is

sometimes called the interaction matrix. Element A_i is the unknown amplitude of the i th basis function, and element E_i is the negative of the axial component of the electric field impressed at the match point of segment i . It follows that the elements of $[E]$ are all set to zero except for those corresponding to the excited segments.

The matrix equation is solved in NEC by Gauss elimination with L-U decomposition. Matrix $[G]$ is factorized into the product of a lower triangular matrix $[L]$ and an upper triangular matrix $[U]$, yielding $[L][U][A] = [E]$. The solution $[A]$ is then computed in two steps: forward substitution to solve $[L][F] = [E]$, and backward substitution to solve $[U][I] = [F]$.

L-U decomposition is the major computational effort and takes approximately $1/3 N^3$ multiplication steps; this causes execution time to rise sharply with the number of segments in the model. Matrices $[L]$ and $[U]$ once obtained are saved in NEC since induced currents may be computed for a number of different excitations. This then requires only a repetition of the forward and backward substitutions.

The importance of correctly ordering certain control lines in the NEC input file can now be understood. Consider for example the two sets of lines below. These request execution (XQ) for all combinations of two excitations and two loadings:

- 1) FR, EX1, LD1, XQ, LD2, XQ, EX2, LD1, XQ, LD2, XQ,
- 2) FR, LD1, EX1, XQ, EX2, XQ, LD2, EX1, XQ, EX2, XQ.

Loading affects the interaction matrix but not excitation. In the first set, the loadings are varied first, so that calculation and factoring of the matrix is required four times. In the second set, however, this is required only twice because excitations are varied first.

The Output Format

The memory limitations inherent to the mini- and micro-computer systems of the EMC Laboratory make it necessary to execute NEC on the larger Cyber 835 system of Concordia University. Input files for the program are created using laboratory facilities and transferred to the Cyber by a process called "spooling out". Solution files obtained there must then be "spooled in" so that the results may be interpreted by suitable graphics programs.

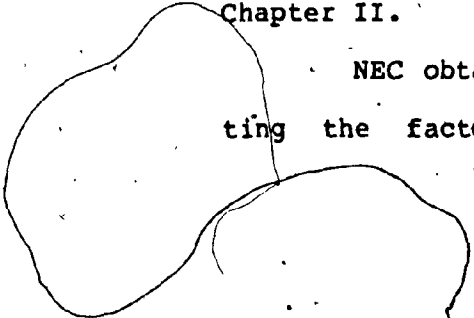
NEC solution files supply exhaustive information about any data requested, much of which is not particularly relevant to the user. The resultant excessive file size is then further aggravated by the output format used. To compress the information and hence reduce the spooling effort, a program called STRIP, written by Concordia professor C. W. Trueman, is in use at the laboratory. This program creates a compressed solution file consisting of the origi-

nal NEC input file to which is appended the solution file with all unnecessary data stripped away. An example of this file appears in Figure 7.

The output data extracted from the solution file include the frequency, the impedances across excited segments, the currents at segment match points in absolute segment order, and radiated fields in the selected planes. Impedances are given in terms of resistance and reactance, currents in terms of magnitude and phase, and electric fields in terms of E-theta and E-phi magnitude. In a second version of STRIP provision is made to retain the phases of the field components. This information package is extracted as many times as there are frequencies contained in the solution file, and the total computer time consumed is retained in the end.

It must be noted that the total current at a segment match point is not the exclusive effect of the particular current basis function associated with that segment. Rather, NEC computes the current by summing the contributions of all basis functions extending onto the segment. It will be seen that this unscrambling of data is not carried on in MININEC. How the author handled this is explained in Chapter II.

NEC obtains its radiated field magnitudes by omitting the factor e^{-jkr}/r from the far field expressions.



```

CN WIRE T-ANTENNA
CN
CN OVER PERFECT GROUND PLANE
CN
CN 4 SEGMENTS
CN
CN COMPUTED
CV
CV 1 2 0.000 0.000 0.000 0.000 0.000 0.000 0.000
CV 2 1 0.000 -0.170 0.000 0.000 0.000 0.000 0.000
CV 3 1 0.000 0.170 0.000 0.000 0.000 0.000 0.000
GE 1
SK
FR 0 0 299.00
GN 1
EX 0 1 1 1.0
RF 0 10 1 0. 0. 10. 0.
RF 0 10 1 0. 70. 10. 0.
CN
FREQUENCY 2770E+03 MHZ
PORT 1 2 = 10604E+02 20550E+02
CURRENTS
.0317E-01 -62.5
.4251E-01 -43.0
.1312E-01 116.9
.1312E-01 116.9
RF 0. 0. 1000E+02 0. 10 1
.186E-14
.215E+00 .322E-14
.425E+00 0.
.625E+00 0.
.809E+00 .166E-14
.971E+00 .166E-14
.111E+01 .166E-14
.121E+01 0.
.127E+01 0.
.129E+01 0.
RF 0. 7000E+02 1000E+02 0. 10 1
.186E-14 .930E-24
.244E+00 .253E-12
.512E+00 .674E-12
.722E+00 .637E-12
.917E+00 .722E-12
.106E+01 .720E-12
.117E+01 .631E-12
.124E+01 .467E-12
.128E+01 .248E-12
.129E+01 .740E-23
CN COMPUTER TIME CONSUMED = 2.766 SECS

```

Fig. 7. Sample solution file as compressed by program STRIP

This may not be thought of as the radiated fields at a radial distance of 1 m unless this is in the far field region.

Validation of Models

In the design of a wire-grid model certain modelling guidelines must be followed, such as detailed in the NEC User's Guide (Burke and Poggio, 1980). For example, wire segmentation must be fine enough so that segment lengths allow sufficient resolution in the computed currents, and wire radii must be kept compatible with the various thin-wire approximations of the code. A description is given here of the modelling guidelines for NEC and of a program written by the author to test models against these rules.

Modelling Guidelines

Geometrical as well as electrical factors come into play. Geometrically, the segments should follow the paths of conductors as closely as possible, using a piece-wise linear fit on curves.

The main electrical consideration is the segment length Δ relative to the wavelength λ . Good current resolution is obtained for segments as long as 0.1λ ; this is therefore what the user may want to aim for to reduce the number of segments in his model. He might have to use

smaller wires, however, to model critical regions such as the antenna. There is no theoretical minimum segment length, although segments less than 0.001λ lead to numerical inaccuracy and should be avoided. Segments somewhat longer than 0.1λ may be acceptable on long wires with no abrupt changes.

The accuracy of the numerical solution is also dependent on Δ/a , the ratio of segment length to radius. Studies have shown that Δ/a must be greater than about 8 for good field computations, but that reasonable current solutions may be obtained with Δ/a down to 2. Use of the extended thin-wire kernel, invoked by the EK control line, extends the limit on Δ/a to smaller values. With this option, good field computations are obtained with Δ/a down to about 2, and reasonable current solutions with Δ/a down to 0.5.

The limit on the ratio of wavelength to radius, λ/a , is dependent on the tendency of the excitation to produce circumferential current or current variation. The manual suggests for safety that $2\pi a/\lambda$ be kept much less than 1, and otherwise to question the validity of the model. Note now what happens when the previous conditions on Δ/λ and Δ/a are both pushed to their limit. The ratio $2\pi a/\lambda$ becomes $2\pi(\Delta/\lambda)/(\Delta/a) = 2\pi(0.1/0.5) = 0.4\pi =$ approximately 1.26, which is not even less than 1. The con-

clusion is that limits on Δ/λ and Δ/a may not be exploited simultaneously.

Studies have shown that severe errors result when the center of one segment falls within the radius of another. This is most likely to occur where two thick wires connect at a small angle. The extreme case where two segments overlap is meaningless and may result in a singular matrix equation. Finally, a large radius change between connected segments may decrease accuracy. This may be handled by making the radius change in steps over several segments.

Program CHECK

The reader can now appreciate the need of a computer program that would systematically check wire-grid models against the above criteria and report incompatibilities in an orderly manner. Program CHECK was written by the user for this purpose in 1982. A sample output of the program appears in Figure 8. CHECK prints useful statistics for an input wire-grid model and reports 8 types of errors. The first four types are detected by analyzing each wire as a unit, and the last four by analyzing the junction of every pair of connected wires.

The first "individual" incompatibility is the zero length wire, which occurs when the same coordinates are assigned by mistake to the start and end points of a wire.

```

-----
*
* PROGRAM CHECK VERSION 2 REVISION 1 *
*
* NECIN FILE NAME: .NECIN.DAT *
* CHECK FILE NAME: CHECK.OUT *
*
* FREQUENCY: 8.00 MHZ *
* WAVELENGTH: 37.50 M *
* EK OPTION: USED *
*
-----

```

KEY TO THE TABLE BELOW:

UNDER THE INFO COLUMN IS THE HIGHEST LEVEL OF ERROR DETECTED
FOR EACH INDIVIDUAL WIRE: ' ' = ACCEPTABLE

'N' = NOTE

'W' = WARNING

'E' = ERROR

WIRE	TAG	#	ABSOLUTE	RADIUS	LENGTH OF	LENGTH OF	SEG/	SEG/	INFO
#	#	SEC	SEC	#S	(M)	WIRE (M)	SEGS (M)	WAVE	RADIUS
1	1	1	1-	1	0.0100	0.9469	0.9469	0.0253	94.69
2	2	11	2-	12	0.0100	19.7358	1.7942	0.0478	179.42
3	210	1	13-	13	0.6420	1.3569	1.3569	0.0362	2.11
4	211	1	14-	14	0.6420	1.3198	1.3198	0.0352	2.04
5	212	1	15-	15	0.6420	0.7492	0.7492	0.0200	1.17
6	213	1	16-	16	0.6420	1.8774	1.8774	0.0501	2.92
7	254	1	17-	17	0.6410	1.7621	1.7621	0.0470	2.75
8	262	1	18-	18	0.6410	1.7620	1.7620	0.0470	2.75
9	270	1	19-	19	0.6410	1.7620	1.7620	0.0470	2.75
10	284	1	20-	20	0.6410	1.7620	1.7620	0.0470	2.75
11	296	1	21-	21	0.6410	1.8616	1.8616	0.0496	2.90

Fig. 8a. Sample output file of program CHECK,
first part

```

-----
*
*   INDIVIDUAL INCOMPATIBILITIES
*
*
-----

```

KEY TO THE TABLE BELOW:

```

ZERO LENGTH  ERROR:  LENGTH OF WIRE < .01 M
SEC/WAV     NOTE:   .05 < SEC/WAVE < .1
            WARNING: .10 < SEC/WAVE < .2
            ERROR:   SEC/WAVE > .2 OR < .001
SEC/RAD     WARNING: 2.0 < SEC/RAD < 8 WITHOUT EK OPTION
            ERROR:   0.5 < SEC/RAD < 2 WITH EK OPTION
            ERROR:   SEC/RAD < 2.0 WITHOUT EK OPTION
            ERROR:   SEC/RAD < 0.5 WITH EK OPTION
WAV/RAD     ERROR:   WAVE/RAD < 30

```

```

TAG # TYPE OF ERROR: ZERO LENGTH SEC/WAV SEC/RAD WAV/RAD
-----
212 W
213 N

```

```

-----
*
*   INCOMPATIBILITIES AT JUNCTIONS
*
*
-----

```

KEY TO THE TABLE BELOW:

```

COINCIDENCE ERROR: BOTH WIRES COINCIDENT
SEC/SEG     ERROR: LONGER SEGMENT/SHORTER SEGMENT ) 5
RAD/RAD     WARNING: LONGER RADIUS/SHORTER RADIUS ) 5
            ERROR: LONGER RADIUS/SHORTER RADIUS ) 10
SEC/RAD     ERROR: CENTER OF ONE SEGMENT WITHIN OTHER RADIUS

```

```

1ST TAG # 2ND TAG # TYPE: COINCIDENCE SEC/SEG RAD/RAD SEC/RAD
-----
1 212 E
1 213 E
1 296 E
212 262 E

```

Fig. 8b. Sample output file of program CHECK, second part

The second is the seg/wav error. An error is reported if Δ is greater than 0.2λ or less than 0.001λ , a warning if it is greater than 0.1λ , and a note if it is greater than 0.05λ . The third is the seg/rad error. Here the criteria depend on whether the normal or the extended thin-wire kernel is used. Without the EK option, an error is reported if Δ/a is less than 2, and a warning if it is less than 8. With the EK option, the same Δ/a limits are respectively 2 and 0.5.

The fourth individual incompatibility is the wav/rad error. The criterion $2\pi a/\lambda \ll 1$ is equivalent to $\lambda/a \gg 2\pi$ or 6.2832. It was decided to report an error if λ/a is less than 30.

The first incompatibility at junctions is coincidence of wires; i.e. two wires having identical end points. This is most likely to occur if a given wire is inadvertently repeated in the file. The second is the seg/seg error. An error is reported if the segment lengths of two connected wires differ by a factor of more than 5. Checking of this criterion not mentioned in the NEC modeling guidelines was requested by Dr. C.W. Trueman. The third is the rad/rad error. It was decided to report an error if the radii of two connected wires differ by a factor of more than 5.

The fourth incompatibility at junctions occurs between the two connected segments of two connected wires. An error is reported if the center of one segment falls within the radius of the other. An efficient mathematical procedure was worked out to solve this problem as illustrated in Figure 9.

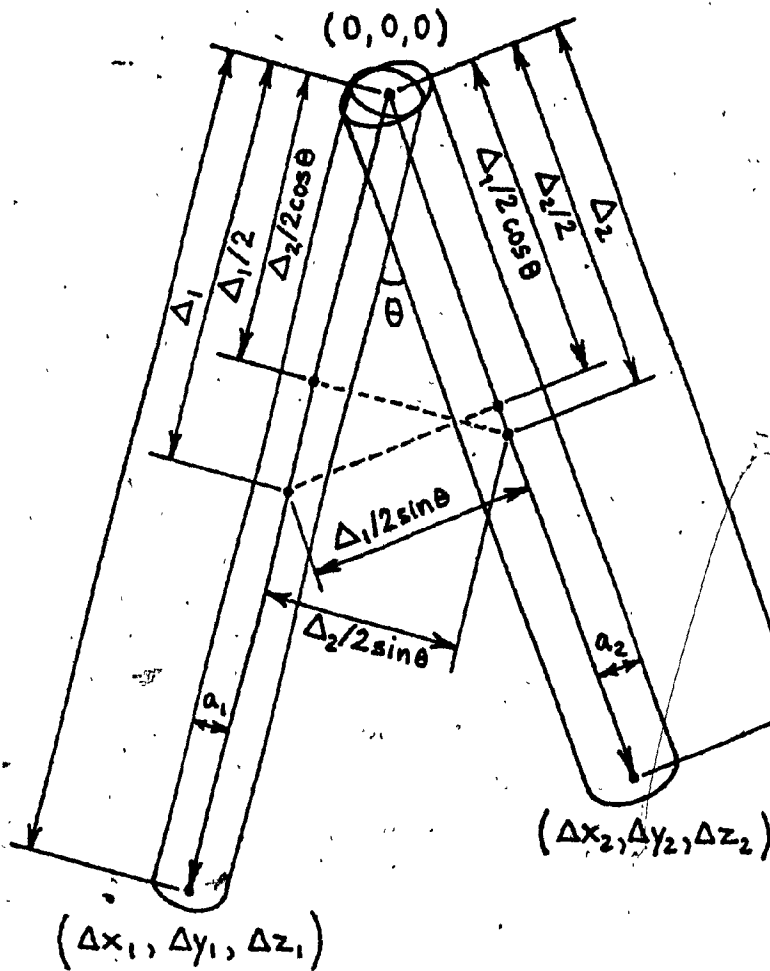


Fig. 9. Checking against the seg/rad error at a junction of two segments at the origin

Segments 1 and 2 are connected at an angle θ , they have radii a_1 and a_2 , and their unconnected ends have coordinates $(\Delta x_1, \Delta y_1, \Delta z_1)$ and $(\Delta x_2, \Delta y_2, \Delta z_2)$ relative to their common end. Squared lengths of segments 1 and 2 are therefore $\Delta_1^2 = (\Delta x_1)^2 + (\Delta y_1)^2 + (\Delta z_1)^2$ and $\Delta_2^2 = (\Delta x_2)^2 + (\Delta y_2)^2 + (\Delta z_2)^2$ and the dot product of the two vectors along the segments is $p = \Delta_1 \Delta_2 \cos \theta = \Delta x_1 \Delta x_2 + \Delta y_1 \Delta y_2 + \Delta z_1 \Delta z_2$.

The dot product is first computed and if it is negative, i.e. θ exceeds 180 degrees, the situation is safe. Otherwise analysis continues and squared lengths of the segments are computed. Figure 9 shows that an error occurs if either of these two conditions is true:

- 1) $(\Delta_2/2) \cos \theta < \Delta_1$ and $(\Delta_2/2) \sin \theta < a_1$,
- 2) $(\Delta_1/2) \cos \theta < \Delta_2$ and $(\Delta_1/2) \sin \theta < a_2$.

These conditions are easily checked by using $\cos \theta = p / \Delta_1 \Delta_2$ and $\sin^2 \theta = 1 - \cos^2 \theta = 1 - p^2 / \Delta_1^2 \Delta_2^2$. The conditions for error then become either of these two:

- 1) $p < 2\Delta_1^2$ and $p^2 > \Delta_1^2 (\Delta_2^2 - 4a_1^2)$,
- 2) $p < 2\Delta_2^2$ and $p^2 > \Delta_2^2 (\Delta_1^2 - 4a_2^2)$.

CHAPTER II

THE MINI-NUMERICAL ELECTROMAGNETICS CODE

The development of a Mini-Numerical Electromagnetics Code (MININEC) is a result of the emergence of the personal computer as an engineering and scientific tool (Julian, Logan, and Rockway, 1982). Although NEC is a powerful tool for many engineering applications, it requires the support of and access to a large main-frame computer system. Such facilities are expensive and not always readily available at research sites. When they do become available, heavy demand usage may result in slow turn-around, even for relatively simple problems. A viable solution is a version of NEC which can be implemented on mini- or microcomputers, as these are becoming more and more affordable as personal computing tools.

For code compactness, MININEC retains of NEC only the basic solution and the most frequently used options, and uses a promising numerical approach identified by Dr. Donald R. Wilton of the University of Mississippi. The result is a 550-statement BASIC program suitable for use on a microcomputer and applicable to small problems. MININEC models may include wires, a perfect ground plane, and lumped element loading. The only excitations supported are voltage

sources. The output may include induced currents and radiated fields.

The Input Format

MININEC, being intended for the analysis of small models, requires input data to be typed interactively by the user. This becomes unnecessarily time-consuming if errors are made in data entry, since these cannot be fixed interactively. It is also impractical if a given model must be tested several times.

The user can always with reasonable effort modify the program so that it will read input data from a file, but then creating input files requires a perfect knowledge of the sequence of data requested by MININEC. This would not be necessary if MININEC recognized input lines by a 2-character label, as in NEC, but the creators of the program must have rejected this scheme to keep the size to a minimum.

The approach used by the author to save precious time on data entry was to split MININEC into two separate programs, one for data entry and the other for execution. The first program, called MINIMOD, was formed by extracting from MININEC all of its statements that would prompt for and read data, and adding output statements to echo the entered data to a file. The result is a program identical in ap-

pearance to MININEC that neither computes nor outputs results, but merely serves as a guide in the preparation of a MININEC input file (Larose, 1985a). The second program is MININEC itself, modified to read from an input file such as that created by MINIMOD, and to write computed results to a file rather than list them on the terminal.

In the above scheme errors in data entry can be corrected by editing the input file before executing MININEC. In testing a given model with different solution parameters, the same input file can be edited as necessary from one run to the other.

The outcome of a small run of the interactive version of MININEC appears in Figure 10. A few input parameters appear that were not referred to in NEC. These are the end connections, used to describe the geometry, and the pulse numbers, used to locate excitations and lumped impedance loading. This makes it already apparent that MININEC is less user-oriented than NEC, a result to be expected from such a small program.

To first explain end connections, suppose the user is specifying wire k and must enter its end 1 connection. This number indicates how end 1 of wire k connects to the structure already present. If thus far, end 1 of wire k hangs in free space, end 1 connection is zero; if it connects to the ground plane, end 1 connection is $-k$. If end 1

MINI-NEC

40

ANTENNA GEOMETRY:
NO. OF WIRES? 3

WIRE NO. 1
NO. OF SEGMENTS? 2
END ONE COORDINATES (X,Y,Z)? 0,0,0
END ONE CONNECTION? -1
END TWO COORDINATES (X,Y,Z)? 0,0,.07958
END TWO CONNECTION? 0
RADIUS? .004
WIRE NO. 2
NO. OF SEGMENTS? 1
END ONE COORDINATES (X,Y,Z)? 0,-.170423,.07958
END ONE CONNECTION? 0
END TWO COORDINATES (X,Y,Z)? 0,0,.07958
END TWO CONNECTION? -1
RADIUS? .004
WIRE NO. 3
NO. OF SEGMENTS? 1
END ONE COORDINATES (X,Y,Z)? 0,.170423,.07958
END ONE CONNECTION? 0
END TWO COORDINATES (X,Y,Z)? 0,0,.07958
END TWO CONNECTION? -1
RADIUS? .004

**** ANTENNA GEOMETRY ****

X	COORDINATES			RADIUS	CONNECTION PULSE		
	Y	Z			END1	END2	NO.
0	0	0		.004	-1	1	1
0	0	.03979		.004	1	0	2
0	0	.07958		.004	0	-1	3
0	0	.07958		.004	0	-1	4

CHANGE GEOMETRY (Y/N)? N

PROGRAM CONTROL:
FREQUENCY(MHZ)? 299.8
WAVELENGTH - 1 METERS
ENVIRONMENT (1-FREE SPACE, 2-GROUND)? 2
NO. OF EXCITATIONS? 1
PULSE NO., VOLTAGE MAGNITUDE, PHASE (DEGREES)? 1,1,0
CURRENT PRINTOUT (Y/N)? Y
RADIATION PATTERN (Y/N)? Y
ZENITH ANGLE: INITIAL, INCREMENT, NUMBER? 0,10,10
AZMUTH ANGLE: INITIAL, INCREMENT, NUMBER? 0,90,2
NO. OF LOADS? 0

Fig. 10a. Entry of antenna geometry and program control in a sample run of MININEC

*** SOURCE DATA ***
 PULSE 1 VOLTAGE = (1 , 0 J)
 CURRENT = (7.82482E-03 , -.0262972 J)
 IMPEDANCE = (10.39469 , 34.93388 J)
 POWER = 3.91241E-03 WATTS

***** CURRENT DATA *****

PULSE NO.	REAL (AMPS)	IMAGINARY (AMPS)	MAGNITUDE (AMPS)	PHASE (DEGREES)
1	7.82482E-03	-.0262972	2.743667E-02	-73.42945
2	7.831601E-03	-2.806269E-02	.029135	-74.4069
3	-3.683276E-03	1.334897E-02	.0138478	105.4254
4	-3.683268E-03	1.334894E-02	1.384777E-02	105.4254

*** PATTERN DATA ***

ZENITH ANGLE	AZIMUTH ANGLE	HORIZONTAL PATTERN (DB)	VERTICAL PATTERN (DB)
0	0	-120.6995	-999
10	0	-120.3611	-10.73953
20	0	-121.1709	-4.814202
30	0	-121.4488	-1.458249
40	0	-122.203	.7941588
50	0	-123.7433	2.392665
60	0	-125.8585	3.528284
70	0	-129.6487	4.294394
80	0	-134.7863	4.738849
90	0	-999	4.88471
0	90	-256.4617	-120.6995
10	90	-256.5276	-10.73953
20	90	-257.0046	-4.814201
30	90	-257.4258	-1.458249
40	90	-258.6939	.7941595
50	90	-260.8504	2.392665
60	90	-262.8965	3.528284
70	90	-265.5999	4.294394
80	90	-270.9288	4.738849
90	90	-298.4107	4.88471

CHANGE PATTERN (Y/N)? N
 CHANGE EXCITATION (Y/N)? N
 CHANGE CONTROL (Y/N)? N
 CONTINUE (Y/N)? N
 Ok

Fig. 10b. Source, current and pattern data computed in a sample run of MININEC

connects to wire i already entered, then the magnitude of end 1 connection is i . The sign is positive if end 1 of wire k connects to end 2 of wire i ; this indicates the current reference directions of the two wires are consistent. If on the other hand end 1 of wire k connects to end 1 of wire i , end 1 connection is negative. If now end 1 of wire k connects to the ends of two wires i and j already entered, the user has the choice of using either i or j , as the magnitude of end 1 connection. The reason all this information is required is that MININEC would need too much extra coding to track wire connections all by itself.

With the advent of MININEC, the need was soon felt for a program that could rapidly convert already existing NEC input files to the MININEC input format for comparative studies. This has led to the creation of program MINIGEN (Larose, 1985a), which reformats the geometry section of a NEC input file and appends to it the standard program control described in Chapter I.

The only significant work involved in MINIGEN is the determination of the end connections for each wire. For this purpose, the entire geometry is first stored in memory, and then the user is prompted for the environment (free space or ground). The procedure for finding end connections of wire i appears in the flowchart of Figure 11. If a ground plane is present, one end of wire i can possibly con-

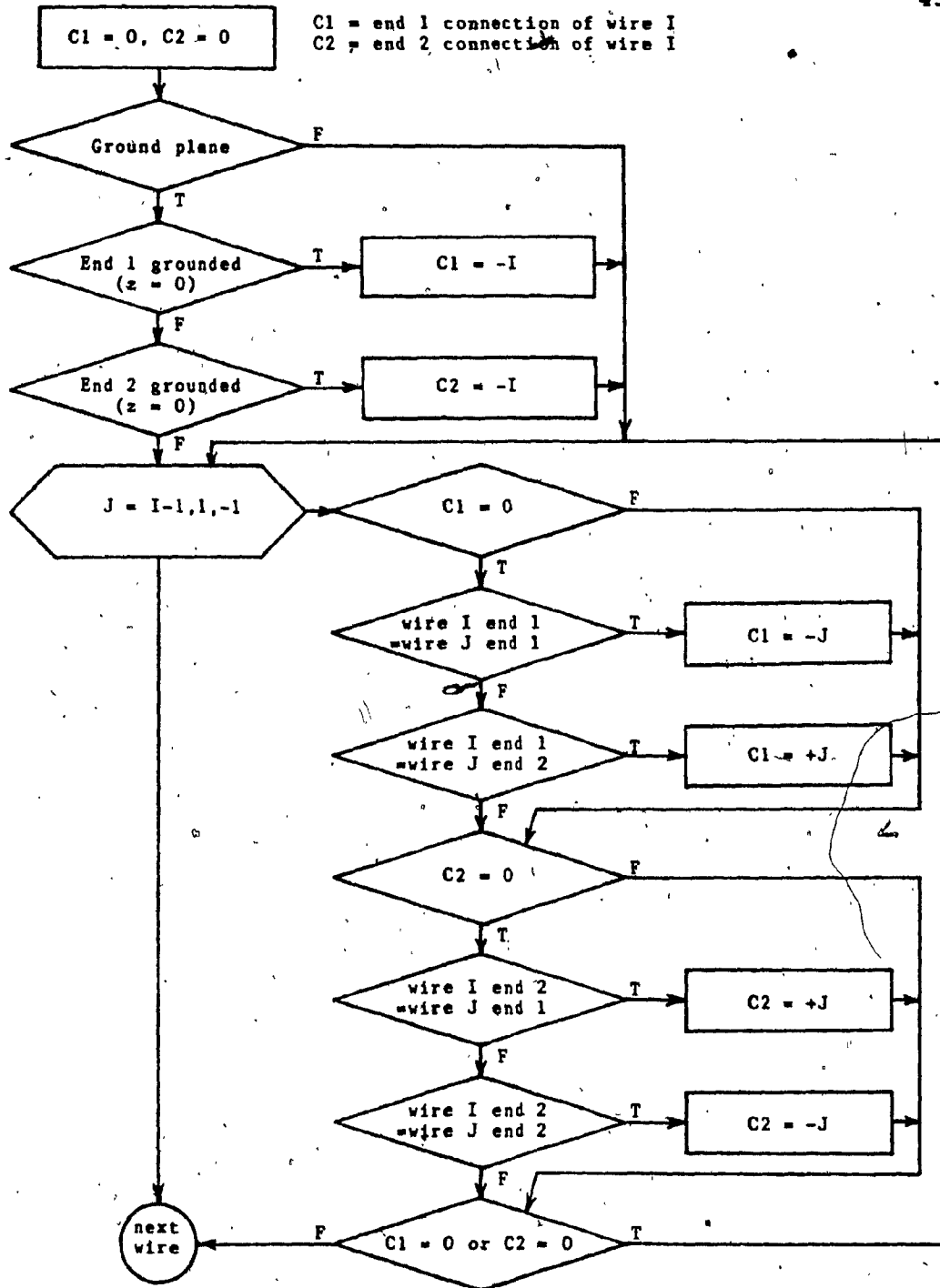


Fig. 11. Procedure for finding end connection of wire I in program MINIGEN

nect both to the ground and to previous wires in the list. Since connection to ground is easier to detect, this condition is checked first for each end. It is assumed that the two wire ends cannot both connect to ground, as this situation would be meaningless. The search for wire connections backward from the previous wire is an arbitrary convention which in practice gives faster execution because it is more likely that wire i would connect to the previous wire than to the first.

Pulse Numbering

Pulse numbers can now be explained; these are references to particular current basis functions used by the program. A basis function in MININEC consists of a square pulse of unit magnitude extending from the center of a segment to the center of another connected segment. The location and numbering of the pulses on a model depends on the order in which the user enters the wires and on the end connections he specifies.

Figure 12a shows the basis functions on the first wire of a structure, with end connections 0 and 0. Pulses are numbered consecutively from node 1 to node 2. Figure 12b shows the addition of a second wire connected to the first, with end connections 1 and 0. A current pulse extends from wire 2 to wire 1 as shown. Figure 12c shows the

addition of a third wire connecting to both wires 1 and 2, with end connections 0 and -1. A current pulse extends from wire 3 to wire 1. If connections had been 0 and 2, then the pulse would have extended from wire 3 to wire 2.

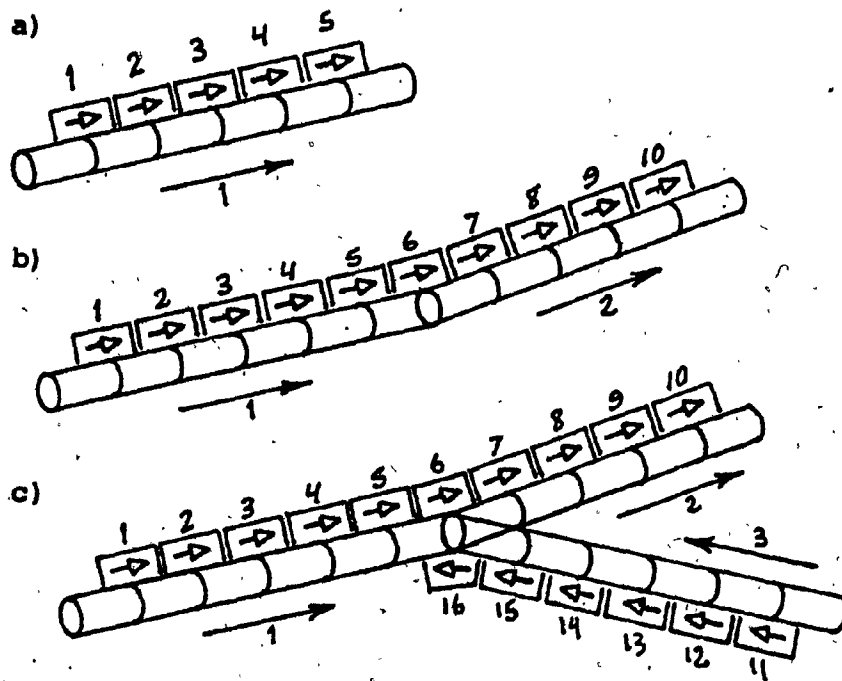


Fig. 12. Definition of MININEC current basis functions in the course of geometry entry. In c), end 2 connection of wire 3 is -1

The reader may now guess that an excitation specified at pulse 1 is simply a voltage source connected across the length of wire over which pulse 1 extends. The same can be said for impedance loading. In the peculiar case where

an excitation or loading must be specified across a multiple-wire junction, the user must be careful to create a current pulse over the desired pair of segments at that junction by using the proper connection data. Otherwise the connection scheme at multi-wire junctions is totally arbitrary. Different current pulse expansions at junctions lead to different solutions for the pulse magnitudes, but always in such a way that the total current distribution remains everywhere unchanged. This will be demonstrated in the next section.

During early experimentation with MININEC, clearly meaningless results were obtained for some of the smaller structures that were tested. The problem was traced down to the geometry section of the program, and was clearly defined as follows: MININEC is not set up to process structures containing wires to which less than two pulses are assigned. The resulting limitations were that wires with two free ends at the time they were specified had to include at least three segments, and that wires with one end free at the time they were specified had to include at least two segments. It was concluded that the authors of the program wrote the code under the assumption that wires were finely segmented. Successful corrections were brought to the code and a report was written (Larose, 1984) that was sent to the creators of MININEC. Reply was received informing that a problem had

indeed been noticed, and thanking the author for its solution.

The Solution Procedure

It is apparent from the above explanation of the current expansion that at a junction of N wires, $N-1$ current basis functions will be defined. This is all that is required to impose Kirchoff's current law at the junction, and hence MININEC implicitly enforces current continuity at junctions. Another condition implicitly enforced is the tapering down of current to zero at free wire ends. Since this is theoretically true for infinitely thin wires only, some accuracy is lost here for thicker wires in comparison to NEC, where a general relationship is used. Nevertheless, this seems a very small price to pay for the resultant program compactness.

Figure 13 illustrates the fact that the particular connection scheme used at a multiple-wire junction affects in no way the total current distribution computed. Three identical models were created, for which different current expansions were obtained as shown in a), b) and c) by varying wire order and end connections. In all three cases pulse 1 was excited and the total current distribution computed would amount to precisely that illustrated in d).

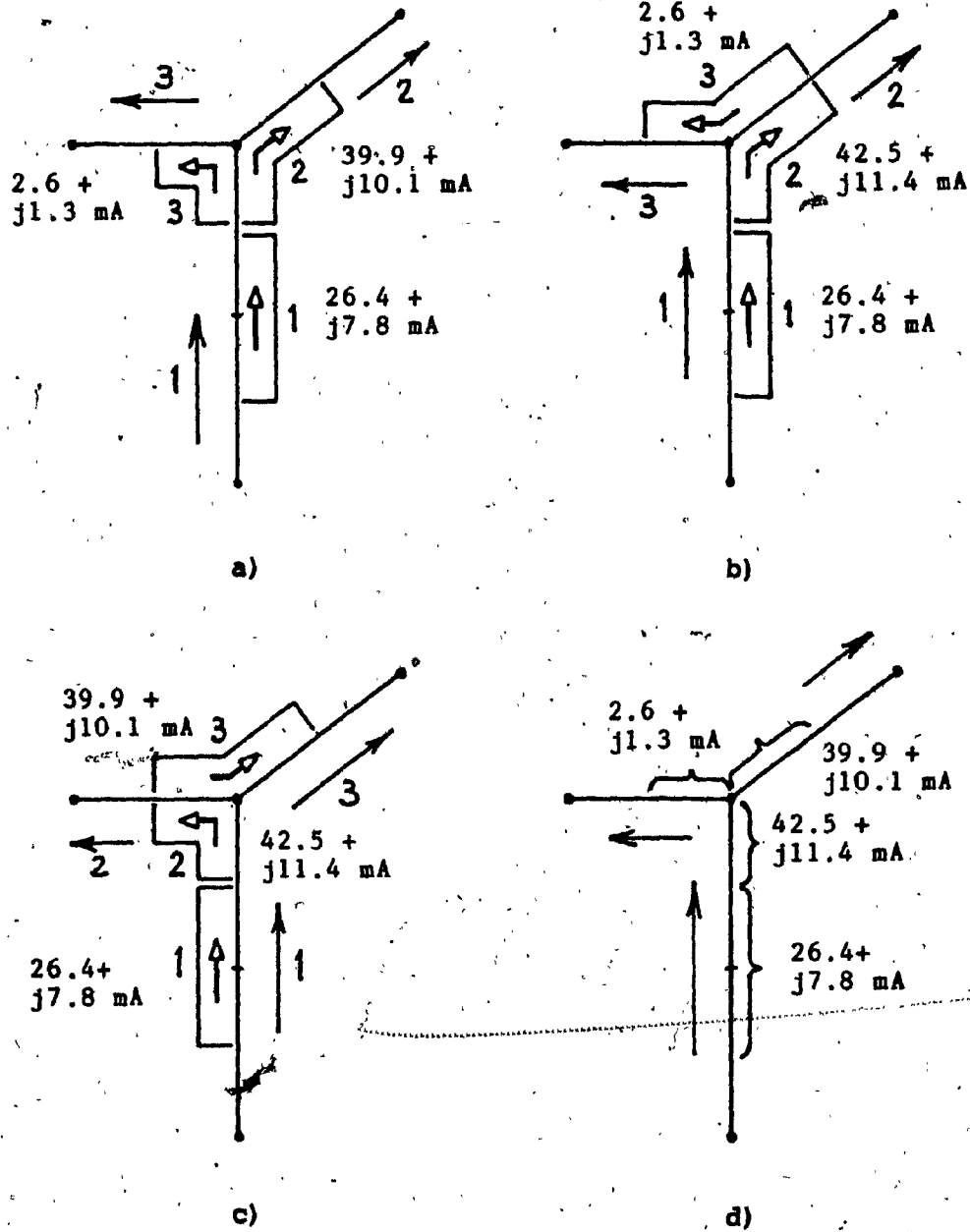


Fig. 13. In a), b), and c), use of three different MININEC current expansions on the same model, resulting in the same current distribution shown in d)

A peculiar result of the MININEC formulation is that the number of basis functions N , and hence the order of the interaction matrix to be solved, is not equal to the total number of segments. It is apparent from Figure 12 that if a network has S segments, then $S-1$ pulses will be defined. This is only true, however, for a network with no closed paths. For example, in Figure 14a where the network forms one closed loop, $N = S$, and in Figure 14b with two closed loops, $N = S+1$. By extension, the general rule becomes

$$N = (S-1) + L,$$

where L is the number of independent loops.

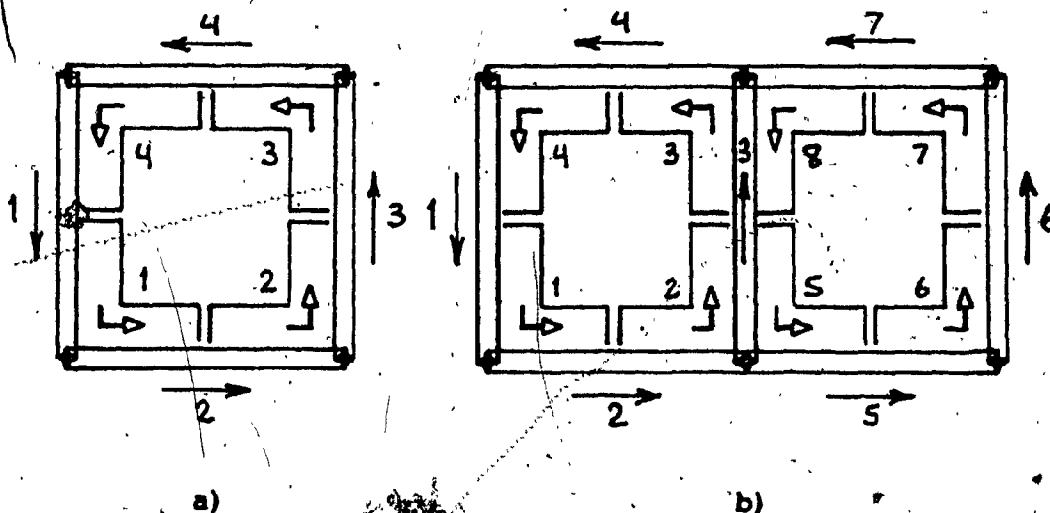


Fig. 14. Networks with a) one and b) two independent loops, and pulses defined

An immediate consequence is that MININEC would be less efficient in the analysis of smooth surfaces, which are modeled as a grid of wires forming several adjacent loops. The weakness of the above equation is that L may be difficult to determine by inspection. For a network consisting of several unconnected parts, L may become theoretically negative, which is physically difficult to appreciate.

It is known from linear network theory that $L = W - P + 1$, where W is the number of wires, or branches, and P is the number of different points, or wire nodes. By substitution, a more exact expression can be obtained:

$$N = (S-1) + (W-P+1) = S + (W-P).$$

Therefore the term $(W-P)$ is the increase introduced in the order of solution by the MININEC method of formulation compared to that of NEC. This number can be easily determined for models created via DIDEK (see Chapter VI) because then the number of nodes is available. Note that the two formulas above do not apply if the network has connections to a ground plane.

MININEC integrates currents over segment surfaces in a way similar to NEC when the EK option is in effect. The major difference is that point matching is not used; rather, the electric field boundary condition is satisfied on the average over the domain of each current pulse. In

method of moments terminology, a set of N weighting functions are used, which consist of square pulses of unit magnitude defined in the domains of the N basis functions. Hence basis and weighting functions are identical in MININEC; this is known as Galerkin's method. The i th equation of the interaction matrix is obtained by multiplying the electric field boundary condition

$$\hat{s} \cdot \bar{L}(I(s)) = -\hat{s} \cdot \bar{E}^i$$

by the i th weighting pulse and integrating over its domain. The right-hand side in particular becomes after integration simply the negative of the voltage V applied at the location of pulse i .

A number of approximations are made to facilitate the integrations on the left-hand side; these are based on the assumption that electrical quantities vary sufficiently smoothly over each segment. For this reason the authors of MININEC refer to their approach as a modified Galerkin procedure.

The Output Format

The EMC laboratory has at its disposal a number of graphics program written over the years to help visualize electromagnetic phenomena on wire-grid models. This software is standardized to read NEC output files as com-

pressed by program STRIP, discussed in Chapter I. In order to apply the same graphical tools to MININEC results, program MSTRIP was written by the author (Larose, 1985a) to compress MININEC output files to the standard format.

Referring back to the interactive MININEC run of Figure 10, two difficulties in the output file conversion become apparent. Firstly, currents computed are the magnitudes of the current pulse functions and not the current magnitudes at the center of each segment. Secondly, radiated fields are dB values and not linear values in V/m. Both problems were overcome as explained below.

The current at the center of a given segment is estimated by first finding the current on each of its two halves. The total current on the first segment half is obtained by summing the contributions of all current pulses extending over it, and similarly for the total current on the second segment half. Averaging the two currents thus obtained yields the desired value. It was confirmed, after examination of typical current patterns on wires, that averaging the currents should be done in complex arithmetic, i.e. by adding the complex numbers and dividing by two rather than averaging current magnitude and phase separately.

If m current pulses extend on the first segment half and n on the second half, the current at the segment center

may be expressed as:

$$I = 1/2 \left[\sum_{i=1}^m I_i + \sum_{i=m+n}^{m+n} I_i \right],$$

or equivalently,

$$I = 1/2 \sum_{i=1}^{m+n} I_i,$$

which means all pulse magnitudes may be added in any order and the sum divided by two.

Program MSTRIP contains an algorithm that keeps track of absolute segment numbers and pulse numbers as the geometry is being read. This allows the program to maintain lists of all the pulses extending over each segment. After the complete geometry is read, the proper current magnitudes can be added up for each segment and the result divided by two to yield the current at the segment center.

In MININEC, the zero dB reference for the radiated fields is the isotropic level. Therefore, a linear field value E is converted to its dB equivalent E_{dB} by the formula $E_{dB} = 20 \log(E/E_{iso})$. The base 10 logarithm is not available in BASIC, so that MININEC must use the natural logarithm, and the formula becomes $E_{dB} = (20/\ln 10) \ln(E/E_{iso}) = 8.686 \ln(E/E_{iso})$. The squared value E^2 is also used in

practice because this is what is first generated by the relations used to derive the radiated fields. A more efficient formula is therefore $E_{dB} = 4.343 \ln(E^2/E_{iso}^2)$. The factor $1/E_{iso}^2$ is computed once and for all and denoted K so that the final expression is

$$E_{dB} = 4.343 \ln(KE^2).$$

Evaluation of K calls for the total radiated power P , which figures in the source data of the MININEC output (see Figure 10), and the definition of the isotropic level. The isotropic level is defined as that electric field which, if radiated uniformly in all directions and in one polarization, would result in the same radiated power. Dropping as usual the e^{-jkr}/r term, the radial distance may be considered as 1 m, and the radiation area as $4\pi(1)^2 = 4\pi$. Hence the isotropic level satisfies the relation $E_{iso}^2/2\eta_0 = P/4\pi$, which equates power densities. From this $K = 1/E_{iso}^2 = (2\pi/\eta_0)/P$. Substituting $\eta_0 = 376.73$, the final result is $K = 0.016678/P$.

Knowing how MININEC obtains its dB field values (see above), an accurate formula was derived and written into MSTRIP to exactly recover the linear values of the electric fields. From $E_{dB} = 8.686 \ln(E/E_{iso})$ one obtains

$$E = E_{iso} e^{E_{dB}/8.686}$$

and since $1/E_{iso}^2 = 0.016678/P$, E_{iso} is computed once and for all as $(P/0.016678)^{1/2}$.

Language Conversions

For the purpose of faster program execution, MININEC and MSTRIP were converted from BASIC to FORTRAN by the author and installed on the university CYBER 835 as well as on the LSI-11/73 and CROMEMCO systems of the EMC laboratory. Accompanying utility software was installed there as well so that all machines would provide a suitable MININEC working environment.

In the language conversion of MININEC some important strategies were resorted to as explained below. First, all variables in BASIC are treated as real, which is not the case in FORTRAN, where some variables default to integers unless otherwise noted. To handle this situation, all variables were declared real through an IMPLICIT statement. Selected variables were then declared as integers if they caused compilation errors, for example when used as array subscripts. Of course, it had to be proved that these variables were used exclusively as integers throughout the program.

Several variable names in MININEC were used at the same time as a single variable name and as an array name, a forbidden condition in FORTRAN. In each of these cases the

array name had to be made different from the single variable name to avoid conflicts.

Another major difference in BASIC is that subroutines, called using the GOSUB statement, do not allocate independent storage locations for variable names appearing also in the main program; hence a list of arguments does not need to be passed. Converting the subroutines of MIN-INEC to standard FORTRAN subroutines would have required the identification of all those variables common to both the subroutines and the main program. The preferred scheme was to simply replace the RETURN statements with assigned GO TO statements, the transfer destination being set just before a subroutine is called.

CHAPTER III

GRAPHICS SOFTWARE DEVELOPMENTS

Graphical techniques implemented in various display programs of the EMC Laboratory are sometimes of little help in the perception and interpretation of electromagnetic phenomena on wire-grid models. A number of display programs written by the author over the past years have served to fill certain gaps in the area. Three of these programs are briefly described below. For a thorough explanation of the input data requirements and execution sequences, the reader is referred to the report especially written for this purpose (Larose, 1985b).

Logarithmic Impedance Plots

Impedance curves are best represented by plotting together resistance and reactance versus frequency on the same scales. A logarithmic scale for the impedance gives better resolution, but then one must give up plotting a certain range of values near the zero mark. Ordinary plotting programs cannot handle this special situation. The usual way to circumvent the problem is to flip the negative portions of the reactance curve to the positive-ohms region, but then positive and negative portions of the curve must be

distinguished using different line styles, and clarity of the display suffers.

For the above reasons a new graphics program was written to obtain just the desired type of display. The plotting package DIGPLOT, a subset of DIGRAF (Warner, 1979), was selected because of its several annotation options for simple two-dimensional graphs. The resulting program was called DIGIMP (DIG for DIGPLOT, IMP for impedance) and was used to produce all impedance plots appearing in this work.

Color Displays of Currents With SPCTRM

The general way in which original EMC Lab graphics programs represent induced currents on wire-grid models is to display each segment with a vertical line extending from its center whose length is proportional to the current magnitude. For complex structures the resulting display becomes meaningless as the current lines become too cluttered for differentiation. The problem is handled with varying success by using different line styles, different colors on color screens, or by displaying the currents on specific wire paths at a time.

A more satisfactory approach in representing wire currents has been investigated by the author, and found worthy of being implemented in a new general-purpose current display program. In this approach, current magnitude or

phase information on a segment is carried by the color in which the segment itself is drawn, no visual aid being added. The use of color hues does not convey information as accurately as current lines, but does give a qualitative appreciation of current distribution unequalled so far.

Use of Color for Current Magnitude

A sequence of colors inspired from the white light spectrum is used for representing current magnitudes; hence the display program is called SPCTRM. SPCTRM is written for execution on a NORPAK color screen, which produces colors from combinations of the fundamental red, green and blue tints. The display color is set by calling subroutine SETRGB(IR,IG,IB), where IR, IG and IB are integers ranging from 0 to 15 that represent the desired amounts of red, blue and green respectively. For example, the background color, black, is obtained by setting all three integers to zero, and white is obtained by setting all three to 15. The number of different colors that can be displayed is theoretically 16^3 , or 4096, resulting in excellent color resolution.

A systematic method of generating the palette of rainbow colors was found by experimentation. This is a continuous succession of hues passing through red, magenta, blue, cyan, green, yellow and red again, closing the loop.

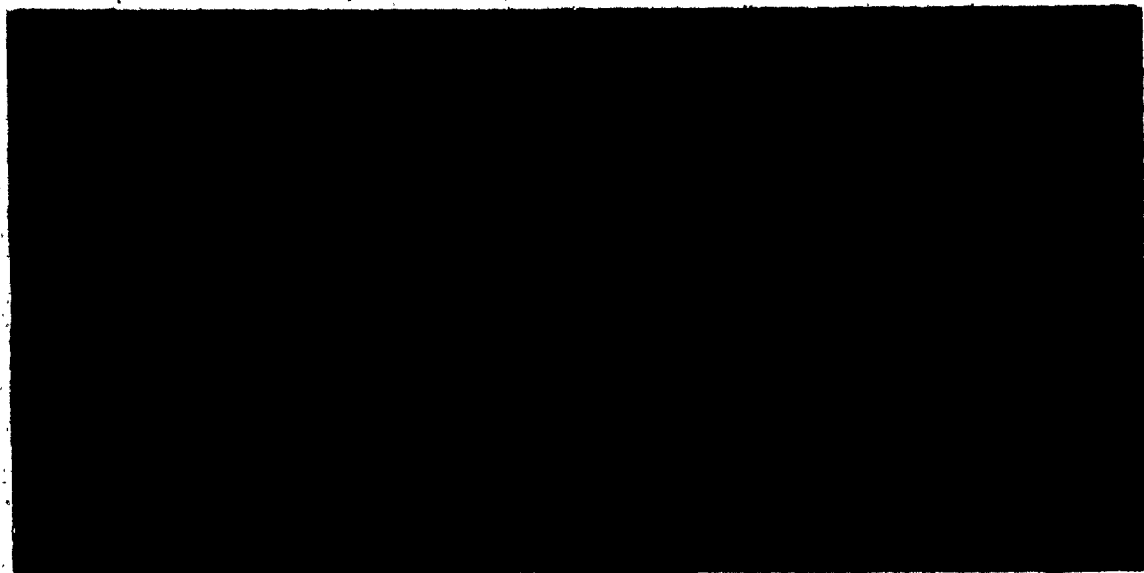
It was closely approximated by a sequence of 90 colors formed by combinations of two fundamental colors at a time. In particular, magenta was produced by combining red and blue, cyan by combining blue and green, and yellow by combining green and red. Table 1 shows precisely how the 90 colors were produced and numbered. Resolution is good enough that adjacent hues are barely distinguishable from each other.

In current magnitude displays, the sequence of colors that best matches the white light spectrum is used. It consists of the 61 colors numbered 30 through 90, i.e. from blue to red. Blue is equated to zero current, and red is equated to the maximum current on the model displayed. For intermediate colors a linear relationship is assumed between color number and the corresponding current level. Figure 15a shows a SPCTRM current magnitude display obtained in this manner. The color spectrum used is most effective because blue is a dull color suitable for low currents, whereas red stands out the most and attracts attention to the highest currents.

It can be of interest to vary the relative current ranges covered by each color to bring more segments into the blue or red ends, and thus affect the color resolution. Program SPCTRM uses for this purpose a "resolution index", defined as the ratio of the current range covered by a given

TABLE 1. SEQUENCE OF 90 COLORS WITH SETRGB PARAMETERS

NUMBER	IR	IG	IB	COLOR	NUMBER	IR	IG	IB	COLOR
0	15	0	0	RED	45	0	15	15	CYAN
1	15	0	1	.	46	0	15	14	.
2	15	0	2	.	47	0	15	13	.
3	15	0	3	.	48	0	15	12	.
4	15	0	4	.	49	0	15	11	.
5	15	0	5	.	50	0	15	10	.
6	15	0	6	.	51	0	15	9	.
7	15	0	7	.	52	0	15	8	.
8	15	0	8	.	53	0	15	7	.
9	15	0	9	.	54	0	15	6	.
10	15	0	10	.	55	0	15	5	.
11	15	0	11	.	56	0	15	4	.
12	15	0	12	.	57	0	15	3	.
13	15	0	13	.	58	0	15	2	.
14	15	0	14	.	59	0	15	1	.
15	15	0	15	MAGENTA	60	0	15	0	GREEN
16	14	0	15	.	61	1	15	0	.
17	13	0	15	.	62	2	15	0	.
18	12	0	15	.	63	3	15	0	.
19	11	0	15	.	64	4	15	0	.
20	10	0	15	.	65	5	15	0	.
21	9	0	15	.	66	6	15	0	.
22	8	0	15	.	67	7	15	0	.
23	7	0	15	.	68	8	15	0	.
24	6	0	15	.	69	9	15	0	.
25	5	0	15	.	70	10	15	0	.
26	4	0	15	.	71	11	15	0	.
27	3	0	15	.	72	12	15	0	.
28	2	0	15	.	73	13	15	0	.
29	1	0	15	.	74	14	15	0	.
30	0	0	15	BLUE	75	15	15	0	YELLOW
31	0	1	15	.	76	15	14	0	.
32	0	2	15	.	77	15	13	0	.
33	0	3	15	.	78	15	12	0	.
34	0	4	15	.	79	15	11	0	.
35	0	5	15	.	80	15	10	0	.
36	0	6	15	.	81	15	9	0	.
37	0	7	15	.	82	15	8	0	.
38	0	8	15	.	83	15	7	0	.
39	0	9	15	.	84	15	6	0	.
40	0	10	15	.	85	15	5	0	.
41	0	11	15	.	86	15	4	0	.
42	0	12	15	.	87	15	3	0	.
43	0	13	15	.	88	15	2	0	.
44	0	14	15	.	89	15	1	0	.
45	0	15	15	CYAN	90	15	0	0	RED



a)

b)



c)

d)

Fig. 15. SPCTRM current magnitude displays with different resolution indices: a) $r=1$ (linear case), b) $r=1.03$, c) $r=1.06$, and d) $r=1.09$

color to the range covered by the previous color. Figure 16 illustrates how the total current range is distributed among the 61 colors available.

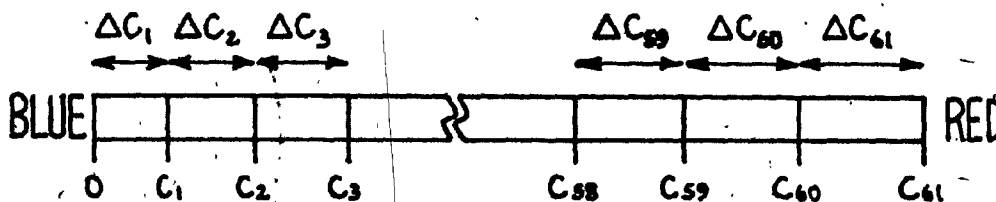


Fig. 16. Distribution of the 61 colors on the current magnitude scale

If the resolution index is 1, all colors cover an equal current range and we have the linear condition described earlier. If however the resolution index is made greater than 1, the current intervals are smaller in the blue end and increase regularly towards the red end. This means more colors are available in the low current end and therefore segments with small currents benefit from improved color resolution. Segments are assigned colors closer to the red end, so that the resulting display appears more colorful. If on the other hand the resolution index is made less than 1, segments with high currents benefit from the improved resolution, and the resulting display loses color. Figure 15 compares the effect of using different resolution indices on the same wire-grid model.

Referring back to Figure 16, the resolution index r can be defined by the relation

$$\Delta C_i = r \Delta C_{i-1}, \quad i = 2, 3, \dots, 61.$$

To fully define the spectrum under this condition, it is necessary to determine the values of each of the C_i 's. The first step in doing so is the evaluation of the first interval ΔC_1 . The relation obtained above can be rewritten as $\Delta C_i = r^{i-1} \Delta C_1$, and by substituting into

$$\sum_{i=1}^{61} \Delta C_i = C_{61}, \quad \text{one obtains}$$

$$\sum_{i=1}^{61} r^{i-1} \Delta C_1 = C_{61}, \quad \text{or} \quad \Delta C_1 \sum_{i=1}^{61} r^{i-1} = C_{61}.$$

The latter sum is a geometric series, whose value can be obtained from the general expression

$$\sum_{i=1}^n r^{i-1} = \frac{r^n - 1}{r - 1} \quad (\text{Spiegel, 1968}). \quad \text{It follows that}$$

$$\Delta C_1 \frac{r^{61} - 1}{r - 1} = C_{61}, \quad \text{or finally} \quad C_1 = C_{61} \frac{r - 1}{r^{61} - 1}.$$

The last step is to get

$$\Delta C_i = r^{i-1} \Delta C_1 = r^{i-1} C_{61} \frac{r-1}{r^{61}-1}, \text{ from which}$$

$$\begin{aligned} C_i &= \sum_{j=1}^i \Delta C_j = \sum_{j=1}^i r^{j-1} C_{61} \frac{r-1}{r^{61}-1} = C_{61} \frac{r-1}{r^{61}-1} \sum_{j=1}^i r^{j-1} \\ &= C_{61} \frac{r-1}{r^{61}-1} \frac{r^i-1}{r-1} = C_{61} \frac{r^i-1}{r^{61}-1}. \end{aligned}$$

Using l'Hopital's rule, the value of C_i when r is 1 (linear case) can be determined as follows:

$$\lim_{r \rightarrow 1} C_{61} \frac{r^i-1}{r^{61}-1} = C_{61} \lim_{r \rightarrow 1} \frac{ir^{i-1}}{61r^{60}} = C_{61} \frac{i}{61},$$

which is the expected result.

Use of Color for Current Phase

The fact that the progression of rainbow colors forms a closed loop allows an even more fascinating application of color graphics to the representation of current phase. Figure 17 shows how the range of possible phase angles, -180 degrees to +180 degrees, is distributed around the color circle. The actual FORTRAN expression relating phase to color number is

$$ICOL = INT((PHA)/4.+45.).$$

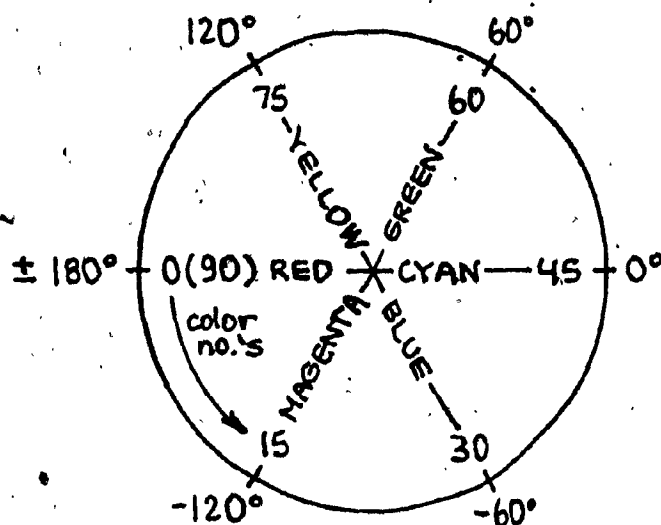
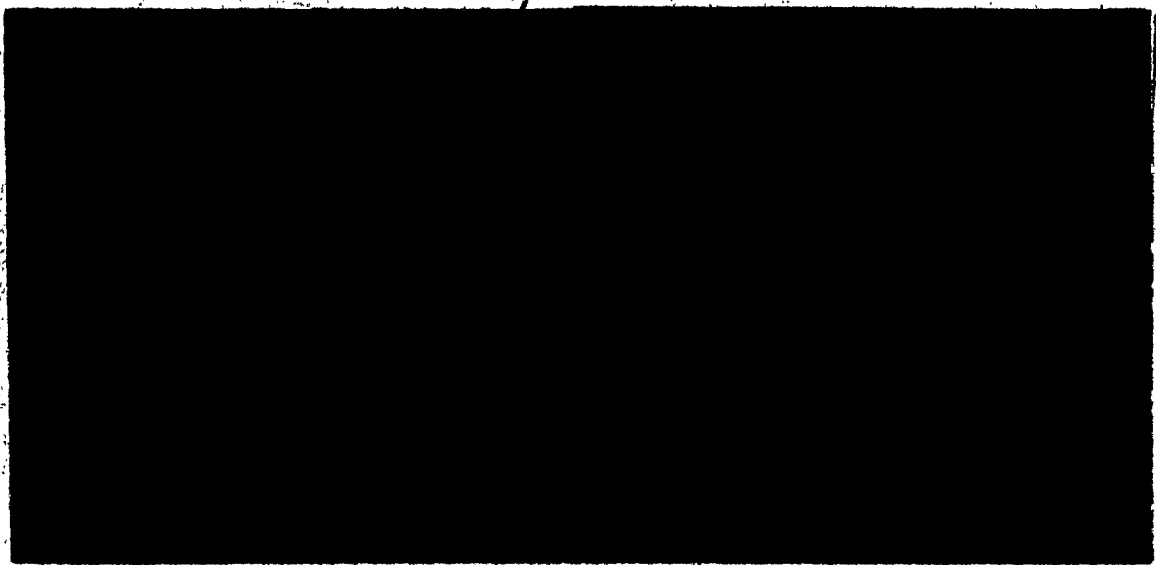


Fig. 17. Distribution of the 90 colors around the phase circle

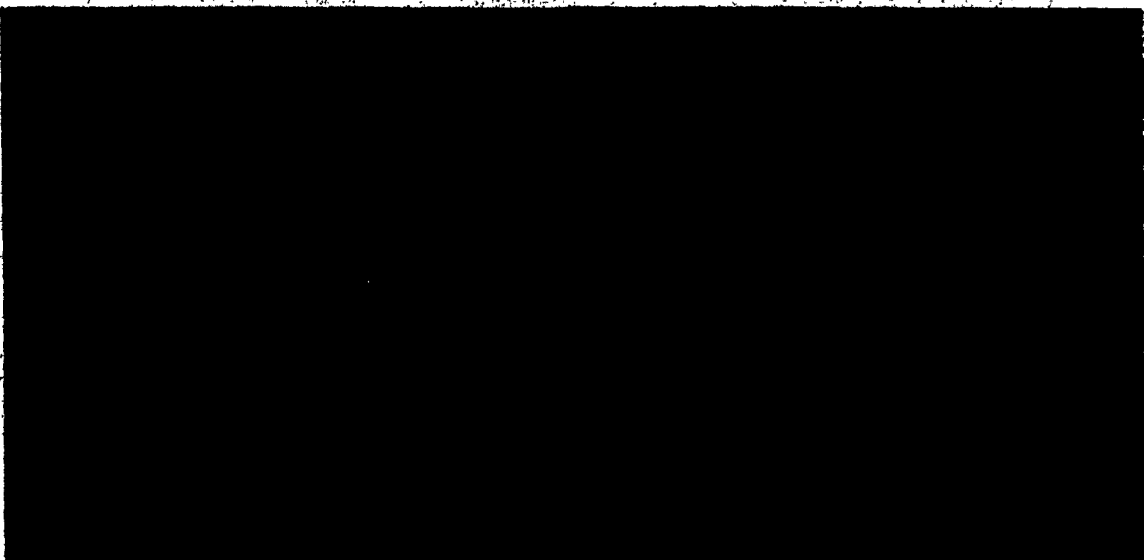
Note the interesting fact that opposing colors in the circle are complementary colors, i.e. negatives of each other in photographic terms. Hence two segments with currents out of phase by a complete 180 degrees are represented by complementary colors. With some practice the complementary pairs cyan-red, blue-yellow and magenta-green are easily recognized on current phase displays. Note also that red is used for both -180 and +180 degrees, as they are really identical phases, and that this most striking color is appropriate for the phase farthest from the reference phase of the excitation, usually zero degrees.

Figure 18a shows a SPCTRM current phase display obtained as explained above. Current reference directions are



a)

b)



c)

d)

Fig. 18. SPCTRM displays with modes 2 to 5: current phase a) with or b) without arrows, and plain geometry c) with or d) without tag numbers

by necessity indicated by an arrow on each segment. For economy of space the color circle is reproduced in the legend under the form of two horizontal strips. The arrangement is such that complementary angles and colors are located on different strips at the same horizontal position.

It is convenient to mention at this point the capability in SPCTRM of reversing wires at the user's will. This can be used to enforce a consistent current reference direction along a critical wire path, and hence track better the phase variation along it. A wire reversal manifests itself on display by a change of arrow direction in all the segments and a complementing of the segment colors. Mathematically, a complementary color is obtained by applying a bias of 45 to the original color number. If the color number is less than or equal to 45, the bias is positive, but if it greater than 45, the bias is negative. This is achieved by the FORTRAN assignment statement

$$ICOL = ICOL + ISIGN(45, 45 - ICOL),$$

where ISIGN is the sign transfer function of the second parameter to the first.

The User Interface

Having had to cope for several years with unfriendly current display programs, the author has put emphasis in

writing SPCTRM on completeness, clarity, minimum typing and speed of execution. Commands are available for obtaining help of a general nature or on specific topics, so that a beginner can use the program without expert assistance. The status of the program, in terms of the display options currently in effect, can also be obtained at any time.

SPCTRM features a choice of 8 different viewport layouts inspired from the wire-grid modelling program DIDEK (Kubina, Cerny, and Gaudine, 1984) (see Chapter VI). These are illustrated in Figure 19. Once a viewport layout has been chosen, a command allows the user to switch from one viewport to the other.



Fig. 19. Choice of 8 viewport layouts in SPCTRM

Five display modes are available: current magnitude, current phase with or without arrows, and plain geometry with or without tag numbers. Arrows for current phase are optional to account for the rare cases when they are not needed and unnecessarily clutter the display. The plain geometry mode produces neutral white on black displays useful for reference purposes. The wire tags that can be added are a precious help in referencing wires for which SPCTRM must take special action. Figure 18 shows in b), c) and d) SPCTRM displays using the three last modes described.

Other display parameters that can be selected by the user are the rank of the desired frequency in the input file, the viewing angle in terms of theta and phi, and the resolution index as described earlier. A most powerful capability of SPCTRM inspired once more from DIDEK is the zooming feature. Initially the program is in the "automatic rescale" mode, in which displays are automatically scaled to fill the available viewport area. A "blow-up" command allows the user to specify a desired magnification, which stays in effect for subsequent displays until further magnification is specified or auto-rescaling is re-activated with the "rescale" command.

The blow-up command ^{is} magnifies a desired critical region of a display by a process involving a trackball. First, a display is produced with the display options cur-

rently in effect, and a red box half the size of the viewport superimposes itself on the drawing. The trackball then allows the upper-right and lower-left corners of that red box to be moved to independent locations so that it will enclose the area to be magnified. In the end, the user signals when he has finished positioning the box, and the box vanishes. Subsequent displays are scaled so that the desired region fills the available viewport area. Figure 20 illustrates the zooming process in two stages.

Another powerful aspect of SPCTRM, inspired this time from an earlier current display program by Dr. C. W. Trueman, is the support of wire lists. In the default state of the program, displays include all wires irrespective of the input geometry. Through an "edit list" command, a finite list of wire tag numbers can be created, which is used in all subsequent displays until the list is further modified or until it is reset with the "reset list" command. The "edit list" command is a subsystem in itself because the various ways provided to efficiently edit wire lists require a set of commands separate from the SPCTRM menu. Two other commands are also available to write wire lists to disk files and then read them back when needed.

In its initial state, SPCTRM adjusts the current scale such that the maximum current displayed always corresponds to the red end of the spectrum. Hence the current

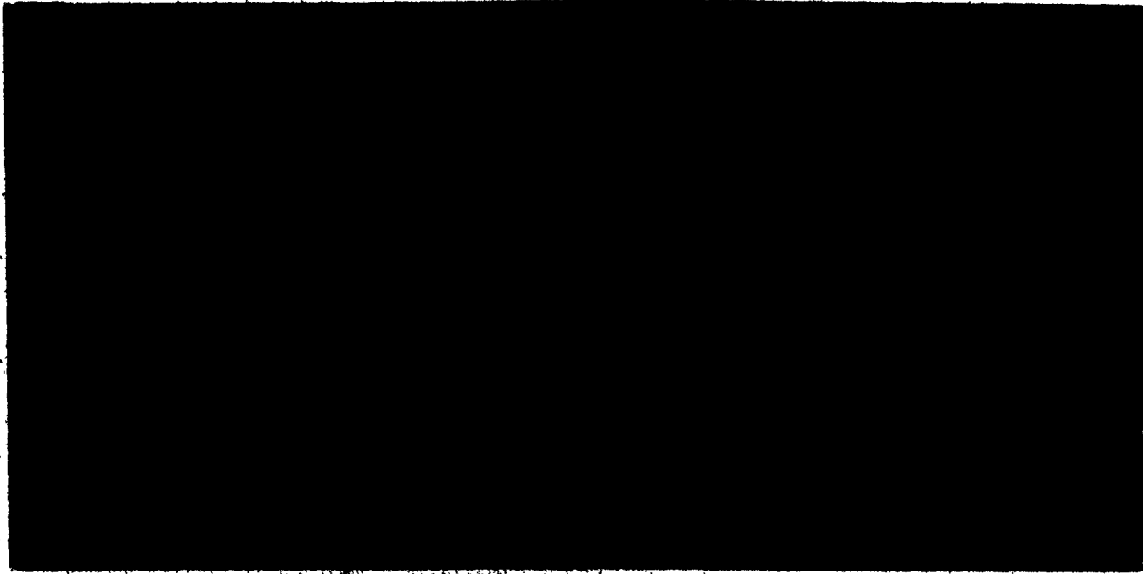
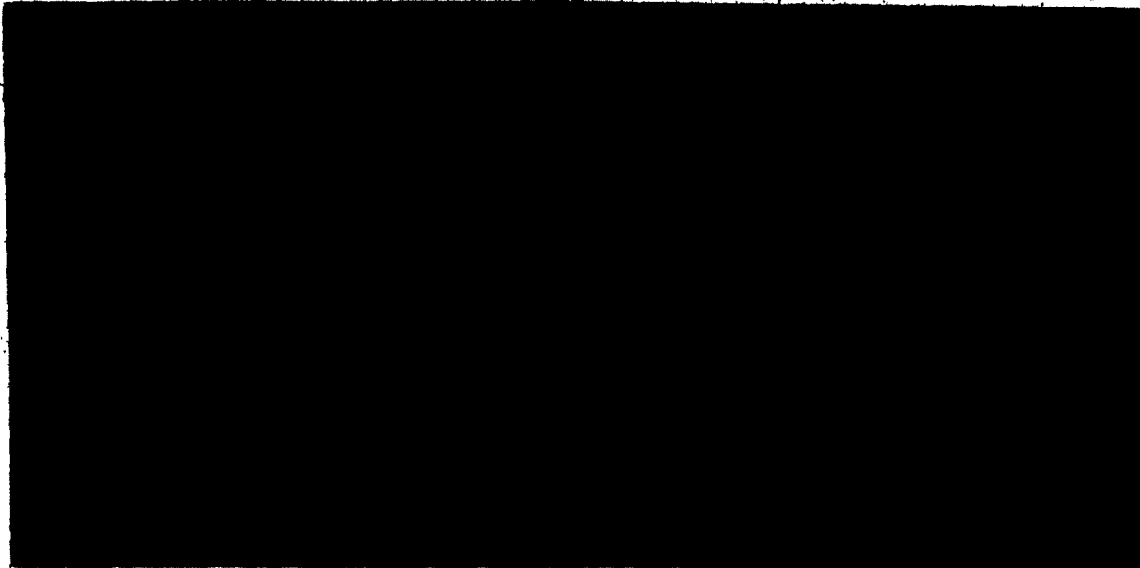


Fig. 20. SPCTRM zooming process in two stages



a)

b)

Fig. 21. Effects of freezing current scale: a) current distributions at two different frequencies, b) currents on complete wire list and partial wire list.

scale is adjusted as the input solution file is changed or as the wire list is modified. In some cases, however, it would be convenient to "freeze" the current scale so that several current distributions would be compared on a same scale. A command for this purpose is available and acts as a switch to make the current range variable or fixed.

Figure 21a shows current distributions at two different frequencies with a fixed current range. The display having the smallest maximum current is clearly identified by the truncation of the spectrum along the current scale. Figure 21b shows how this feature applies to wire lists. The top display was obtained first, and then the list in the first bottom viewport was displayed after the current range was frozen. The list was then displayed again in the second viewport after the current range was allowed to adjust, resulting in full current resolution.

To reduce keyboard input to a minimum, SPCTRM allows the user to store in memory, using appropriate commands, up to four values of each of the following display parameters: input solution file name, frequency rank, viewing angle, blown-up view, wire list file name, and resolution index. Stored values can be retrieved as necessary with equally simple commands. Other characteristics not detailed here contribute to make of SPCTRM one of the most advanced and useful tools in the EMC laboratory.

Displays of Radiation Patterns with MOVIE.BYU

Figure 22 shows the spherical coordinate system used at the EMC Laboratory to describe the radiation characteristics of vehicle-mounted antennas. It is a right-handed coordinate system where in navigational terminology x is forward, y is port and z is the top. Negative axis directions are aft, starboard and bottom. Theta is the angle measured from the z-axis and phi is the angle measured on the x-y plane from the x-axis to the y-axis.

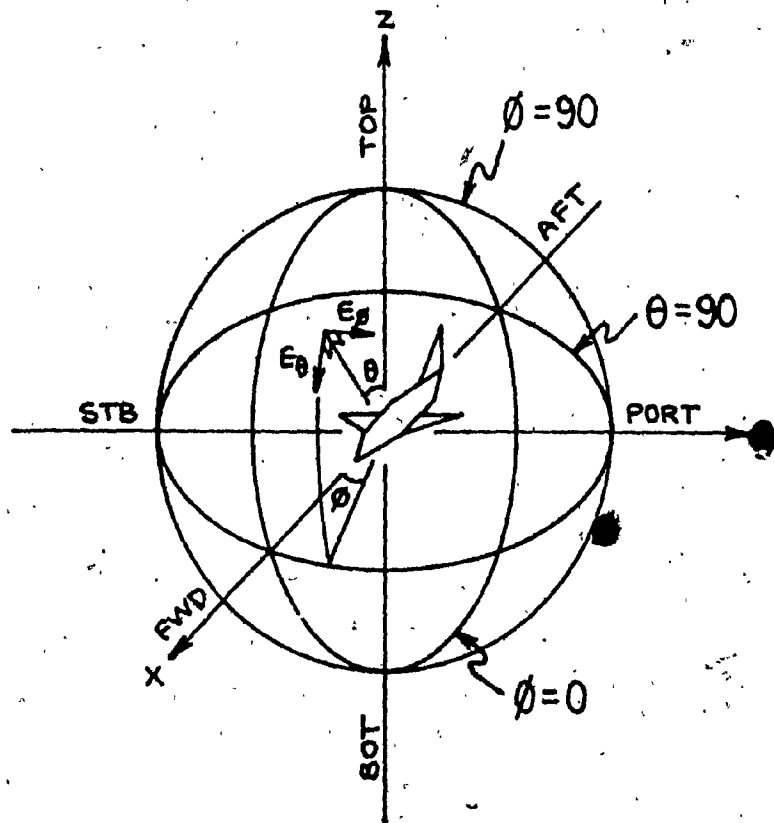


Fig. 22. Standard spherical coordinate system

Radiation patterns fall in two categories. In azimuth patterns, θ is fixed, and ϕ , or the azimuth angle, varies in constant increments from 0 to 360 degrees. In elevation patterns, ϕ is fixed, and θ varies in constant increments from 0 to 360 degrees. Those patterns referred to as the principal plane patterns are measured in the x , y , and z planes, or equivalently, they may be thought of as the azimuth pattern $\theta = 90$ and the two elevation patterns $\phi = 0$ and 90 degrees.

The radiation characteristics of a vehicle-mounted antenna can be adequately described by a set of azimuth patterns spanning the θ sector in which communication must be established. Hence a graphical method that would allow several azimuth patterns to be displayed together could convey all the radiation information at a glance. Up to recently, the altitude plot was the only graphical approach implemented at the EMC Laboratory for this purpose, and it is still mainly used throughout the second part of this work. Figure 23a shows the E - θ and E - ϕ altitude plots for a set of azimuth patterns from $\theta = 0$ to 180 degrees, i.e. the complete sphere of radiation. Opacity of the surfaces obtained is simulated by a hidden-line procedure. Note the similarity with the Mercator mapping technique for the surface of the globe.

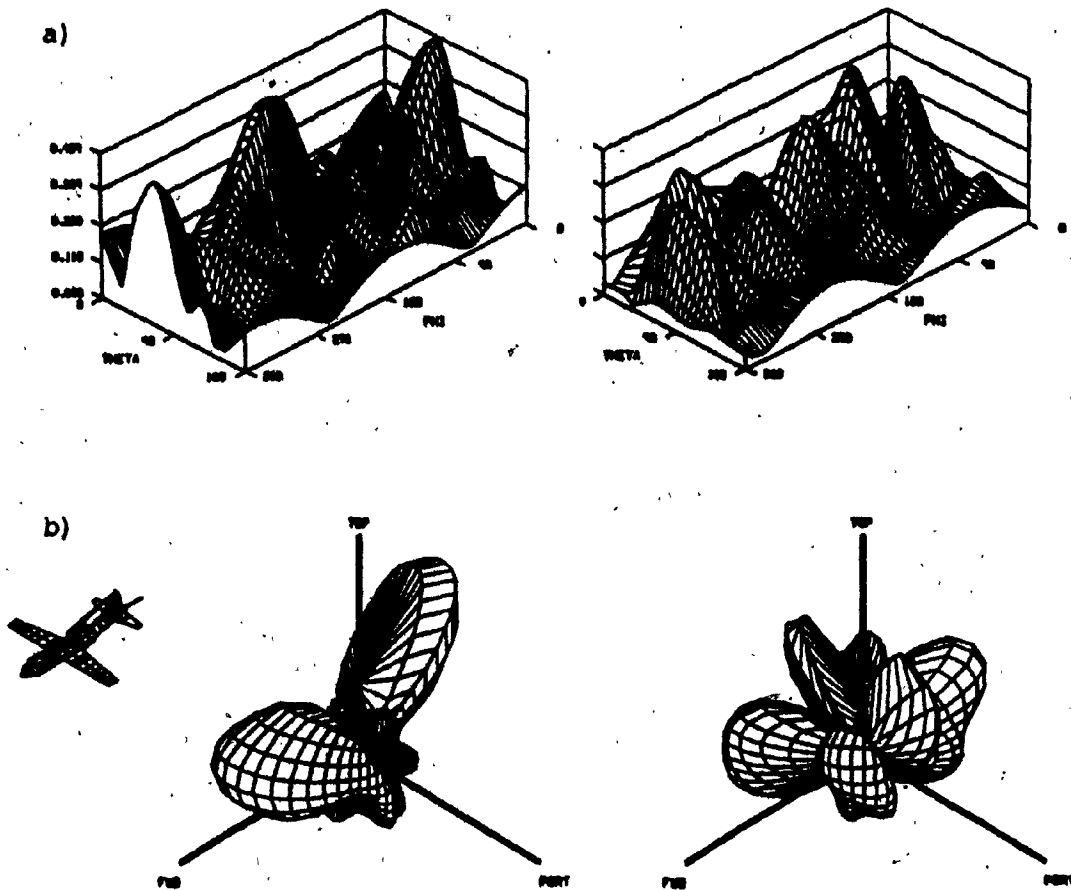


Fig. 23. Comparison of a) altitude plots of azimuth patterns with b) MOVIE.BYU plots

The main disadvantage of this representation is that the perception of the antenna's radiation characteristics is incomplete until the surfaces are mentally wrapped around the antenna in the correct manner. With the acquisition of the 3-D graphics system MOVIE.BYU 1981 (Christiansen and Stephenson, 1985), it became possible to translate this natural mental image into reality and hence drastically reduce

the interpretation effort. To illustrate the advantages, Figure 23b shows the same set of patterns as in a) obtained through the use of MOVIE.BYU system modules.

The Plotting Process

The MOVIE.BYU system consists of 7 FORTRAN programs for the display and manipulation of n-sided polygons, solid elements, and contour lines. For the purposes described above, only two modules are exploited. DISPLAY is used to apply the Watkin's hidden line/surface algorithm to the desired surface and then write a save file containing the display information. COMPOSE is used to read that save file and display the information with the desired scaling and positioning. Finally, a labelling program by the author is used to complete the display with useful information, including a drawing of the wire-grid model.

A program called TDPAT (Three-Dimensional PATtern) was written to control execution of the programs mentioned above and thus minimize user involvement. In conformity with a minimum of user specifications, TDPAT translates radiation pattern information into the form of a DISPLAY input file and writes command files to execute the necessary programs in the desired manner.

Among the user specifications is the name of the input file of patterns, the desired frequency if more than

one is present, and the theta interval defining the set of azimuth patterns to be displayed. Next comes the type of data desired, which may be E-theta or E-phi polarizations, or even power density, a worthwhile innovation in the EMC Laboratory. Power density S is easily obtained from E_θ and E_ϕ by the formula $S = (E_\theta^2 + E_\phi^2) / 2\eta_0$ (Stutzman and Thiele, 1981) or simply by $S = E_\theta^2 + E_\phi^2$ in the present case since relative magnitude alone is required. The final specification is the viewing angle of the surface. For this the user has eight choices, defined by whether a top or bottom view is desired, and by the quadrant number from 1 to 4.

The surface submitted to DISPLAY is constructed from an array of points. A point is defined for each radiation direction contained in the patterns, and is positioned in that same direction from the origin. The distance of the point from the origin is proportional to the magnitude of the desired quantity in the same direction. If for example E-theta is desired, and its magnitude is E in the direction defined by θ and ϕ , TDPAT computes a point given by $X = E \sin\theta \cos\phi$, $Y = E \sin\theta \sin\phi$, and $Z = E \cos\theta$ by simple conversion of coordinates.

TDPAT defines a surface patch from each group of four adjacent nodes spanning a pair of theta and a pair of phi values. The result is an array of adjacent quadrilateral patches forming a compact surface, as each interior node

is being shared by four patches. Patches are in general warped, that is, non-planar. The problems that this causes for the visible line/surface algorithm are handled in DISPLAY by a polygon subdivision process. The reader will notice from Figure 23b that the nearest halves of the x, y and z axes are represented by 3 extra thin patches added to the pattern.

After TDPAT has written a DISPLAY input file describing all required patches, it writes a command file to execute DISPLAY with the correct sequence of commands. These cause the pattern to be rotated and scaled as necessary and centered on the screen. Perspective is removed and clipping planes are brought at a safe distance. Watkin's algorithm is invoked and a save file is requested.

Rotation is such that the three axes project to the same length on the screen. As Figure 24a illustrates, this requires a viewing angle with an elevation of $\pm\text{-arctan}(1/\sqrt{2}) = \pm\text{-35.26}$ degrees and an azimuth of 45, 135, 225 or 315 degrees. The length of the axes is such that on the display they are guaranteed to extend further from the origin than the maximum extension of the pattern. This results in the maximum size of the pattern that still allows clear labelling of the axes. Figure 24b, which illustrates the worst case, shows that if V_{\max} is the maximum value of the pattern, the length L of the axes should be

such that $\cos(35.26^\circ) = V_{\max}/L$, or $L = V_{\max}/\cos(35.26^\circ) = V_{\max}/\sqrt{2/3} = \sqrt{1.5} V_{\max}$. It must be noted that the same value of V_{\max} is assumed for a matching pair of E-theta and E-phi patterns, so that they can be compared on the same scale. This value of V_{\max} is taken as the maximum field component plotted, whatever polarization it may be.

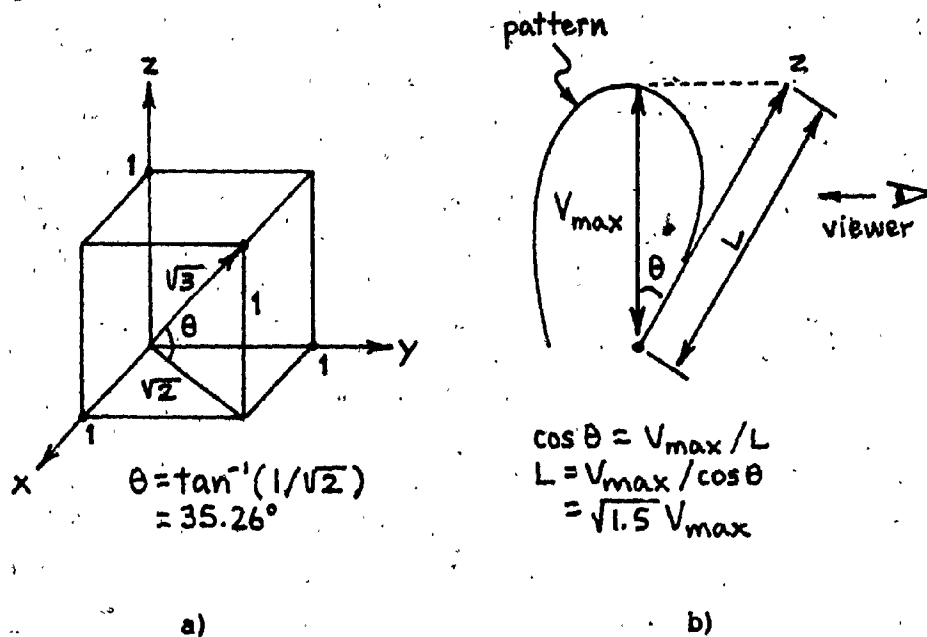


Fig. 24. Derivations for MOVIE.BYU plots: a) viewing angle, b) axis length

The last function of TDPAT is to write a second command file to execute sequentially program COMPOSE and the labelling program mentioned earlier, and therefore produce a complete display.

Elemental Pattern Shapes

With the possibility of now producing realistic pattern displays, it becomes of special interest to be able to recognize the elemental pattern shapes produced by a short dipole in different orientations. Figure 25a shows the E-theta, E-phi, and power density patterns for a vertical half-wave dipole. In b) and c) the same patterns are pictured for the dipole inclined at 45 and 90 degrees respectively towards the x-axis (forward). Note that the E-phi pattern remains constant in shape but varies in amplitude. This can be understood by visualizing an inclined dipole as the superposition of vertical and horizontal dipoles. Note also that the power density pattern is constant in shape but is oriented according to the dipole.

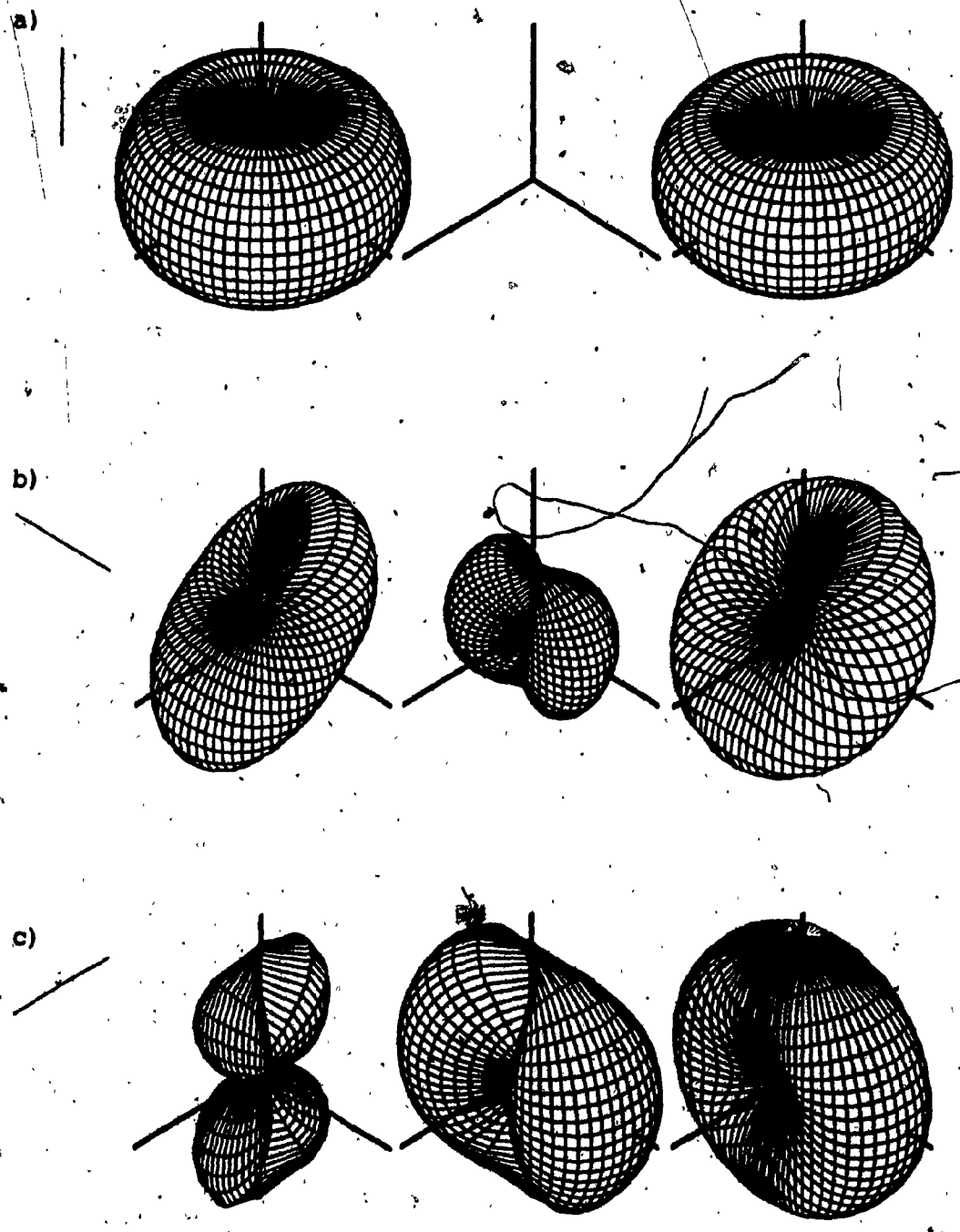


Fig. 25. E-theta, E-phi and power density patterns of a short dipole: a) vertical, b) inclined 45 degrees towards x axis, c) horizontal along x axis

CHAPTER IV

NUMERICAL TECHNIQUES

A number of programs exploiting various numerical techniques² are in use at the EMC Laboratory to extend the usefulness of the available antenna analysis programs. This chapter gives a theoretical description of two of these programs, ISOLEV and EFAR, and includes improvements and modifications that were made by the author since the programs were originally written by Bahsoun in 1981.

Program ISOLEV

ISOLEV (ISOTropic LEVel) (Bahsoun and Kubina, 1981)² is a program that reads a solution file as compressed by STRIP (or MSTRIP) and computes useful statistics about the radiated fields. These data, which are not supplied by the antenna analysis program, are then inserted between the frequency line and the impedance line(s) as a new copy of the solution file is being written. Figure 26 shows a complete set of these statistics, which include the maximum electric field, the radiated power, and the isotropic level. The three last values are assessment parameters for HF aircraft antennas: the radiation pattern efficiency (R.P. efficiency), the percentage of power in the E-theta polari-

zation ($\%E$ -theta), and the percentage of useful E -theta power (sub- $\%E$ -theta).

CM		
CM	MAXIMUM FIELD STRENGTH	0.191E+00
CM		
CM	TOTAL RADIATED POWER	0.321E-03
CM		
CM	ISOTROPIC LEVEL	0.139E+00
CM		
CM	R. P. EFFICIENCY	55.642
CM		
CM	$\%E$ -THETA POWER	64.687
CM		
CM	SUB- $\%E$ -THETA POWER	35.981

Fig. 26. Statistics computed and inserted by ISOLEV into the input solution file

The maximum electric field is the maximum value found in the patterns; this may equally well be a horizontal or a vertical component. This value is read from the solution file by pattern display programs for calibration purposes. The remaining ISOLEV statistics are explained in the next sections.

Radiated Power and Isotropic Level

Antenna analysis programs NEC and MININEC do supply a value of input power that is obtained from the voltage source magnitudes, the induced currents at the centers of the excited wire sections, and the power formula $P = 1/2 \operatorname{Re}(VI^*)$. This however was found by experience to be an

inaccurate value of radiated power, becoming even negative in some cases and therefore of no physical meaning. An accurate value of radiated power is required as a step in deriving an isotropic field magnitude that can be used in pattern comparisons. For this reason ISOLEV computes its own value of radiated power from the set of azimuth patterns available in the solution file. If the azimuth patterns do not cover the complete range $\theta = 0$ to 180 degrees, the power radiated in the given sector only is computed and written, and the four remaining parameters are skipped since they require a knowledge of the total power radiated.

Radiated power is obtained by integrating the power density

$$S(\theta, \phi) = \frac{E_{\theta}^2(\theta, \phi) + E_{\phi}^2(\theta, \phi)}{2\eta_0}$$

over the surface of the sphere of radius 1 m, for which $dS = d\phi \sin\theta d\theta$:

$$P = \int_{\theta=0}^{\pi} \int_{\phi=0}^{2\pi} \frac{E_{\theta}^2(\theta, \phi) + E_{\phi}^2(\theta, \phi)}{2\eta_0} d\phi \sin\theta d\theta.$$

This can be broken up into the power contributions of each polarization, i.e. $P = P_{\theta} + P_{\phi}$, where

$$P_{\theta} = \frac{1}{\eta_0} \int_{\theta=0}^{\pi} \int_{\phi=0}^{2\pi} \frac{E_{\theta}^2(\theta, \phi)}{2} d\phi \sin\theta d\theta,$$

$$P_{\phi} = \frac{1}{\eta_0} \int_{\theta=0}^{\pi} \int_{\phi=0}^{2\pi} \frac{E_{\phi}^2(\theta, \phi)}{2} d\phi \sin\theta d\theta.$$

Denoting the middle integrals $S_{\theta}(\theta)$ and $S_{\phi}(\theta)$, the above is rewritten as

$$1) P_{\theta} = \frac{1}{\eta_0} \int_0^{\pi} S_{\theta}(\theta) \sin\theta d\theta, \quad S_{\theta}(\theta) = \int_0^{2\pi} \frac{E_{\theta}^2(\theta, \phi)}{2} d\phi,$$

$$2) P_{\phi} = \frac{1}{\eta_0} \int_0^{\pi} S_{\phi}(\theta) \sin\theta d\theta, \quad S_{\phi}(\theta) = \int_0^{2\pi} \frac{E_{\phi}^2(\theta, \phi)}{2} d\phi.$$

The notation S implies surface integration, and indeed it can be easily shown that the middle integrals represent the areas of the azimuth patterns on polar plots.

The detailed derivation of P_{θ} alone is explained here, as it parallels that of P_{ϕ} . Various integration techniques must be exploited to approximate the integrals from the discrete values available. In a typical problem, $m+1$ azimuth patterns are available, with theta values and E-theta pattern areas denoted respectively by θ_i and $S_{\theta i}$, $i=0, \dots, m$. Each pattern includes the same $n+1$ phi values equally spaced from 0 to 360 degrees. Because n is usually made large enough to ensure adequate pattern resolution, the trapezoidal rule is a good approximation to the evaluation of $S_{\theta i}$:

$$S_{\theta i} = \frac{2\pi/n}{2} \left[\frac{E_{\theta}^2(\theta_i, 0)}{2} + \sum_{j=1}^{n-1} E_{\theta}^2(\theta_i, 2\pi j/n) + \frac{E_{\theta}^2(\theta_i, 2\pi)}{2} \right].$$

Recognizing that $E_{\theta}^2(\theta_i, 0) = E_{\theta}^2(\theta_i, 2\pi)$, the expression reduces to

$$S_{\theta i} = \frac{\pi}{n} \sum_{j=1}^n E_{\theta}^2(\theta_i, 2\pi j/n).$$

The last step in obtaining P_{θ} is the integration of $S_{\theta}(\theta) \sin\theta$, which is known precisely only at the $m+1$ theta values. In a past version of ISOLEV, a linear approximation of $S_{\theta}(\theta) \sin\theta$ was used over each theta interval. Since in the general case the size of the theta intervals varies, the trapezoidal rule had to be modified as follows:

$$P_{\theta} = \frac{1}{\eta_0} \sum_{i=1}^m (\theta_i - \theta_{i-1}) \frac{S_{\theta i} \sin\theta_i + S_{\theta i-1} \sin\theta_{i-1}}{2}.$$

An improved version of this approach is used in the current version of ISOLEV. A piecewise linear approximation of $S_{\theta}(\theta)$ alone is used with the $\sin\theta$ variation taken into account. This is referred to as a modified trapezoidal rule with $\sin\theta$ weighting function. The integral over a sample theta interval is worked out below, and then by extension a complete expression for P_{θ} is derived.

The linear approximation of $S_\theta(\theta)$ from θ_0 to θ_1 is, by first order Lagrange interpolation,

$$\begin{aligned} s_\theta(\theta) &= s_{\theta_0} \frac{\theta - \theta_1}{\theta_0 - \theta_1} + s_{\theta_1} \frac{\theta - \theta_0}{\theta_1 - \theta_0} \\ &= \frac{s_{\theta_1} - s_{\theta_0}}{\theta_1 - \theta_0} \theta + \frac{s_{\theta_0} \theta_1 - s_{\theta_1} \theta_0}{\theta_1 - \theta_0} = A\theta + B. \end{aligned}$$

The integral over this interval is then

$$\begin{aligned} \int_{\theta_0}^{\theta_1} (A\theta + B) \sin \theta d\theta &= A \int_{\theta_0}^{\theta_1} \theta \sin \theta d\theta + B \int_{\theta_0}^{\theta_1} \sin \theta d\theta \\ &= A \left[\sin \theta - \theta \cos \theta \right]_{\theta_0}^{\theta_1} + B \left[-\cos \theta \right]_{\theta_0}^{\theta_1} \\ &= A (\sin \theta_1 - \sin \theta_0 + \theta_0 \cos \theta_0 - \theta_1 \cos \theta_1) \\ &\quad + B (\cos \theta_0 - \cos \theta_1). \end{aligned}$$

Substituting the expressions for A and B, the integral after some manipulation simplifies to

$$\frac{s_{\theta_1} - s_{\theta_0}}{\theta_1 - \theta_0} (\sin \theta_1 - \sin \theta_0) + s_{\theta_0} \cos \theta_0 - s_{\theta_1} \cos \theta_1,$$

and summing the contributions of the m theta intervals,

$$P_\theta = \frac{1}{\eta_0} \sum_{i=1}^m \left[\frac{s_{\theta_i} - s_{\theta_{i-1}}}{\theta_i - \theta_{i-1}} (\sin \theta_i - \sin \theta_{i-1}) + s_{\theta_{i-1}} \cos \theta_{i-1} - s_{\theta_i} \cos \theta_i \right]$$

A simplification of the above expression was discovered by the author and will be implemented in ISOLEV in the near future to improve the computations. Cancelling out of terms becomes obvious when the sum is explicitly listed as follows:

$$\begin{aligned} & \frac{S_{\theta_1} - S_{\theta_0}}{\theta_1 - \theta_0} (\sin \theta_1 - \sin \theta_0) + S_{\theta_0} \cos \theta_0 - S_{\theta_1} \cos \theta_1 \\ & + \frac{S_{\theta_2} - S_{\theta_1}}{\theta_2 - \theta_1} (\sin \theta_2 - \sin \theta_1) + S_{\theta_1} \cos \theta_1 - S_{\theta_2} \cos \theta_2 \\ & + \frac{S_{\theta_3} - S_{\theta_2}}{\theta_3 - \theta_2} (\sin \theta_3 - \sin \theta_2) + S_{\theta_2} \cos \theta_2 - S_{\theta_3} \cos \theta_3 \\ & + \dots \end{aligned}$$

From this,

$$P_{\theta} = \frac{1}{\eta_0} \left[\sum_{i=1}^m \frac{S_{\theta_i} - S_{\theta_{i-1}}}{\theta_i - \theta_{i-1}} (\sin \theta_i - \sin \theta_{i-1}) + S_{\theta_0} \cos \theta_0 - S_{\theta_m} \cos \theta_m \right]$$

As was explained in Chapter II, the isotropic level is defined by the relation $E_{\text{iso}}^2 / 2\eta_0 = P / 4\pi$, from which $E_{\text{iso}} = \sqrt{P\eta_0 / 2\pi}$. This field value is used by the pattern comparison program PATCMP, which is used for most figures in part two of this work. The program compares on the same polar graph equivalent patterns from two solution files. If this comparison is to be at all meaningful, the difference

that might exist in the power levels of the two solution files must be compensated for by proper relative scaling of the patterns. PATCMP scales the two patterns compared so that the two isotropic levels coincide on the polar graph; thus it looks as if the two sets of patterns radiated equal amounts of power.

The Military Standard MIL-A-9080 (USAF)

A standard set of 21 azimuth patterns from theta = 0 to 180 degrees is in use at the EMC Laboratory and is listed in Table 2. As the table indicates, the set is characterized by approximately constant increments of 0.1 in $\cos\theta$. This is in accordance with the military standard MIL-A-9080 (USAF) and has the advantage of a simplified calculation of radiated power, as explained below.

Since $d(\cos\theta)/d\theta = -\sin\theta$, it follows that in the original expression

$$P_{\theta} = \frac{1}{\eta_0} \int_0^{\pi} S_{\theta}(\theta) \sin\theta d\theta,$$

$\sin\theta d\theta$ can be replaced by $-d(\cos\theta)$ and the limits of integration changed from 0 and π to $\cos(0)$ and $\cos(\pi)$:

$$P_{\theta} = \frac{-1}{\eta_0} \int_1^{-1} S_{\theta}(\theta) d(\cos\theta) = \frac{1}{\eta_0} \int_{-1}^1 S_{\theta}(\theta) d(\cos\theta).$$

If now the MIL-SPEC angles are used, S_{θ} is known at constant

increments of .1 in $\cos\theta$, and the standard trapezoidal rule can be used:

$$P_{\theta} = \frac{1}{\eta_0} \frac{.1}{2} \left(s_{\theta 0} + \sum_{i=1}^{19} 2s_{\theta i} + s_{\theta 20} \right).$$

TABLE 2

THE 21 MIL-SPEC ANGLES AND THEIR COSINES

Theta no.	Theta	Cos(theta)
0	0	1.000
1	25	.906
2	37	.799
3	45	.707
4	53	.602
5	60	.500
6	66	.407
7	72	.309
8	78	.208
9	84	.105
10	90	.000
11	96	-.105
12	102	-.208
13	108	-.309
14	114	-.407
15	120	-.500
16	127	-.602
17	135	-.707
18	143	-.799
19	155	-.906
20	180	-1.000

In the original version of ISOLEV by Bahsoun, surprisingly enough, the higher-order approximation of Simpson's composite rule was in use:

$$P_{\theta} = \frac{1}{\eta_0} \frac{.1}{3} \left(s_{\theta 0} + \sum_{i=1}^{10} 4s_{\theta 2i-1} + \sum_{i=1}^9 2s_{\theta 2i} + s_{\theta 20} \right).$$

A supplementary reason for using the MIL-SPEC angles is that ISOLEV cannot yet compute the three aircraft assessment parameters for a set of angles other than the standard set. Therefore the next section dealing with the assessment parameters will assume the standard set of angles.

HF Aircraft Assessment Parameters

When it comes to judging the adequacy of an aircraft model, the antenna engineer often has no choice but to compare massive amounts of measured and computed data. What ISOLEV offers as a practical solution is the computation of three assessment parameters that use the pattern integration introduced earlier. This provides a summary of the radiation characteristics that helps in the discrimination process and at the same time gives an indication of system performance.

The assessment parameters are based on the need to maintain adequate communication beyond the line of sight. That is because aircraft, and particularly the CP-140 long range patrol aircraft (see Part Two), are often flown at low altitudes but at large distances from the receiving station. The propagation modes that are effective in these conditions are the ground wave mode and the skywave mode (Bahsoun, 1982). A ground wave is most suitable for a highly conductive ground such as sea water; this also applies to the

CP-140 as it is being used for undersea detection and coastal and arctic patrol.

Adequate coverage in the $\theta = 90$ plane alone is not a sufficient requirement to excite the ground wave mode because of the manoeuvres that aircraft usually perform. A study of HF military communications requirements has determined that good communication should be maintained over the sector ± 30 degrees from the horizontal, i.e. $\theta = 60$ to 120 degrees (Bahsoun, 1982). Hence the R.P. efficiency η_p is defined as the percentage of the total power being radiated in this sector. This has become a standard in the aircraft industry, and may be thought of as the percentage of useful power. Mathematically, this can be expressed as

$$\eta_p = \frac{\int_{\theta=\pi/3}^{2\pi/3} \int_{\phi=0}^{2\pi} \frac{E_\theta^2(\theta, \phi) + E_\phi^2(\theta, \phi)}{2\eta_0} d\phi \sin\theta d\theta}{\int_{\theta=0}^{\pi} \int_{\phi=0}^{2\pi} \frac{E_\theta^2(\theta, \phi) + E_\phi^2(\theta, \phi)}{2\eta_0} d\phi \sin\theta d\theta} \times 100\%$$

The standard set of angles is particularly suited to R.P. efficiency computations since it specifically comprises the patterns limiting the desired sector. Denoting useful power P_u , η_p can be computed as

$$\eta_p = P_u/P \times 100\%$$

where $P = P_\theta + P_\phi$, and similarly $P_u = P_{u\theta} + P_{u\phi}$, the sum of

its E-theta and E-phi contributions. These can be obtained using the trapezoidal rule in conjunction with Table 2:

$$P_{u\theta} = \frac{1}{\eta_0} \frac{.1}{2} \left(S_{\theta 5} + \sum_{i=6}^{14} 2S_{\theta i} + S_{\theta 15} \right),$$

$$P_{u\phi} = \frac{1}{\eta_0} \frac{.1}{2} \left(S_{\phi 5} + \sum_{i=6}^{14} 2S_{\phi i} + S_{\phi 15} \right).$$

This would not be as straightforward for a general set of azimuth patterns not comprising the angles 60 and 120 degrees.

Because power is rapidly attenuated in the ground wave mode when the electric fields are horizontally polarized (Bahoun, 1982), the performance of the antenna is optimum when as much power as possible is radiated in the vertical component (E-theta). Therefore a percent E-theta parameter is defined as

$$\%E_{\theta} = \frac{\int_{\theta=0}^{\pi} \int_{\phi=0}^{2\pi} \frac{E_{\theta}^2(\theta, \phi)}{2\eta_0} d\phi \sin\theta d\theta}{\int_{\theta=0}^{\pi} \int_{\phi=0}^{2\pi} \frac{E_{\theta}^2(\theta, \phi) + E_{\phi}^2(\theta, \phi)}{2\eta_0} d\phi \sin\theta d\theta} \times 100\%.$$

This gives the ratio of the power contributed by the vertical field components alone to the total power, and can be computed as

$$\%E_{\theta} = P_{\theta}/P \times 100\%$$

The last parameter, the useful percent E-theta or sub-%E-theta, is especially useful since it examines the above two requirements: that power be radiated in the useful sector and in the vertical polarization. It is denoted $\%E_{\theta}^*$ and is defined as the percentage of the total power that is radiated in the sector theta = 60 to 120 degrees and in the vertical polarization:

$$\%E_{\theta}^* = \frac{\int_{\theta=\pi/3}^{2\pi/3} \int_{\phi=0}^{2\pi} \frac{E_{\theta}^2(\theta, \phi)}{2\eta_0} d\phi \sin\theta d\theta}{\int_{\theta=0}^{\pi} \int_{\phi=0}^{2\pi} \frac{E_{\theta}^2(\theta, \phi) + E_{\phi}^2(\theta, \phi)}{2\eta_0} d\phi \sin\theta d\theta} \times 100\%$$

With the standard set of angles, this can be computed as

$$\%E_{\theta}^* = P_{u\theta}/P \times 100\%$$

In the case of inadequate ground conductivity, a skywave mode of propagation dominates. This requires radiation at high elevation angles, but as Bahoun (1982) showed for a number of helicopter antennas, high elevation angle radiation is present with the HF wire antennas of the CP-140 (Part Two). The polarization radiated is also arbitrary because of the polarization rotation in the ionosphere (Bahoun, 1982). Therefore the three assessment parameters computed by ISOLEV do provide accurate indication of HF antenna

performance for this work.

Program EFAR

EFAR (Electric Far fields) (Bahsoun, 1981) is a program that calculates far field radiation patterns from a given current distribution on a wire-grid model. It reads a geometry and its induced wire currents from a NEC solution file, and allows the user to scale any wire currents by any factor, including zero, which has the effect of deleting the currents. A new solution file is then recopied with the corresponding patterns now computed from the modified set of currents. This is useful to determine the far field contribution of selected wires, or the effect of a small current perturbation.

Bahsoun wrote his initial version as a function of the Antenna Modelling Program AMP, the predecessor of NEC, and other students in the months that followed modified the program for compatibility with NEC and use on the Cyber computer. By the time the author resorted to EFAR for analysis of currents on a recent ship model, changes in laboratory format conventions had outdated the program.

A complete rewrite was started to improve the program structure and facilitate the addition of needed features. In the process, the validity of the theoretical formulation was examined and improvements were brought to

enhance the computational efficiency.

Theoretical Formulation of EFAR

Bahsoun in his original report on EFAR (1981) derived an expression for the far field of an infinitesimal current element with arbitrary location and orientation. The starting point for this was the far field expression for a z-directed current element $I ds$ located at the origin, as shown in Figure 27a:

$$d\vec{E} = \frac{jk\eta_0}{4\pi} \sin\theta \hat{\theta} \frac{e^{-jkr}}{r} I ds.$$

If the current element is now located at \vec{r}' and directed along unit vector \hat{s} , as shown in Figure 27b, the expression must be reformulated for computing the field in the global coordinate system, phase referred to the origin. From the figure, $\sin\theta = |\hat{s} \times \hat{R}|$, or using the parallel ray approximation, $\sin\theta = |\hat{s} \times \hat{r}|$. Unit vector $\hat{\theta}$ is obtained as $\hat{\theta} \times \hat{R} = \hat{\theta} \times \hat{r}$, where

$$\hat{\theta} = \frac{\hat{s} \times \hat{R}}{|\hat{s} \times \hat{R}|} = \frac{\hat{s} \times \hat{r}}{|\hat{s} \times \hat{r}|}. \text{ Therefore } \hat{\theta} = \frac{(\hat{s} \times \hat{r}) \times \hat{r}}{|\hat{s} \times \hat{r}|}, \text{ from which}$$

$$\sin\theta \hat{\theta} = (\hat{s} \times \hat{r}) \times \hat{r}.$$

By the parallel ray approximation, distance R can be approximated by $r-d$, where $d = \vec{r}' \cdot \hat{r}$, or the projection of vector

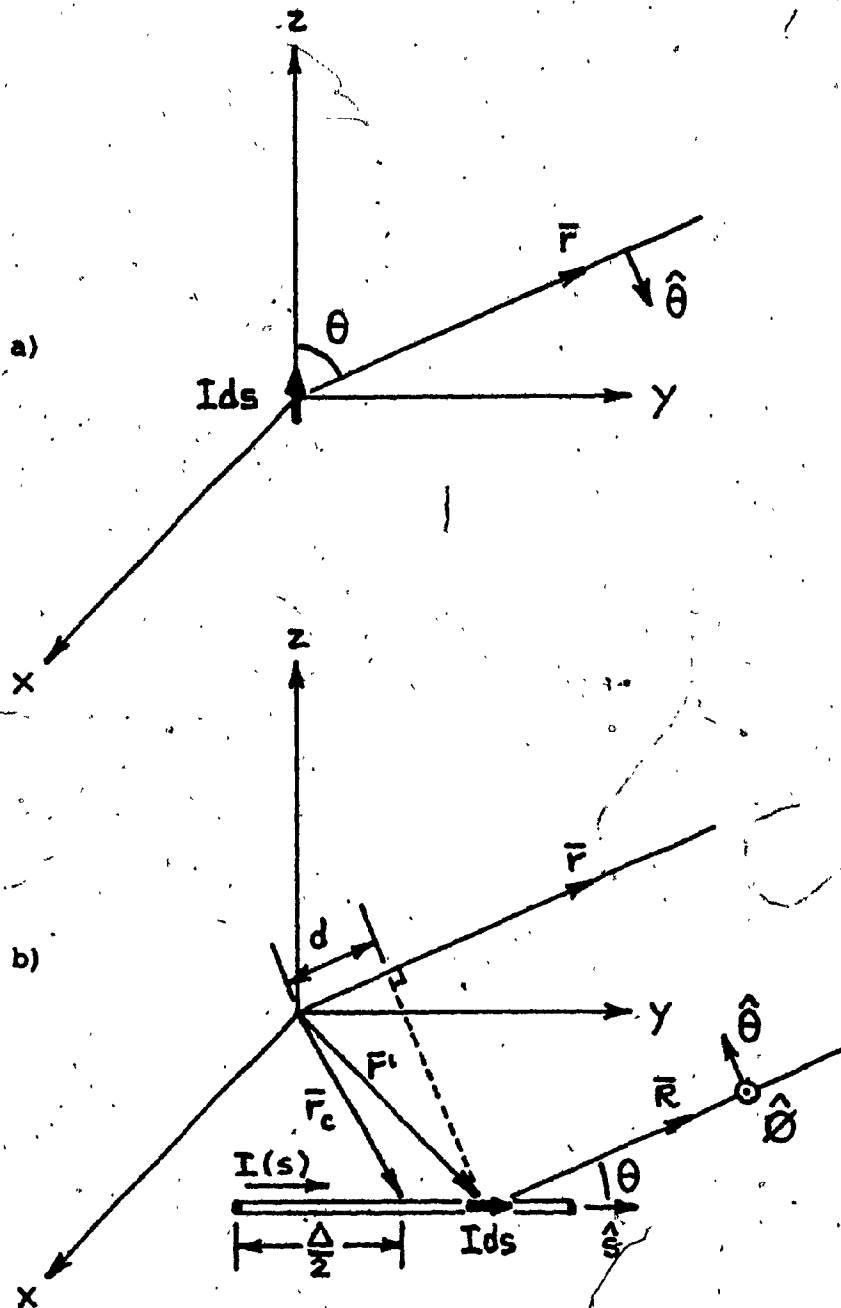


Fig. 27. a) A z -directed current element at the origin, and b) its use in deriving the far field of a segment of arbitrary location

\vec{r}' onto vector \vec{r} . Therefore

$$R = r - \vec{r}' \cdot \hat{r}.$$

This is used in the phase term but is approximated in the denominator as

$$R = r$$

since in this case, only the amplitude is affected and $r \gg \vec{r}' \cdot \hat{r}$. Substituting the above into the original expression gives

$$\begin{aligned} d\vec{E} &= \frac{jk\eta_0}{4\pi} (\hat{s} \times \hat{r}) \times \hat{r} \frac{e^{-jk(r - \vec{r}' \cdot \hat{r})}}{r} Ids \\ &= \frac{jk\eta_0}{4\pi} (\hat{s} \times \hat{r}) \times \hat{r} \frac{e^{-jkr}}{r} e^{jk\vec{r}' \cdot \hat{r}} Ids. \end{aligned}$$

If a unique field value is desired for each radiation direction, the term e^{-jkr}/r must be dropped, as it is done in NEC and MININEC:

$$d\vec{E} = \frac{jk\eta_0}{4\pi} (\hat{s} \times \hat{r}) \times \hat{r} e^{jk\vec{r}' \cdot \hat{r}} Ids.$$

The variation with distance then becomes implied in the numerical field values.

A numerically simpler form of the above was obtained by the author through the vector identity $(\vec{A} \times \vec{B}) \times \vec{C} =$

$\bar{B}(\bar{A} \cdot \bar{C}) - \bar{A}(\bar{B} \cdot \bar{C})$ (Spiegel, 1968). Thus

$$(\hat{s} \times \hat{r}) \times \hat{r} = \hat{r}(\hat{s} \cdot \hat{r}) - \hat{s}(\hat{r} \cdot \hat{r}) = \hat{r}(\hat{s} \cdot \hat{r}) - \hat{s},$$

and

$$d\bar{E} = \frac{jk\eta_0}{4\pi} [\hat{r}(\hat{s} \cdot \hat{r}) - \hat{s}] e^{jk\bar{r}' \cdot \hat{r}} I ds.$$

This expression may serve as the building block to derive the radiated fields of a wire segment.

The theoretical formulation of EFAR must correspond as well as possible with the far field formulation of the antenna analysis programs if reliable pattern comparisons are to be made. In these programs, because of restrictions on the wavelength to radius ratio (Chapter I), the effect of wire radius is neglected in the far field computations. Hence EFAR must obtain the far field of a segment by a simple line integral along the segment axis, as suggested by Figure 27b. The figure shows a segment of length Δ centered at \bar{r}_c and directed along unit vector \hat{s} . Summing the contributions of the current elements, the total far field is obtained as

$$\bar{E} = \frac{jk\eta_0}{4\pi} [\hat{r}(\hat{s} \cdot \hat{r}) - \hat{s}] \int e^{jk\bar{r}' \cdot \hat{r}} I(s) ds.$$

To express the integrand in terms of s , \bar{r}' can be replaced

by $\bar{r}_c + s\hat{s}$, in which case s ranges from $-\Delta/2$ to $\Delta/2$. This gives

$$\begin{aligned}\bar{E} &= \frac{jk\eta_0}{4\pi} [\hat{r}(\hat{s}\cdot\hat{r}) - \hat{s}] \int_{-\Delta/2}^{\Delta/2} e^{jk(\bar{r}_c + s\hat{s})\cdot\hat{r}} I(s) ds \\ &= \frac{jk\eta_0}{4\pi} [\hat{r}(\hat{s}\cdot\hat{r}) - \hat{s}] e^{jk\bar{r}_c\cdot\hat{r}} F(I(s)),\end{aligned}$$

where $F(I(s))$ is an integral function of the current distribution given by

$$F(I(s)) = \int_{-\Delta/2}^{\Delta/2} e^{jks\hat{s}\cdot\hat{r}} I(s) ds.$$

The problem that arises in evaluating $F(I(s))$ is that solution files supply only the current at the center of a segment, that is, at $s=0$. EFAR copes with this by assuming the current distribution

$$I(s) = CI(0)\Delta\delta(s),$$

where C is a scale factor that can be specified by the user. This is equivalent to a current element located at $s=0$, and with current moment equal to that of the segment if it had a uniform current distribution $CI(0)$ throughout. Other current distributions can be assumed, but this one has the advantage of resulting in the simplest formulation possible. Inserting into the integral, the sifting property of the

delta function gives

$$F = e^{jk(0)\hat{s}\cdot\hat{r}} CI(0)\Delta = CI(0)\Delta,$$

and hence the far field becomes

$$\bar{E} = \frac{jk\eta_0}{4\pi} [\hat{r}(\hat{s}\cdot\hat{r}) - \hat{s}] e^{jk\bar{r}_c\cdot\hat{r}} CI(0)\Delta.$$

This expression was further improved by the author

as

$$\bar{E} = \frac{jk\eta_0}{4\pi} [r(\bar{\Delta}\cdot\hat{r}) - \bar{\Delta}] e^{jk\bar{r}_c\cdot\hat{r}} CI(0),$$

where $\bar{\Delta} = \Delta\hat{s}$ is the vector from the start point to the end point of the segment and is easily computed by subtraction of end coordinates. Unit vector \hat{r} is obtained from θ and ϕ as $\sin\theta\cos\phi\hat{x} + \sin\theta\sin\phi\hat{y} + \cos\theta\hat{z}$, by standard conversion of coordinates.

If the contributions of the N segments of the model are added up, the total far field in the direction defined by \hat{r} becomes

$$\begin{aligned} \bar{E} &= \frac{jk\eta_0}{4\pi} \sum_{i=1}^N [\hat{r}(\bar{\Delta}_i\cdot\hat{r}) - \bar{\Delta}_i] e^{jk\bar{r}_{ci}\cdot\hat{r}} C_i I_i(0) \\ &= E_x\hat{x} + E_y\hat{y} + E_z\hat{z}. \end{aligned}$$

The E-theta and E-phi components can be obtained by project-

ing \bar{E} on the unit vectors $\hat{\theta}$ and $\hat{\phi}$ respectively. These are given by

$$\begin{aligned}\hat{\theta} &= \cos\theta\cos\phi\hat{x} + \cos\theta\sin\phi\hat{y} - \sin\theta\hat{z}, \\ \hat{\phi} &= -\sin\phi\hat{x} + \cos\phi\hat{y}.\end{aligned}$$

Hence

$$\begin{aligned}E_{\theta} &= \bar{E} \cdot \hat{\theta} = E_x \cos\theta\cos\phi + E_y \cos\theta\sin\phi - E_z \sin\theta, \\ E_{\phi} &= \bar{E} \cdot \hat{\phi} = -E_x \sin\phi + E_y \cos\phi.\end{aligned}$$

Validation of EFAR

A test that has served to validate EFAR is to execute the program on a wire-grid model with its unperturbed NEC or MININEC currents, i.e. using $C_i=1$ for $i=1$ to N . The patterns thus computed by EFAR are then compared with the original patterns to see how close they match. This test, whenever it has been conducted, has resulted in nearly perfect agreement of patterns on linear scale plots. The proof is nevertheless incomplete and it can still be feared that the formulation will fail under special circumstances.

Investigation was made by the author into the effect of neglecting segment lengths in the formulation of EFAR. For this purpose the more realistic current distribution

$$I(s) = CI(0), \quad -\Delta/2 < s < \Delta/2,$$

was assumed for trial. This distributes the current moment

uniformly over the segment length. Substituting into the expression for $F(I(s))$,

$$\begin{aligned}
 F &= \int_{-\Delta/2}^{\Delta/2} e^{jk\hat{s}\hat{r}} CI(0) ds = CI(0) \left[\frac{e^{jk\hat{s}\hat{r}}}{jk\hat{s}\hat{r}} \right]_{-\Delta/2}^{\Delta/2} \\
 &= CI(0) \frac{e^{jk\Delta\hat{s}\hat{r}/2} - e^{-jk\Delta\hat{s}\hat{r}/2}}{jk\hat{s}\hat{r}} = CI(0) \frac{2\sin(k\Delta\hat{s}\hat{r}/2)}{k\hat{s}\hat{r}} \\
 &= CI(0) \Delta \frac{\sin(k\Delta\hat{s}\hat{r}/2)}{k\Delta\hat{s}\hat{r}/2} = CI(0) \Delta \text{Sa}(k\Delta\hat{s}\hat{r}/2)
 \end{aligned}$$

where $\text{Sa}(x)$ is the sine-over-argument function $\sin(x)/x$, illustrated in Figure 28 over the range $x=0$ to π .

Therefore the extra term $\text{Sa}(k\Delta\hat{s}\hat{r}/2)$ is introduced as compared to the current element case. To appreciate the effects of this extra term, assume for simplicity a z -directed segment. The normalized E-theta pattern resulting from the current element approximation is known to be

$$E_{\theta}(\theta) = \sin\theta.$$

Now with the uniform current distribution approximation, this is scaled down by the term $\text{Sa}(k\Delta\hat{s}\hat{r}/2)$, where $\hat{s}\hat{r} = \hat{z} \cdot (\sin\theta\cos\phi\hat{x} + \sin\theta\sin\phi\hat{y} + \cos\theta\hat{z}) = \cos\theta$, and $k = 2\pi/\lambda$. The scaling term then becomes $\text{Sa}[(\Delta/\lambda)\pi\cos\theta]$. It has a maximum of one when the argument is zero, i.e. $\theta = \pi/2$. Therefore the normalized E-theta pattern becomes simply

$$E_{\theta}(\theta) = \sin\theta \text{Sa}[(\Delta/\lambda)\pi\cos\theta].$$

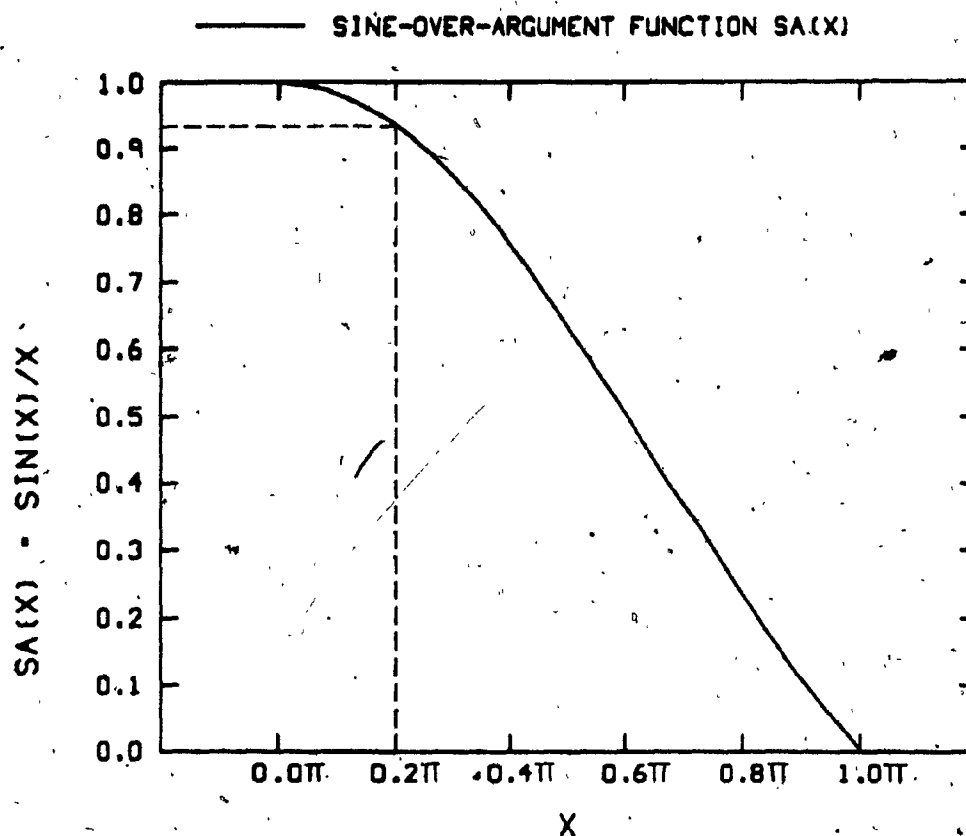


Fig. 28. Graph of the sine-over-argument function over the interval $(0, \pi)$.

The effect of the Sa term is strongest when the segment is as long as is permissible, that is, 0.2λ (Chapter I). This brings the argument to a maximum of 0.2λ , causing the Sa function to drop as low as 0.935 (see Figure 28). In this worst case the normalized pattern is

$$E_{\theta}(\theta) = \sin\theta \text{ Sa}(.2\pi \cos\theta),$$

and Figure 29 compares this with the current element pat-

tern. The small pattern difference that appears did not seem sufficient to justify the introduction of the Sa function into the formulation of EFAR and the subsequent increase in computer time.

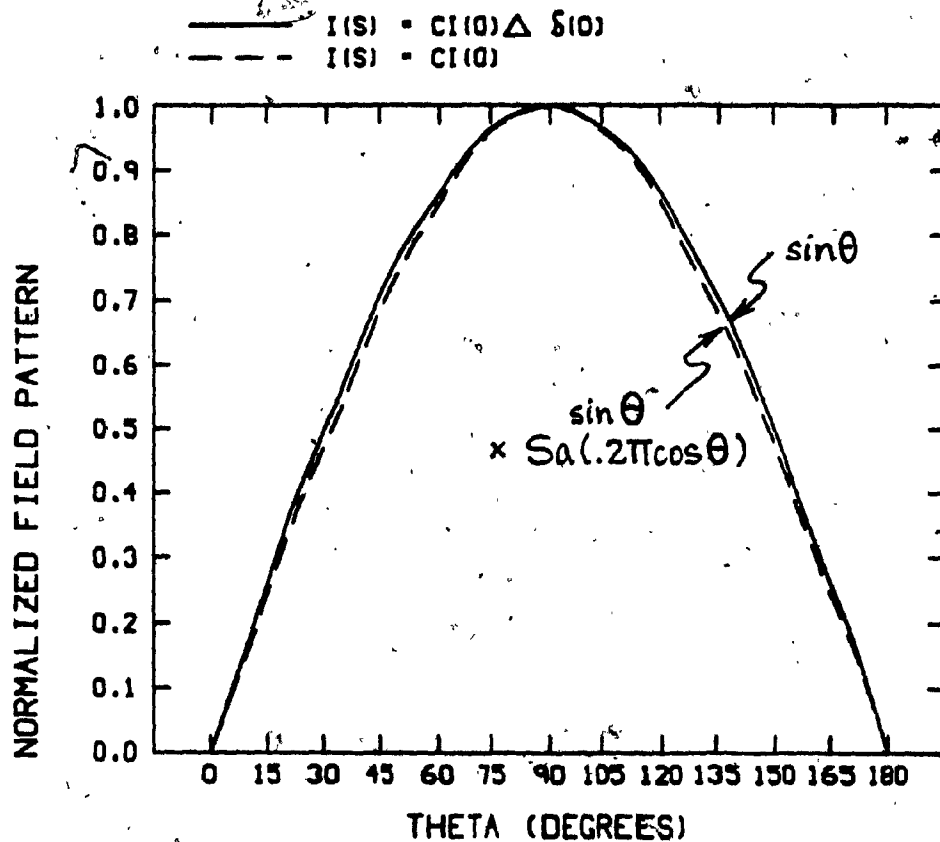


Fig. 29. Comparison of the normalized far field patterns of a current element (solid line) and a $.2\lambda$ segment (dashed line)

It has been complained in the past that EFAR would not accurately reproduce radiated fields in the null regions, with visible consequences on decibel plots.

Suggested solutions to the problem call for the use of more realistic current distributions on the segments. The ideal option is of course the exact recovery of the current basis functions that were computed by NEC or MININEC. However, linear interpolation of current from one segment center to the other would be easier to program and the scheme would be independent of the particular antenna analysis program that was used to obtain the currents.

Effect of Ground Plane

The major enhancement brought to EFAR by the author is the ability to detect the ground plane option in a solution file and to take appropriate action. By image theory (Stutzman and Thiele, 1981), a segment over a perfect ground plane can be replaced by the segment and its image both in free space. The image is simply a mirror reflection of the actual segment carrying the negative of the actual current. This is illustrated in Figure 30.

Thus the presence of a ground plane effectively doubles the number of segments and the computation time. For a given segment, the far field expression must be evaluated a second time after negating $I(0)$ and the z components of \vec{r}_c and \hat{s} .

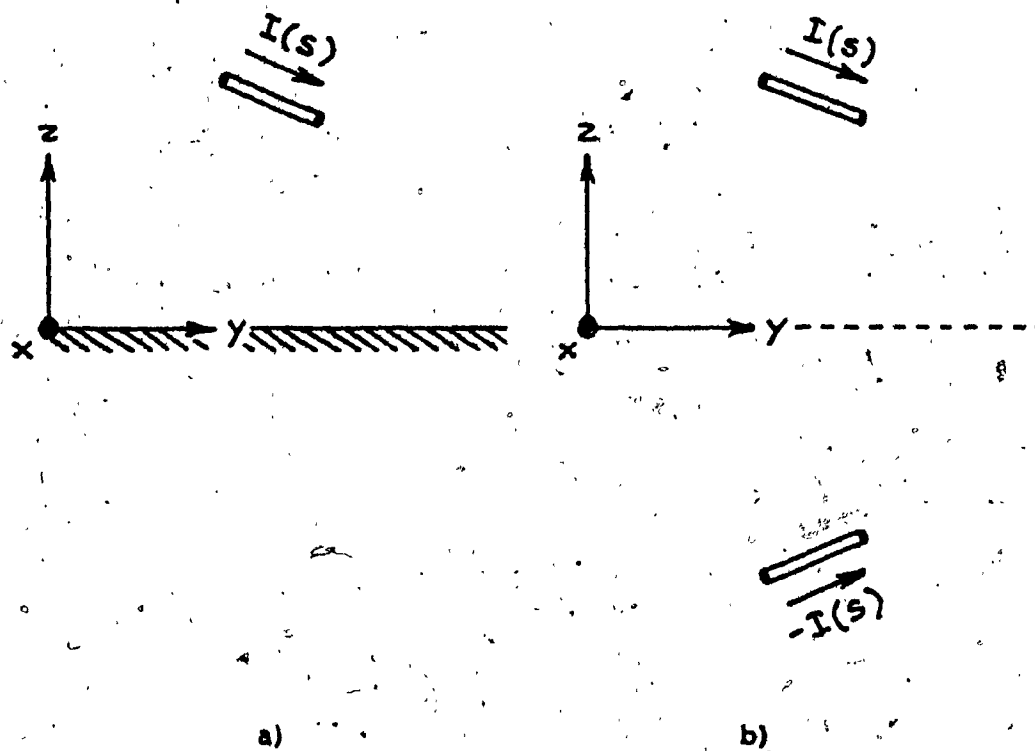


Fig. 30. a) Current-carrying segment over a perfect ground plane, and b) equivalent free-space situation.

PART TWO

CP-140/AURORA HF ANTENNA INSTALLATION

CHAPTER V

THE P3V-1 HF INSTALLATION

The CP-140/Aurora is Canada's modern long range patrol aircraft, whose counterpart in use by the U.S. Navy and other nations is called the P-3C/Orion. The complement of avionic equipment and the antenna installation on this specific airframe have been updated many times since the days of the commercial Lockheed "Electra". Wire antennas were introduced on early versions of the airframe to provide the important long-range communication capability. The CP-140 presently features a dual HF installation consisting of port and starboard wire antennas of dissimilar lengths.

The overall objective of the CP-140 project was to derive computer models that could be used in the analysis of the operational performance of the HF system. Thus the thrust of the modelling effort was to be directed at the testing of the modelling topology and modelling guidelines that would produce radiation patterns (and impedance) over the HF band, 2-30 MHz, closest to measured results.

Some time ago, Lockheed undertook radiation pattern measurements on a scale-model of the P3V-1, the first military version of the airframe. The data became available to the EMC Laboratory through Lockheed Report, LR 13565 (Archer,

1961). The HF configuration consisted at that time of port and starboard wire antennas of identical lengths. Modelling work was nevertheless started on the P3V-1 configuration of HF antennas because experimental data were not available for the present configuration.

The Measurements

The P3V-1 HF antenna installation is shown in Figure 31. It consists of port and starboard wire antennas with feed points at the same fuselage station (FUS STA 452) and approximately 38 inches off the centerline. On the actual aircraft they terminate at the same vertical stabilizer station (VSS 191) in a V-connection of insulators that separates the open ends of the antennas. On the scale model, however, the starboard antenna was connected to VSS 129 and was thus approximately 35 inches shorter (as shown in Figure 31). This change was made to eliminate any possible chance of the HF installation interfering with the operation of the deicer heating element on the leading edge of the vertical stabilizer (Archer, 1961). It is not known whether each antenna was measured with the passive antenna installed or not, and if so, whether the latter was shorted or terminated in 50 ohms. Cruising conditions were simulated in the measurements, which is equivalent to the default condition of the antenna analysis programs (free space).

The same measured data were available for both antennas and for each of the even frequencies from 2 to 24 MHz. The E-theta and E-phi patterns were available in the cuts $\phi = 0$ and 90 degrees, and $\theta = 60, 70, 80, 90, 100, 110$ and 120 degrees. Supplementary E-theta patterns were also available in the cuts $\theta = 50, 75, 85, 95, 105$ and 130 degrees. Patterns were in the classic analog polar plot form, and therefore had to be manually digitized (via digitizing tablet) in order to produce the pattern comparisons that follow. For convenience in pattern display and file structure, the E-phi patterns matching the supplementary E-theta patterns were artificially generated by interpolation and extrapolation. Isotropic levels and percentage of cross polarization ($\%E\text{-}\phi$) were also available; hence E-theta percentage could be obtained as $100\% - \%E\text{-}\phi$. Finally, the essential sections of the impedance curves were available over the range 1.6 to 25.4 MHz. These had to be digitized as well for the purposes of the impedance display program DIGIMP, introduced in Chapter III.

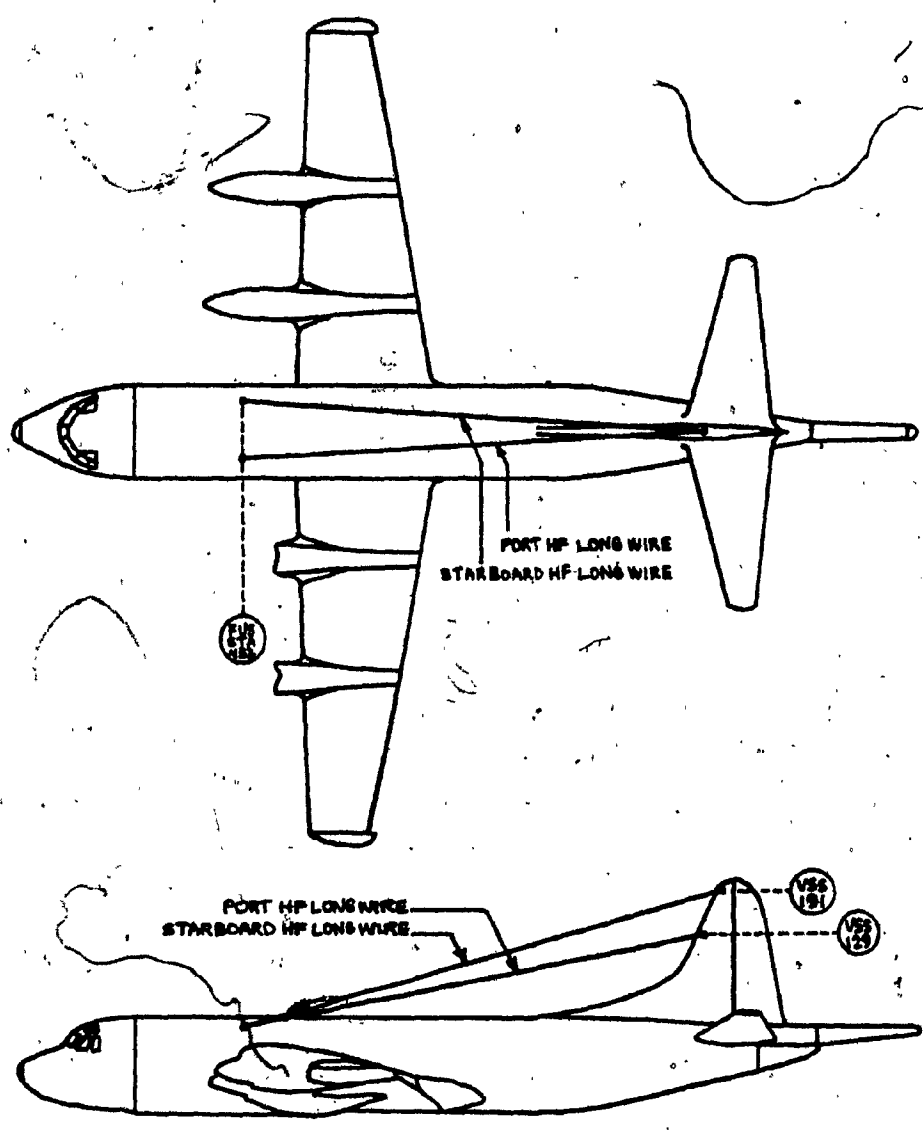


Fig. 31. P3V-1 HF antenna installation

Model Generation

The starting point of model generation for antenna analysis purposes was a detailed wire-grid model of the CP-140 airframe that had been digitized from a plastic model kit. Having not been constructed with M.O.M. testing in view, the model was neither electromagnetically equivalent to the actual aircraft nor suitable for NEC analysis. Nevertheless it was to serve as a reliable reference for future model development. After close examination by the author, it was found to contain a number of anomalies in the windshield, the engines and the fuselage connections of the wings and stabilizers. These were corrected and the resulting model is contrasted with the original one in Figure 32; it is now appropriately referred to as the "public relations" (PR) model.

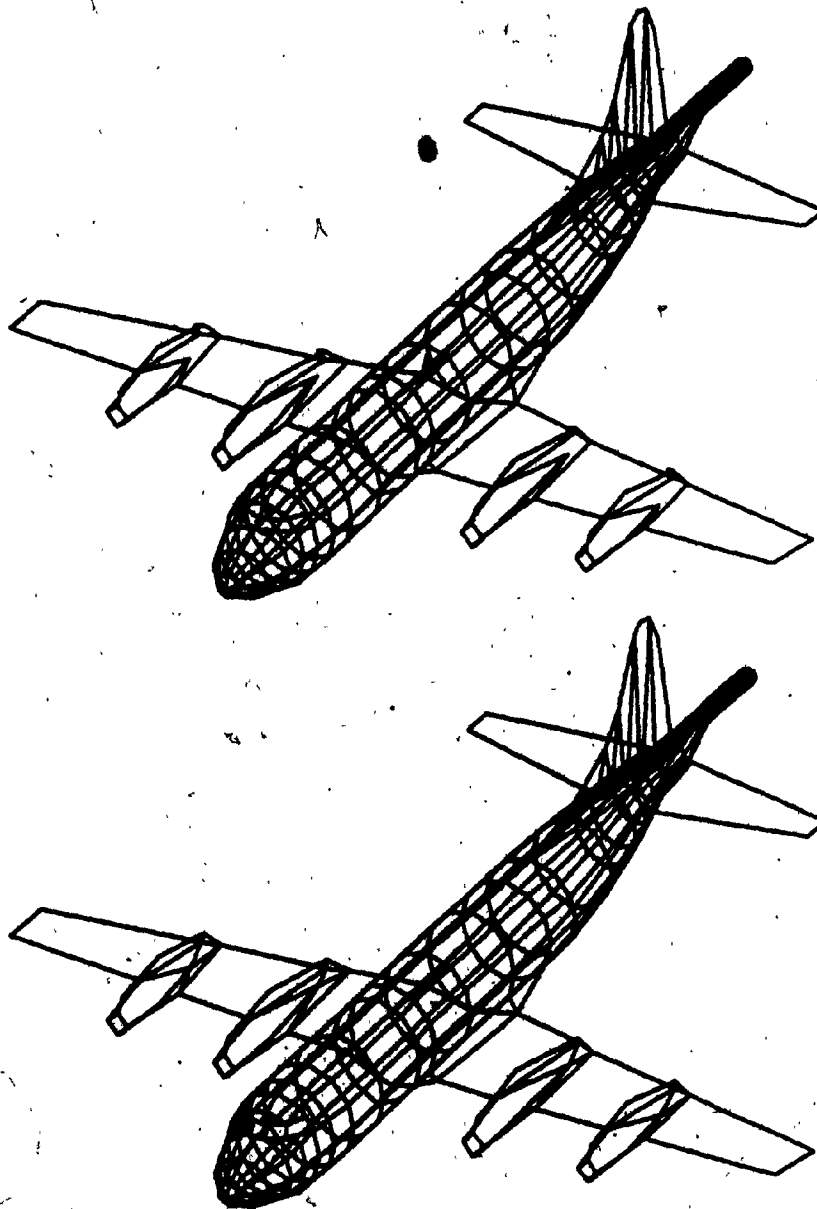


Fig. 32. Original PR (public relations) model and present version with anomalies corrected (windshield, engines, etc.).

Thin stick models

Models of simple topology are attractive because they are easy to generate and fast to use with antenna analysis programs. Since computation time varies as approximately the cubed power of the number of segments, simple models are relatively inexpensive in terms of CPU time, as compared to more complex ones. Along this line of thought, a first P3V-1 model was built with single wires along center lines of the main features of the aircraft. The result appears in Figure 33a and is referred to as a "stick" model. The geometry file was created by hand, the necessary coordinates being extracted or derived from the PR model and an antenna arrangement print for the P3V-1 aircraft.

The stick model is oriented in the positive x direction in accordance with laboratory conventions, and the origin is arbitrarily located at the junction point of the wings and the fuselage. Since in practice the wings connect at a level below the axis of the fuselage, a compromise was made by lowering the wire for the fuselage to the level of the tip of the aircraft's nose, and by raising the wings to the same level.

With the intention of testing first the port antenna, it was connected as shown to the fuselage by a radially directed feed element 1' long (the source segment), and was terminated 2' away from the vertical stabilizer to account

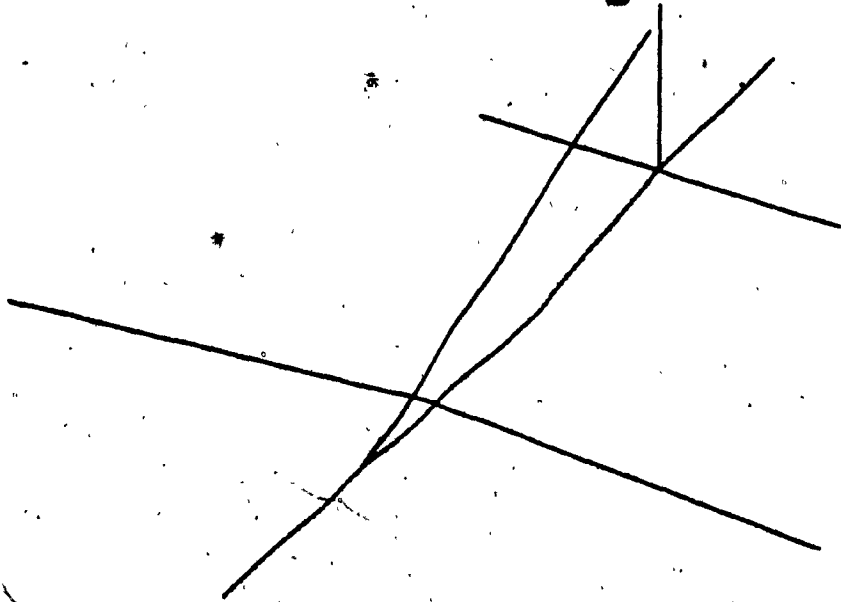
for the insulated portion. It was logical to assume of course that the starboard antenna (passive) had been left installed during measurements of the port antenna, but without the possibility of corroboration, all possibilities had to be considered. Hence the starboard antenna was initially left out.

Radius considerations were neglected at this stage by assuming a uniform value of .01 m throughout, making the model a "thin" one. Wires were segmented enough so as to not exceed the $.2\lambda$ criterion at 30 MHz, the HF frequency of smallest wavelength. This resulted in 65 segments of maximum length $.2(c/f) = .2(300 \text{ Mm/s})/(30 \text{ MHz}) = 2 \text{ m}$. This made the feed element the shortest segment, with a Δ/λ ratio at 2 MHz of $(.3048 \text{ m})/(300/2) = .002$, which still exceeds the recommended lower limit of .001, but introduces seg/seg errors at the wire ends. For the purposes of this work, the thin model with one antenna (port) will be referred to as model T1.

To account for the possible presence of the starboard antenna during measurements, a new model was derived by adding to model T1 the starboard antenna shorted. This added 13 segments, bringing the total to 78. The resulting geometry with both antennas is illustrated in Figure 33b and will be called model T2. To model the third possible state of the starboard antenna and thus complete the investiga-

tion, a load of 50 ohms was later added to the starboard feed element of model T2. Of course the resulting loaded model, which will be called model T2L, still appears as in Figure 33b.

a)



b)

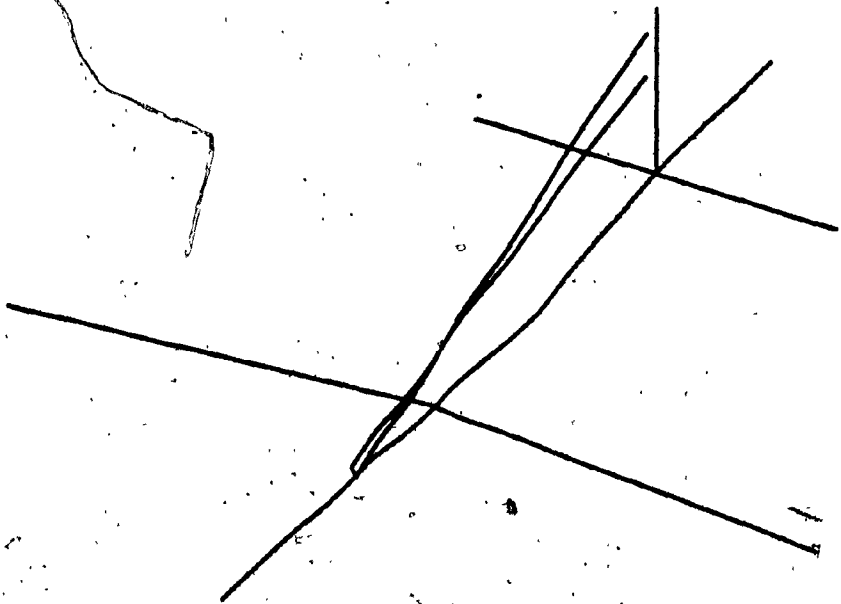


Fig. 33. P3V-1 stick models T1 (a) and T2 or T2L (b)

Fat stick models

Differences between computed and measured results lead to an examination of possible parameters or topology that should be varied. Hence it was decided to select new radius values that would be within the limits of the isoperimetric inequalities (Jaggard, 1979). The lower and upper radius limits are such that cross-sectional areas and perimeters, respectively, are preserved. To be on the safe side in regard to NEC modelling guidelines, the lower limit was observed. Therefore three new models corresponding to the earlier thin ones were derived and are illustrated in Figure 34. They are referred to as the "fat" or "tapered" models. The cross-sectional areas of the fuselage were estimated from the PR model, and for lack of detail those of the wings and stabilizers were measured directly from the plastic model kit. The resulting radius values were then scaled down by a factor of .928 in a desire to keep the seg/rad ratios greater than or equal to one. Note that this is in the warning zone of program CHECK. The radius of the antennas was kept at .01 m, but feed elements had to be lengthened so that they would emerge 1' from the surface of the fuselage.

Tapering of the radius along wires could have been readily achieved by insertion of GC lines in the geometry section, but the resulting format would have become incompatible with the existing model display software. Therefore

the segments of each wire were redefined as independent wires so that they could be assigned different radius values. This increased the number of wires but did not affect the number of segments and hence the execution time.

Lengthening of the feed elements effectively removed the seg/seg errors at the nodes, but caused the wires to slightly exceed $.2\lambda$ at 30 MHz. The larger radii on the rest of the model introduced obvious rad/rad errors at the antenna feed points, caused the wav/rad criterion to be violated above 6 MHz, and caused some wires to become embedded inside the fuselage (feed elements and first wing segments). These various incompatibilities were tolerated for the purposes of initial testing. In the sections that follow, the fat models will be referred to as models F1, F2 and F2L.

In an attempt to remove some of the above incompatibilities, a last model was derived from model F1 by reducing the radii along the fuselage. The result appears in Figure 35. A fixed radius value corresponding to the maximum radius of the wings was used from the tip of the nose to the vertical stabilizer. This caused the wav/rad criterion to be satisfied at up to 12 MHz, and the center of the feed element to emerge outside of the fuselage. This revision will be called model F1'.

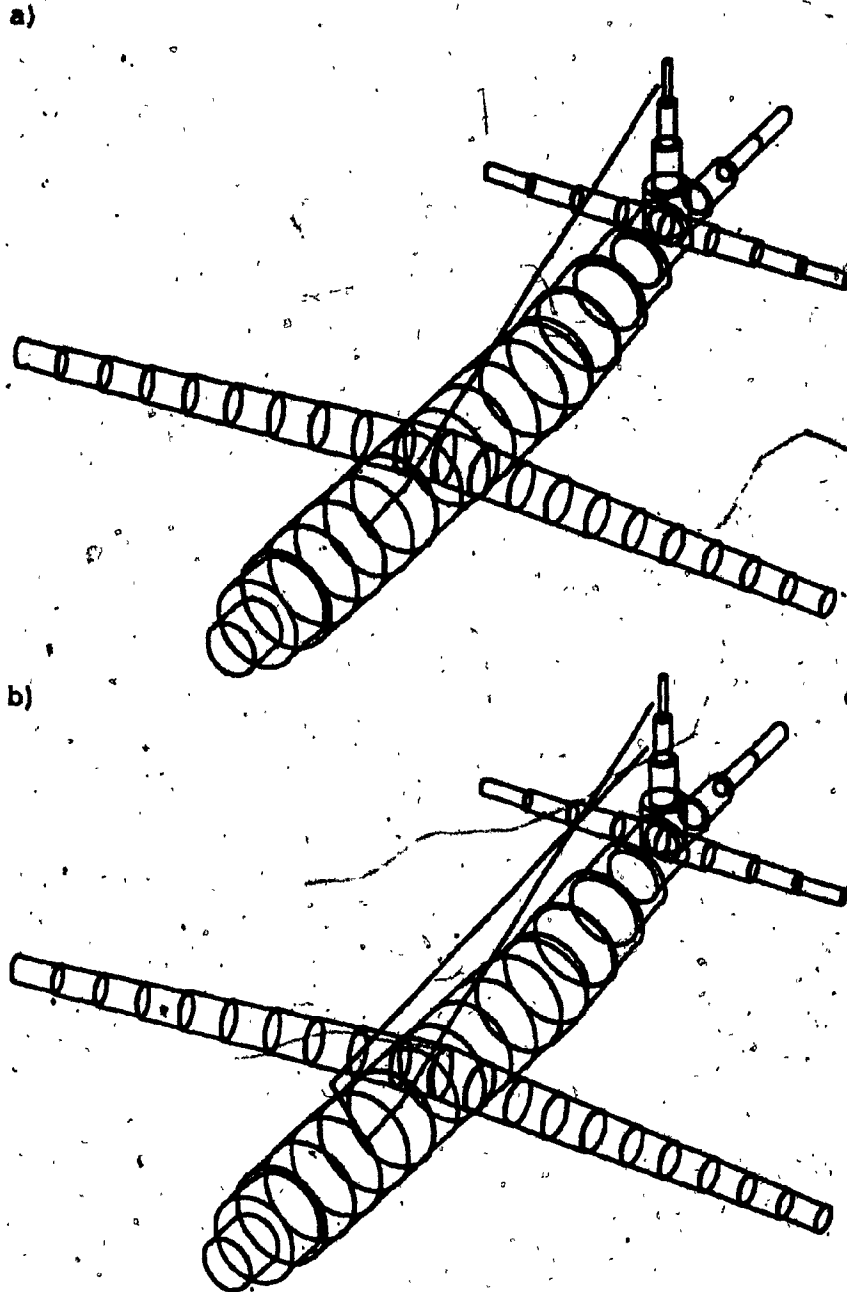


Fig. 34. PSV-1 stick models F1 (a) and F2 or F2L (b)

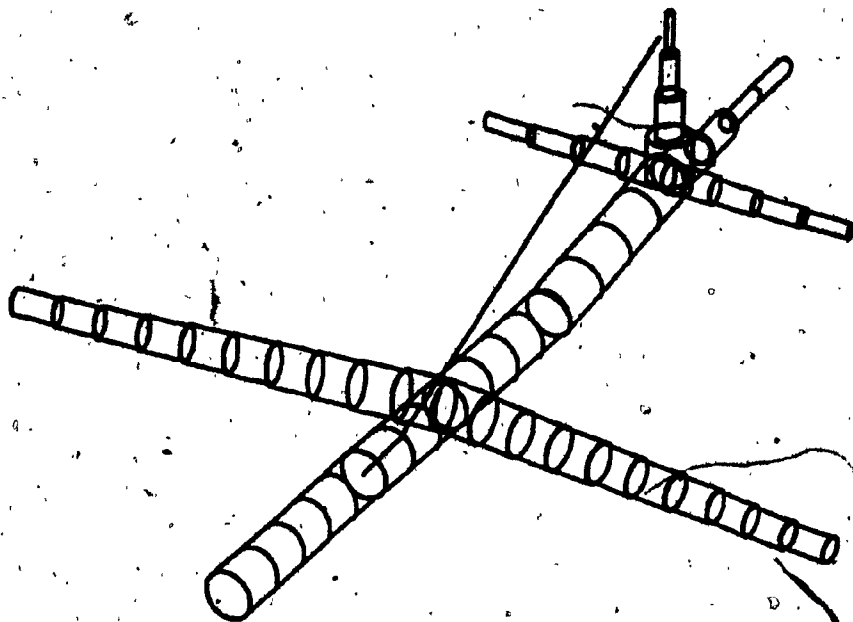


Fig. 35. P3V-1 stick model Fl'

Radiation Patterns

In all P3V-1 model testing that was carried on and is reported below, excitation was applied to the port antenna, and computation of principal plane plus MIL-SPEC radiation patterns was requested. Typical running times were of the order of 50 CPU seconds. Model T1 was tested first at even frequencies from 2 to 12 MHz to permit comparisons with the available experimental data. Measured and computed radiation patterns were compared in the principal planes as shown in Figure 36. The location of lobes and nulls are typical of the HF antennas on this airframe, but agreement in an absolute sense cannot be expected, and in some cases the results can be misleading. At 2 MHz, severe discrepancies are observed in the relative E-theta and E-phi levels, and there is a serious difference in the E-theta pattern tilt angle for the phi=0 plane. At 4 and 8 MHz, however, the agreement is good, and at 6, 10 and 12 MHz, the agreement is fair.

Model T2 was tested at the same frequencies as for model T1 and principal plane patterns were obtained. At 6, 8 and 10 MHz, the patterns were similar to those of model T1, but not so at the other frequencies, as shown in Figure 37. At 2 MHz, there is a slight improvement in pattern agreement, while at 4 MHz, there is some deterioration. At 12 MHz, still greater difference is found but the pattern

agreement is comparable on the average. These seemingly contradictory results did not help clarify the status of the starboard antenna.

To investigate further, model T2L was tested at the frequencies at which models T1 and T2 had differed. The principal plane patterns at 2 and 4 MHz appear in Figure 38. At 2 MHz, the results are similar to those of model T2, which had been superior to model T1 at that frequency. At 4 MHz, however, the results are similar to those of model T1, which had been superior to model T2 at that frequency. This alone favors model T2L and suggests that the starboard antenna had been terminated in 50 ohms during measurements. No conclusions can be drawn from the results at 12 MHz.

Differences in the patterns of models T1 and T2 are a consequence of mutual coupling between the port and starboard antennas, which might interfere with the operation of the HF system. To find out whether this phenomenon occurs to any greater extent at intermediate frequencies, models T1 and T2 were tested at 5, 9, and 11 MHz. Negligible coupling was detected at 9 MHz, but strong coupling at 5 and 11 MHz as shown in Figure 39.

Model F1 was tested next at even frequencies from 2 to 12 MHz, the EK option being selected to account for the low seg/rad ratios. The principal plane patterns obtained are shown in Figure 40. The pattern agreement shows sub-

stantial improvement over model T1 at the three lower frequencies. At 2 MHz in particular, the tilt angle of the E-theta pattern in the $\phi=0$ plane is improved, and at 4 MHz, the agreement of patterns becomes very good. It follows that radii tapered to correspond to aircraft sectional areas produce better results than a small uniform radius. At the higher frequencies, however, the pattern agreement as a whole is not improved. This may be attributable to the fact that the wav/rad criterion starts to be violated past 6 MHz.

Model F2 was tested at the usual frequencies and its patterns were compared to those of model F1. Inter-antenna coupling was apparent at all frequencies, but to various extents: weakest at 2 and 6 MHz and strongest at 12 MHz. As in models T1 and T2, it seemed impossible to conclude anything as to the state of the starboard antenna. Figure 41 shows for example a deterioration in pattern agreement at 8 MHz, and an improvement at 12 MHz. Model F2L was tested at these two frequencies, and the results did not permit the drawing of any conclusions.

As for the thin models, a search was made for frequencies of greater inter-antenna coupling. Models F1 and F2 were tested at 5 and 11 MHz because of the precedents in the thin model case. Coupling was rather weak at 5 MHz but extremely strong at 11 MHz, as shown in Figure 42.

A single test was made on model F1' at 2 MHz to determine if anything could be gained from the smaller rad/seg ratios along the fuselage. The results that appear in Figure 43 are intermediate in quality between those of models T1 and F1; hence the model was not tested further.

To illustrate the use of altitude plots in pattern comparisons, Figure 44 shows the complete set of measured E-theta and E-phi azimuth patterns at 2 MHz, as compared to the computed results of models T1, F1' and F1. Only those computed patterns from theta = 53 to 127 degrees are plotted because this set of MIL-SPEC angles closely matches the set of measured patterns available, making direct comparison possible. The layout shows clearly the progression in pattern quality from model T1 to model F1.

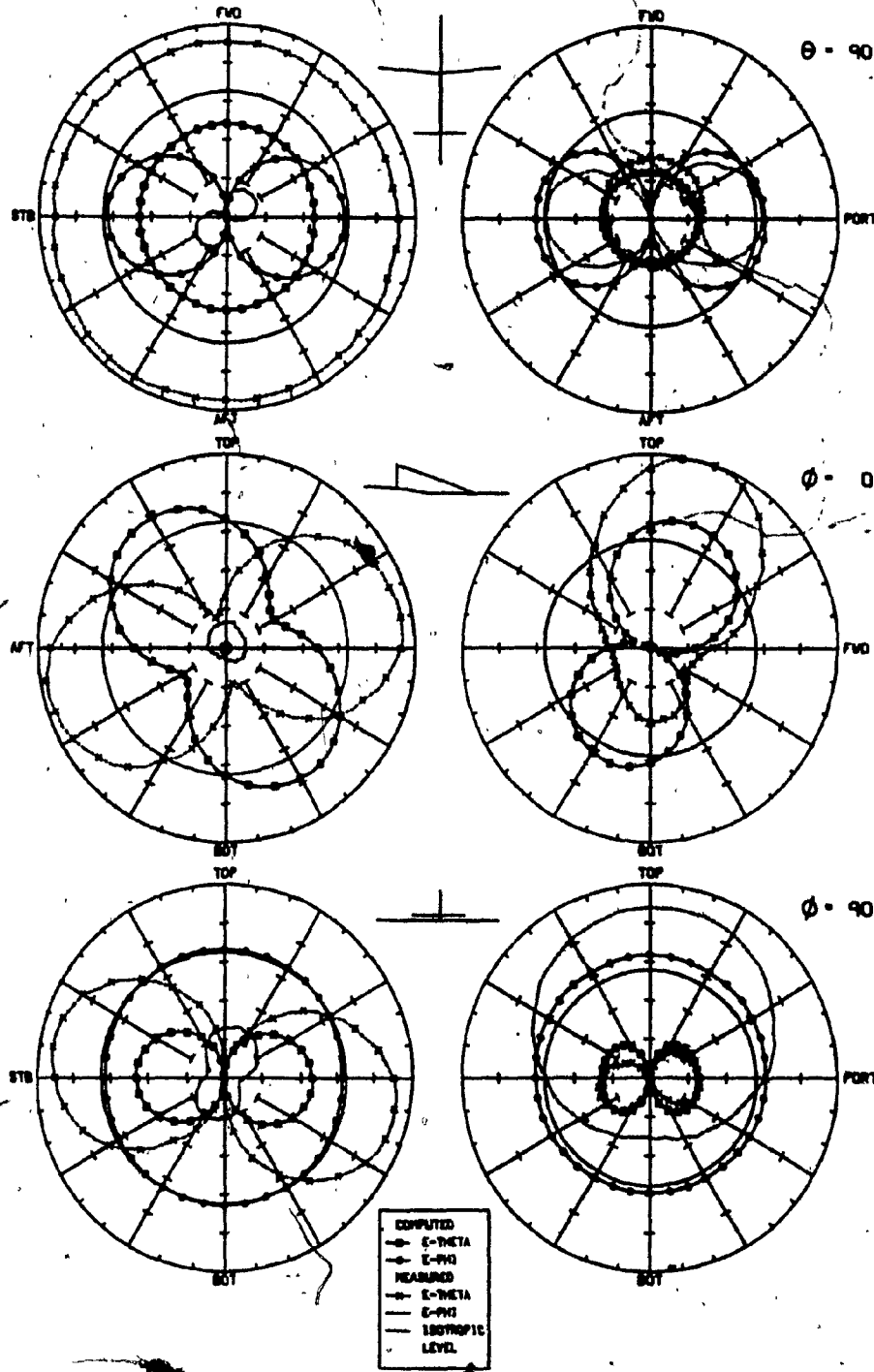


Fig. 36. Comparisons of measured and computed principal plane patterns for model T1 at 2 and 4 MHz

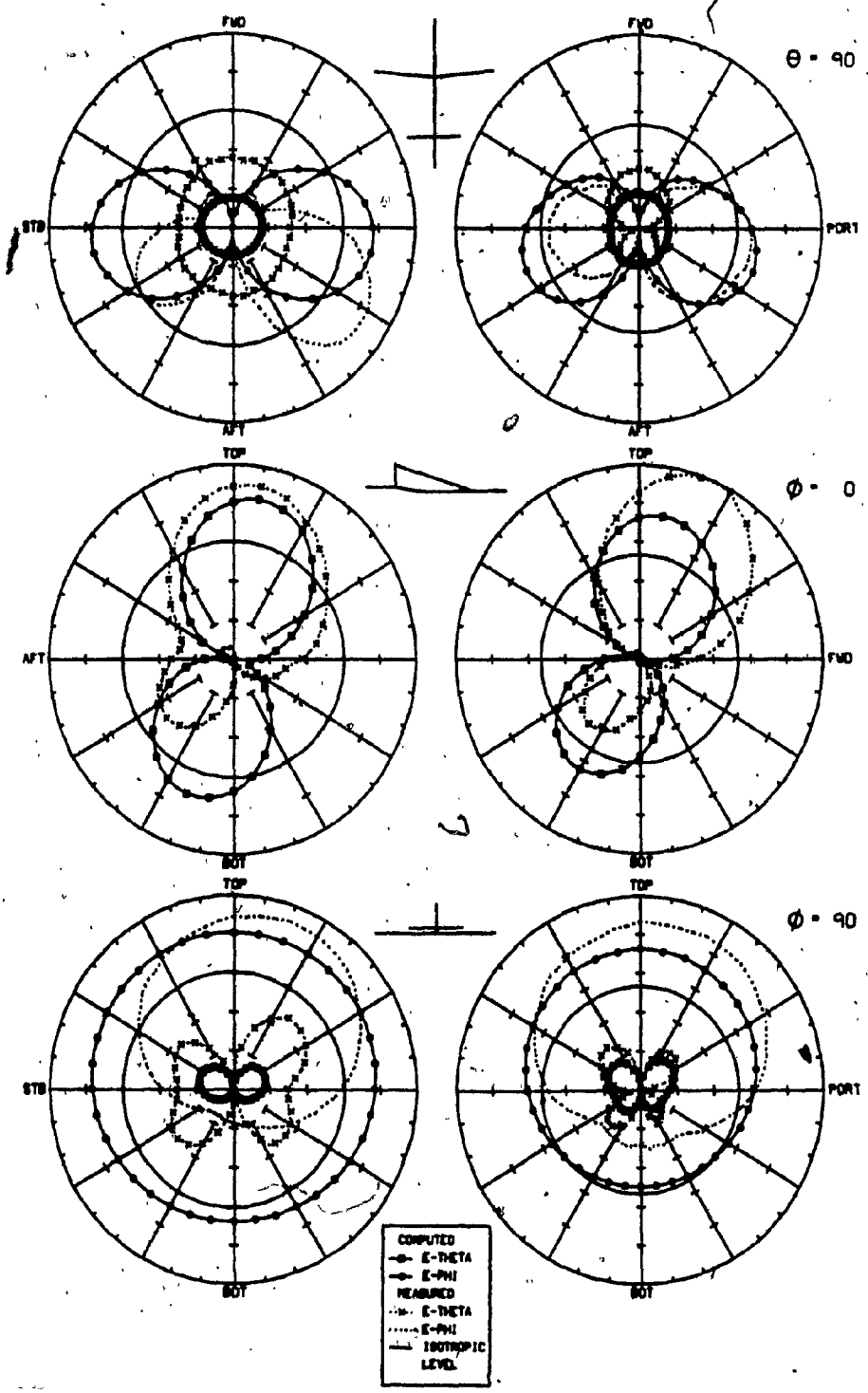


Fig. 36-continued. Comparisons of measured and computed principal plane patterns for model T1 at 6 and 8 MHz

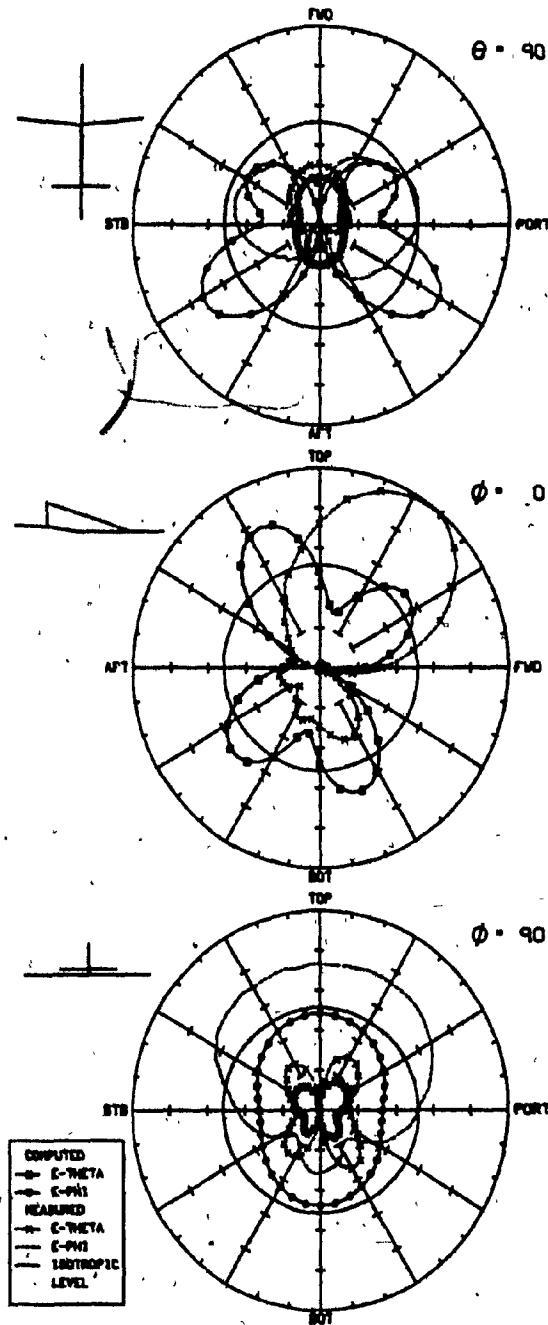


Fig. 36-continued. Comparisons of measured and computed principal plane patterns for model T1 at 10 MHz

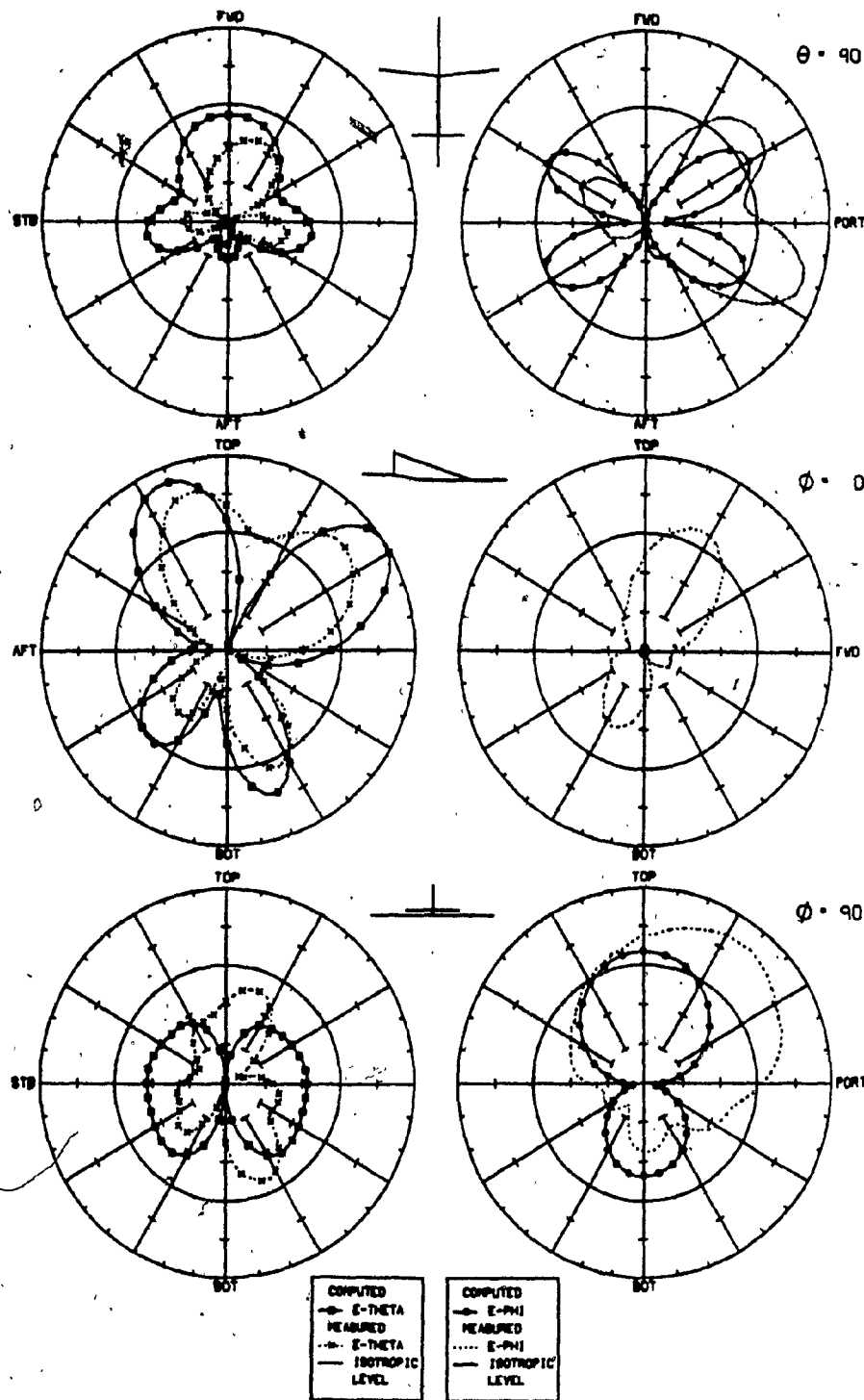


Fig. 36-continued. Comparisons of measured and computed principal plane patterns for model T1 at 12 MHz

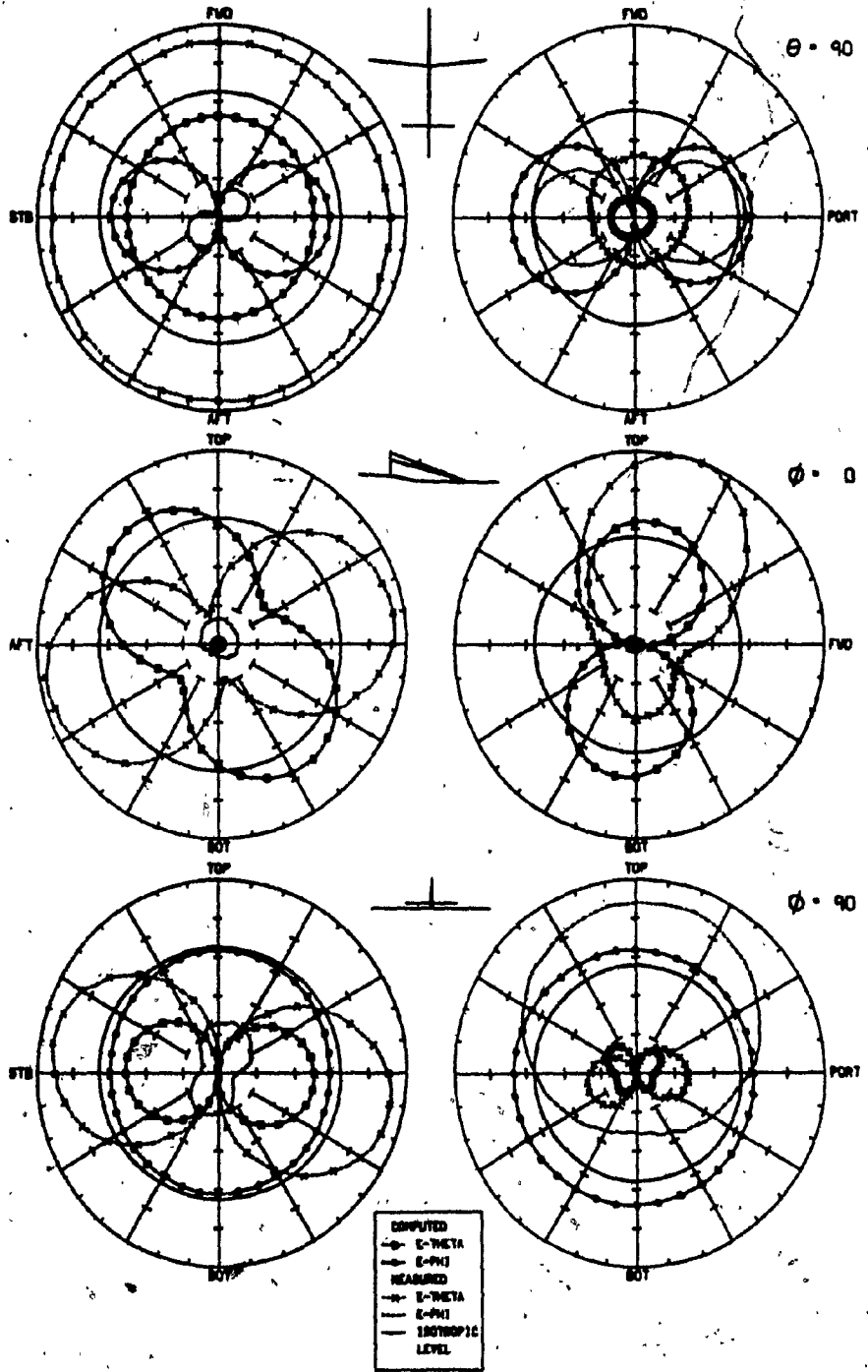


Fig. 37. Comparisons of measured and computed principal plane patterns for model T2 at 2 and 4 MHz

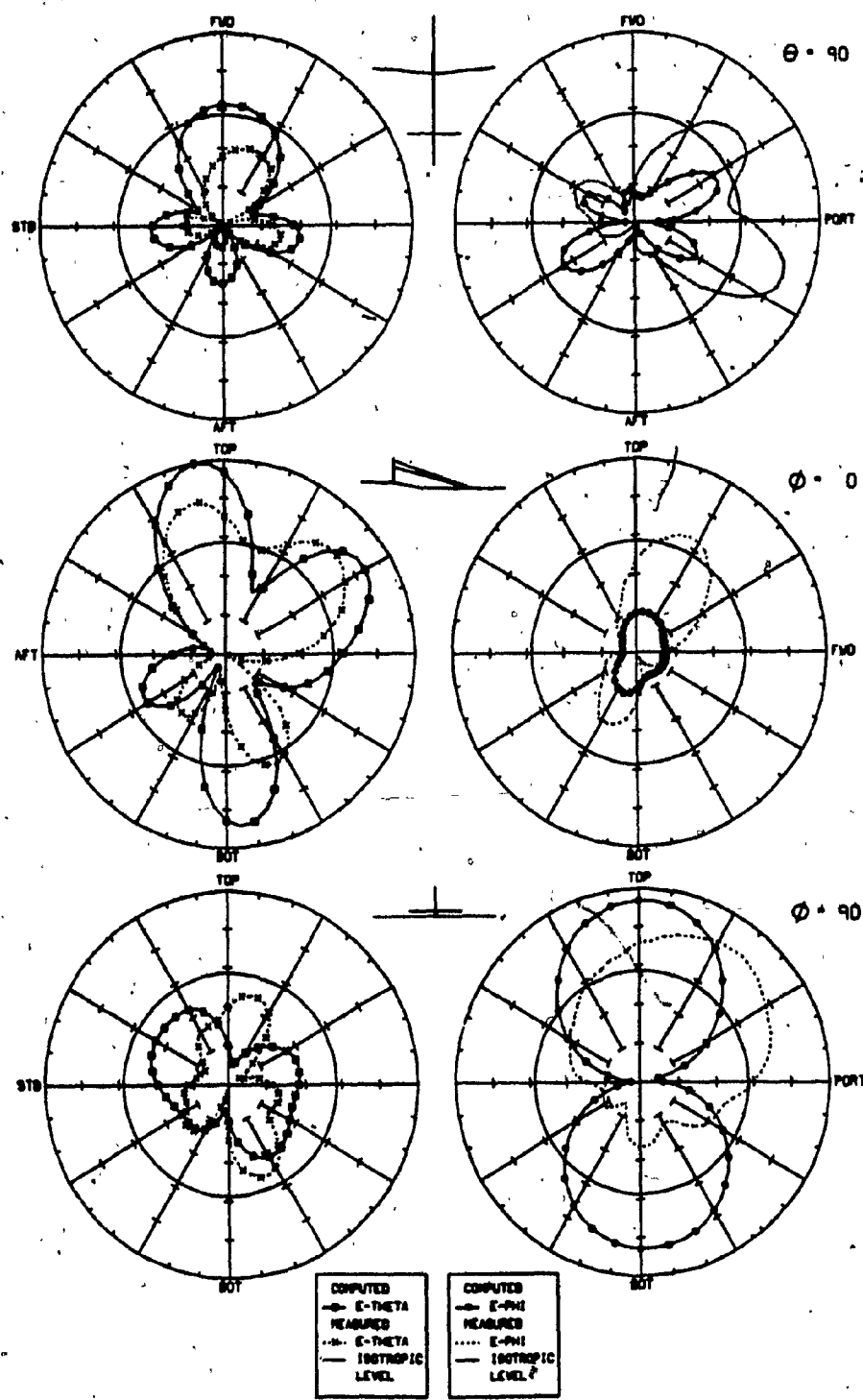


Fig. 37-continued. Comparisons of measured and computed principal plane patterns for model T2 at 12 MHz

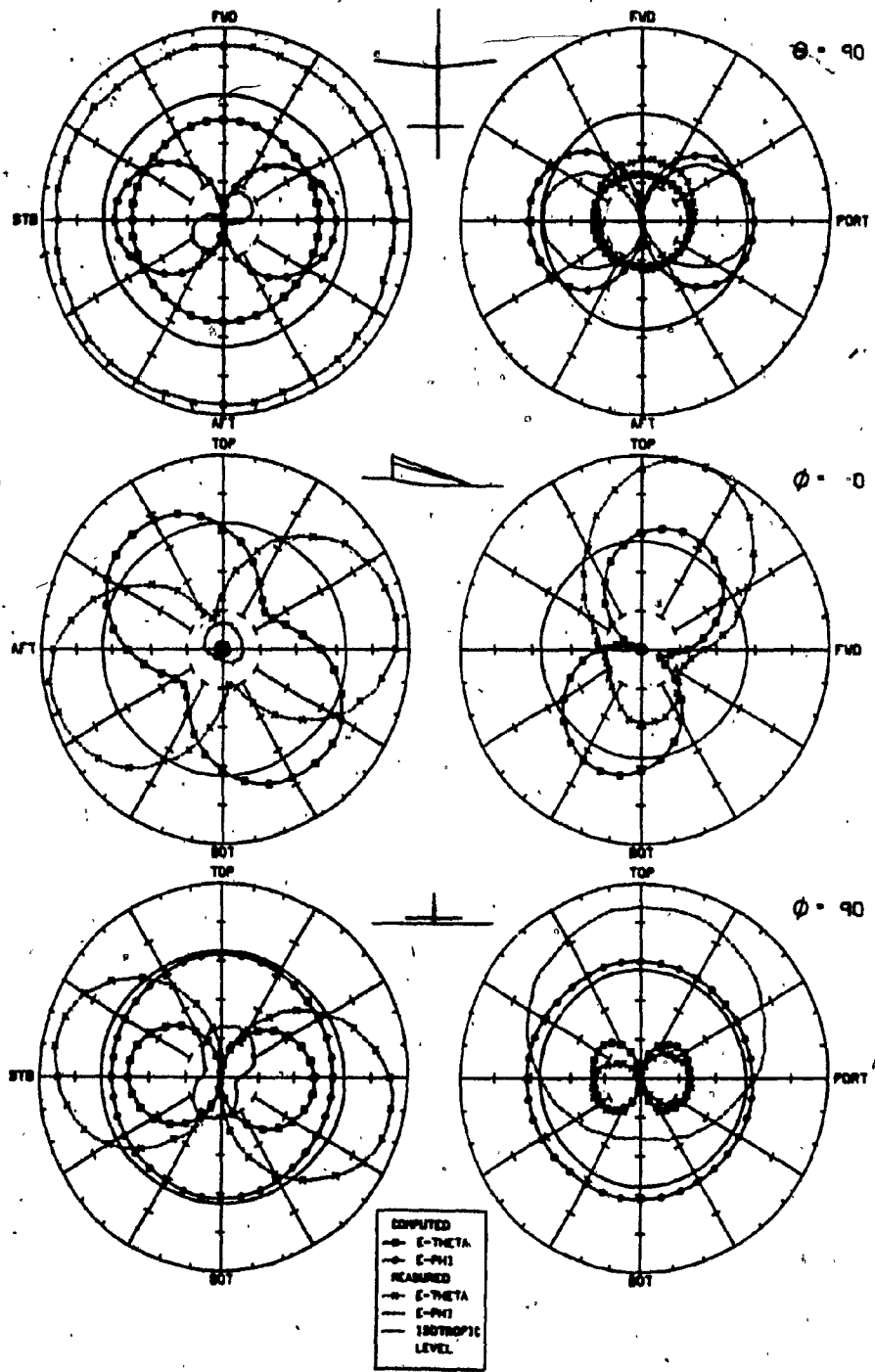


Fig. 38. Comparisons of measured and computed principal plane patterns for model T2L at 2 and 4 MHz

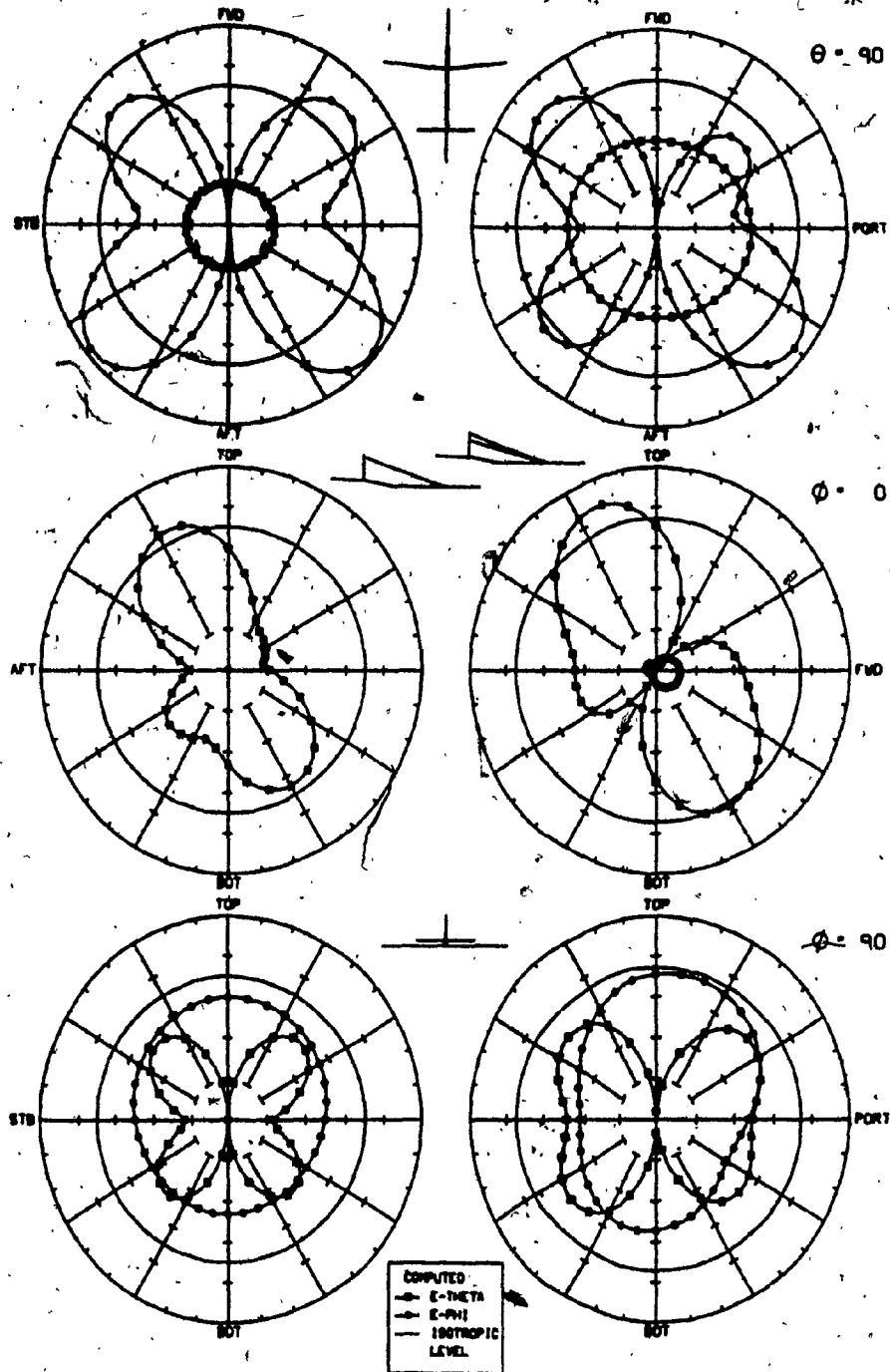


Fig. 39. Principal plane patterns of models T1 and T2 at 5 MHz

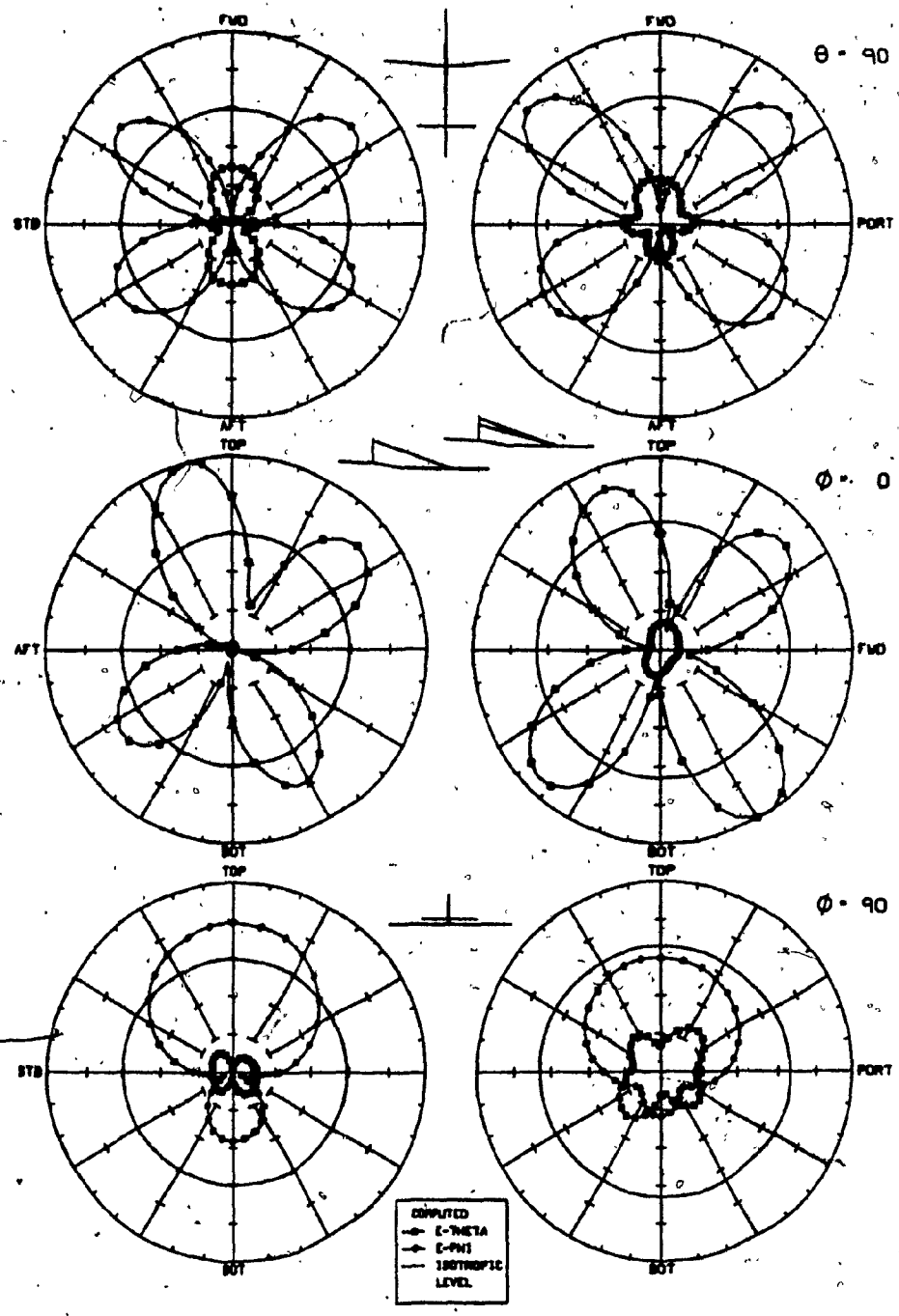


Fig. 39-continued. Principal plane patterns of models T1 and T2 at 11 MHz

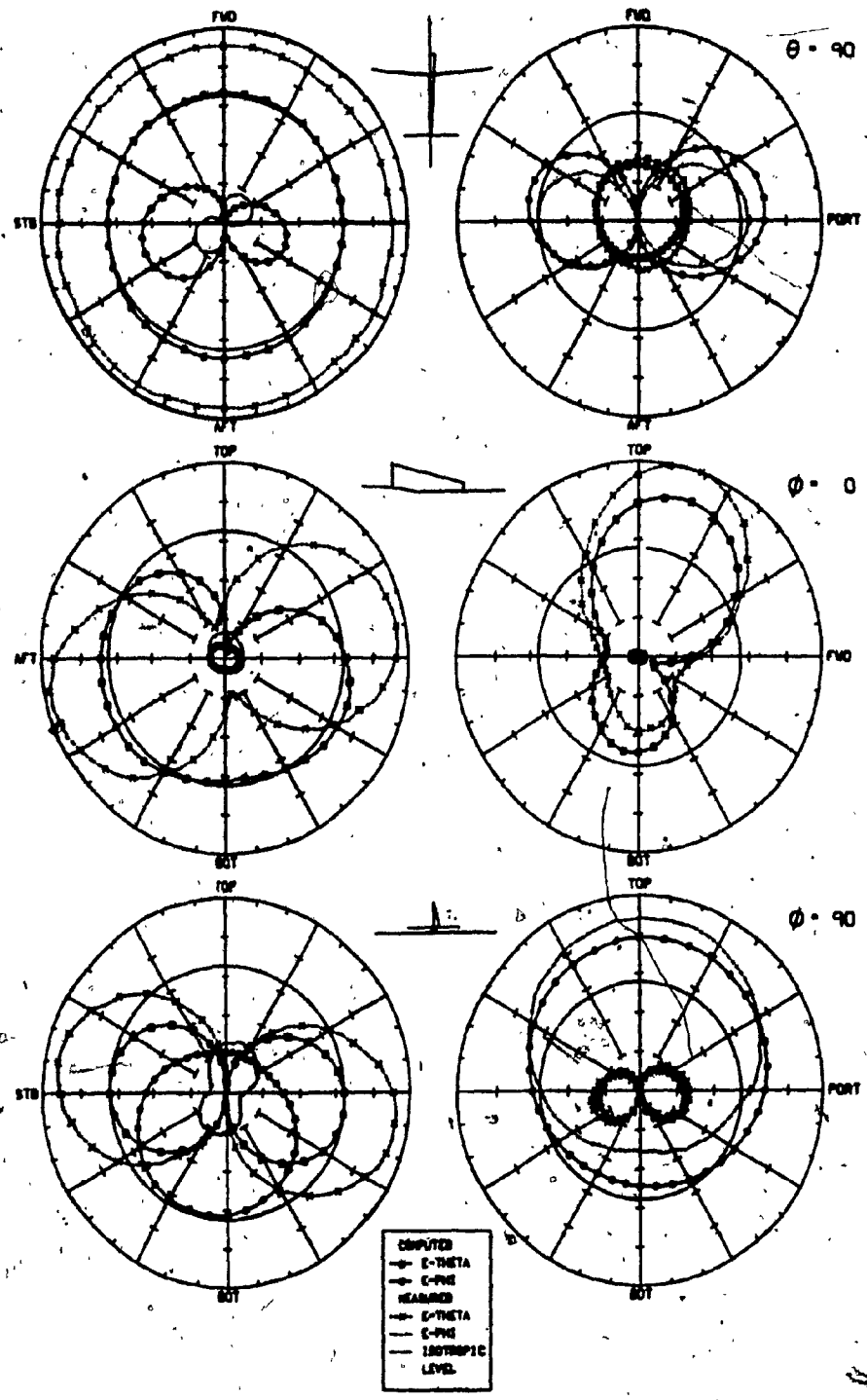


Fig. 40. Comparisons of measured and computed principal plane patterns for model F1 at 2 and 4 MHz

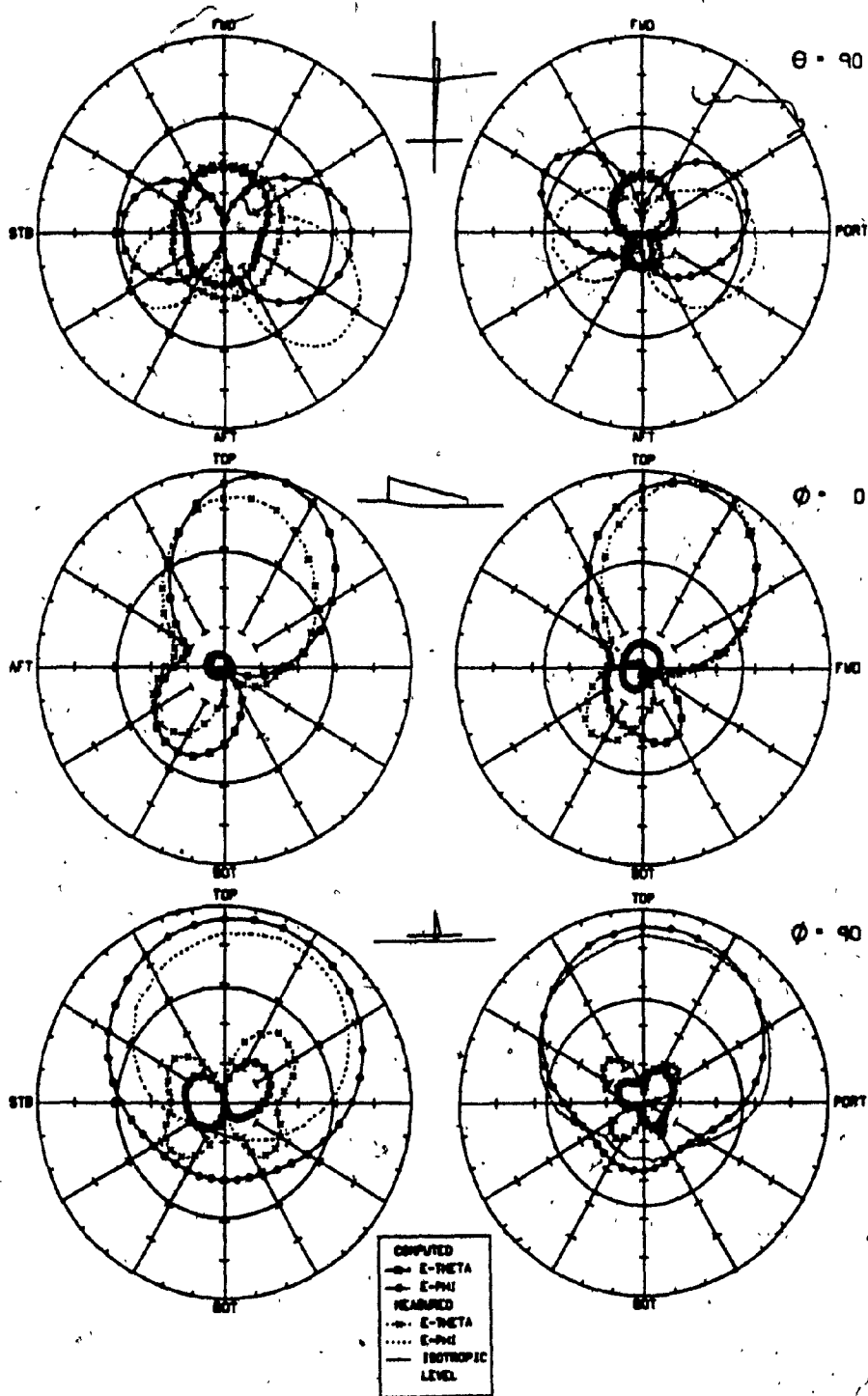


Fig. 40-continued. Comparisons of measured and computed principal plane patterns for model F1 at 6 and 8 MHz

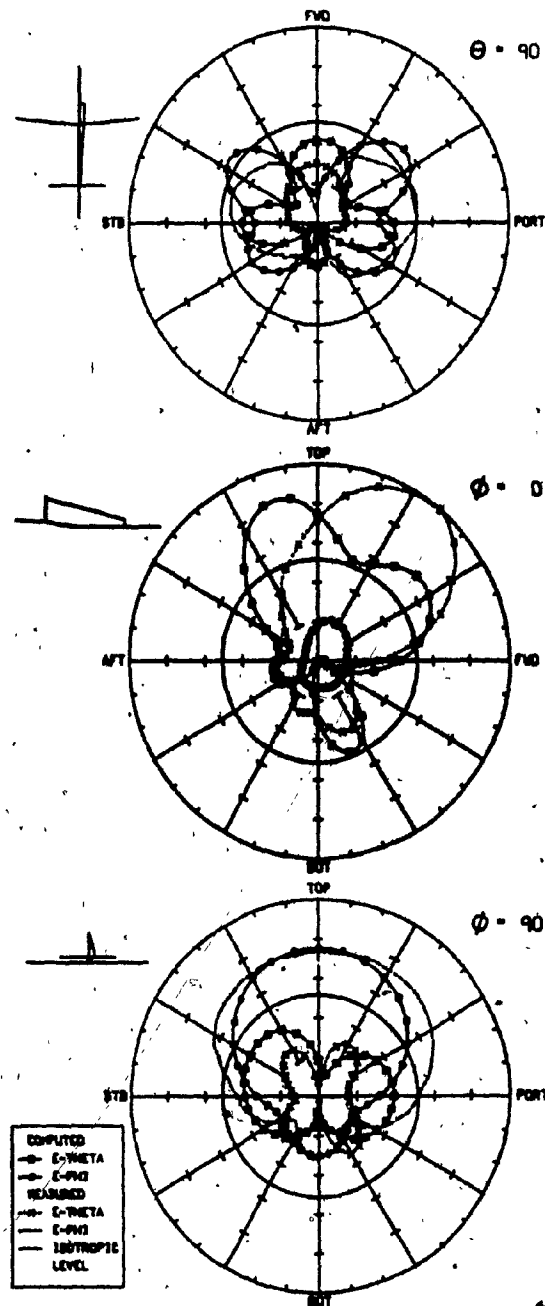


Fig. 40-continued. Comparisons of measured and computed principal plane patterns for model F1 at 10 MHz

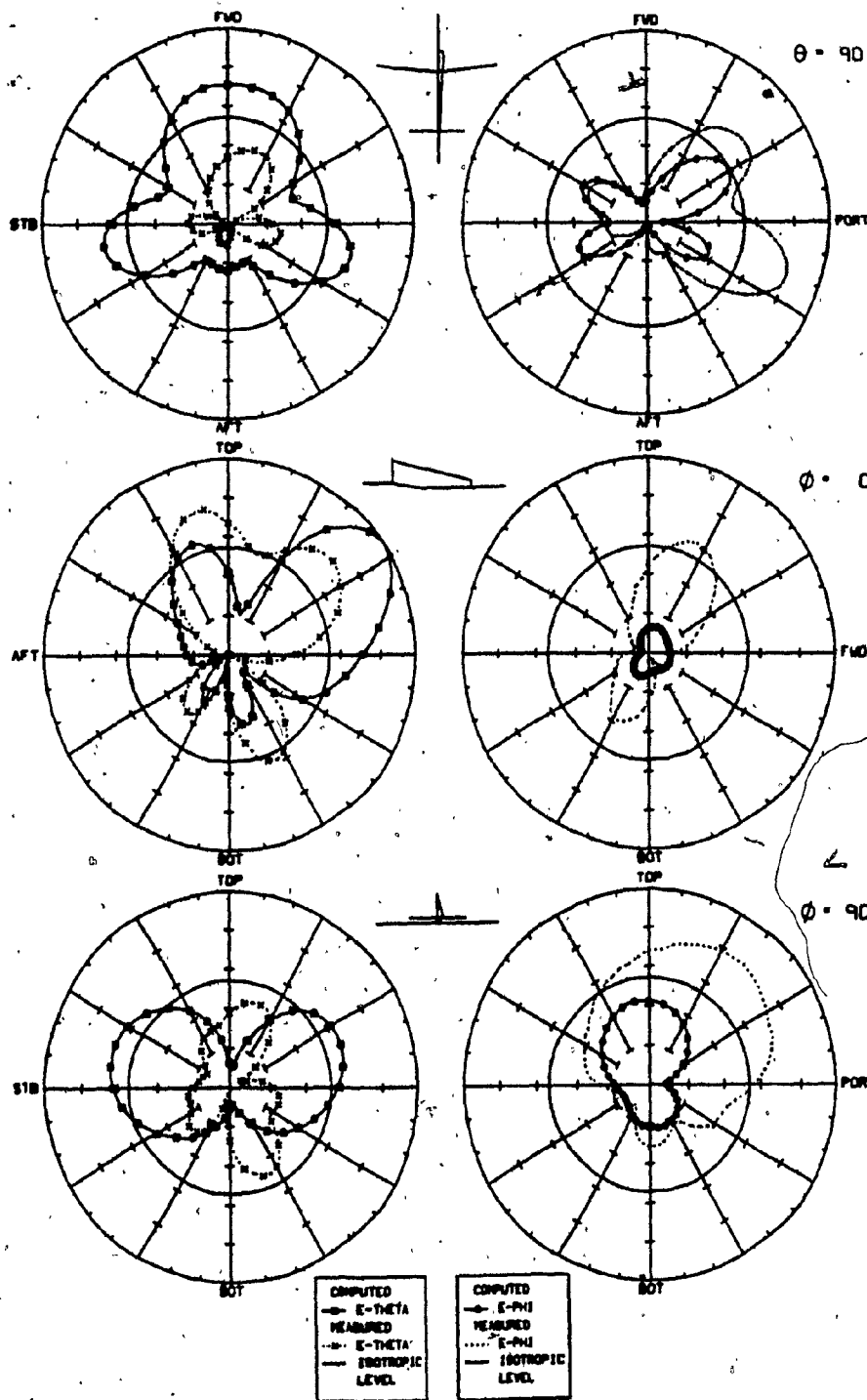


Fig. 40-continued. Comparisons of measured and computed principal plane patterns for model F1 at 12 MHz

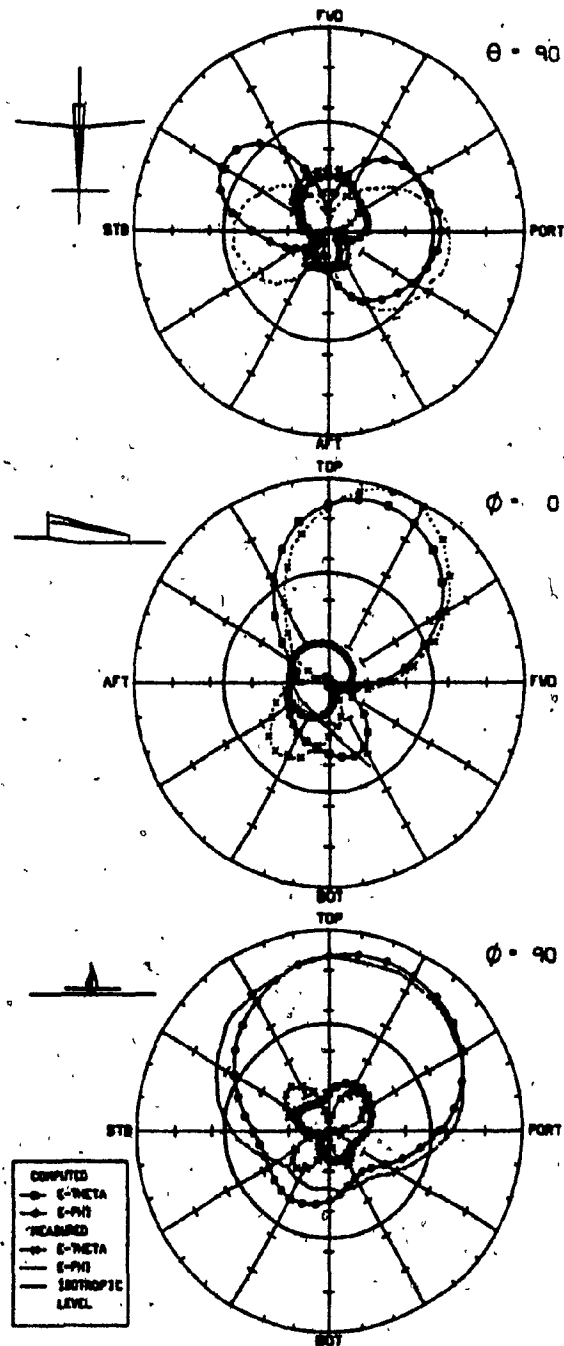


Fig. 41. Comparisons of measured and computed principal plane patterns for model F2 at 8 MHz

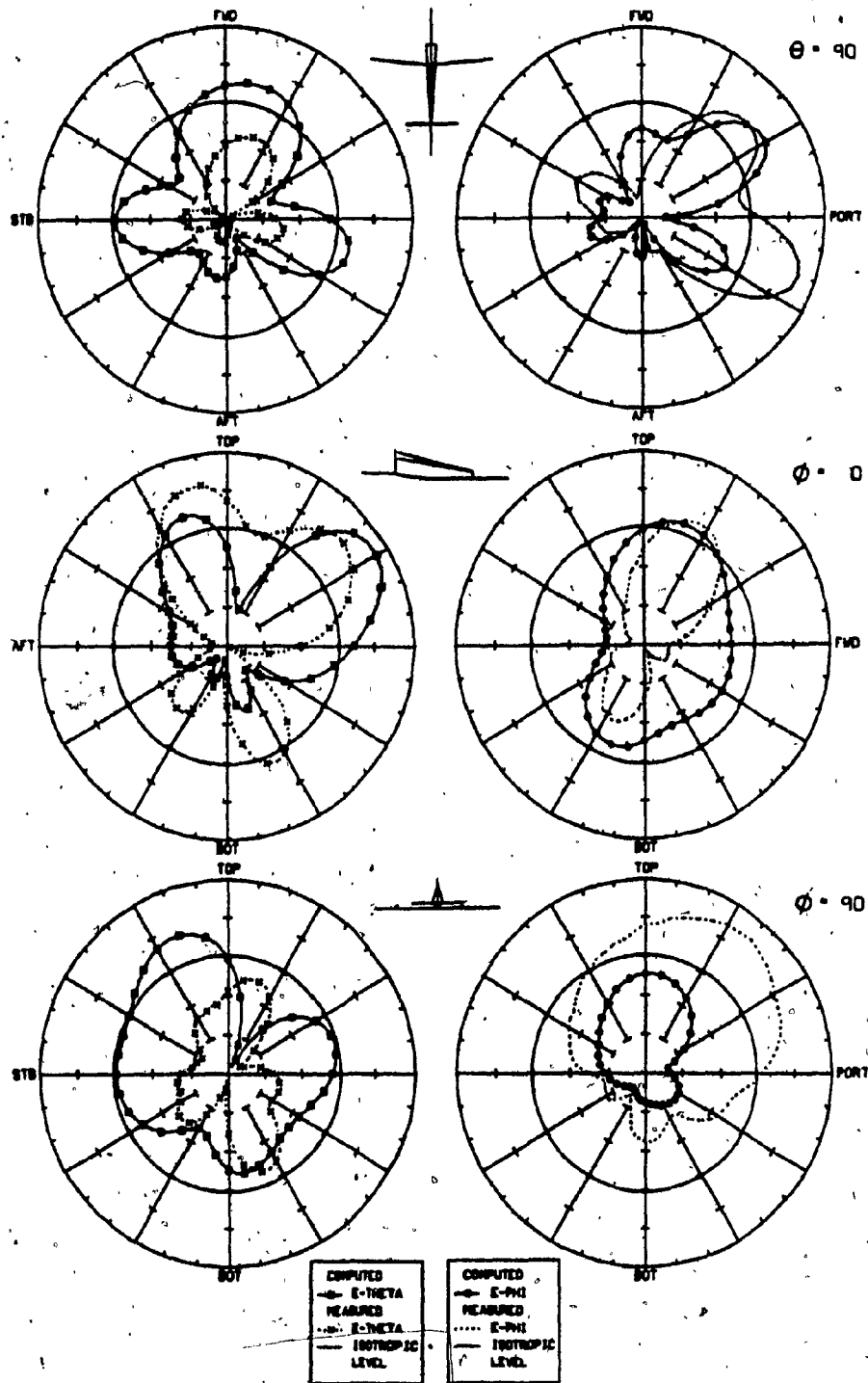


Fig. 41-continued. Comparisons of measured and computed principal plane patterns for model F2 at 12 MHz

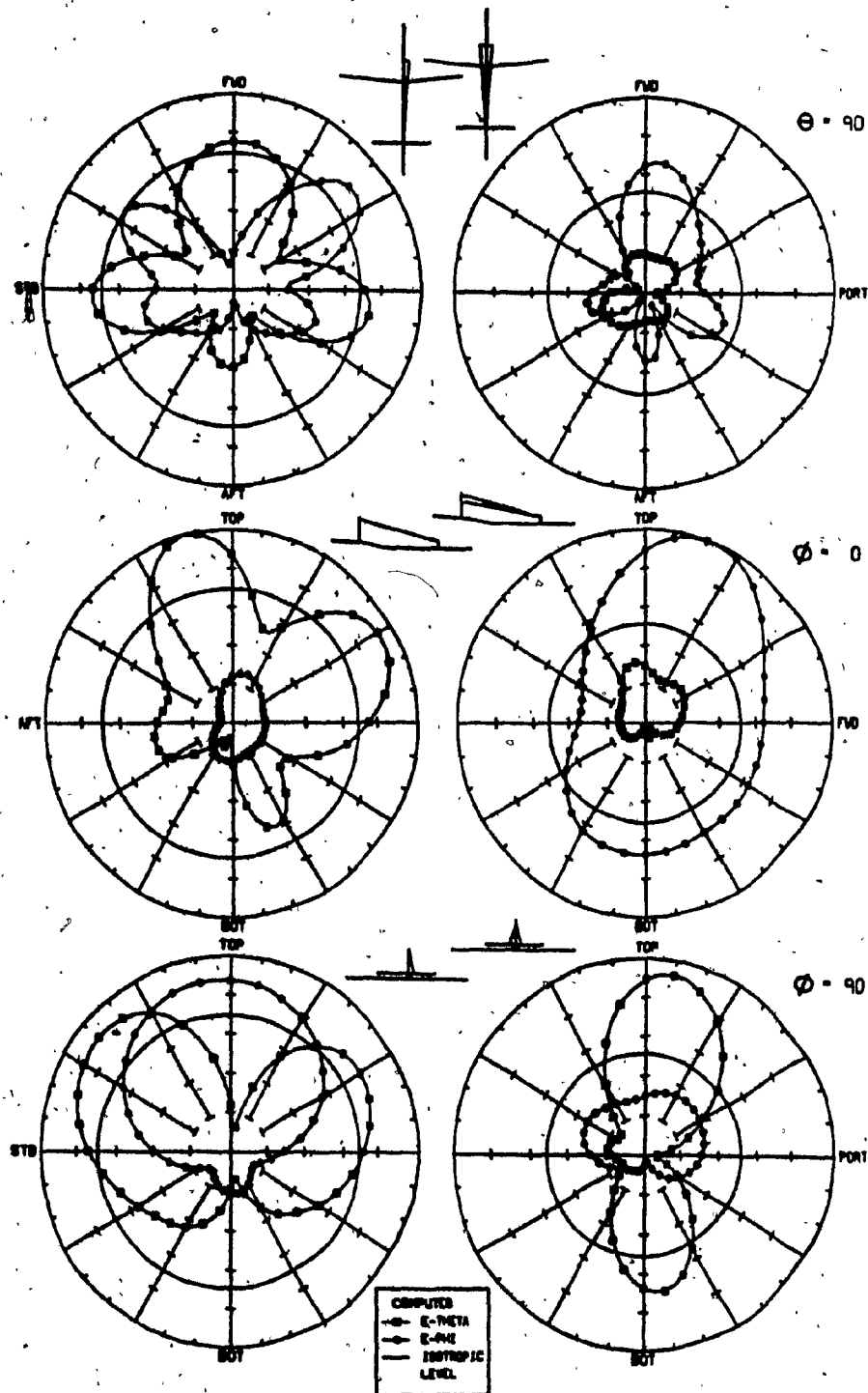


Fig. 42. Principal plane patterns of models F1 and F2 at 11 MHz

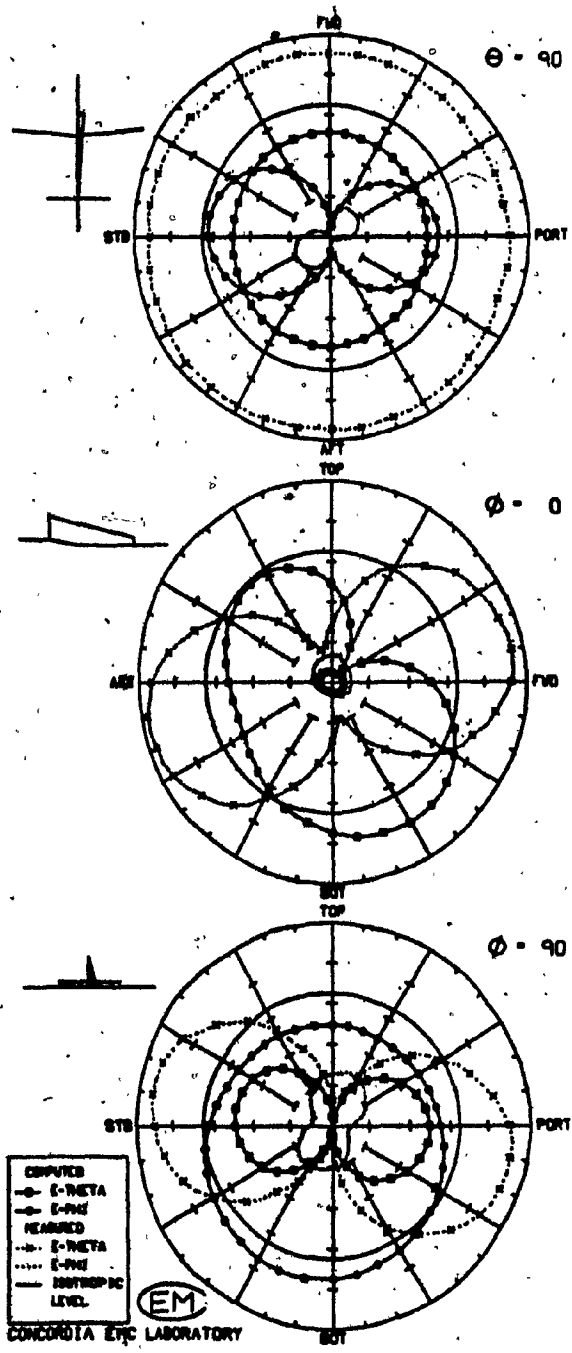


Fig. 43. Comparisons of measured and computed principal plane patterns for model F1' at 2 MHz

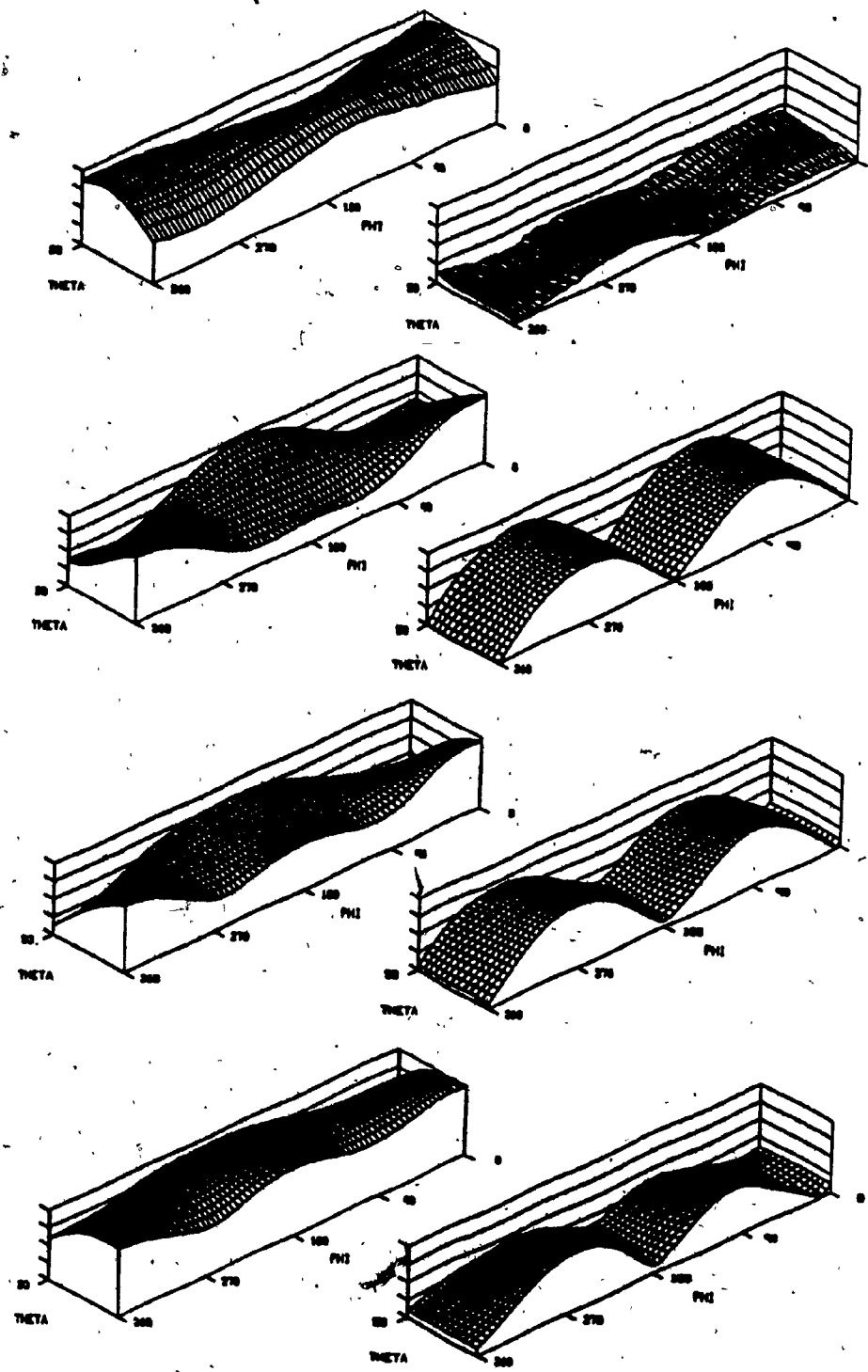


Fig. 44. E-theta and E-phi altitude plots at 2 MHz, measured and computed from models T1, F1', and F1

Percentage of E-theta Power

Comparisons of measured and computed $\%E$ -theta curves will demonstrate the effectiveness of assessment parameters in the process of model discrimination. Figure 45 shows the results for the thin and fat models respectively.

For the thin models, previous conclusions on patterns are confirmed at a glance: worse agreement at 2 MHz, best agreement at 4 and 8 MHz, and inter-antenna coupling at 2, 4, 5, 11 and 12 MHz. Model T2 is indeed superior to model T1 at 2 MHz but inferior at 4 MHz. The fat models yield $\%E$ -theta values superior to those of the thin models at all frequencies except 12 MHz; hence the computed curves track better the experimental one. The graph confirms pattern improvement at the three lower frequencies and strongest inter-antenna coupling at 11 and 12 MHz. Model F2 is indeed inferior to model F1 at 8 MHz but superior at 12 MHz.

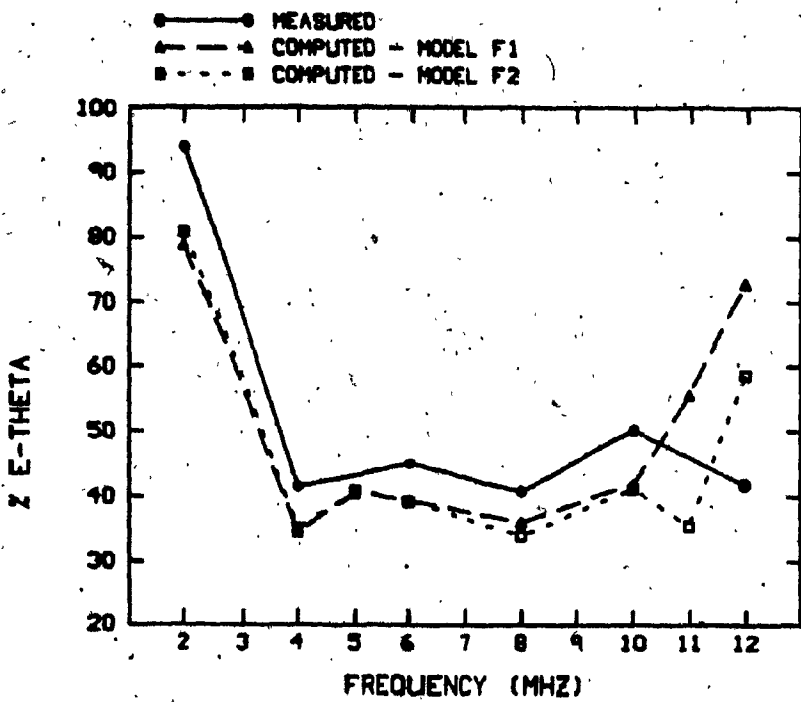
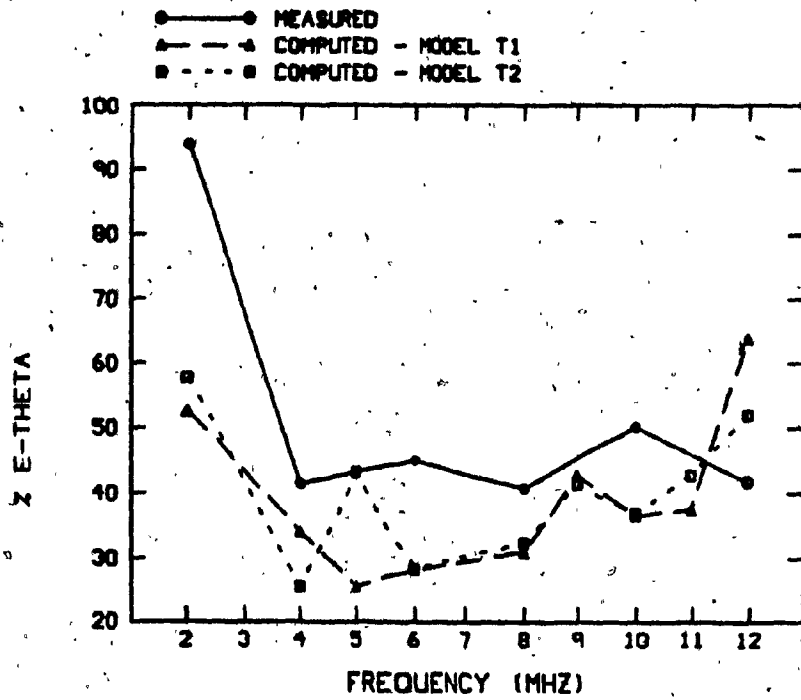


Fig. 45. Comparisons of measured and computed %E-theta curves for P3V-1 thin and fat models

Impedance and Current Distribution

Superiority of fat models over thin ones in terms of pattern agreement is not necessarily reflected in the impedance values. Figure 46 shows comparisons of the measured impedance curves with those obtained from models T1, T2, F1, and F2. As shown in b), the fat models produce abnormally high resistance values at 2 MHz; on the other hand, model F1' yields a meaningless negative resistance of -9.0208 at this frequency (not shown on graph). This gives a slight advantage to the thin models. Models T1 and T2 are also those that track best the measured resistance and reactance curves respectively.

Once again, differences within thin or fat models provide indications of inter-antenna coupling. This is readily apparent from the impedances of the thin models at 4, 5, 11, and 12 MHz, and from those of the fat models at 11 and 12 MHz. An appreciation of the reasons for such impedance changes, and by extension pattern changes, can be obtained from an examination of the current distributions on the antennas. Figure 47 shows the antenna currents on models F1 and F2 at 11 MHz, where strongest coupling was observed. It is seen that the addition of the second antenna brings about an increase on the driven antenna itself. Substantial current is induced as well at the terminals of the passive antenna; this can produce a terminal voltage

that might be high enough to produce interference, or damage the input stage of the receiver, (Kubina, 1983b). Hence input stage protection becomes a necessity.

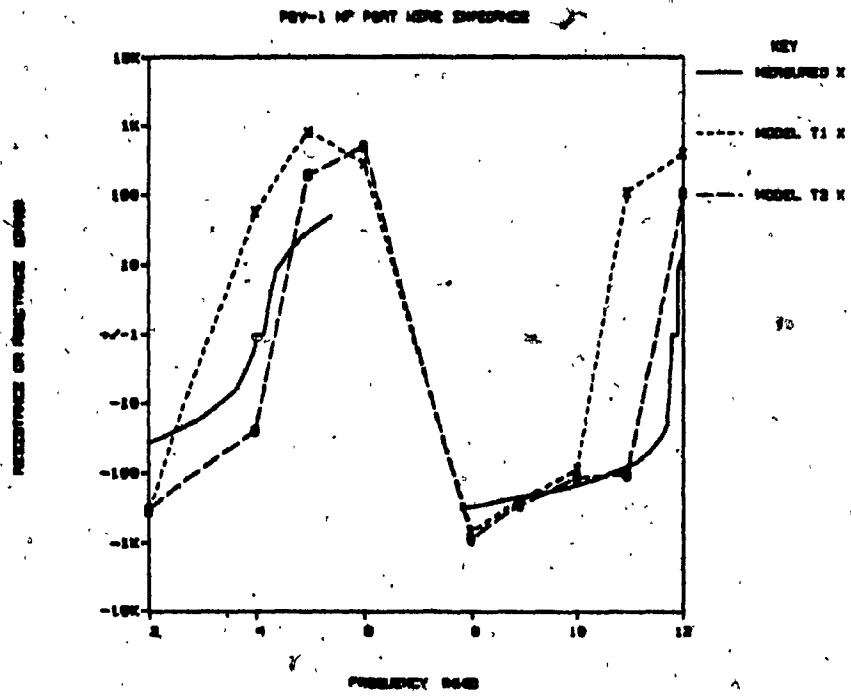
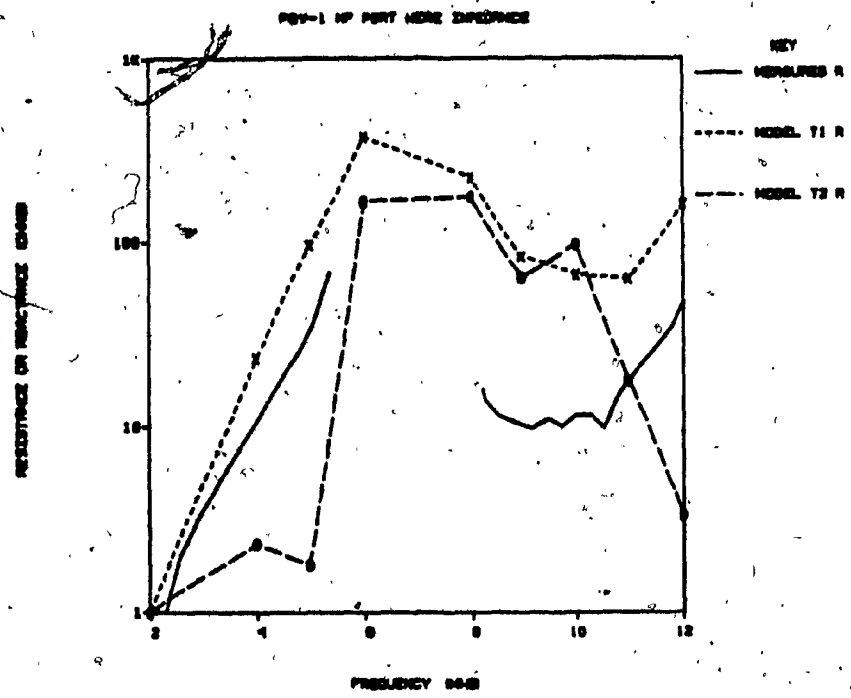


Fig. 46a. Comparisons of measured and computed resistance and reactance curves for P3V-1 thin models

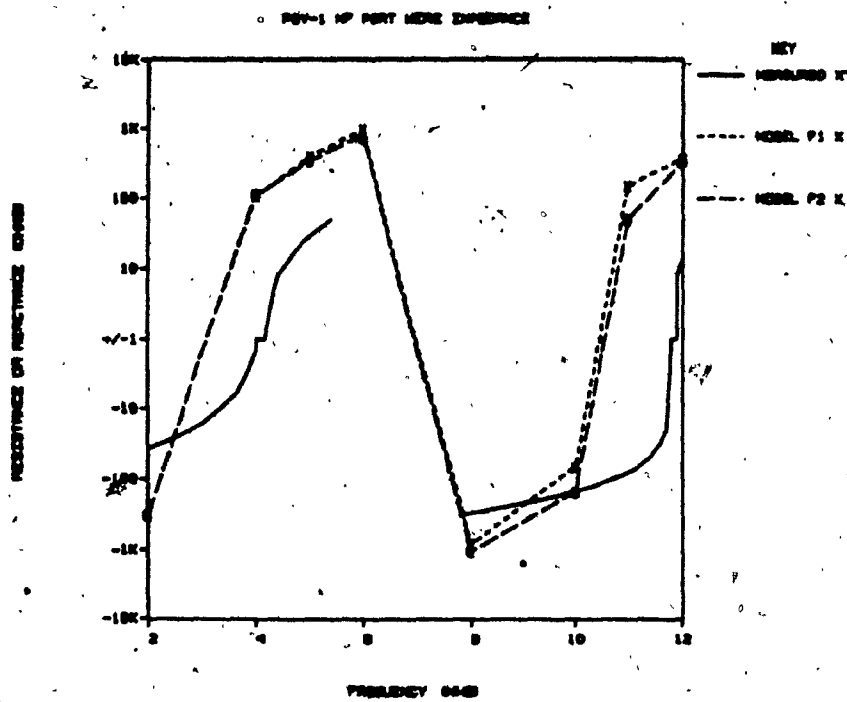
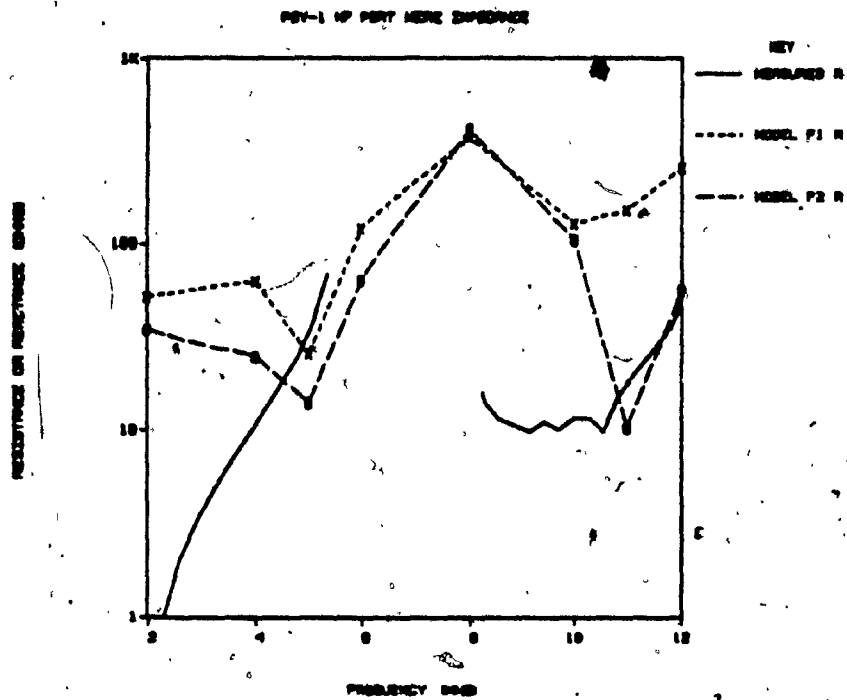


Fig. 46b. Comparisons of measured and computed resistance and reactance curves for P3V-1 fat models

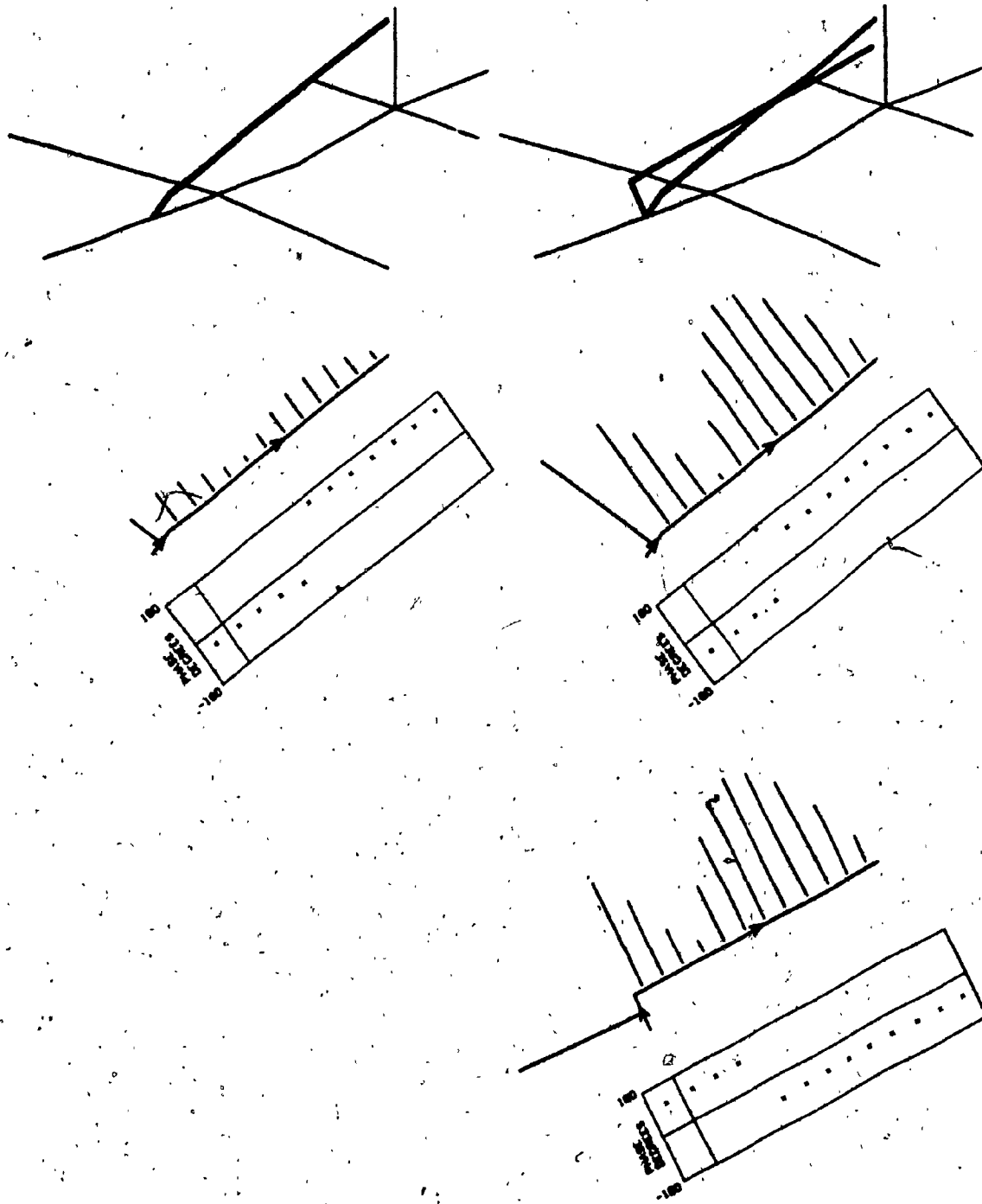


Fig. 47. Magnitudes and phases of antenna currents at 11 MHz on models F1 and F2

CHAPTER VI

THE CP-140 HF INSTALLATION

As work on the P3V-1 HF installation was reaching the state described above, scale-model measurements for the CP-140 HF configuration became available through the Antenna Compatibility Plan (1975) and Lockheed Report LR 29153. It was therefore decided to suspend further work on the P3V-1 installation, which was primarily of historical interest, and to concentrate on the HF configuration now used on the CP-140.

The Measurements

The CP-140 HF antenna installation is shown in Figure 48. It differs from the P3V-1 installation insofar as the antennas are of more dissimilar lengths, the port one originating at TFS (transverse fuselage station) 715.4, and the starboard one originating at TFS 411, which is aft of the wings. Their buttock lines are 28.83L and 57.14R respectively, and they terminate at the same vertical stabilizer station by virtue of a V-connection of insulators.

All data received for this configuration had been measured with each antenna excited in turn, cruising conditions simulated, and constant radiated power at each fre-

quency (and hence a constant isotropic level). The state of the passive antenna was this time clearly defined but different in both reports: terminated in 50 ohms in the Antenna Compatibility Plan, and grounded in LR 29153. The Antenna Compatibility Plan supplied radiation patterns in the principal planes only, and at 2, 6, 15, and 24 MHz. It supplied however an interesting set of E -theta values at 2, 6, 10, 15, 20, 22, 24, 26, 28, and 30 MHz, and continuous impedance curves in the complete HF range (2-30 MHz). The contents of LR 29153 that were at hand consisted of only radiation patterns, but an extensive set of them. The cuts contained were $\phi = 0$ and 90 degrees and $\theta = 30, 45, 50, 60, 70, 80, 85, 90, 95, 100, 110, 120, 130,$ and 135 degrees. The frequencies contained corresponded to the previous set of 2, 6, 10, 15, 20, 22, 24, 26, 28, and 30 MHz.

Because of the primary interest in pattern matching, it was decided that testing of the CP-140 configuration should be done with the passive antenna grounded so that the extensive data set of LR 29153 could be used in the comparisons. E -theta percentages and impedances from the Antenna Compatibility Plan would then be used on the assumption that the 50-ohm loading did not drastically affect these measurements. This assumption was found reasonable after comparison of equivalent patterns from the two reports; negligible differences in pattern level and shape were observed, except

perhaps at 6 MHz. Therefore the patterns of LR 29153, being in the analog plot form, and the impedance curves of the Antenna Compatibility Plan were digitized for the purposes of the data comparisons that will follow.

Model Generation

Because of the results previously noted on the P3V-1 HF configuration, only fat models of the CP-140 were constructed: the familiar stick models, and also more complex models to render the finer details of the airframe structure. For the purposes of this work, these two categories of models will be designated by the letters S (stick) and C (complex).

Stick Models

Model S, illustrated in Figure 49, was derived as the first stick model and as a reference for subsequent model optimization. It was derived from the P3V-1 model F2 by relocation of the antennas to their new feed points. The shorter starboard antenna caused the total number of segments to drop from 78 to 74. As expected, testing of this model yielded some poor results, but improvements were brought in order to determine the degree of agreement that can be achieved from stick models. The optimized models that resulted from this exercise are described below.

Improvements to model S were made one by one in order to properly assess their individual effects. The first attempt at improvement was to obtain source segments that would be located outside of the fuselage. This objective was first met by testing model S again with a new source segment, namely the forwardmost segment of the antenna rather than its feed element. The results not being convincing, a different approach was taken by actually modifying the geometry. The feed elements were first subdivided in two, and the upper segments selected for excitation. The fuselage was then tapered near the feed points so that the new source segments would end up 10 cm above the surface. The drawback was that radius proportions along the fuselage were altered. The resulting model, which will be designated SE (E for emerging), is illustrated in Figure 50a. Details of the starboard antenna connection are shown for clarity. Note that the first forward segment of each antenna was also subdivided for segment length continuity and better current resolution in this critical region. This brought the total number of segments to 78. From model SE, model SE' was obtained by reducing the abrupt radius changes that had not yet been handled at the antenna feed points. The segments of the feed wire were sufficiently increased in radius to convert the previous rad/rad errors to only warnings. The new model is shown in Figure 50b with the starboard antenna

detail.

The next approach that was tested was to thin model S by different scale factors. Unlike models SE and SE', this approach altered all radius values (excepting the antennas which were to remain at 0.01 m), but had the advantage of preserving radius proportions. This led to models ST1, ST2 and ST3 (T for thinned) which are illustrated in Figure 51. The scale factors used were 0.75 and 0.5 in the first two models. The effect was to eliminate several seg/rad warnings for individual wires as well as seg/rad errors at junctions. In the third model, all radii were set to 0.01 m, as in the P3V-1 model T2 but with the full lengths of the feed elements retained. All CHECK errors were removed in the process.

The merits of the above two types of model optimization having been demonstrated, a hybrid model was constructed by combining the characteristics of models SE' and ST2, which had been judged best in their categories. The resulting model will be designated S* and appears in Figure 52a with a detail of the starboard antenna connection. The performance of the model was to make this combined optimization a scheme of choice in future model improvements. In order to remove the rad/rad warnings that were left, model S*' was obtained by providing an additional radius step on the antennas, as shown in Figure 52b.

The next attempt at improving model S was to move the wings forward by one segment, thus making the wires more or less coincident with the forward edge of the actual wings. This approach was successful in tests by Trueman (1979) and can be justified by the fact that the smaller radii of curvature at the edges of the wings attract most of the currents. This gave rise to model SF (F for forward) which appears in Figure 53a. The results being encouraging, the optimization scheme of model S* was applied to model SF. This resulted in model SF*, which appears in Figure 53b.

The last optimization attempt consisted of adjusting the structural lengths of model S so that the most important current path lengths on the actual aircraft would be reproduced. Six different current paths based on Granger and Bolljahn (1955) were considered, as illustrated in Figure 54a. Their lengths were estimated from dimensions available in the CP-140 PR model. The corresponding lengths on model S, as illustrated in Figure 54b, were also obtained and are compared to the previous lengths in Table 3. It is seen that the stick model approximation introduces large percentages of error in the fundamental current path lengths.

TABLE 3
COMPARISON OF CP-140 PATH LENGTHS

Path	True length (m)	Model S (m)	Error (%)
1	34.848	30.256	-13.19
2	13.846	13.332	-3.67
3	31.026	33.928	9.42
4	34.022	35.251	3.66
5	12.016	12.551	4.44
6	11.660	13.391	14.81

Three new models were therefore derived from model S to satisfy some or all of the above path length requirements. They will be called models SA1, SA2 and SA3 (A for adjusted) and they appear in Figure 55. A unique solution was found that would satisfy all six path length requirements. It was applied in model SA1 by lengthening the front portion of the fuselage, the wings and the horizontal stabilizers, and shortening the rest of the fuselage, the vertical stabilizer and the tail.

Unfortunately, since the antenna lengths were to remain untouched, the wings ended up aft of the starboard feed point and the top of the vertical stabilizer below the level of the insulator V-connection. Preserving the length of the fuselage center section (and still attempt to satisfy most path lengths) would have kept the wing position intact, but would have shortened the vertical stabilizer by more than half. It was decided instead to preserve the length of the vertical stabilizer and try to satisfy the other path

lengths. This led to a conflict between paths 2 and 5 as to the length of the horizontal stabilizers. The compromise adopted was to retain their length as in model S, giving rise to model SA2. The model features an even shorter center fuselage section and tail than for model SA1. In model SA3, the lengths of both the vertical stabilizer and the center fuselage section were constrained to those of model S. Of course the previous conflict between paths 2 and 5 arose again, but another conflict appeared between paths 1 and 4 regarding the length of the wings. Lengths of the horizontal stabilizers and wings were therefore kept as in model S, leaving only the front of the fuselage and the tail to be shortened.

A problem with the above length adjustments was that the original number of segments and seg/rad ratios of model S could not be preserved, violating the one-change-at-a-time principle. In fact, in all three models, one less segment resulted, with substantially larger seg/rad ratios along the fuselage,

Models SA1 and SA2, yielding interesting results, were selected for further optimization along the lines of model S*. This gave rise to models SA1* and SA2* which are illustrated in Figure 56a and b. The next and last stick model that was developed was obtained from model S by merging colinear segments as required to make all seg/rad ratios

greater than or equal to 2. The result will be called model SM (M for merged) and is shown in Figure 56c. The short segment squeezed in between the wings and the starboard feed point constituted the only exception. The number of segments went down from 74 to 63, but at the expense of a bandwidth shortened to 10 MHz because of the larger seg/wav ratios.

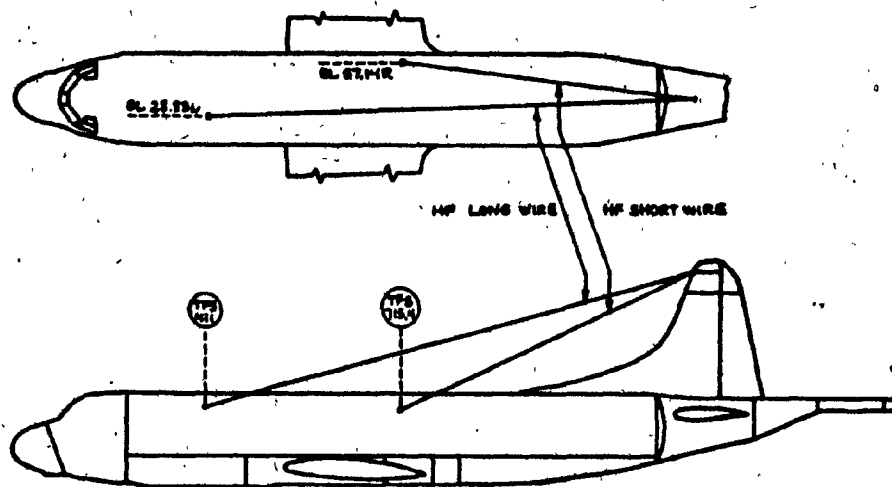


Fig. 48. CP-140 HF antenna installation

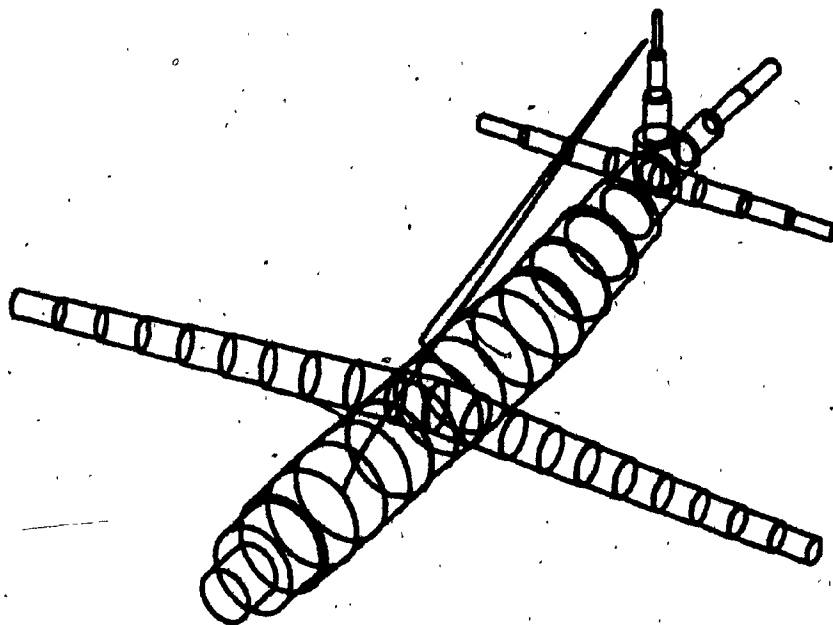


Fig. 49. CP-140 stick model S

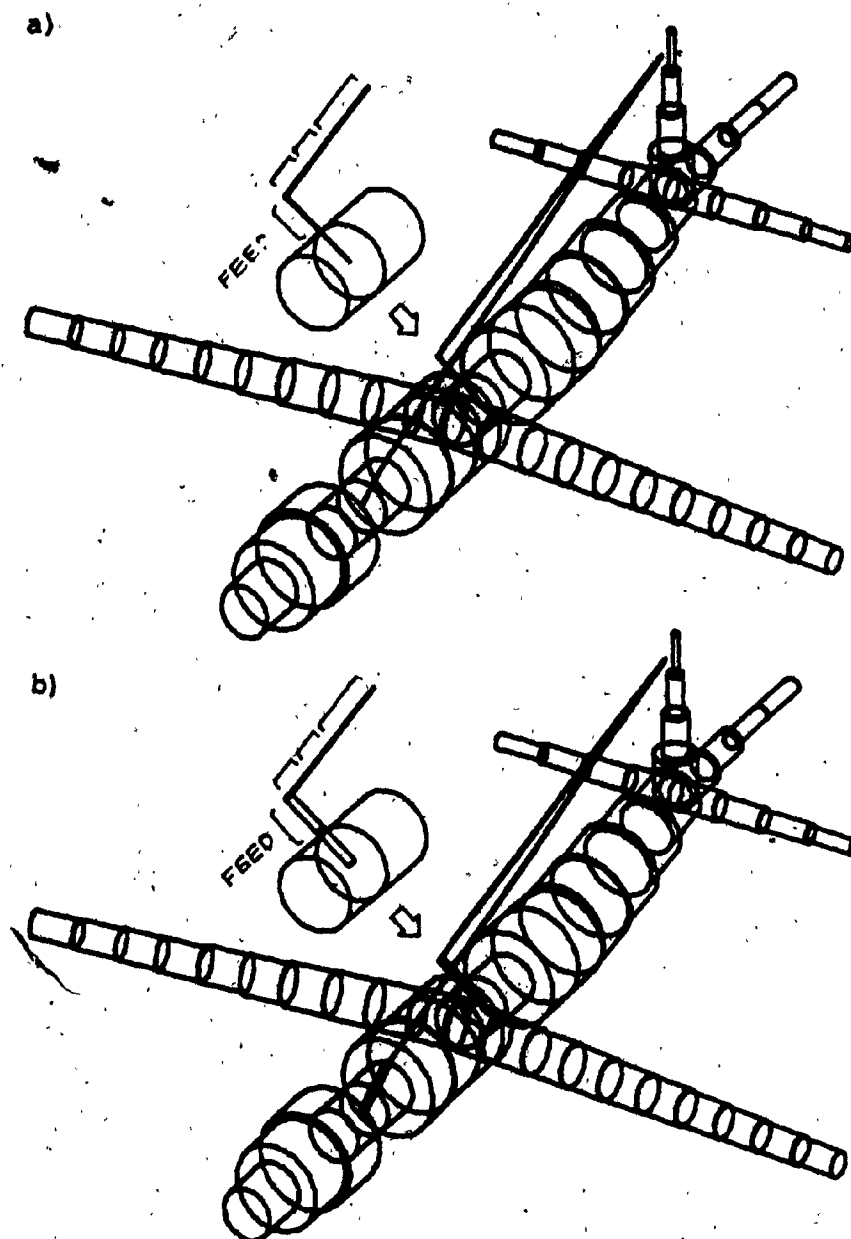


Fig. 50. CP-140 stick models SE (a) and SE' (b) with details of starboard antenna connection.

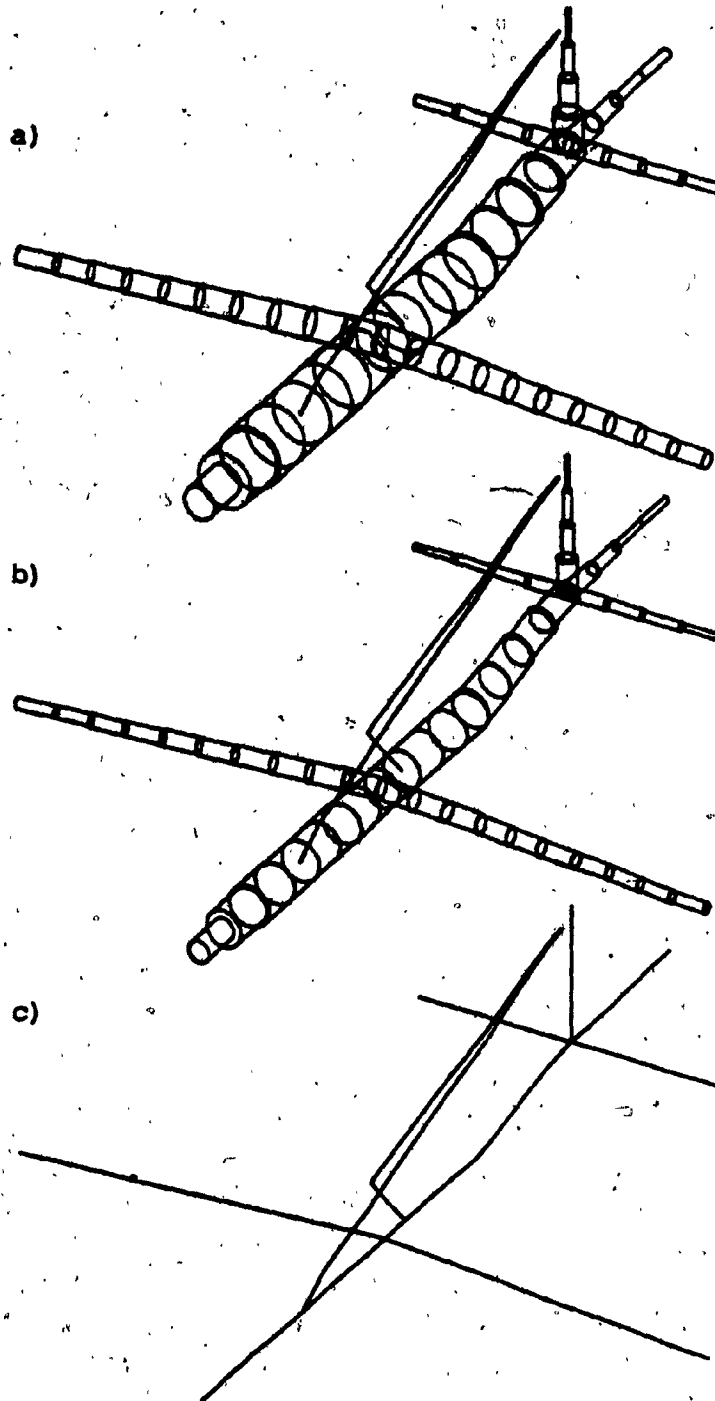


Fig. 51. CP-140 stick models ST1 (a), ST2 (b), and ST3 (c)

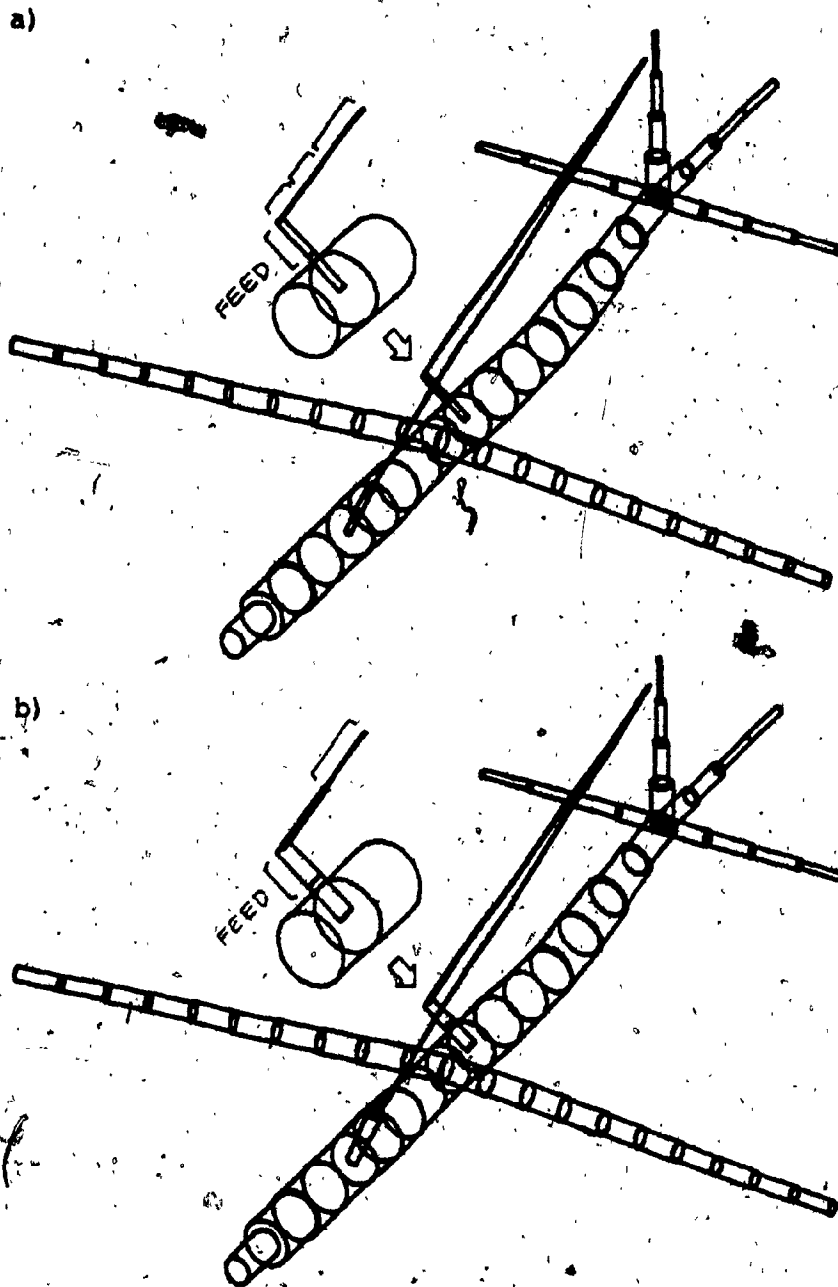


Fig. 52. CP-140 stick models S* (a) and S*¹. (b) with details of starboard antenna connection.

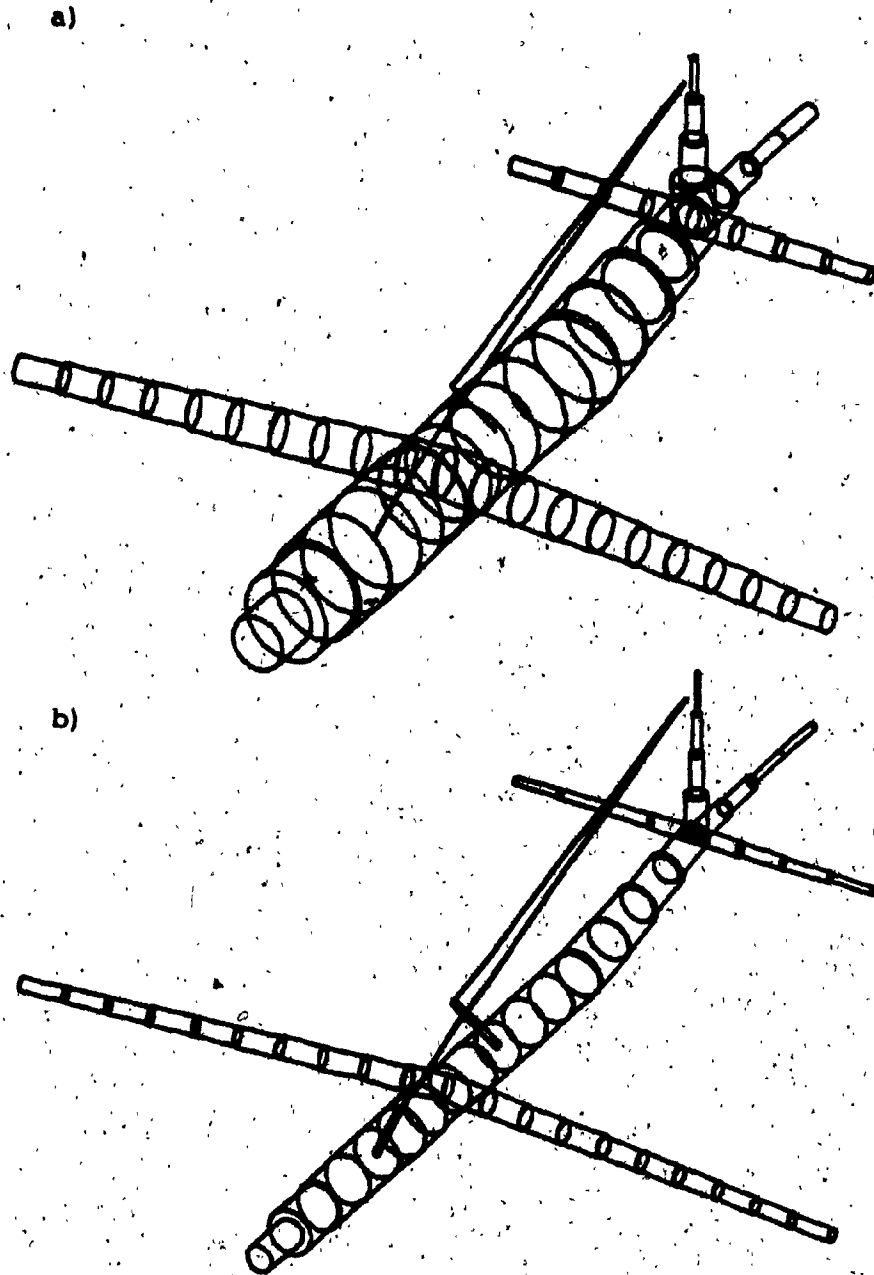


Fig. 53. CP-140 stick models SF (a) and SF* (b)

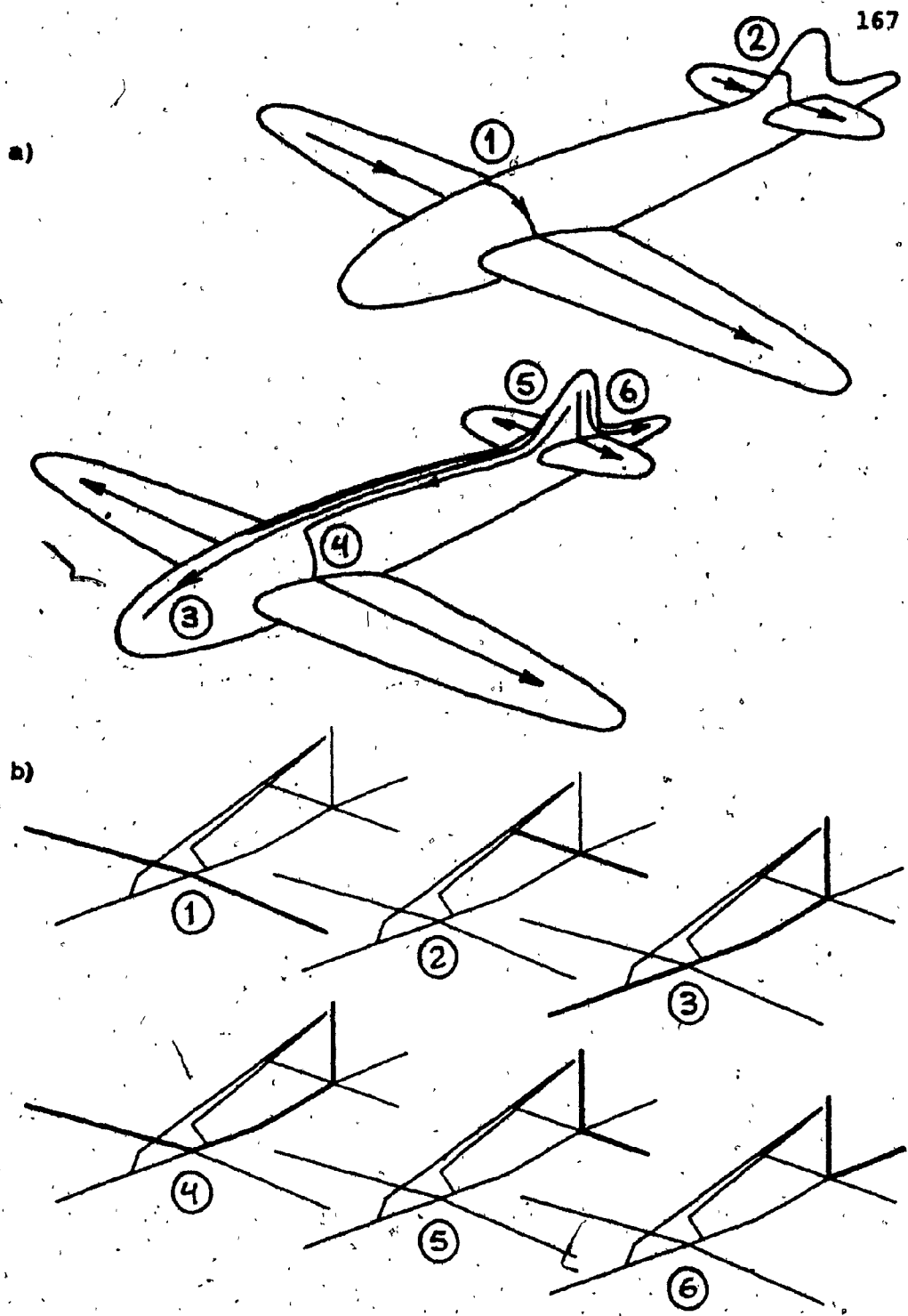


Fig. 54. Six important current paths on the CP-140 (a) and corresponding lengths on model S (b)

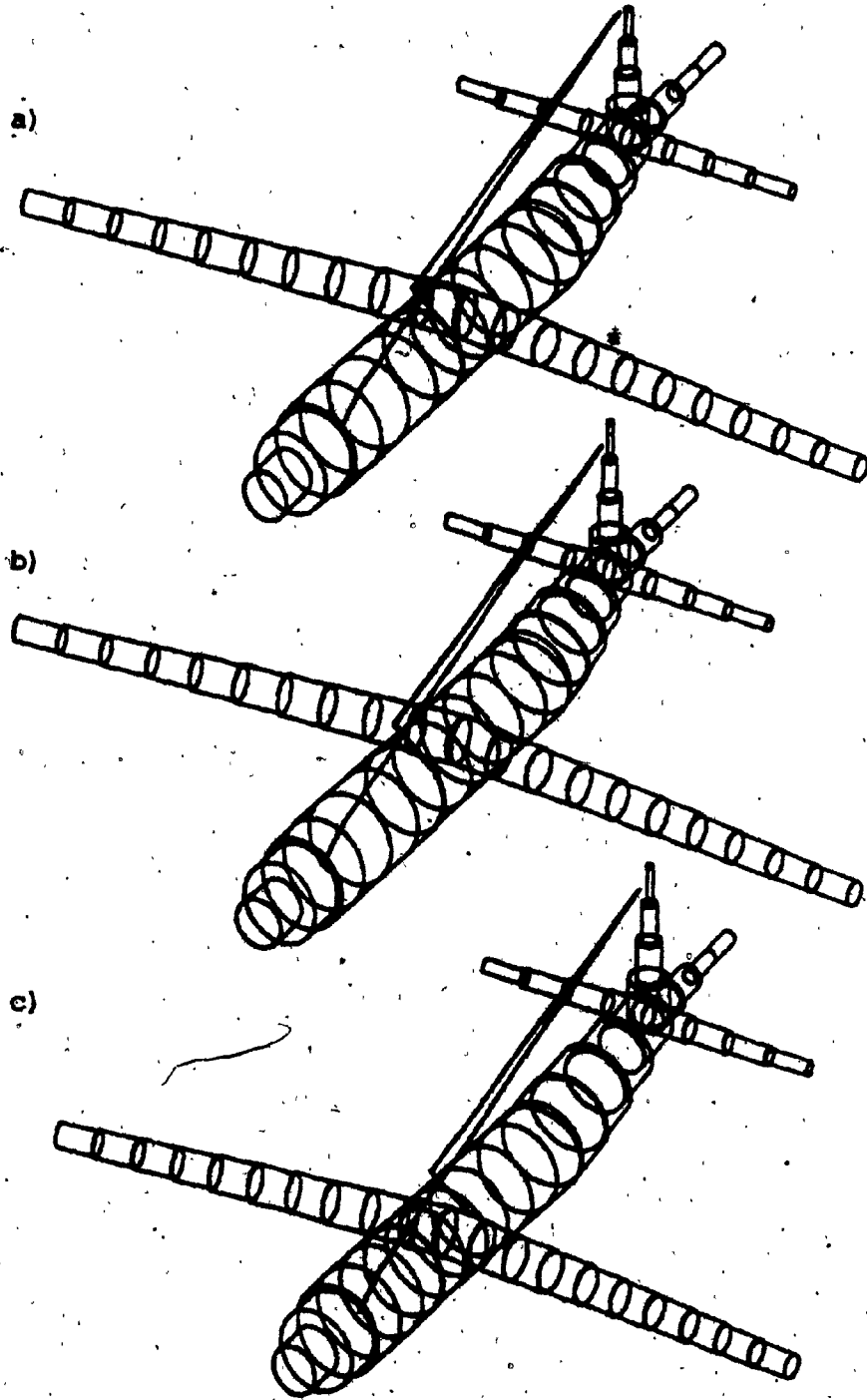


Fig. 55. CP-140 stick models SA1 (a), SA2 (b), and SA3 (c)

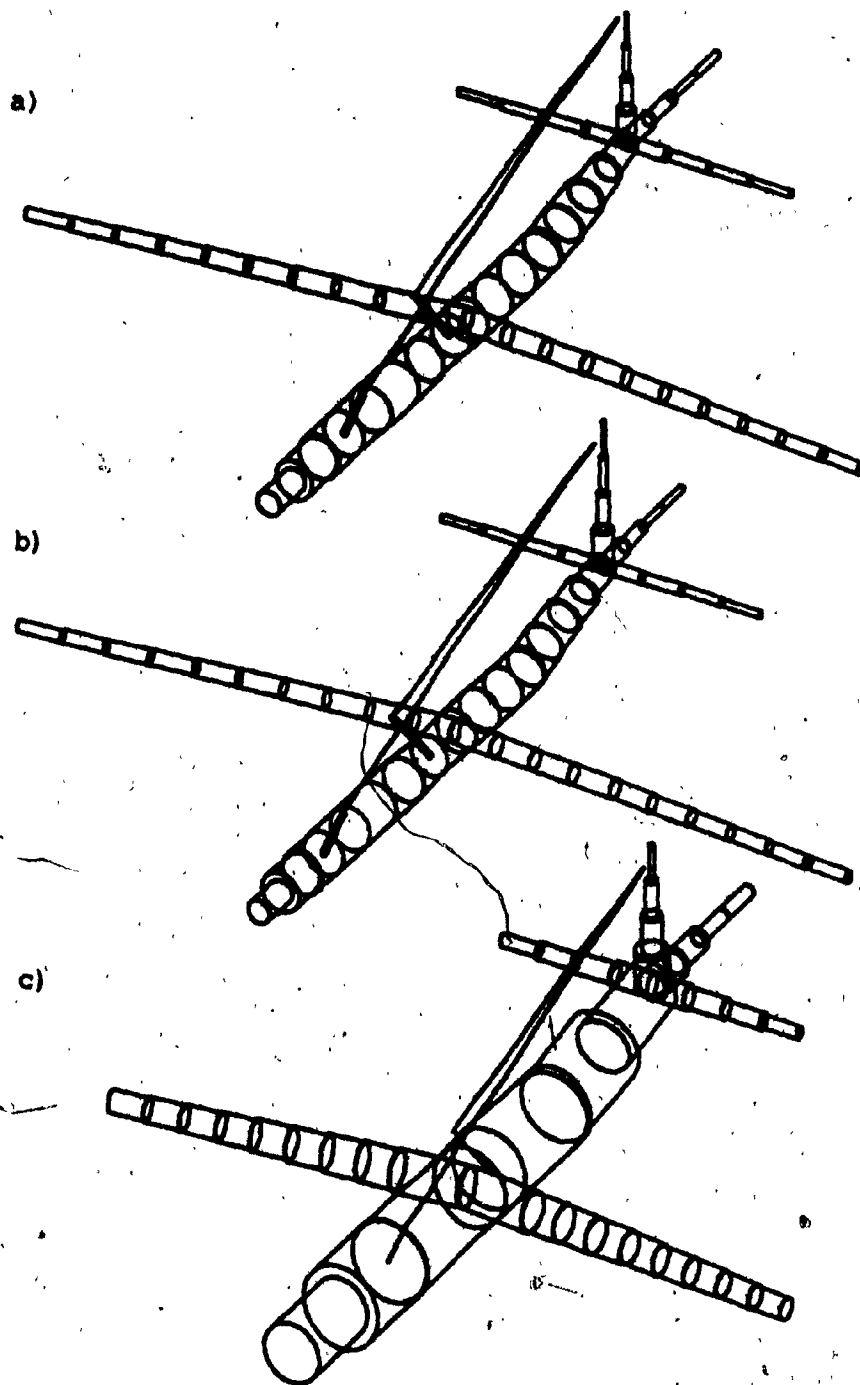


Fig. 56. CP-140 stick models SA1* (a), SA2* (b), and SM (c)

Complex Models

Creation of and modifications on stick models proved to be sufficiently straightforward to be carried out by hand, but the need for a more complex model addressed the need for specialized software assistance. At about that time, wire-grid modelling program DIDEK (Kubina, Cerny, and Gaudine, 1984) became fully operational and ready for its first practical application.

DIDEK performs geometry file management and editing in a most user-oriented manner. Its data organization scheme is based on each wire node being assigned a number by the user. Wires are then referred to by their start and end nodes. But the biggest asset of the program is certainly the possibility of data entry via digitizing tablet. For this purpose it is necessary to obtain orthogonal drawings of the desired model. Each point must be digitized on at least two of the views so that the three coordinates may be transmitted. Hence it is theoretically possible to fully digitize a model from two orthogonal views, say the top and the side views. In practice, however, some points may be difficult to locate precisely on any given view, this being especially true of an aircraft, and all three views are necessary.

In the CP-140 case, the most accurate orthogonal views that could be obtained were computer drawings by ink

plotter of the PR model on 30-inch-wide paper. These were used as a suitable background for tracing the desired outline of the new model. An attempt was made to model each main component of the airframe, excepting the engines, with a compact grid of 0.2-wavelength wires at 30 MHz (2 m). This led to an octogonal approximation of the fuselage, which turned to a quadrilateral approximation in the sections of decreasing cross-sectional area (nose and rear section). Figure 57 shows for example the marking of the desired points and wires over the top and side view drawings of the front fuselage section of the PR model. Digitization could only be performed over such limited sections at a time because the ink drawings would exceed the tablet size (approximately 16 by 16 square inches). The front and back halves of the fuselage as well as the vertical stabilizer were digitized using the top and side views only, whereas the wings and horizontal stabilizers were digitized using only the top and front views. To test a useful feature of DEDIC, the first wing was digitized by hand, and the other was reflected from the x-z plane through the use of a special command. The completed model comprised a total of 327 segments.

Radius values were once again chosen on the basis of equality of cross-sectional areas, that is, the area of a given aircraft cross-section was distributed equally among the wires crossing that section. Figure 58 illustrates this

principle in the special case of a circular cross-section (the fuselage, for example). If R is the radius of the cross-section and n wires are crossing it, they are given radius $r = R/\sqrt{n}$. It must be noted in this approach that since the axes of the wires are made to coincide with the surfaces of the aircraft, the surfaces of the wires themselves exceed the aircraft dimensions. As usual, antennas were assigned a radius of 0.01 m.

The result of this exercise was to be the first of a series of complex models of the CP-140. It will be designated model C and appears in Figure 59. Its true representation, rather messy, is followed for clarity by its thin wire representation. Figure 60a shows the details of the port and starboard antenna connections respectively. The antenna feed elements, connecting this time to the surface of the fuselage and not to its axis, were made one foot long, and a two-foot separation from the edge of the vertical stabilizer was provided. The nodes of the fuselage that naturally fell closest to the feed point locations were displaced as necessary to make the connections. Figure 60b, with the true radius representation, shows that the feed elements became embedded inside the wires of the fuselage to which they were connected. The important discontinuities in segment length and radius at these connections also introduced obvious seg/seg and rad/rad errors. Finally, the

large radius values of the model (up to 0.8 m) caused the wav/rad criterion to start being violated above 12 MHz. These incompatibilities were tolerated in the initial model, but as in the stick model case, corrections were brought in the course of model optimization.

As before, corrections were first implemented one at a time in order to properly assess their individual effects. The first move, illustrated in Figure 60c, was to increase the radii of the feed elements so that the previous rad/rad errors would be converted to warnings. This gave rise to a new model that will be designated C'. Another move was to lengthen the feed elements, as shown in Figure 60d, so that they would emerge one foot from the surface of the wires of the fuselage. Seg/seg errors at the feed elements were thus removed. This new model will be called CE (E for emerging).

Neither of the above corrections having lead to any substantial improvements, a greater step forward was made by attempting to remove all at once the incompatibilities reported by CHECK on model C. The first move in this direction was to have the model satisfy the wav/rad criterion up to 30 MHz. For this purpose all wire radii had to be within a thirtieth of a wavelength at that frequency, that is, $1/3$ m. In order to bring the largest radii (0.8 m) down to this value and at the same time retain radius proportions throughout the model, all wires except the antennas were

thinned by a factor of 5/12. This removed previous seg/rad warnings for individual wires, as well as most seg/rad errors at junctions. The renewed aspect of the model appears in Figure 61a.

Seg/wav errors remained for all wires that exceeded 2 m, but since they exceeded that value only slightly they were left unchanged. Subdividing all these wires in two would have considerably increased the total number of segments while breaking the segment length uniformity that prevailed throughout the model. The only incompatibilities left at this point were wire junction errors involving the feed elements. Figure 61b shows the corrections that were necessary. Comparing with Figure 60, it is seen that three wires were subdivided on the port side and two on the starboard side. Not apparent on the figure is the fact that the forwardmost segment of each antenna was also subdivided. These measures eliminated the remaining seg/seg errors and added 7 segments for a total of 334 segments. To eliminate the remaining rad/rad errors or warnings and at the same time the remaining seg/rad errors at junctions, two intermediate radius values were used, one for the feed elements and one for wires of the fuselage connected to the latter. The resulting model will be referred to as model CF (F for fixed). It was to serve as a new reference in subsequent model optimization or changes in testing parameters.

The last complex model of the CP-140 was derived from model CF by providing a denser grid of wires around each feed point in an attempt to improve impedance values. The resulting model will be called CD (D for denser) and details of its antenna connections appear in Figure 61c. More wires were provided to account for current flow outward of and around the feed points, augmenting the total number of segments to 364. Radii were selected such that no new CHECK errors would be introduced.

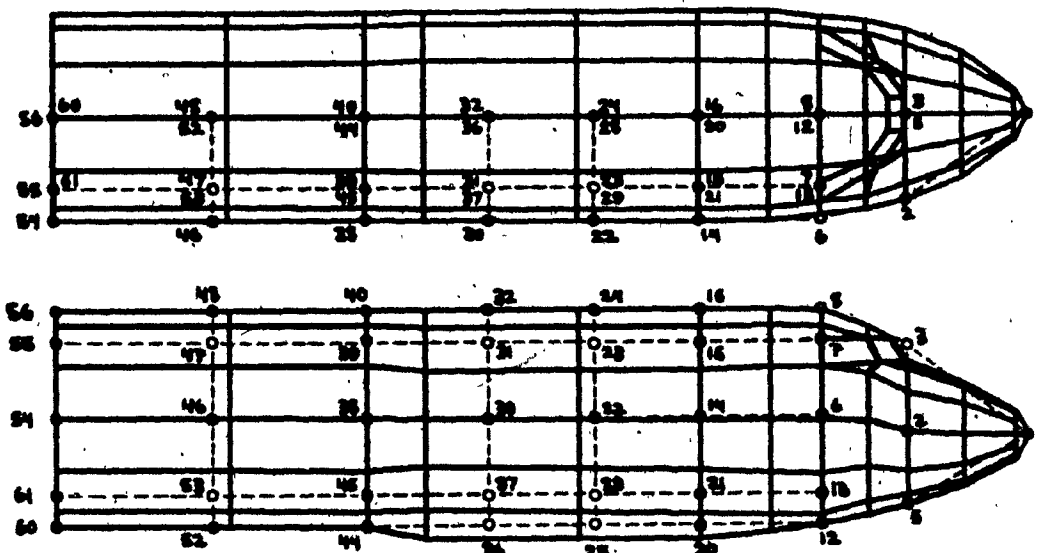


Fig. 57. Markings on drawings of front fuselage section of PR model for purposes of digitization via DIDEK

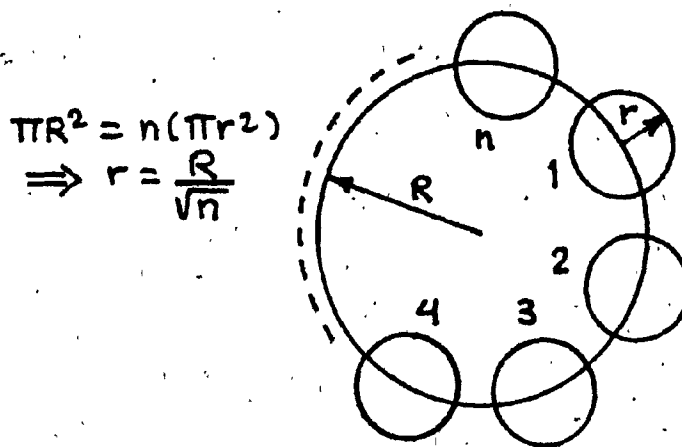


Fig. 58. Choice of wire radii based on area equivalence for a circular aircraft cross-section

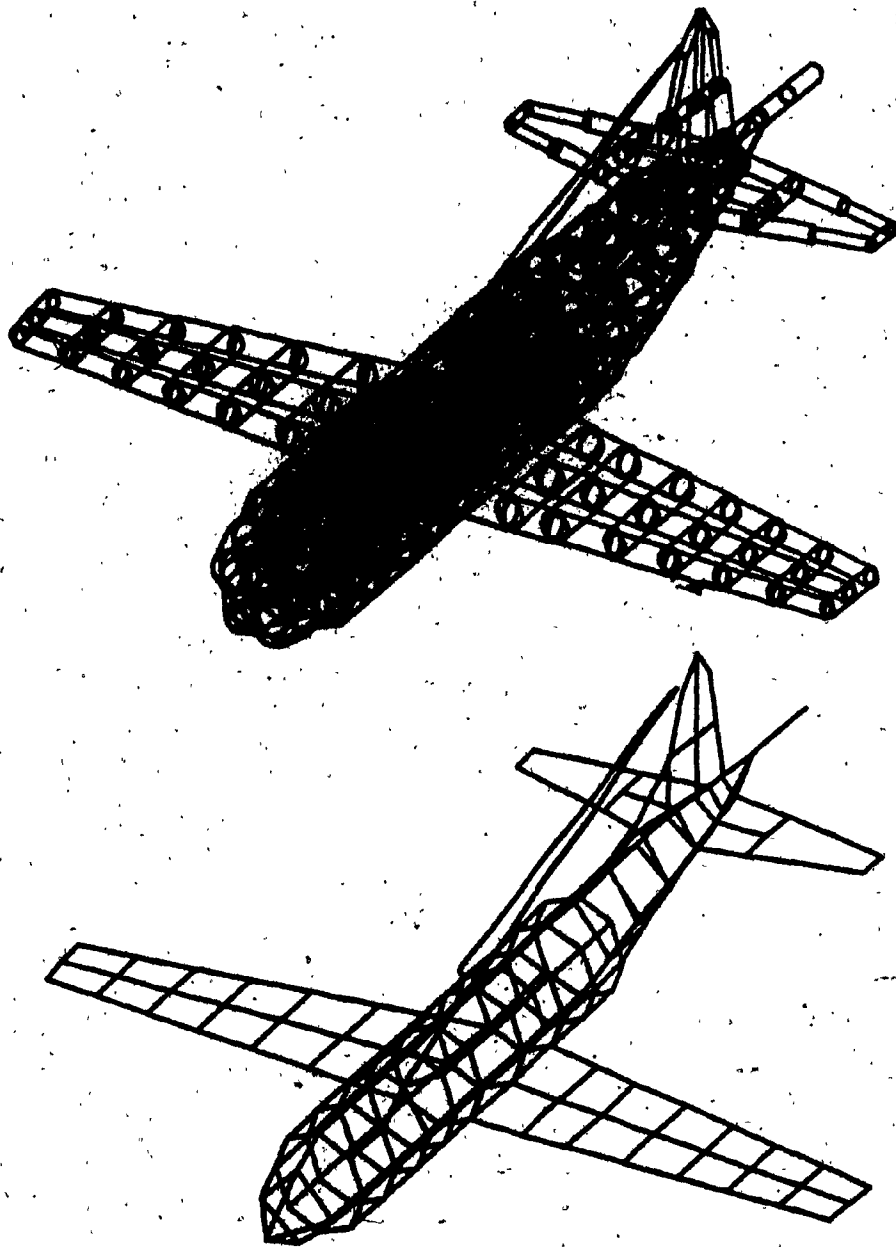


Fig. 59. CP-140 complex model C, true representation and thin wire representation

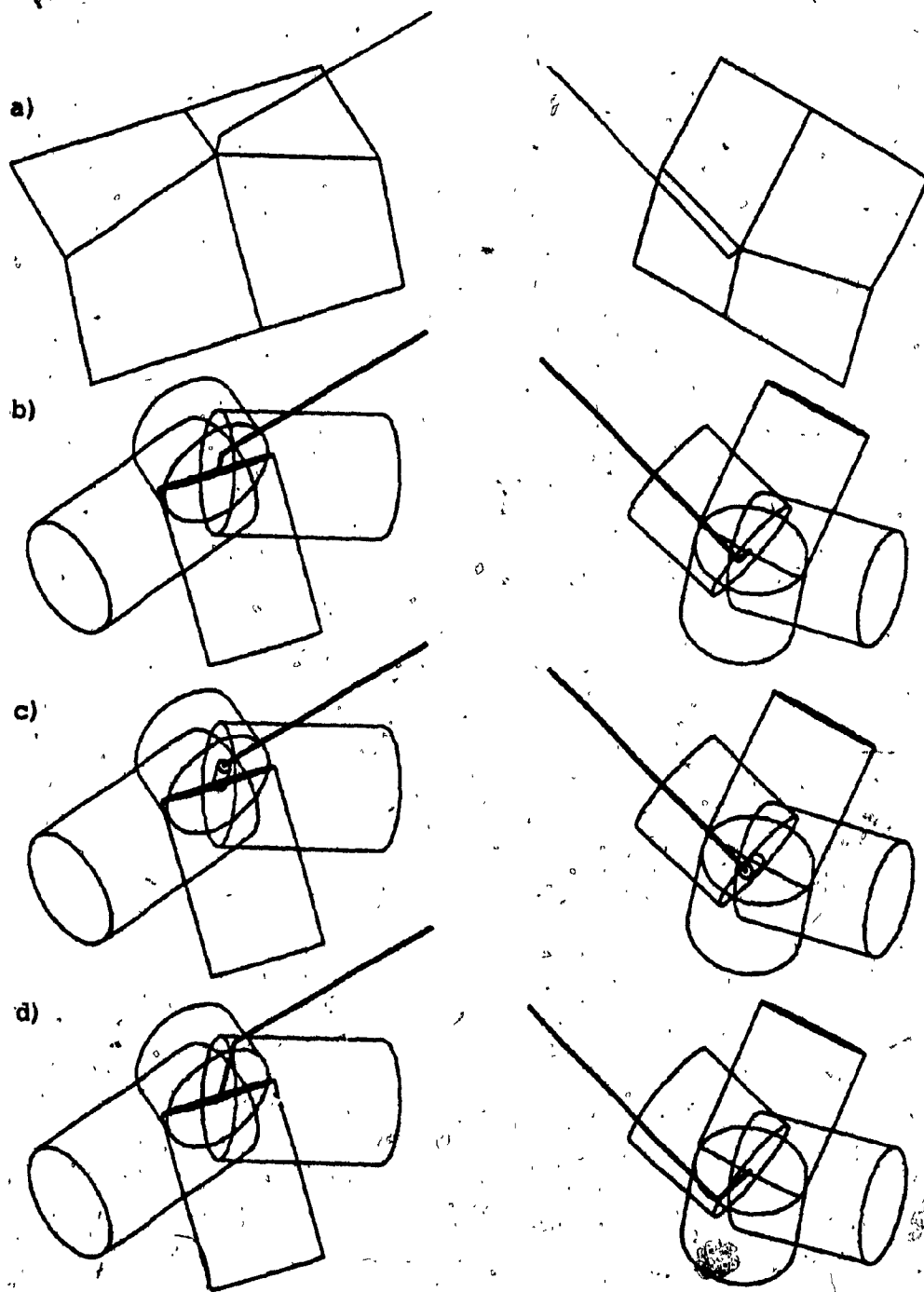


Fig. 60. Details of port and starboard antenna connections on CP-140 complex models. Thin wire representation for model C (a), and true representation for models C' (b), C' (c), and CE (d)

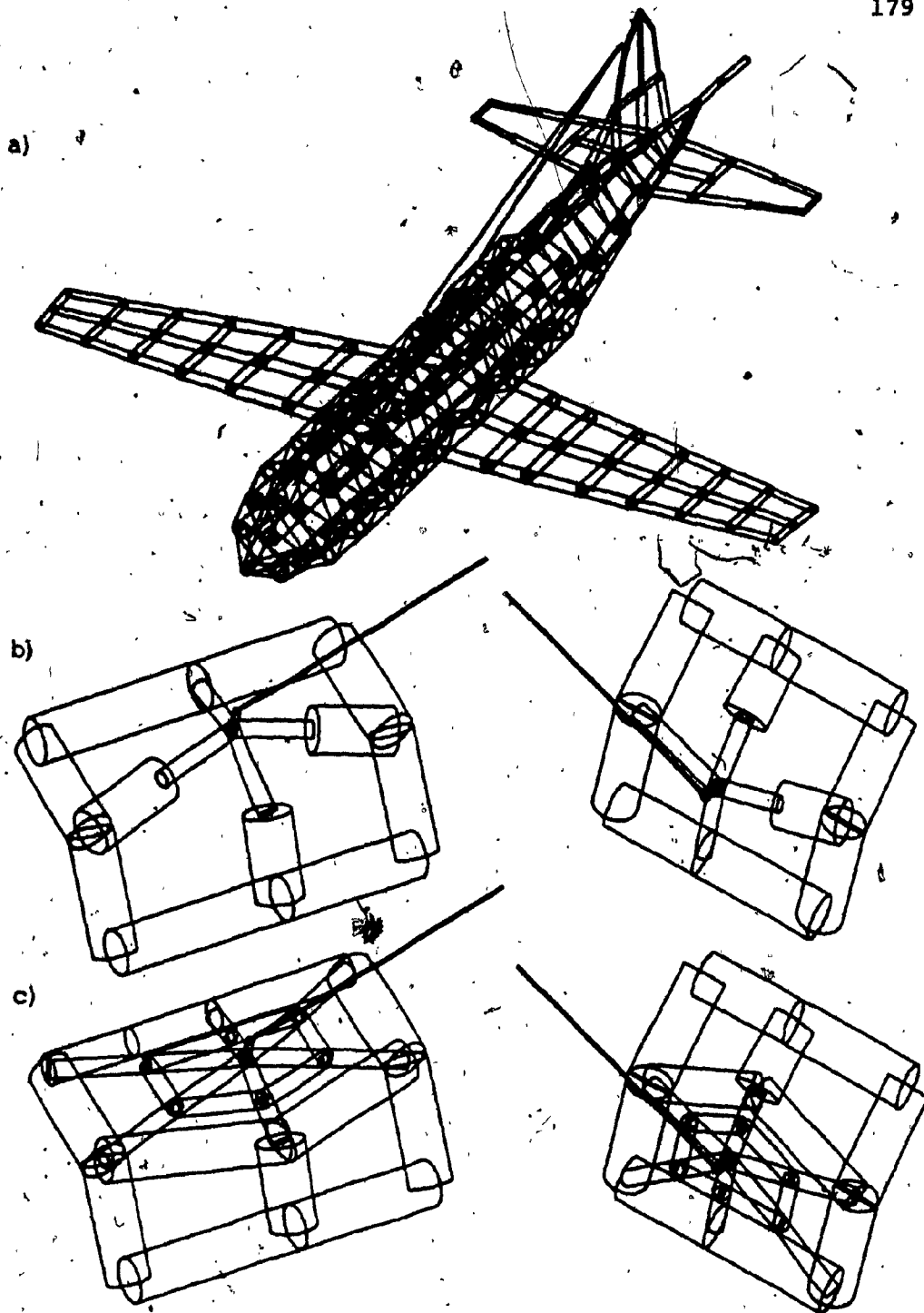


Fig. 61. CP-140 complex model CF (a), with details of port and starboard antenna connections (b). Same details for CP-140 complex model CD (c)

Radiation Patterns

Both antennas, port and starboard, were excited successively at each test frequency of the various CP-140 models.

Stick Models

Model S was tested first over the complete HF range (up to 30 MHz) in frequency increments of 2 MHz. As had been observed for the P3V-1 model F2, disastrous results were obtained at 2 MHz. The measured and computed MOVIE.BYU plots of Figure 62 are particularly effective in showing this. Rather than displaying the partial set of computed conical cuts that best matches the measured set, as is done for altitude plots, the full set can now be displayed without loss of clarity in the comparisons. For the port antenna (Figure 62a), the power density pattern appears as that of an inclined dipole, rather than that of a vertical dipole as it should be. Somewhat better results were obtained for the starboard antenna (Figure 62b). The level of the E-phi pattern is correct but its orientation is off by a full 90 degrees.

Throughout the rest of the frequency sweep, the results that were obtained ranged from bad to good, but interestingly, no trend towards pattern degradation was observed in spite of the wav/rad ratios increasing way past

the limit. In the low frequencies, the best patterns were obtained at 6 MHz. In the high frequencies, the best patterns occurred at 20 MHz but the worst ones at 24 MHz. The principal plane patterns at the four frequencies that have been mentioned so far are shown in Figure 63 for the port antenna and Figure 64 for the starboard antenna.

Because of the poor results obtained at 2 MHz, this was chosen as the test frequency for all optimized stick models. The sequence of patterns thus obtained appears in Figure 65 for the port antenna and in Figure 66 for the starboard antenna. For convenience, altitude plots are used here, with a range of computed patterns from 25 to 135 degrees to best match the measured range of 30 to 135 degrees. In a) of these figures, the measured E-theta and E-phi patterns are followed by those computed from model S, first with the standard excitation, and then with the new one that was tested. The patterns of models SE, SE', ST1, ST2, and ST3 are shown in b), those of models S*, S*', SF, and SF* in c), those of models SA1, SA2, and SA3 in d), and those of models SA1*, SA2*, and SM in e).

The amount of data being presented here illustrates the difficulty that was encountered in interpreting results, drawing conclusions, and deciding on the next moves. In the course of writing, a condensed method of presenting the results was devised and will be used here. It is based on

the assumption that CP-140 models at 2 MHz radiate similarly to an ideal dipole. That this is experimentally the case, at least for model S, can be proved by comparing the MOVIE.BYU plots of Figure 62 with those of Figure 25 for the ideal dipole. It is also proved by the regular occurrence of the ideal dipole E-phi pattern throughout Figures 65 and 66. Small departures from this form are apparent in some models, for example model SF, port antenna. The ideal dipole equivalence can be justified in theory by the fact that the models at 2 MHz are small compared to a wavelength (150 m), and that they radiate waves that are nearly linearly polarized.

It follows therefore that the complete radiation characteristics of a model at 2 MHz can be summarized by the orientation of the equivalent ideal dipole in terms of theta and phi. This orientation was determined for the measured patterns as well as for all stick models by means of a program that searched for the minimum power density in the solution files. The resulting directions were plotted together on graphs of theta versus phi for the port antenna (Figure 67a) and for the starboard antenna (Figure 67b).

The orientation of the equivalent ideal dipole has a simple effect that is interesting to track on the E-phi altitude plots of Figures 65 and 66. The theta angle is seen to be related to the magnitude of the E-phi pattern, whereas

the phi angle is seen to indicate the position where this pattern falls to a minimum (i.e. location of the "valley").

The plots of Figure 67 have the particularity of showing not only the pattern agreement of each model with the measurements, but also the similarities and differences between the models themselves. The distances between the points, however, are not an accurate measure of the angles sustained between the equivalent ideal dipoles, just as the distances between points on a Mercator projection of the globe do not give a true measure of travelling distances. For the port antenna, for example, the equivalent ideal dipole orientation for the measured patterns is at $\theta = 5$ degrees, which is almost vertical, and therefore model SF* with $\theta = 15$ degrees gives the closest pattern orientation. Yet the point representing model SF* is not the closest to that representing the measurements because of the large phi difference. For the starboard antenna, because the point representing the measurements is at $\theta = 30$ degrees and $\sin(30^\circ) = 0.5$, it was best to compress twice as much the theta scale as the phi scale. In this way, a small displacement in any direction from the point representing the measurements amounts to the same magnitude of angular error in the equivalent ideal dipole orientation. Thus the visual impression of Figure 67b is accurate and model SF* can be seen to be the best model for the starboard antenna

(as well as for the port antenna, as we saw).

The magnitude of the angular error in the equivalent ideal dipole orientation is the most exact measure of the performance of each model. Figure 68 marks this value for each model on scales from 0 to 90 degrees, one for the port antenna (a) and one for the starboard antenna (b). The disadvantage of this representation is that the directions of shift of the equivalent ideal dipole orientations are not indicated, and therefore the relations between models are also lost.

Figure 67a shows a relatively simple situation for the port antenna: all points are roughly constant in ϕ but vary widely with θ . The latter angle alone suffices anyway to indicate performance, since the measurements are almost vertical at $\theta = 5$ degrees. Interpretation of results is therefore simplified. In Figure 67b however, the points tend to concentrate in two groups: one shifted in θ from the measurements, and one shifted in ϕ . It was hoped that this would be reflected in some fundamental difference in the characteristics of the models, but no correlation could be identified. Understanding the specific causes of shifts in different directions may still be a worthwhile goal.

A close study of Figure 67 will permit the identification of worthwhile approaches to stick model optimization,

but will also reveal apparent contradictions that cannot be resolved at this stage, especially regarding the starboard antenna. The figure indicates that models SE and SE' gave overall superior results to those of model S. Since the two models are very similar, their points are also in the proximity of each other, as expected. However it seems contradictory that models SE and SE' be the better models for the port and starboard antennas respectively. The effect of increasing the radii of the feed elements is therefore inconclusive.

Model ST1, and model ST2 to a greater degree, show also an improvement over model S. These models, together with models SE and SE', indicate therefore, that it is worthwhile to remove NEC incompatibilities in stick models even if this means sacrificing somewhat on their realism. If however one goes to the extreme, as in model ST3, disappointing results must be expected. This model yielded results actually inferior to those of model S. In Figure 67b it is interesting to notice that a smooth curve can be traced through the points representing the S-ST1-ST2-ST3 sequence of models. Since model ST2 falls on the part of the curve that is closest to measurements, nothing better can be expected from the thinning approach to optimization.

Model S*, a combination of models SE and ST2, gave as anticipated the best results so far for the port antenna.

For the starboard antenna, paradoxically, the results were worse than for model ST2 and hardly better than for model SE (Figure 68b). The results of model S*¹ were practically undistinguishable from those of model S*, confirming the previous observation on model SE¹.

Model SF was an improvement over model S for the port antenna but not so for the starboard antenna. It must be noted that this model introduced for the first time a modification on the actual topology, with the result that the port and starboard antennas were affected in different ways. Another aspect of interest is the large shift between the points of models SF and S in Figure 67b. It is surprising how topological changes of such small magnitude can influence the radiation pattern. The merits of model SF* have already been pointed out.

All three models SA1, SA2, and SA3 showed improvement to various degrees over model S; but optimized models SA1* and SA2* were disastrous. This phenomenon lead one to wonder about the effects of the larger seg/rad ratios brought about by the path length changes. Close examination of the SAn models suggested a correlation between the magnitude of the seg/rad ratios near the port antenna and the quality of the pattern orientation for this antenna. This lead to construction and testing of model SM, which performed better than model S but not to the extent expected.

Nevertheless, the implication is that seg/rad warnings should be taken seriously, and as inferred in Chapter I, reasonable current solutions do not necessarily produce good field solutions.

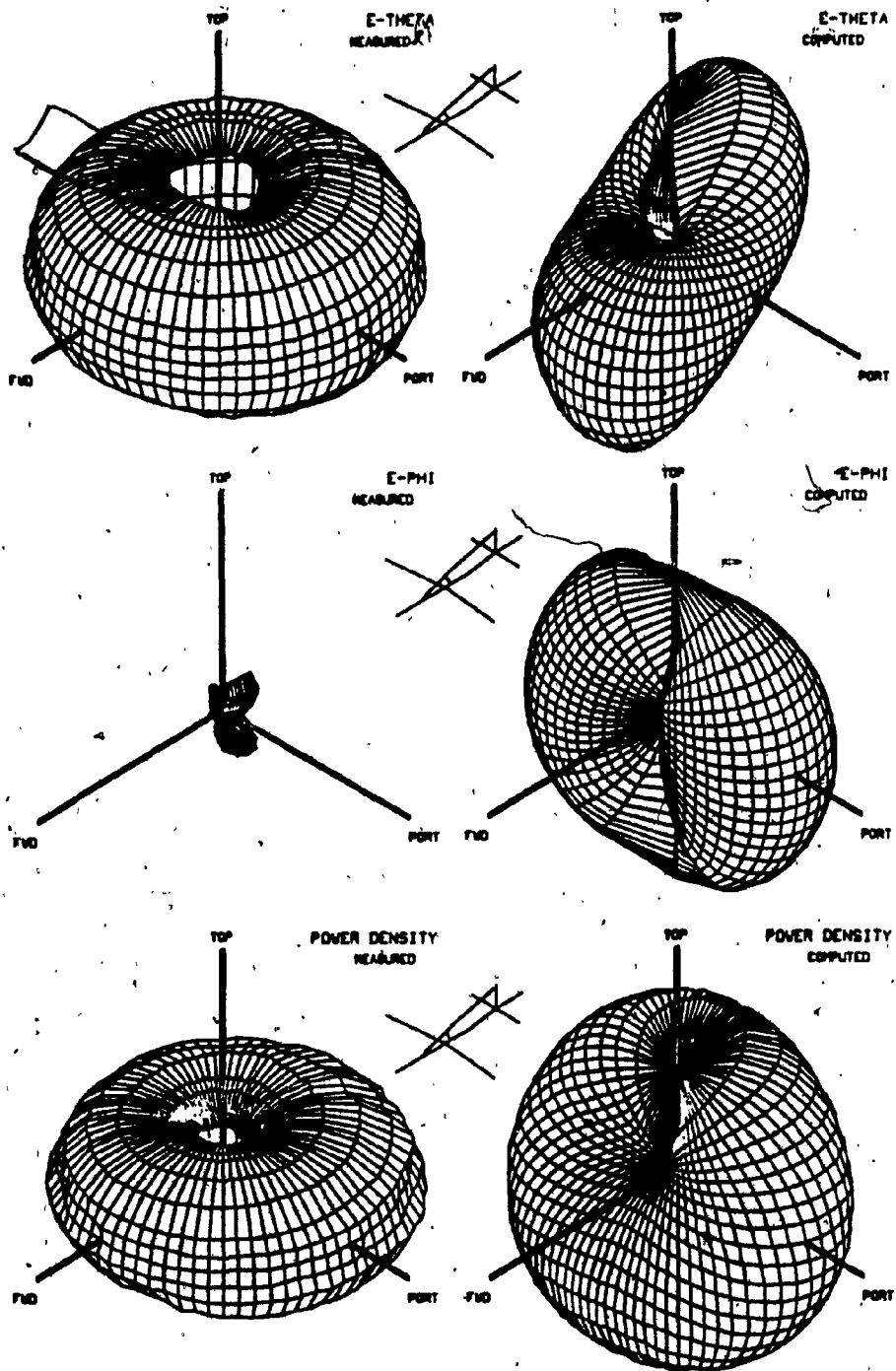


Fig. 62a. MOVIE.BYU plots of radiation patterns for the CP-140 port antenna at 2 MHz, measured and computed from model S

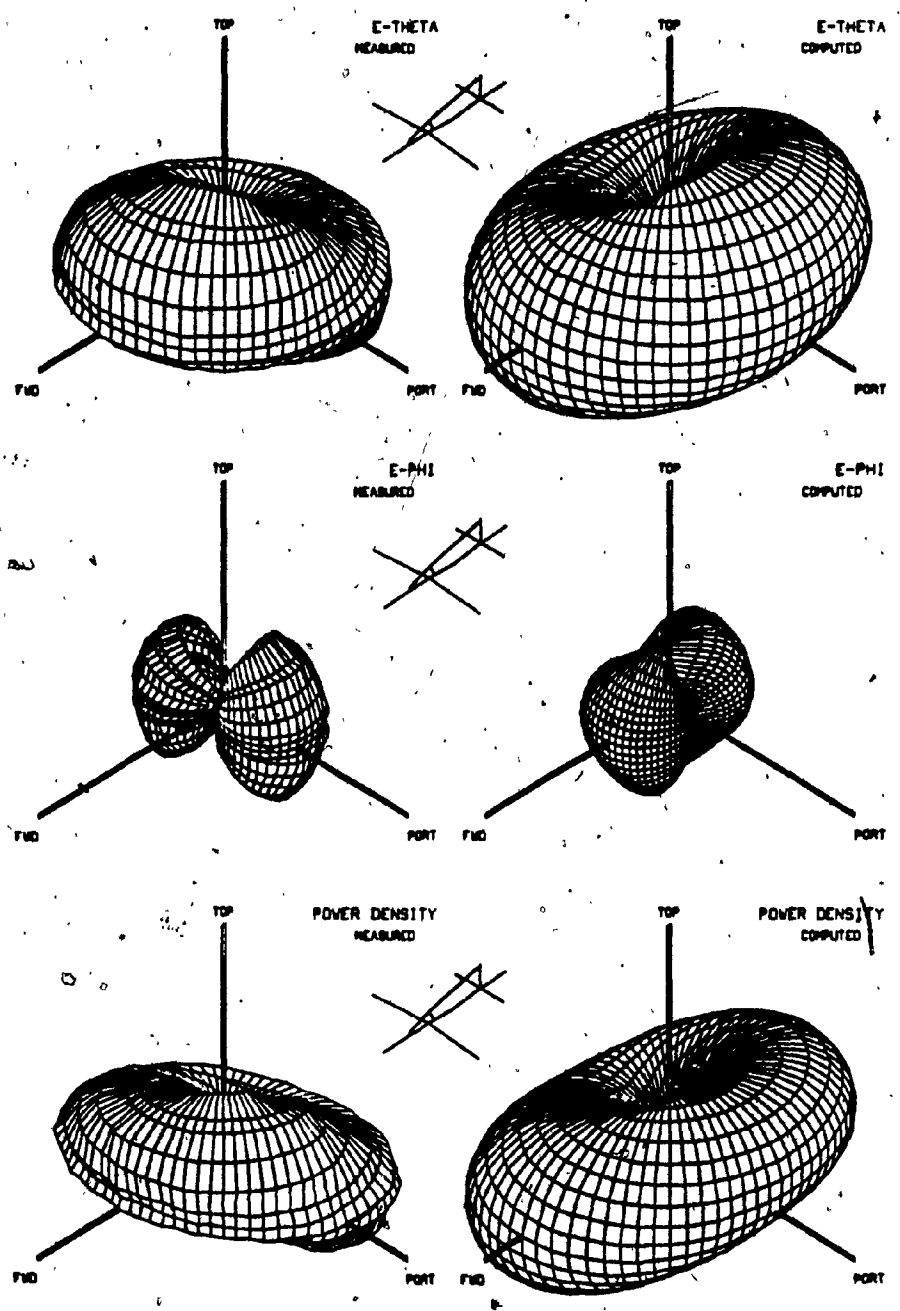


Fig. 62b. MOVIE.BYU plots of radiation patterns for the CP-140 starboard antenna at 2 MHz, measured and computed from model S

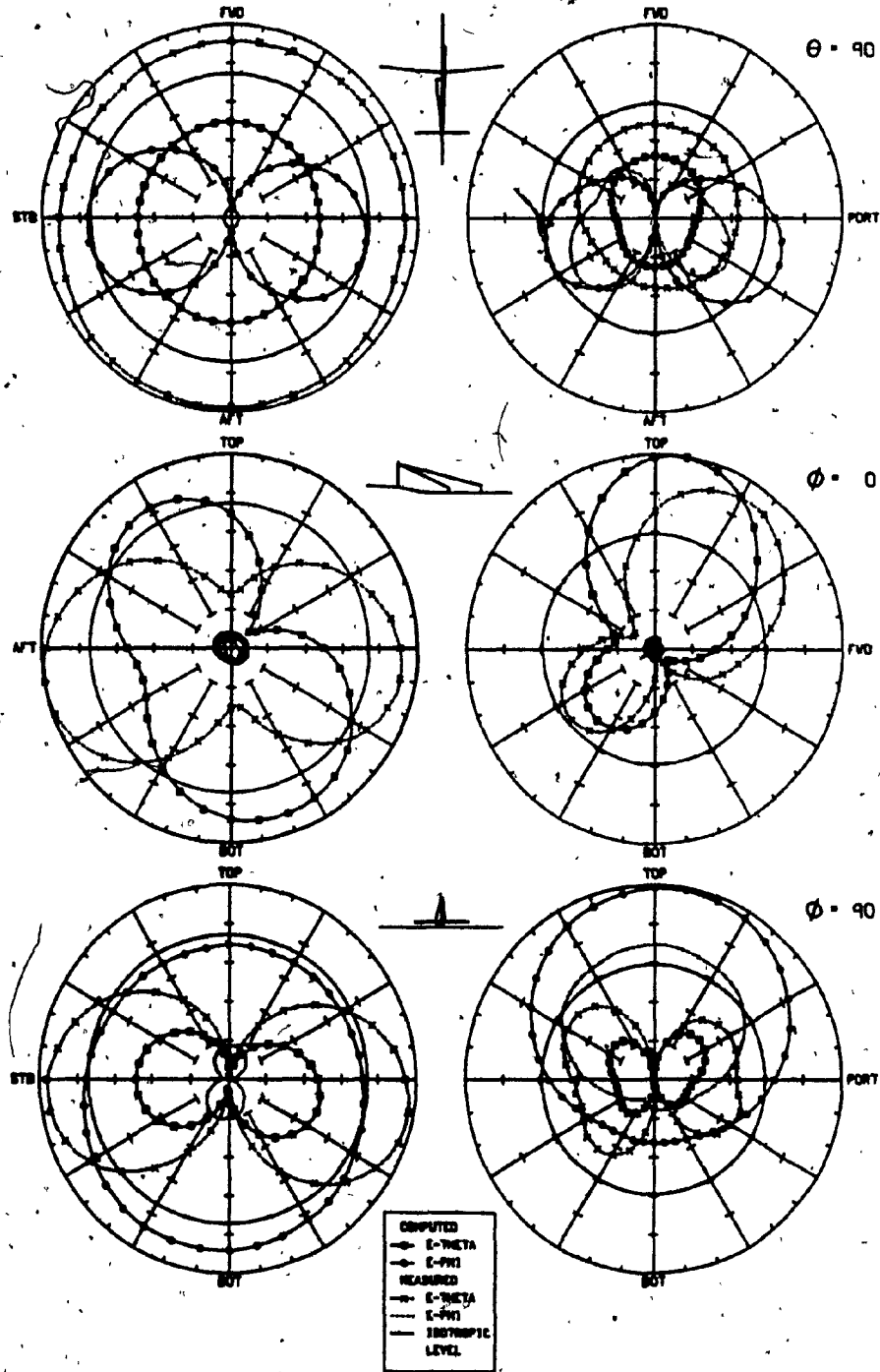


Fig. 63. Comparisons of measured and computed principal plane patterns for model S, port antenna, at 2 and 6 MHz

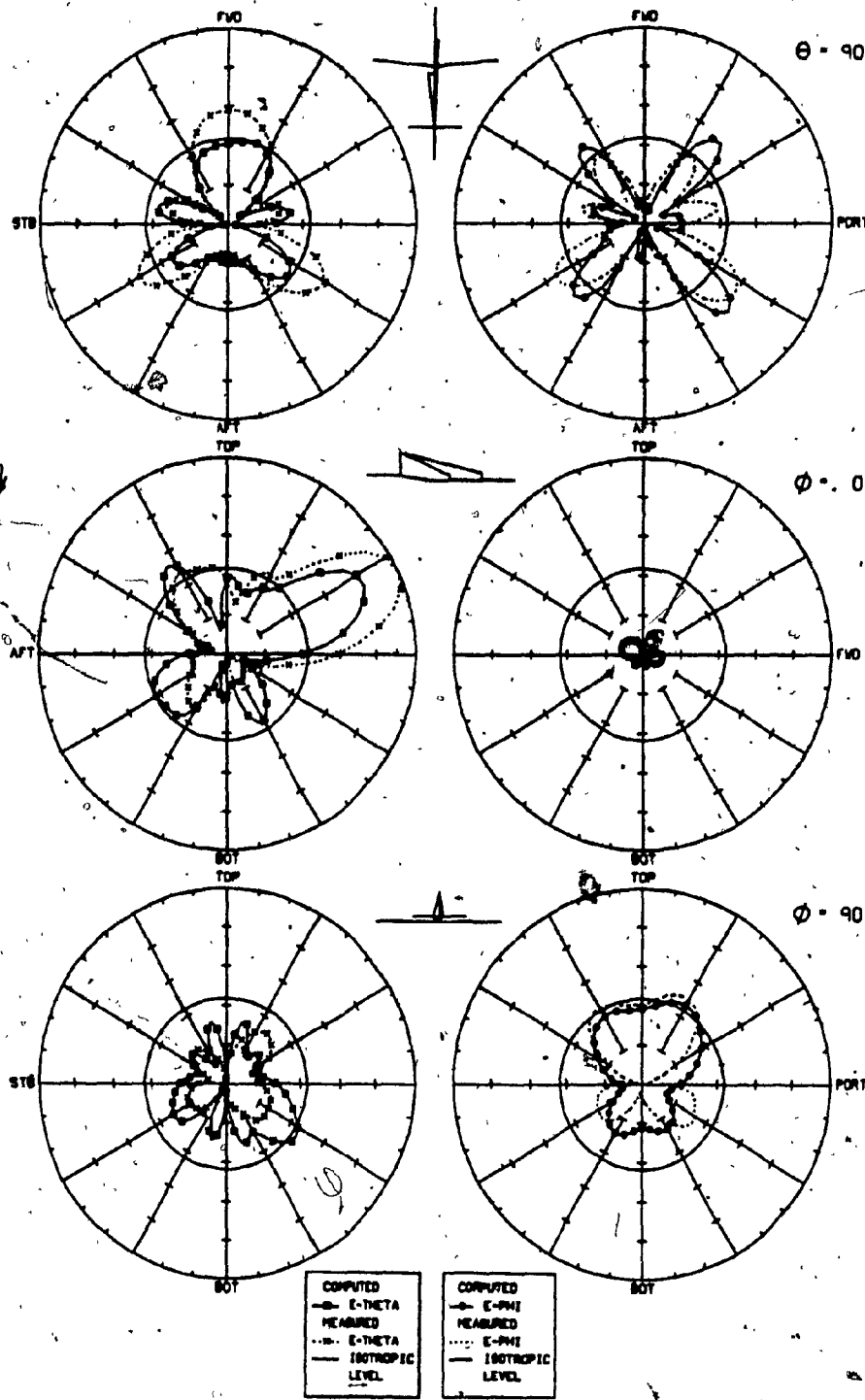


Fig. 63-continued. Comparisons of measured and computed principal plane patterns for model S, port antenna, at 20 MHz

9

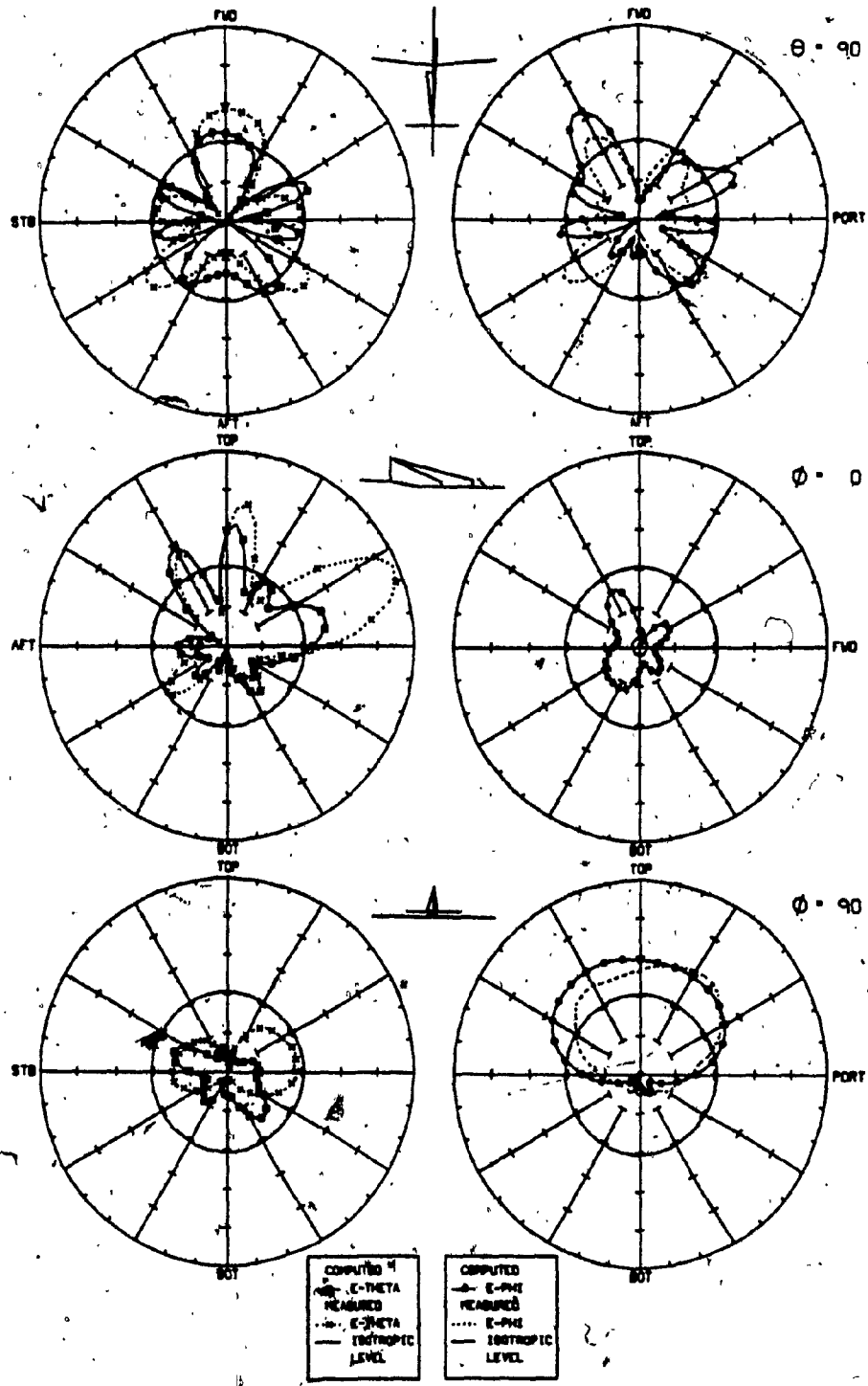


Fig. 63-continued. Comparisons of measured and computed principal plane patterns for model S, port antenna, at 24 MHz

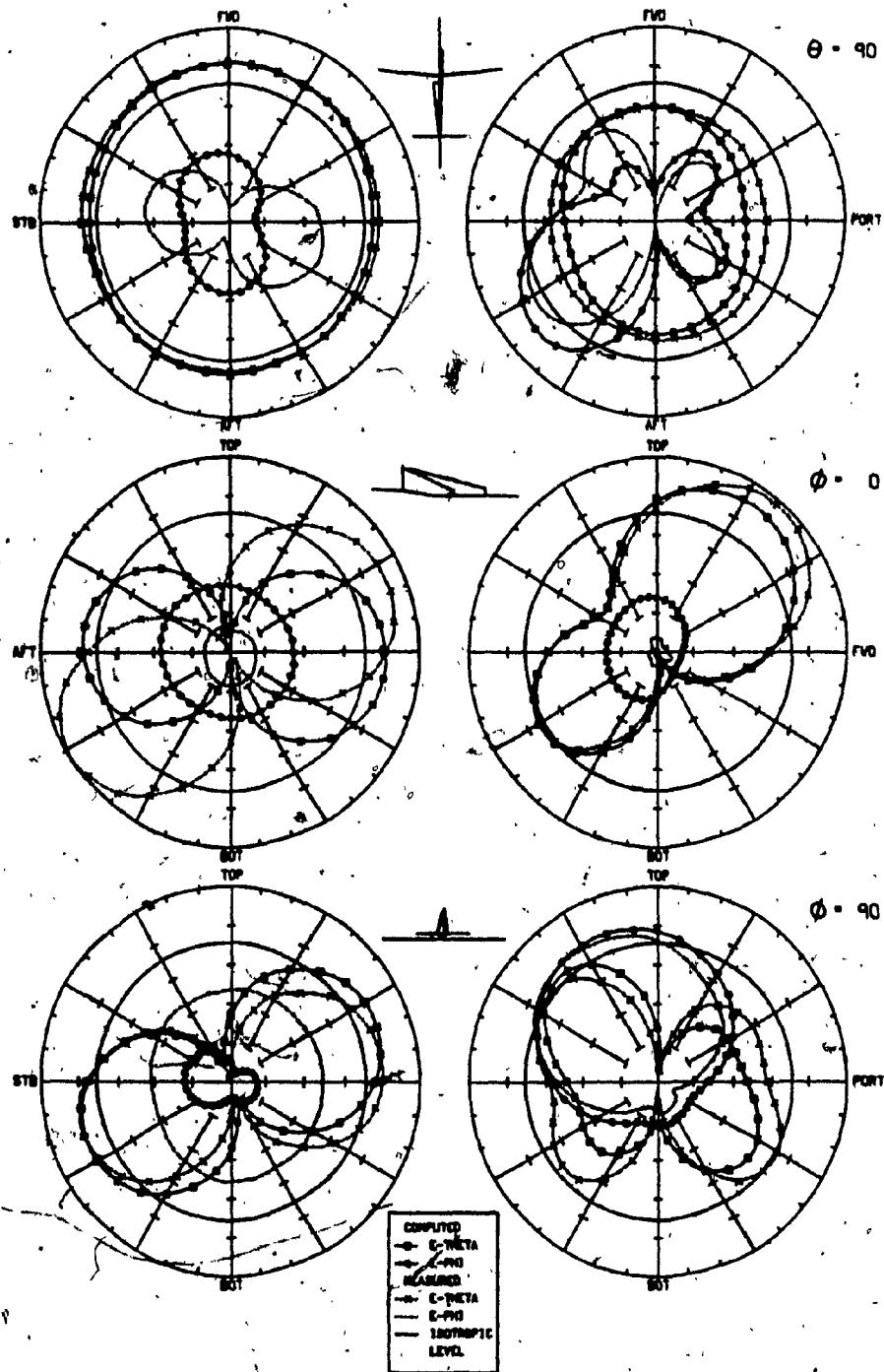


Fig. 64. Comparisons of measured and computed principal plane patterns for model S, star-board antenna, at 2 and 6 MHz

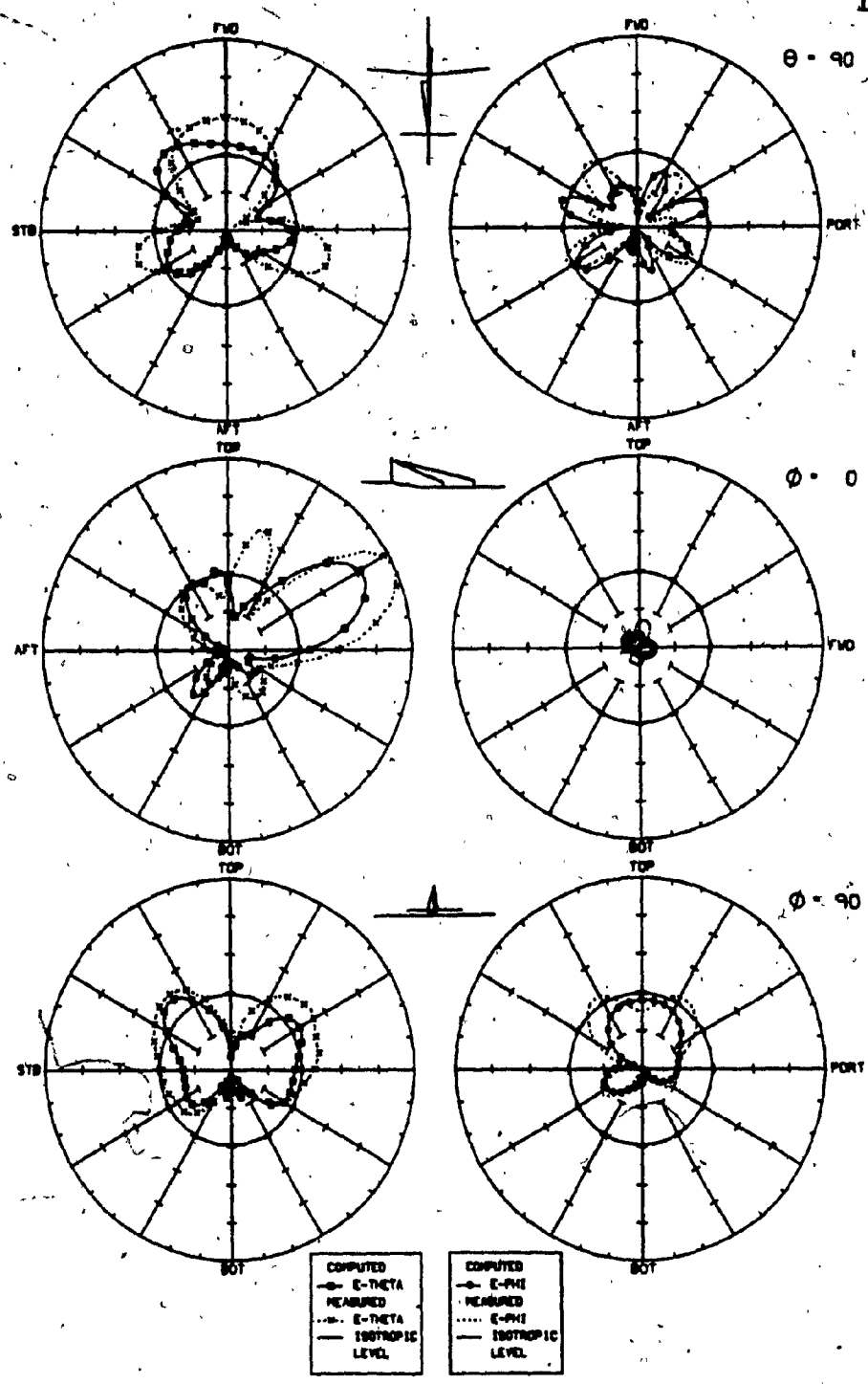


Fig. 64-continued. Comparisons of measured and computed principal plane patterns for model S, starboard antenna, at 20 MHz

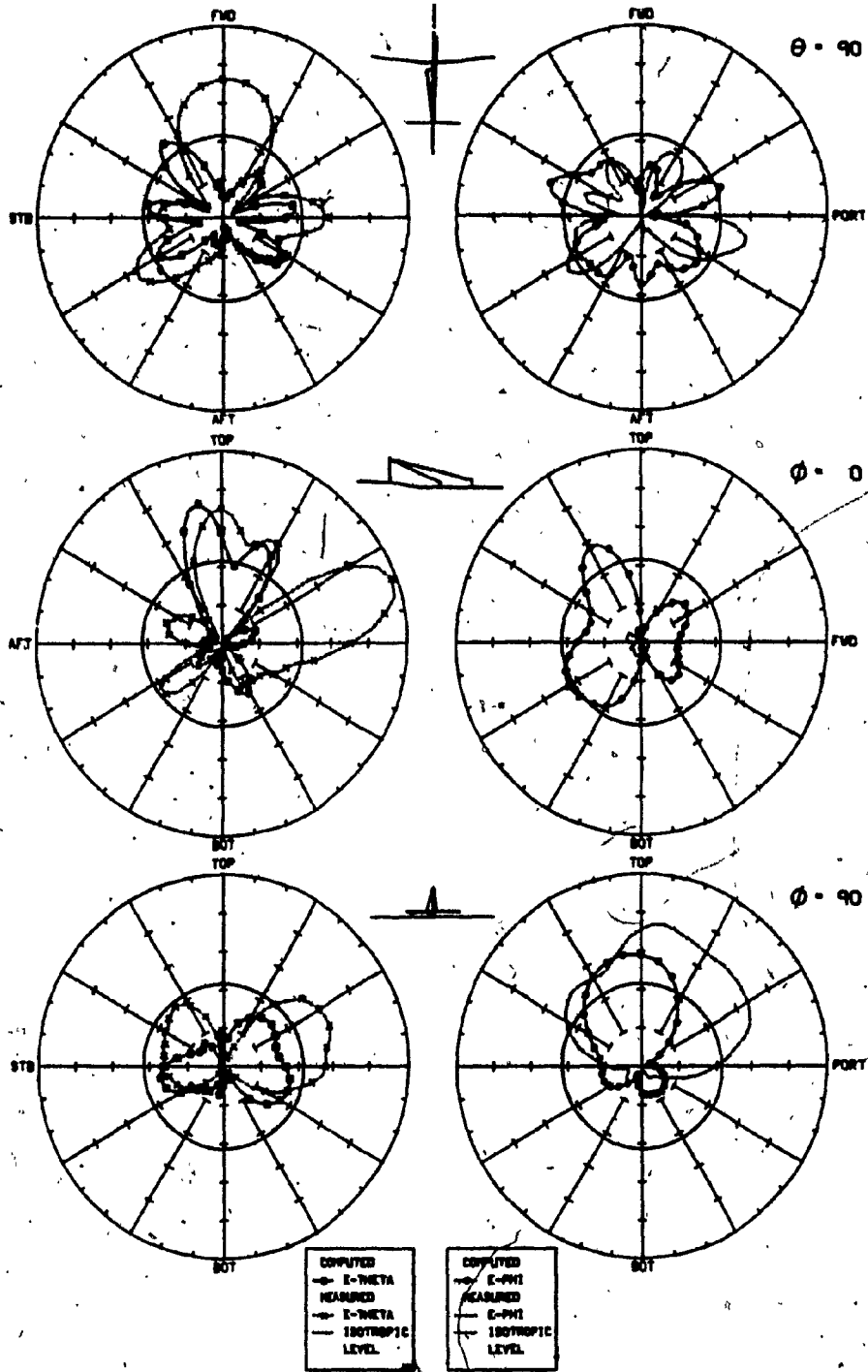


Fig. 64-continued. Comparisons of measured and computed principal plane patterns for model S, starboard antenna, at 24 MHz

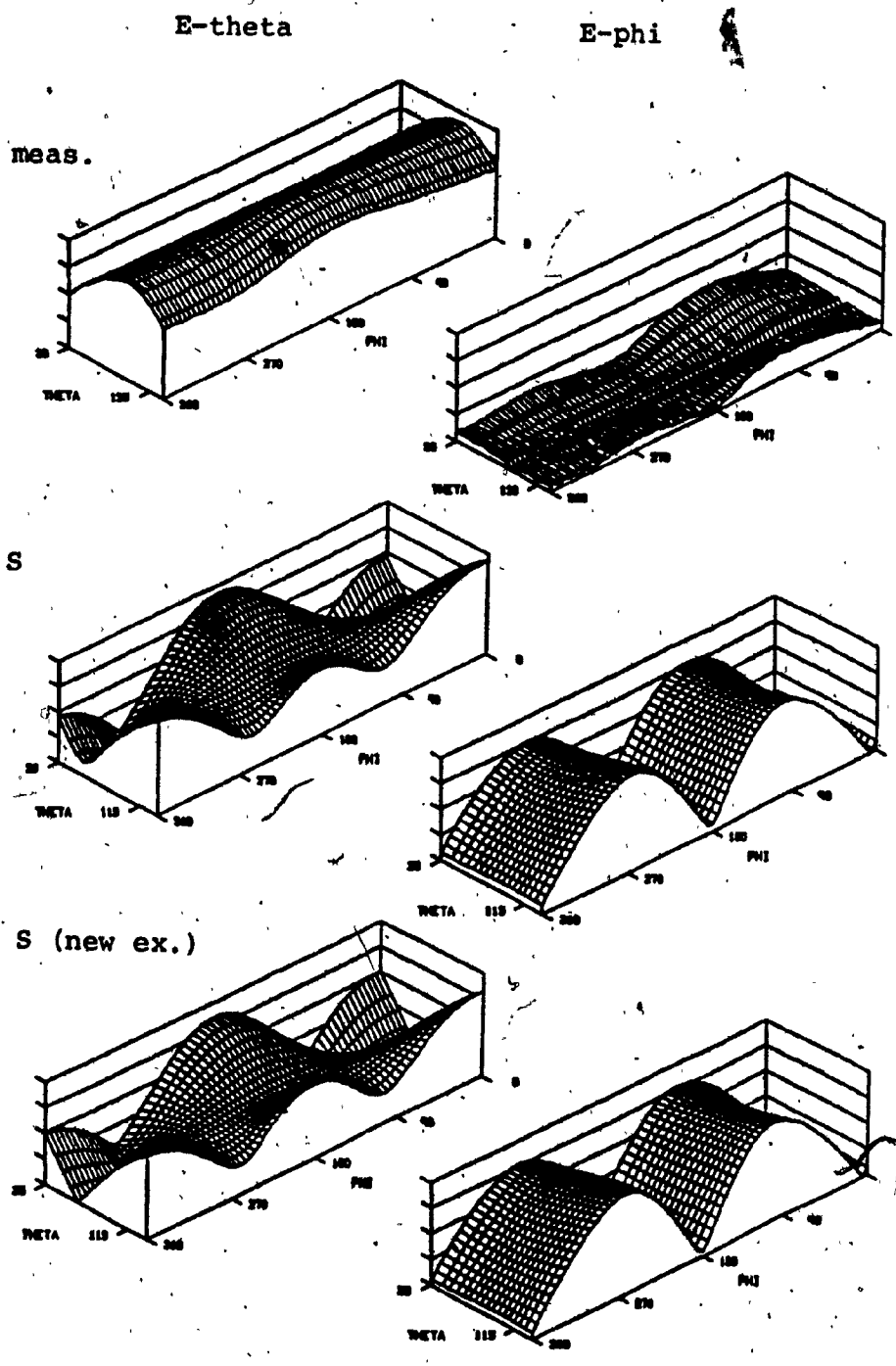


Fig. 65a. E-theta and E-phi altitude plots at 2 MHz, port antenna, measured and computed from model S with standard and new excitations

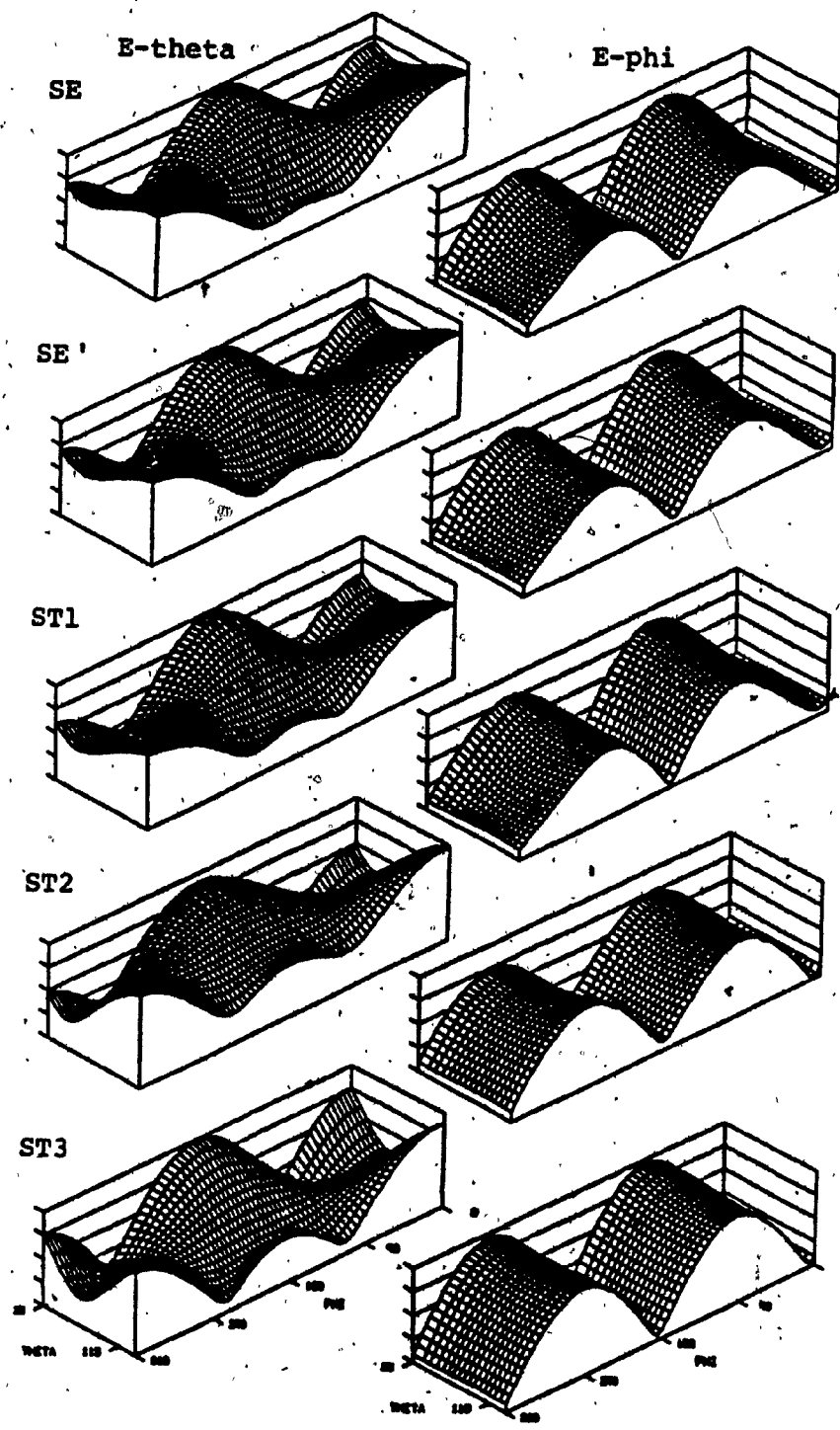


Fig. 65b. E-theta and E-phi altitude plots at 2 MHz, port antenna, computed from models SE, SE', ST1, ST2, and ST3

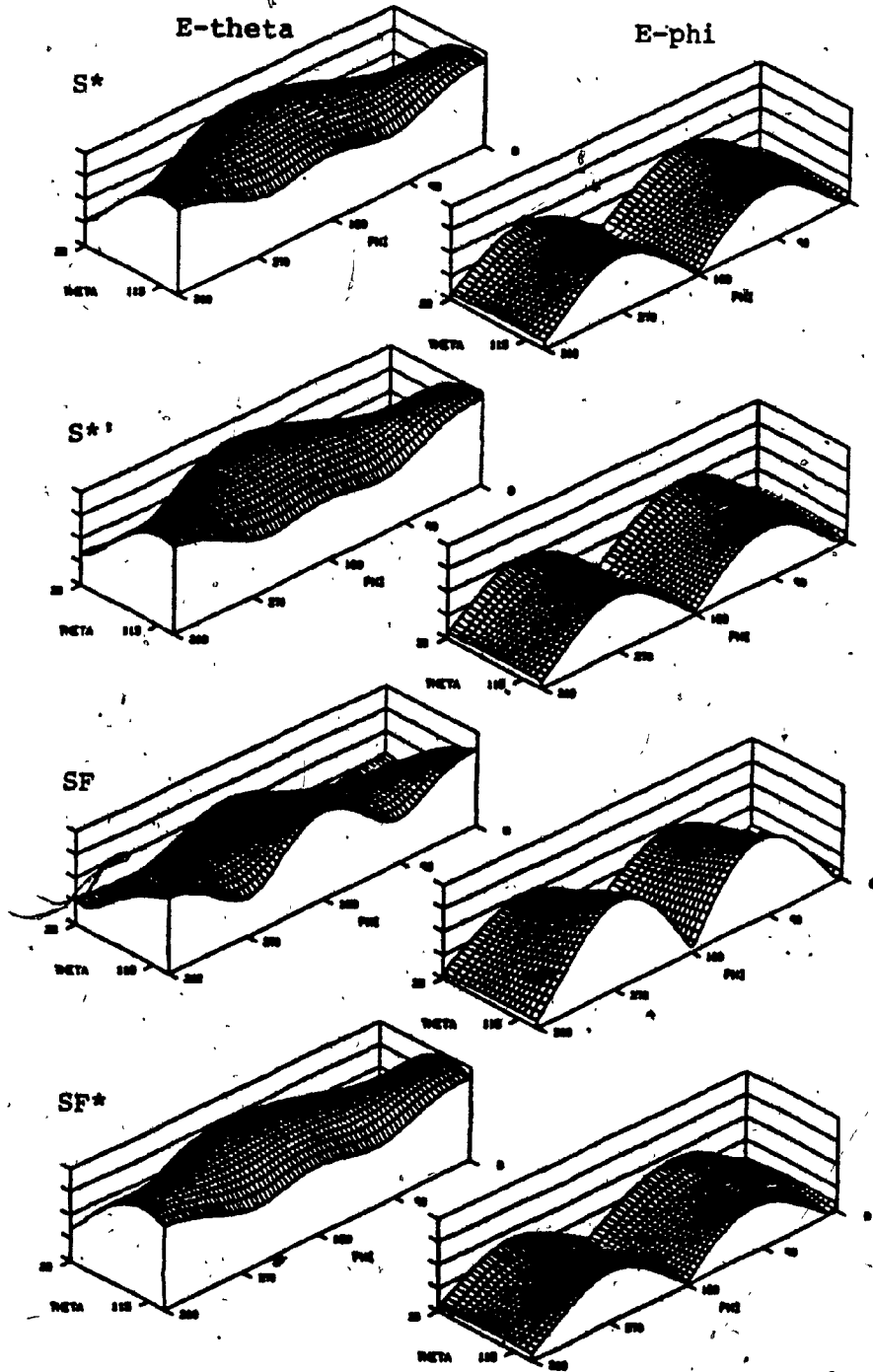


Fig. 65c. E-theta and E-phi altitude plots at 2 MHz, port antenna, computed from models S*, S*', SF, and SF*

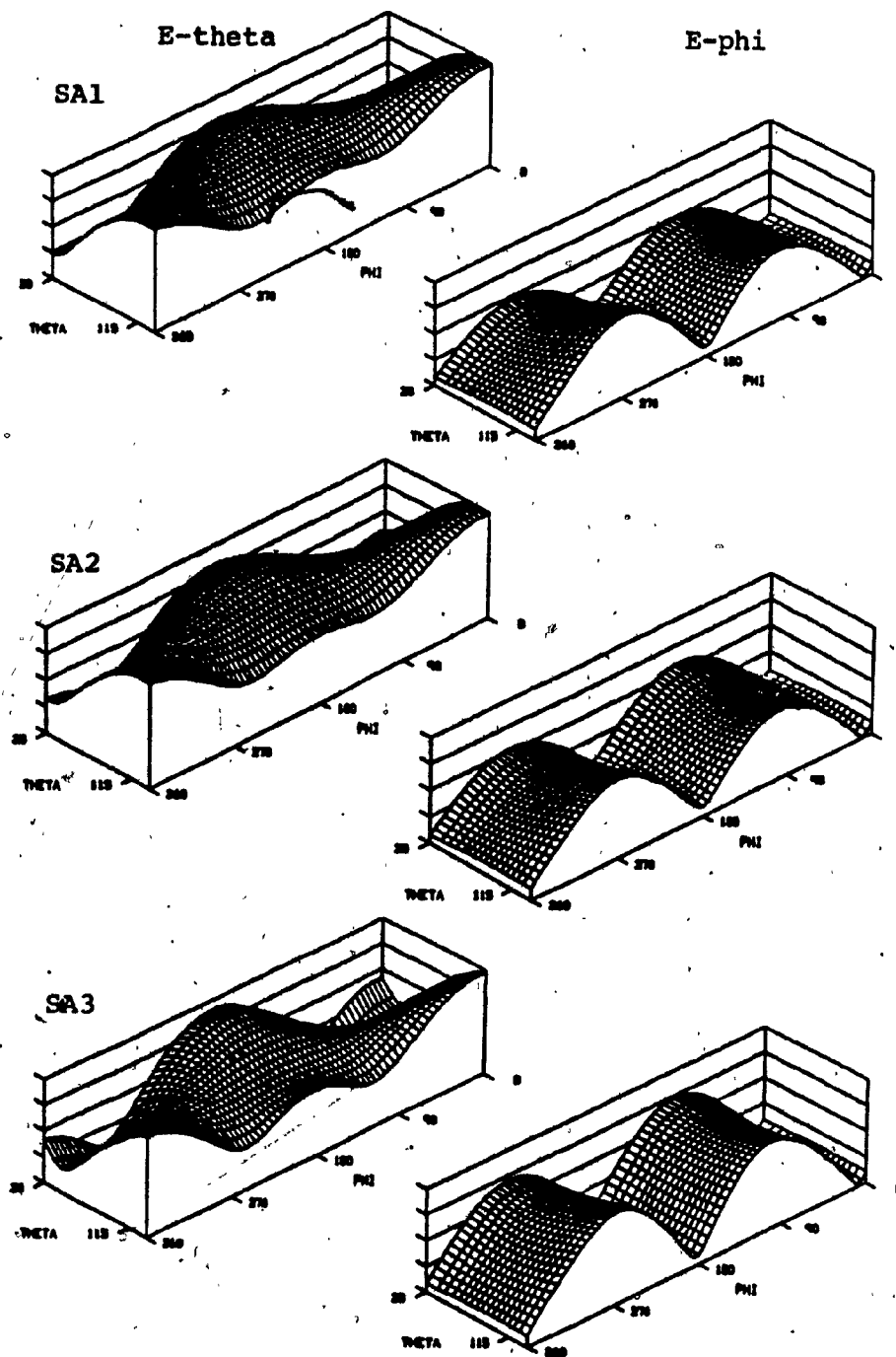


Fig. 65d. E-theta and E-phi altitude plots at 2 MHz, port antenna, computed from models SA1, SA2, and SA3

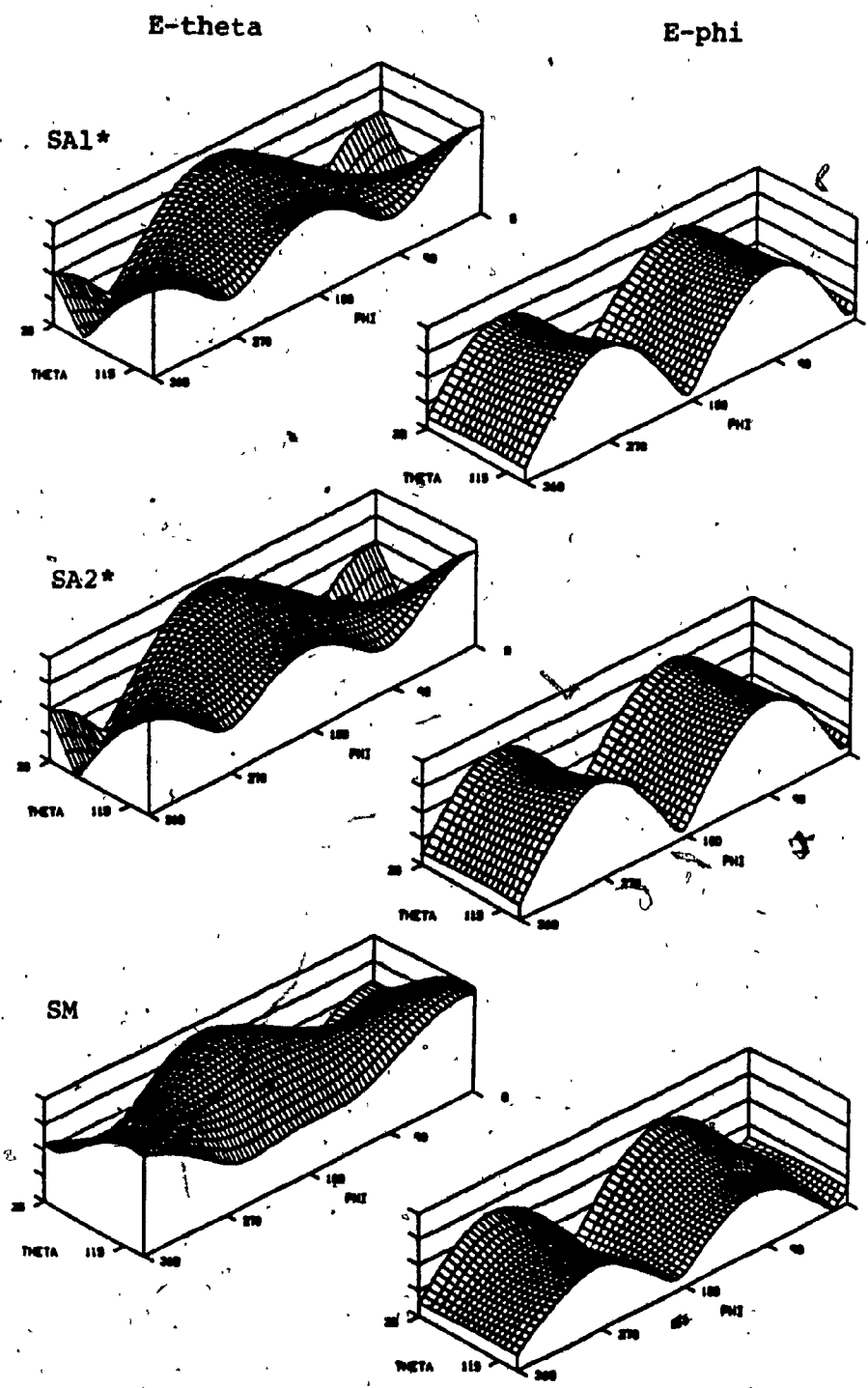


Fig. 65e. E-theta and E-phi altitude plots at 2 MHz, port antenna, computed from models SA1*, SA2*, and SM

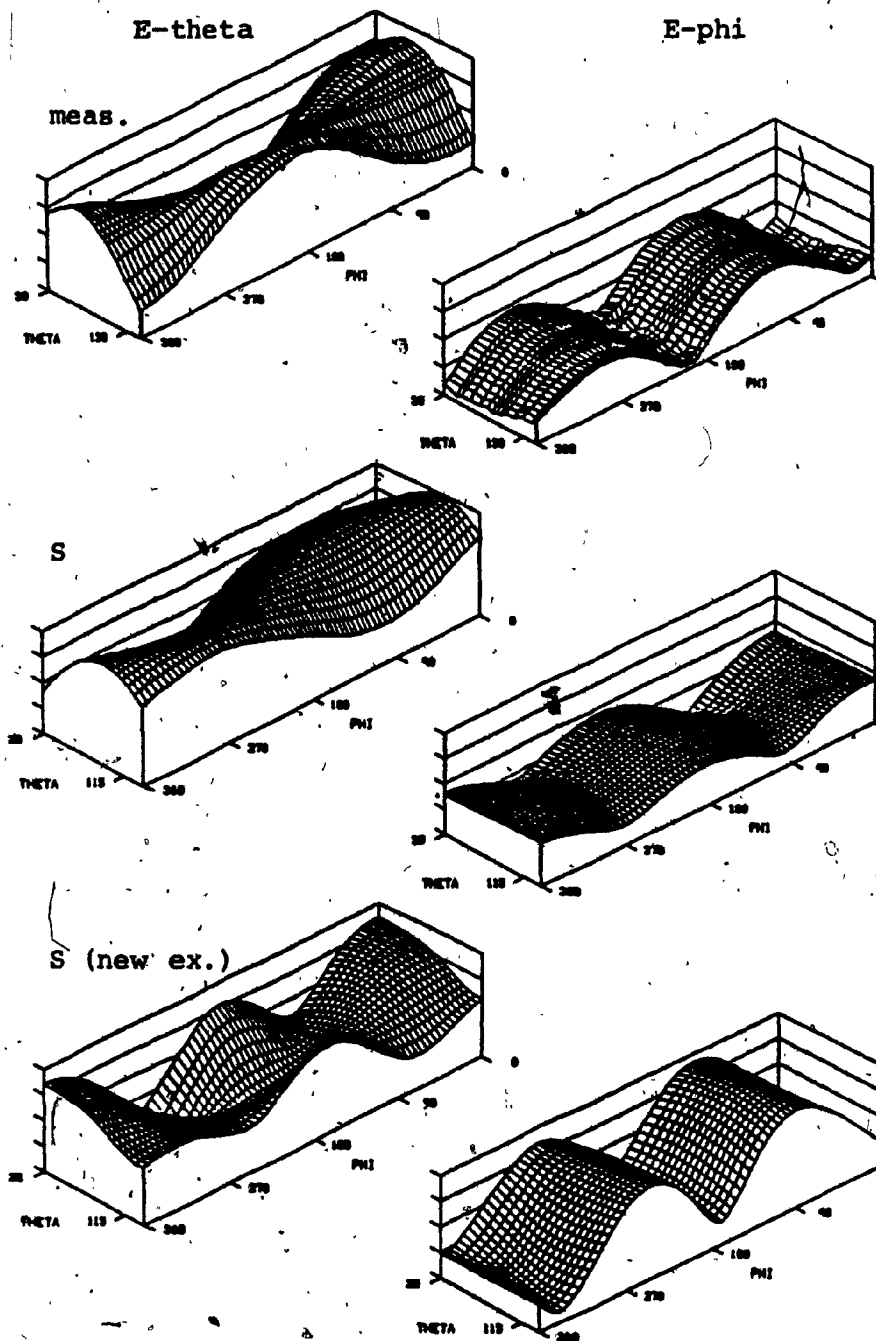


Fig. 66a. E-theta and E-phi altitude plots at 2 MHz, starboard antenna, measured and computed from model S with standard and new excitations

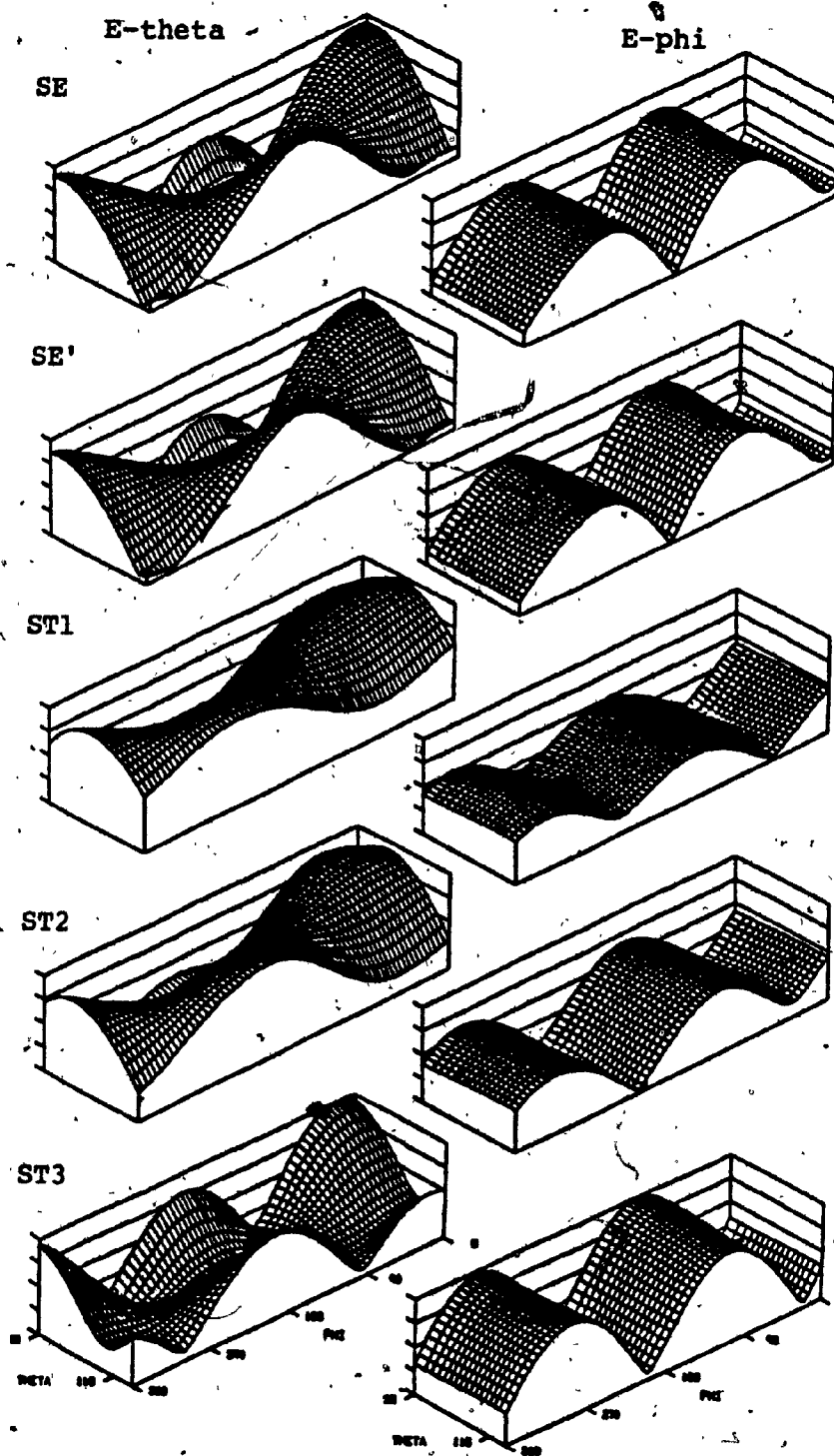


Fig. 66b. E-theta and E-phi altitude plots at 2 MHz, starboard antenna, computed from models SE, SE', ST1, ST2, and ST3

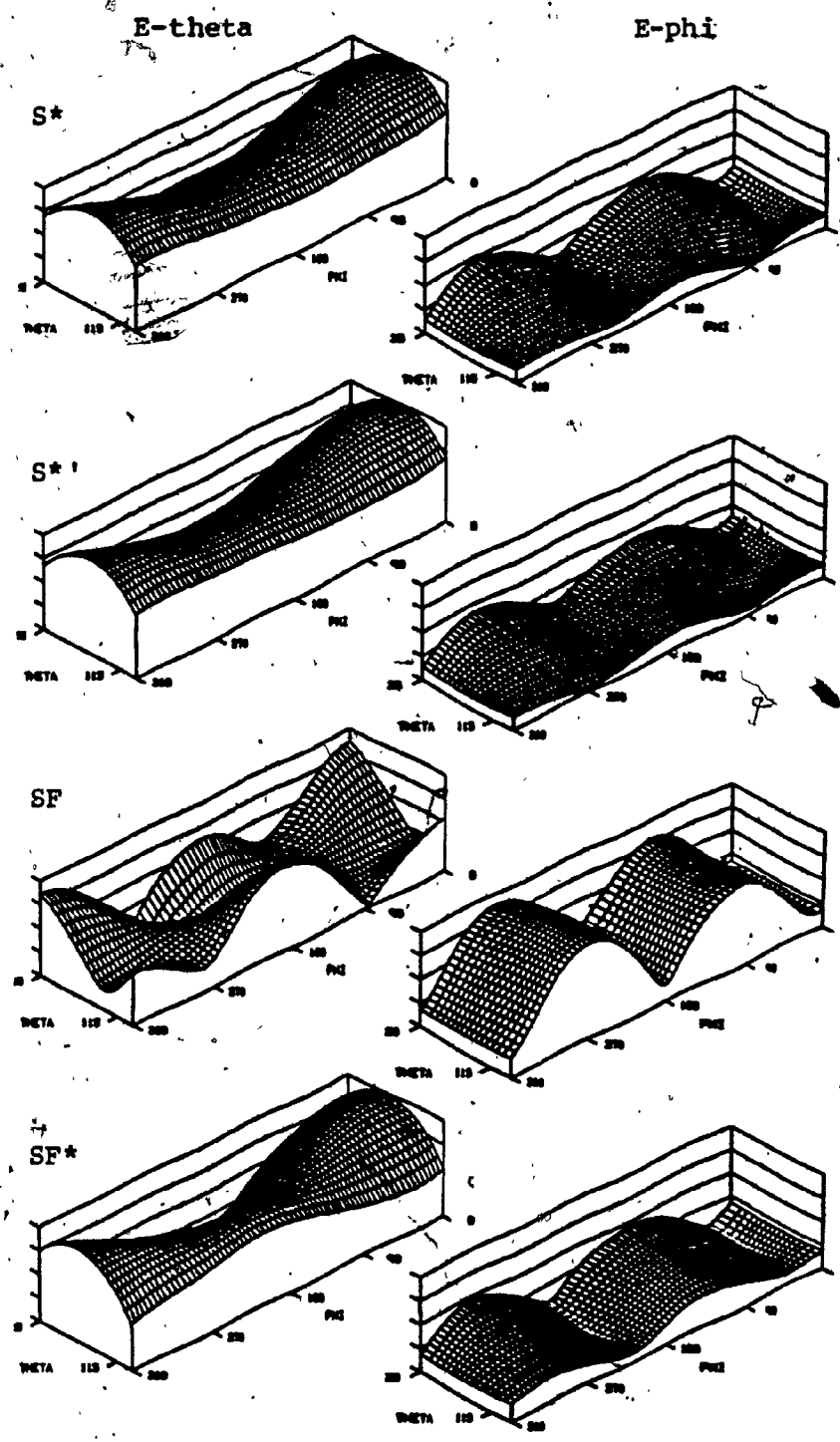


Fig. 66c. E-theta and E-phi altitude plots at 2 MHz, starboard antenna, computed from models S*, S*1, SF, and SF*

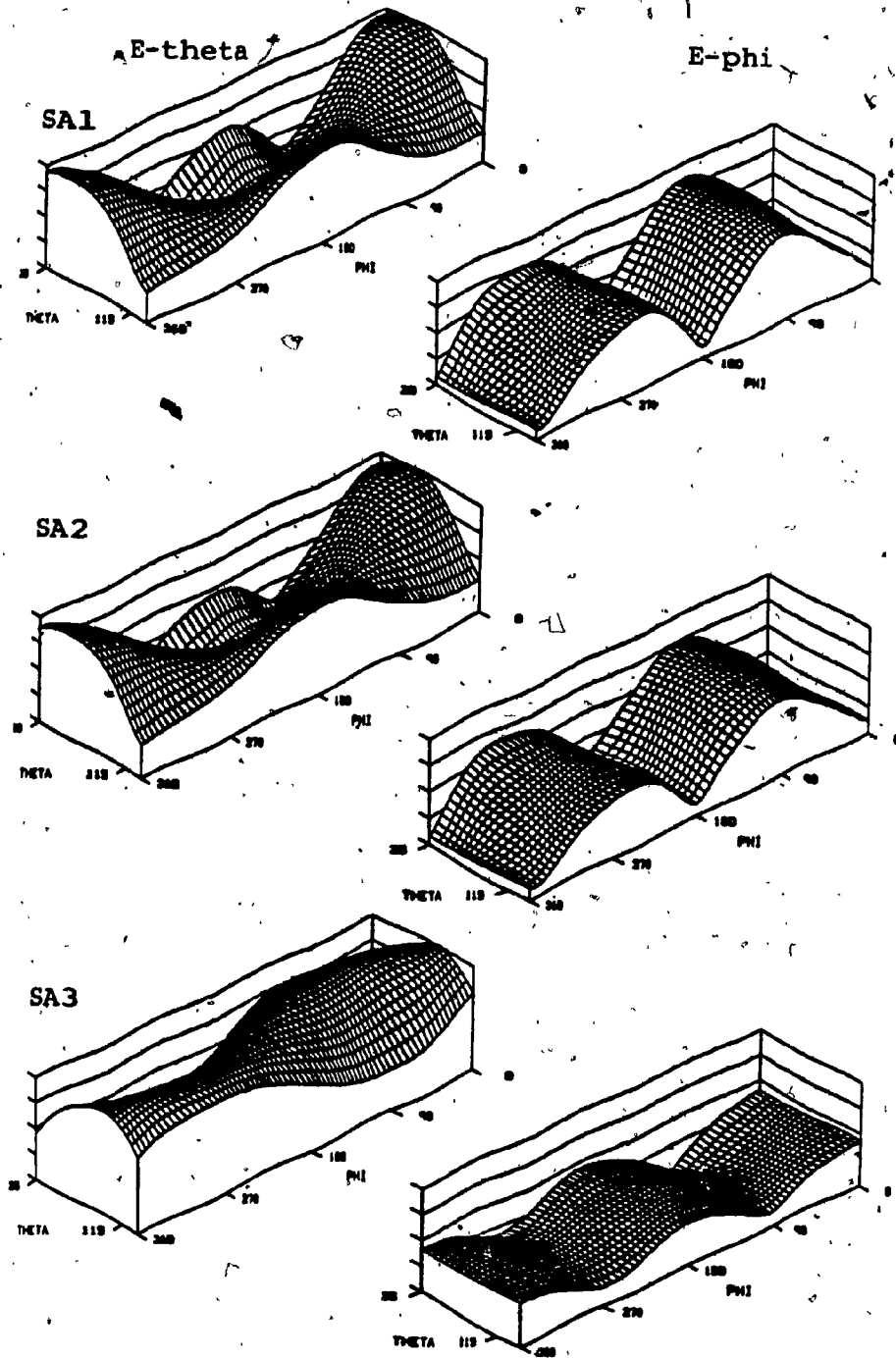


Fig. 66d. E-theta and E-phi altitude plots at 2 MHz, starboard antenna, computed from models SA1, SA2, and SA3

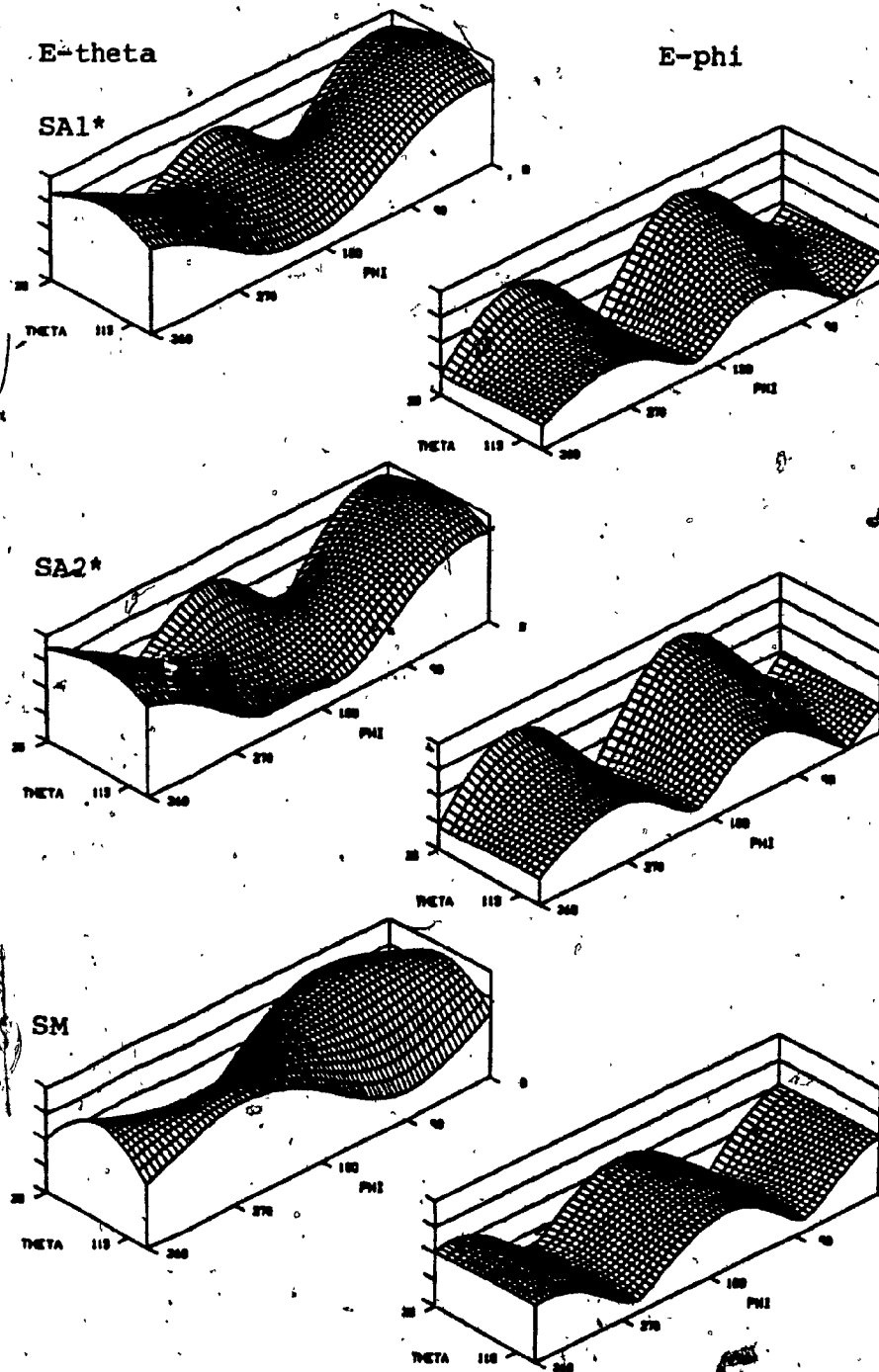


Fig. 66e. E-theta and E-phi altitude plots at 2 MHz, starboard antenna, computed from models SA1*, SA2*, and SM

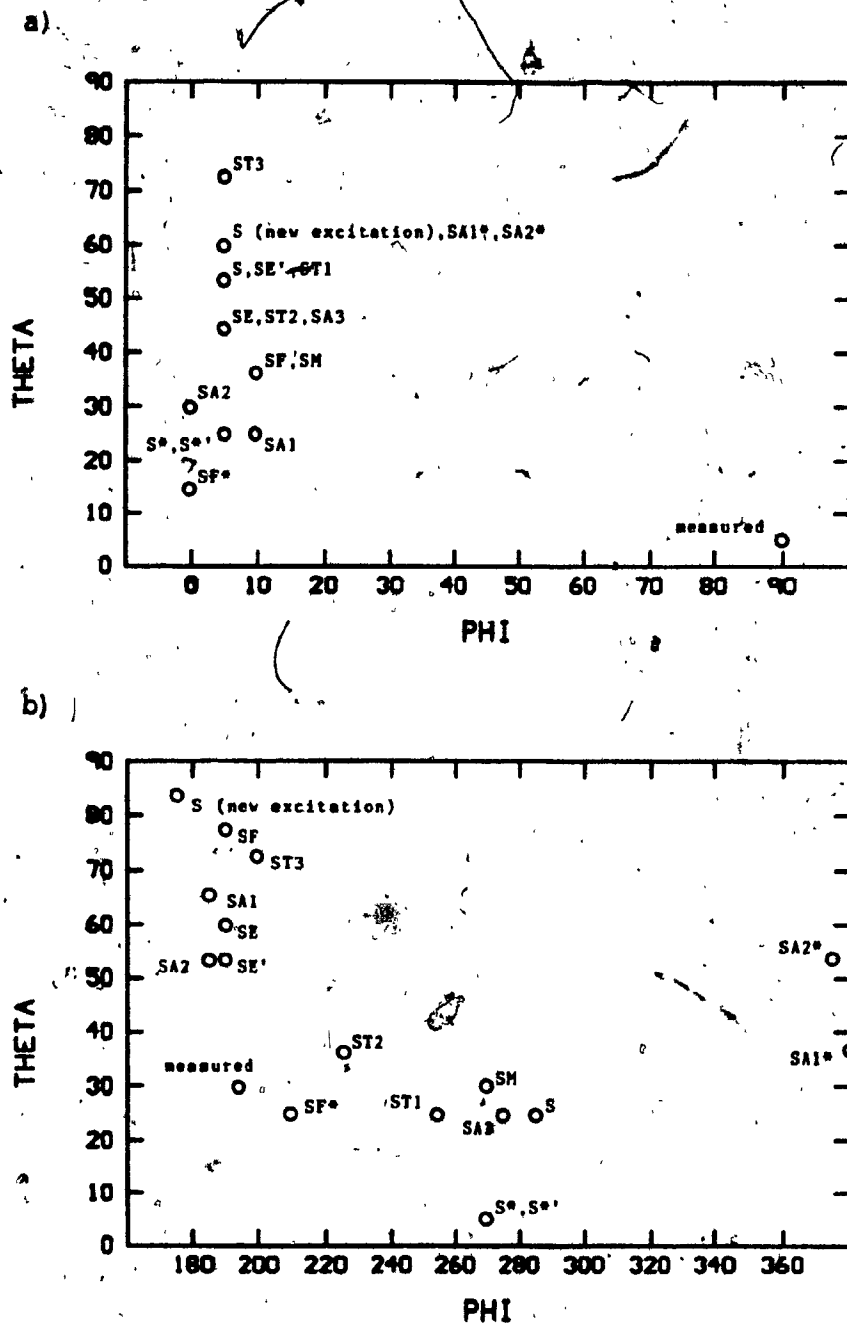


Fig. 67. Equivalent ideal dipole orientations of stick models at 2 MHz for port (a) and starboard (b) antennas

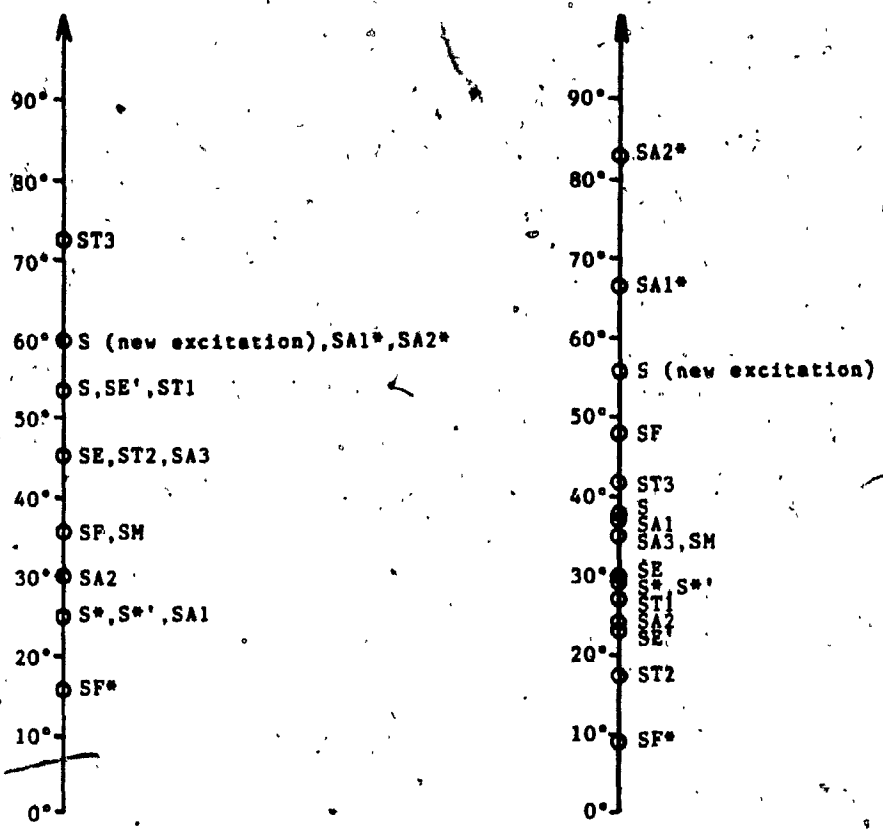


Fig. 68. Magnitudes of angular errors in equivalent ideal dipole orientations of stick models at 2 MHz, port and starboard antennas

Complex Models

In parallel with model S, model C was tested at 2-MHz increments up to 30 MHz. Typical running times were of the order of 750 CPU seconds. This time, drastically improved patterns were obtained at 2 MHz for both antennas, as testified by the MOVIE:BYU plots of Figure 69 (compare with Figure 62). Relative levels of the two polarizations are preserved, and the E-phi pattern for the starboard antenna is correctly oriented. To continue the comparison with model S, principal plane patterns at 2, 6, 20, and 24 MHz are provided in Figure 70 for the port antenna, and in Figure 71 for the starboard antenna. These show consistent improvement over the stick model and a degree of agreement in pattern detail that is required for system range analysis (Kubina, 1983b). Very good to excellent patterns were obtained throughout the HF range, with the exception of 22 and 24 MHz where results were fair.

Optimized complex models were tested at 2 MHz and at the critical frequency of 24 MHz for lower- and higher-frequency tests. The results at 2 MHz are presented once again as equivalent ideal dipole orientations in Figure 72. The same scales as in Figure 67 are used to show the contrast with optimized stick models. Complex models performed well, and the points are this time more concentrated around the point of measurements. Three models, including

model C, actually coincide with the measurements for the port antenna, but this does not occur for the starboard antenna, for which the results once again appear more unstable. The available patterns in the data files allowing for little resolution in the placement of the points, it becomes hazardous to make judgments on the sole basis of these plots, but important observations can still be made.

Figure 72 indicates, as it did for the stick models, that an increase in the radius of the feed element does not affect the radiation pattern by the fact that models C and C' have coincident points. Model CE, on the other hand, is considerably shifted from model C, probably because it features the only optimization that displaced the antennas. It appears as the least successful of the complex models series. Model CF shows a small shift from measurements for the port antenna, but good agreement for the starboard antenna, with the best ϕ value so far. Model CD coincides with measurements for the port antenna; for the starboard antenna it exactly matches the ϕ value but shows a disturbing upward shift in θ . Hence the absence of CHECK errors in the last two models did not bring overall improvements to already remarkable patterns, and therefore complex models appear to be surprisingly tolerant of NEC incompatibilities.

At 24 MHz, the results can be summarized as follows: no change for model C', and little change for model CE. Model CF, however, introduced large pattern changes, beneficial for the port antenna, and inconclusive for the starboard antenna. Model CD yielded similar results to those of model CF. The best illustration of improvement appears in the principal plane patterns of Figure 73 for model CD, port antenna. It seems that some NEC incompatibilities of model C that were removed in model CF have had a detrimental effect at that particular frequency.

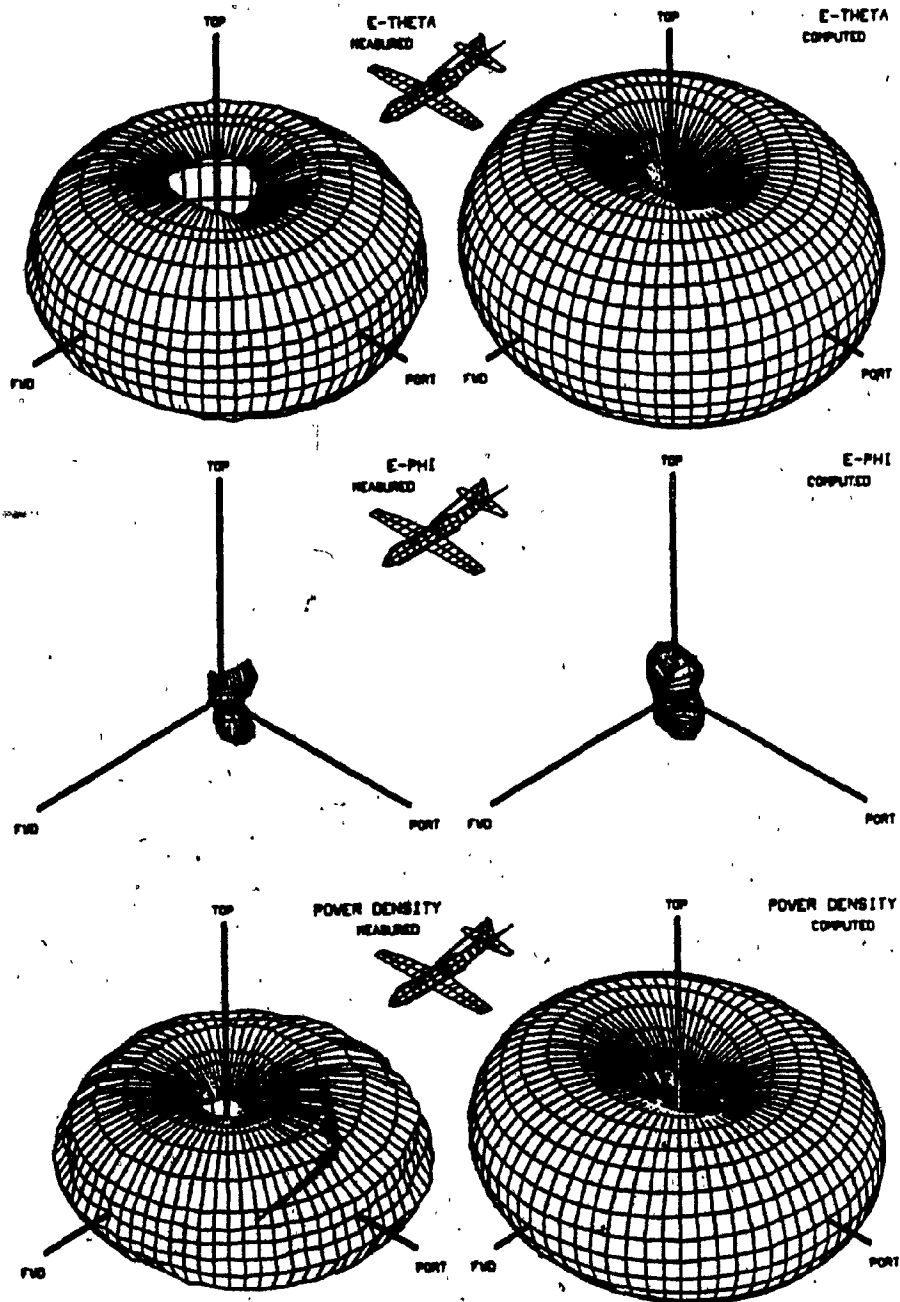


Fig. 69a. MOVIE.BYU plots of radiation patterns for the CP-140 port antenna at 2 MHz, measured and computed from model C.

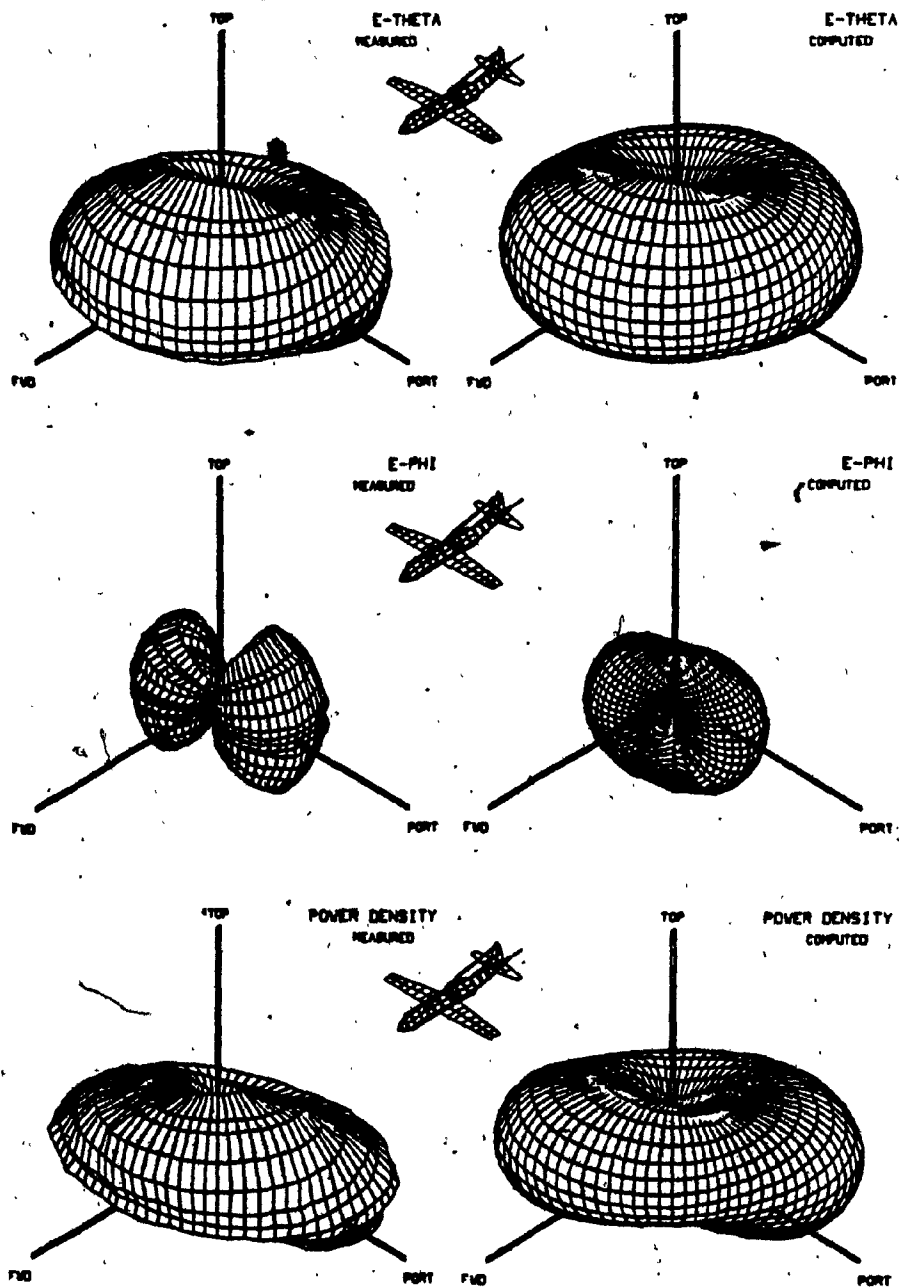


Fig. 69b. MOVIE.BYU plots of radiation patterns for the CP-140 starboard antenna at 2 MHz, measured and computed from model C.

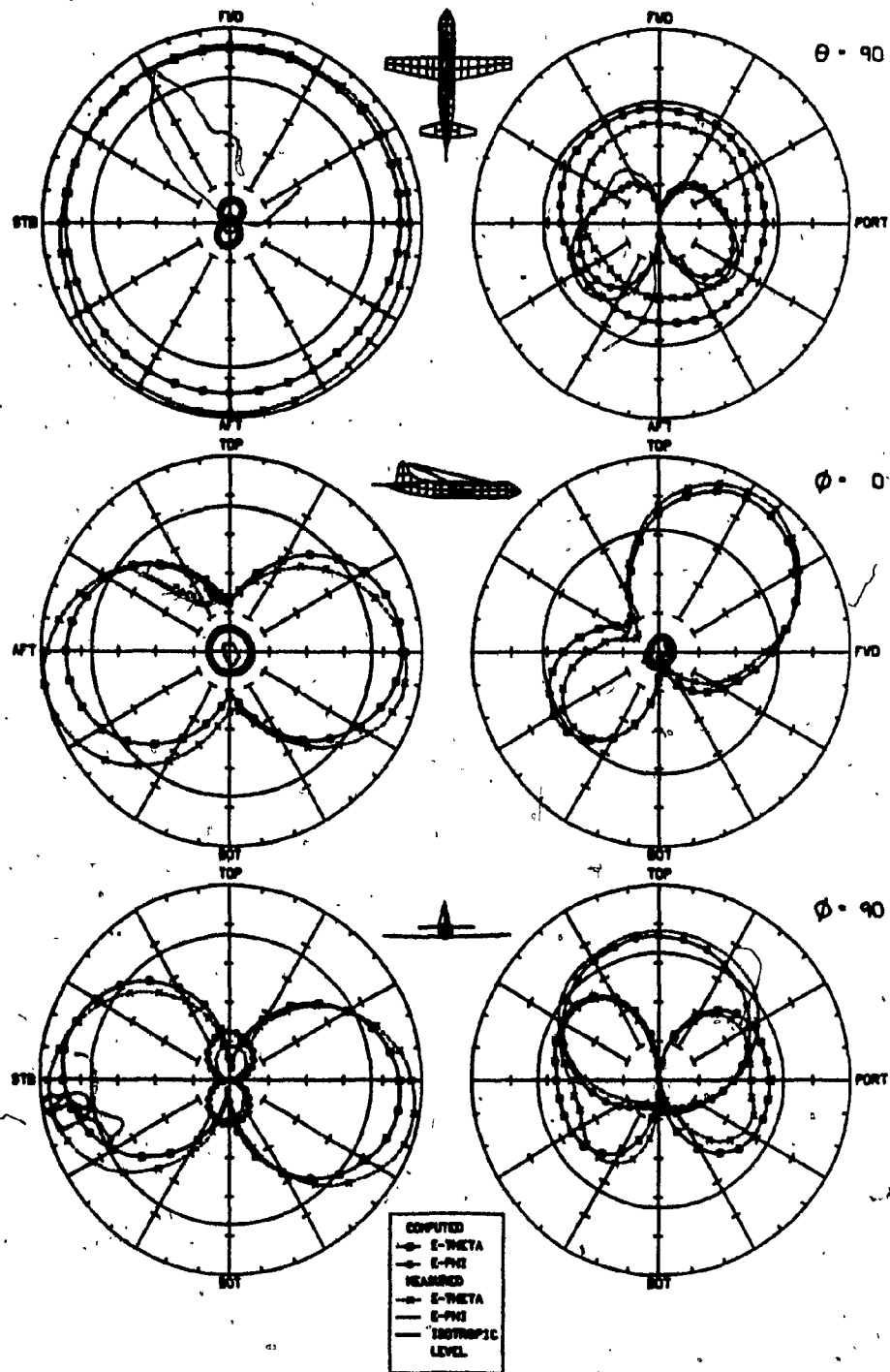


Fig. 70. Comparisons of measured and computed principal plane patterns for model C, port antenna, at 2 and 6 MHz

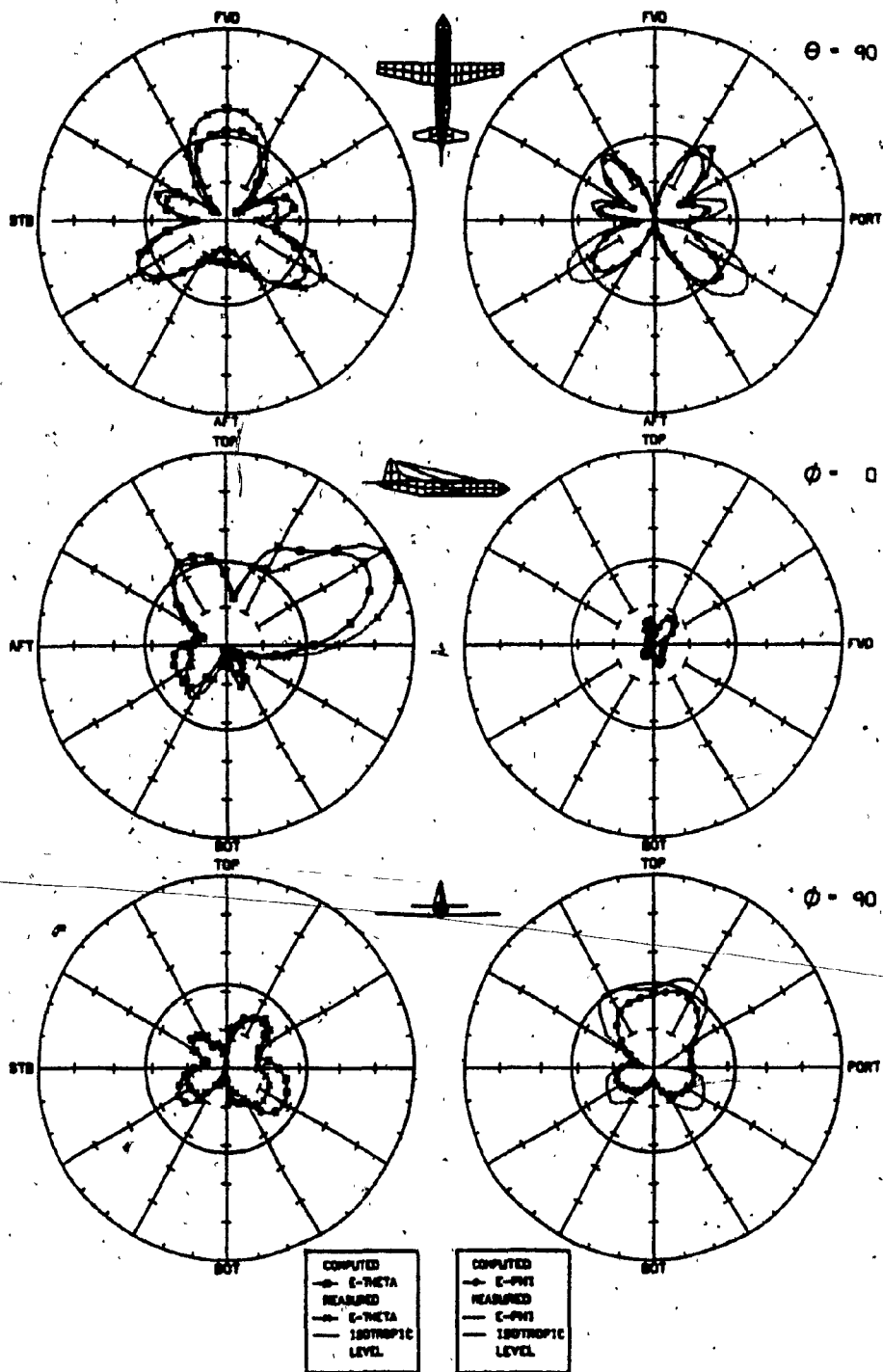


Fig. 70-continued. Comparisons of measured and computed principal plane patterns for model C, port antenna, at 20 MHz

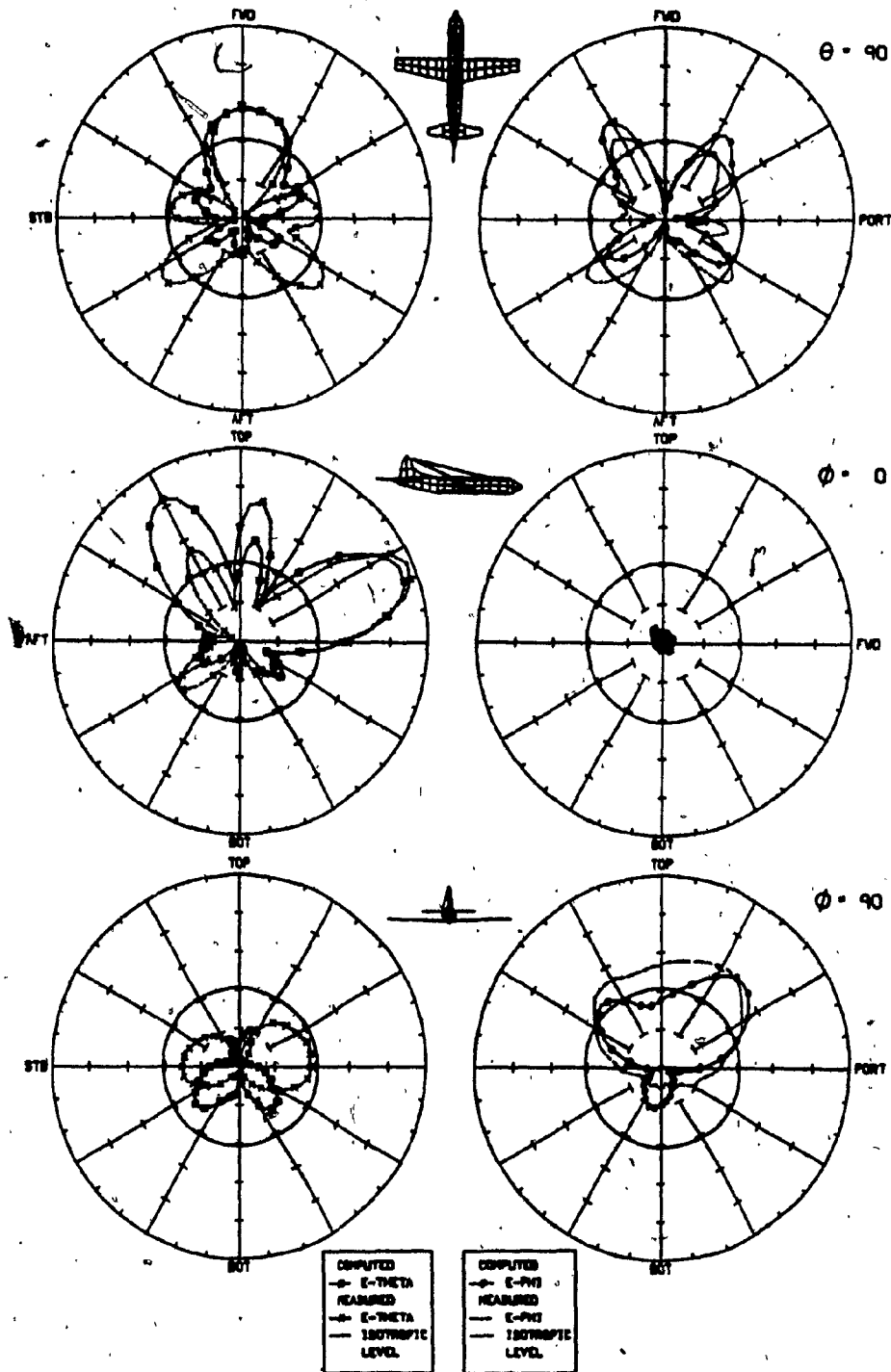


Fig. 70-continued. Comparisons of measured and computed principal plane patterns for model C, port antenna, at 24 MHz

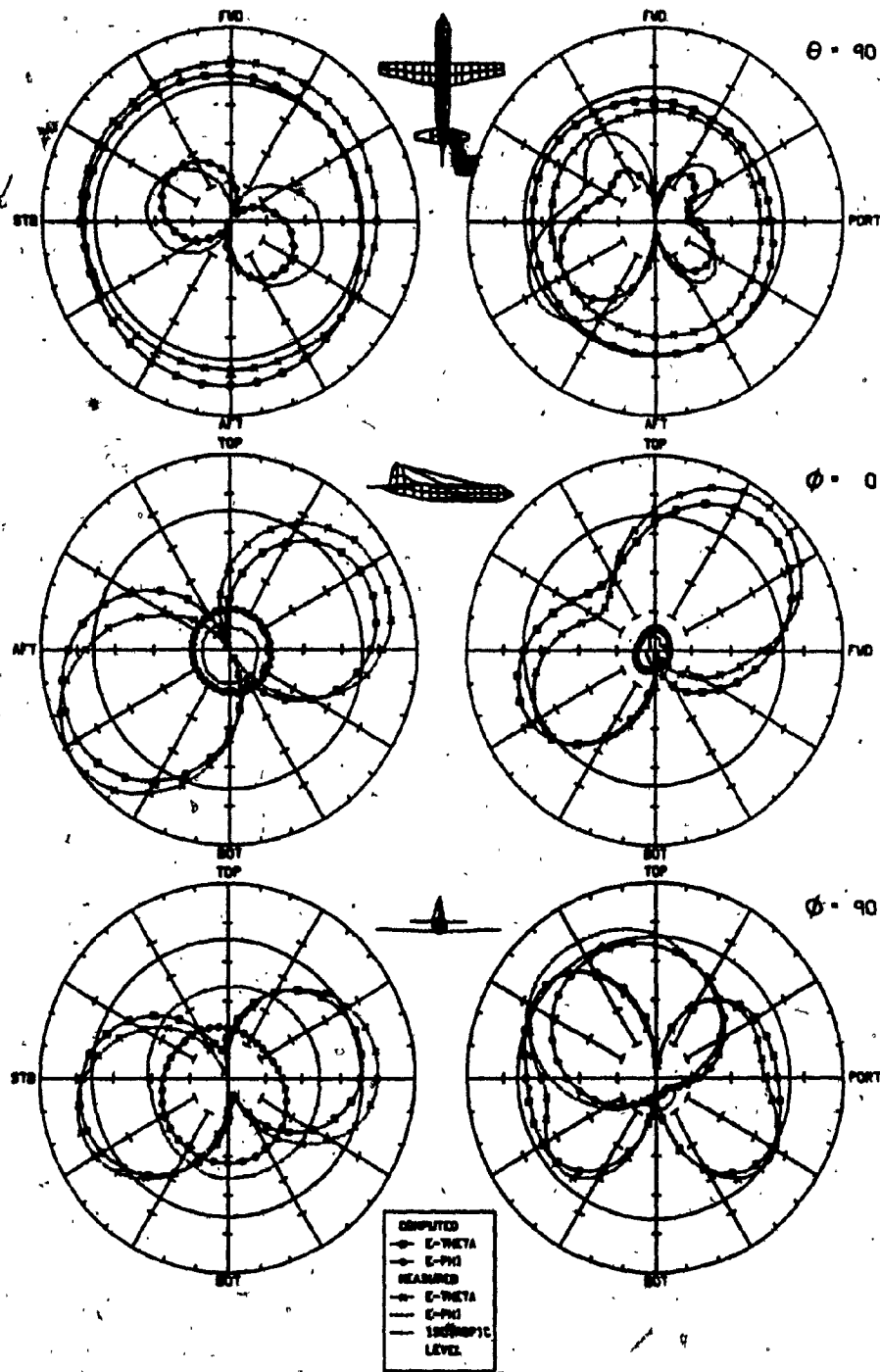


Fig. 71. Comparisons of measured and computed principal plane patterns for model C, star-board antenna, at 2 and 6 MHz

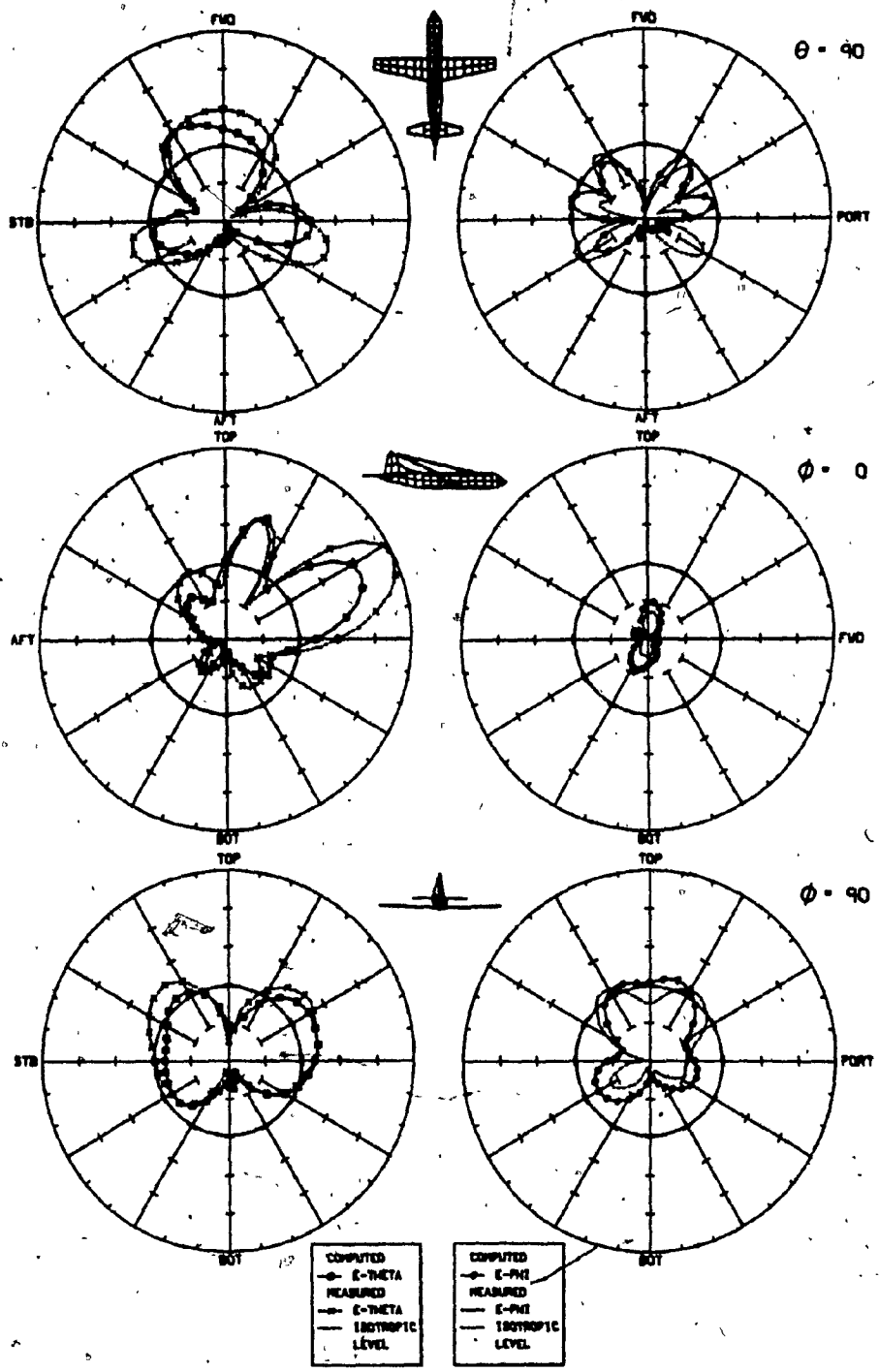


Fig. 71-continued. Comparisons of measured and computed principal plane patterns for model C, starboard antenna, at 20 MHz

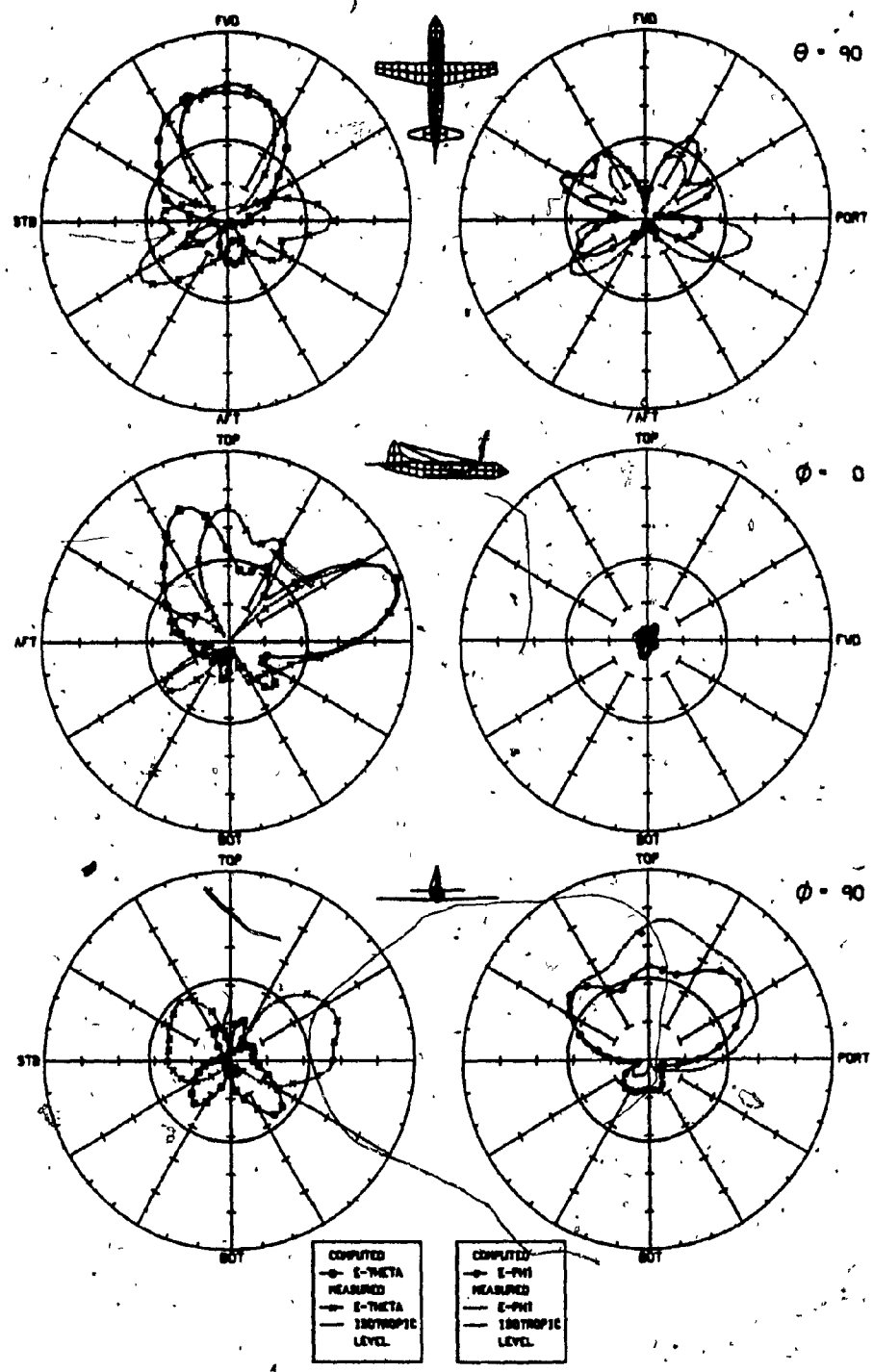


Fig. 71-continued. Comparisons of measured and computed principal plane patterns for model C, starboard antenna, at 24 MHz

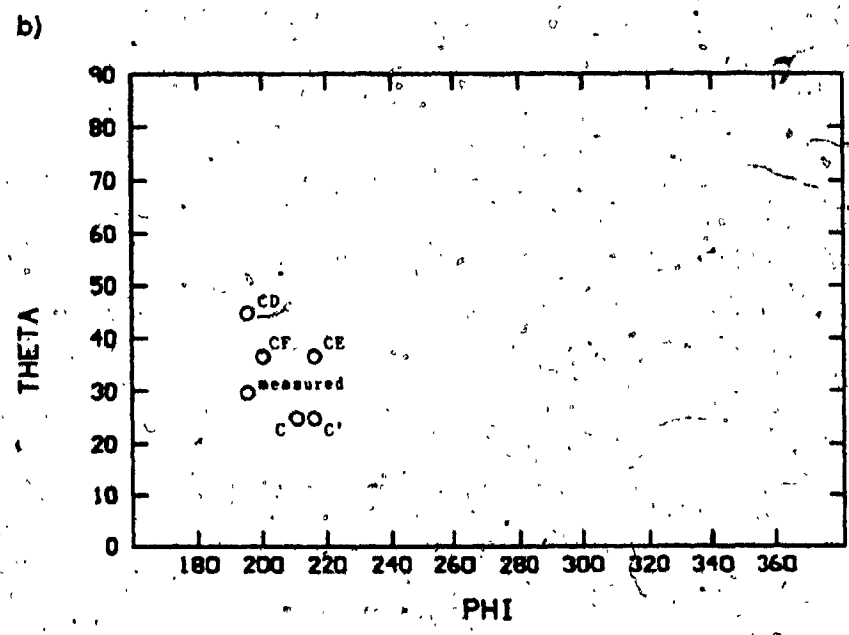
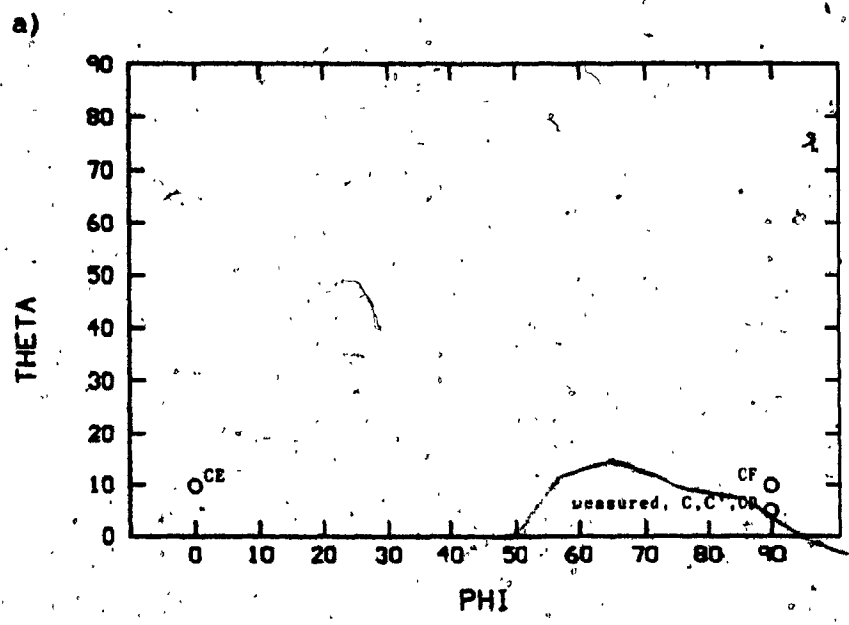


Fig. 72. Equivalent ideal, dipole orientations of complex models at 2 MHz for port (a) and starboard (b) antennas

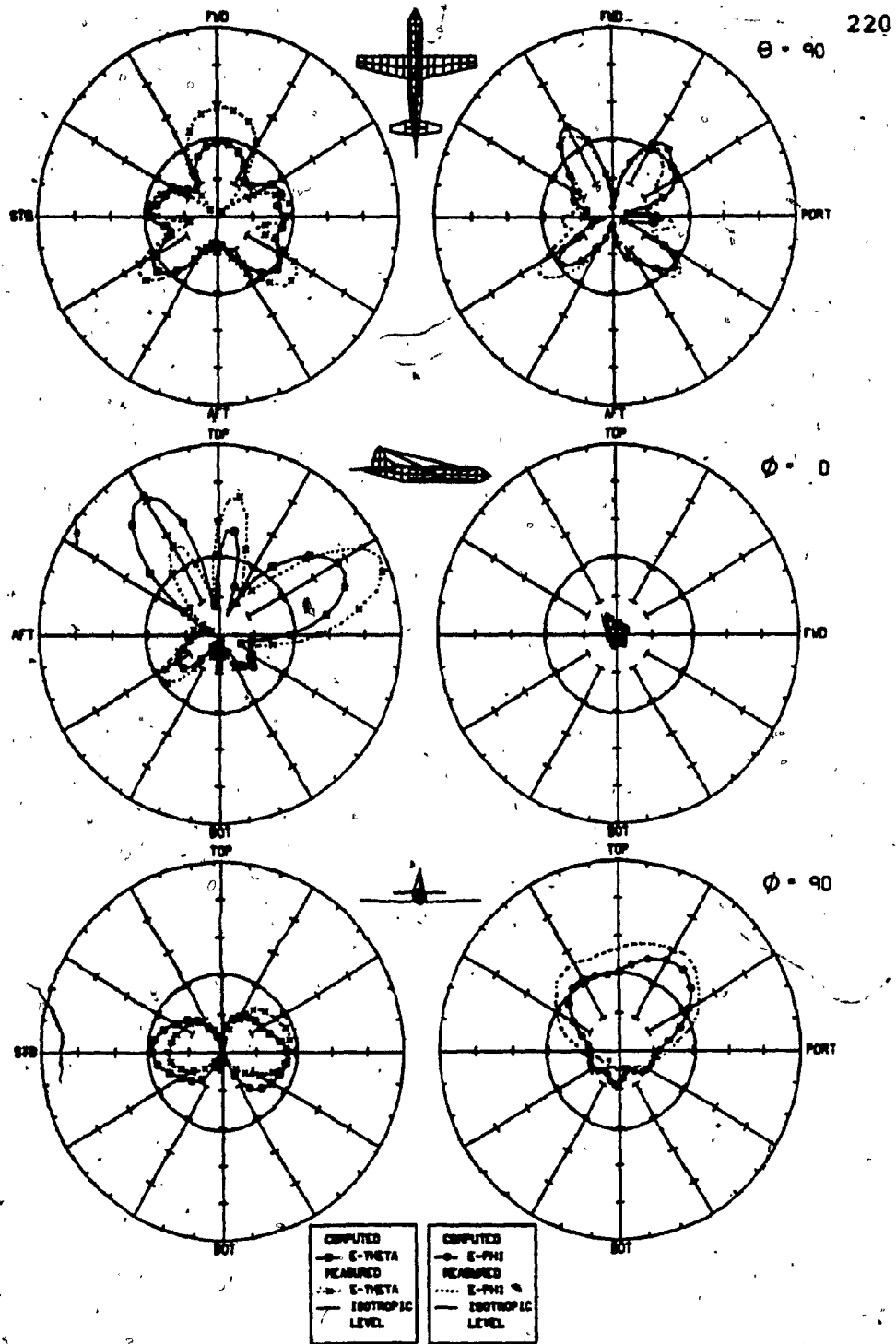


Fig. 73. Comparisons of measured and computed principal plane patterns of model CD, port antenna, at 24 MHz

Miscellaneous Tests

Three special tests on a CP-140 model were made that are of interest and will be described here. Model S was chosen for computing economy, and the starboard antenna at 6 MHz was selected because of the satisfactory results obtained under those conditions.

In the first test, MININEC was executed on the EMC laboratory CROMEMCO system to generate the standard set of patterns. This permitted direct comparison with NEC results as shown in Figure 74. The measured altitude plots are followed by those computed by NEC and MININEC respectively. The MININEC plots look somewhat smoother than the NEC ones and hence the lobe structure is not reproduced as well. The differences are nevertheless slight, unlike what was suggested by the first reporting of the author on this test run (1985a). In that report, an error in stripping the MININEC output file had resulted in squaring the electric fields, giving the illusion of a large deviation from the NEC results and a consequent poor agreement with measurements.

The small differences between NEC and MININEC patterns can be accounted for by the use of different basis and weighting functions, but also by the enforcement of different constraints at wire junctions. In the present case the latter factor is of special importance, considering the severe incompatibilities of model S at certain wire junc-

tions. In this context the results of the MININEC test run must be viewed as very encouraging. It can be expected that models satisfying the modelling guidelines will produce nearly identical results irrespective of the antenna modelling program used. The advantages of using the laboratory-owned CROMEMCO system can then be exploited.

The importance of the two remaining tests stems from the necessity of flying the CP-140 at sometimes very low heights above sea surface. This condition was modelled by raising as necessary the coordinates of model S above $z=0$ level, and by specifying a perfect ground plane in the NEC control section. The lowest point of model S, taking into account radius values, was brought to heights of 1 m and 30 m above the x-y plane. The results are shown as altitude plots in Figure 75. For direct comparison, the patterns of model S in free space are shown only from $\theta = 0$ to 90 degrees, followed by the patterns obtained at 1 m and 30 m above sea level respectively. Both ground plane tests show E_{ϕ} vanishing at $\theta = 90$ degrees due to the electric field boundary condition at the surface of a conducting medium. The patterns at 1 m show some resemblance to the free-space patterns, but at 30 m appears a succession of peaks and nulls along the θ range.

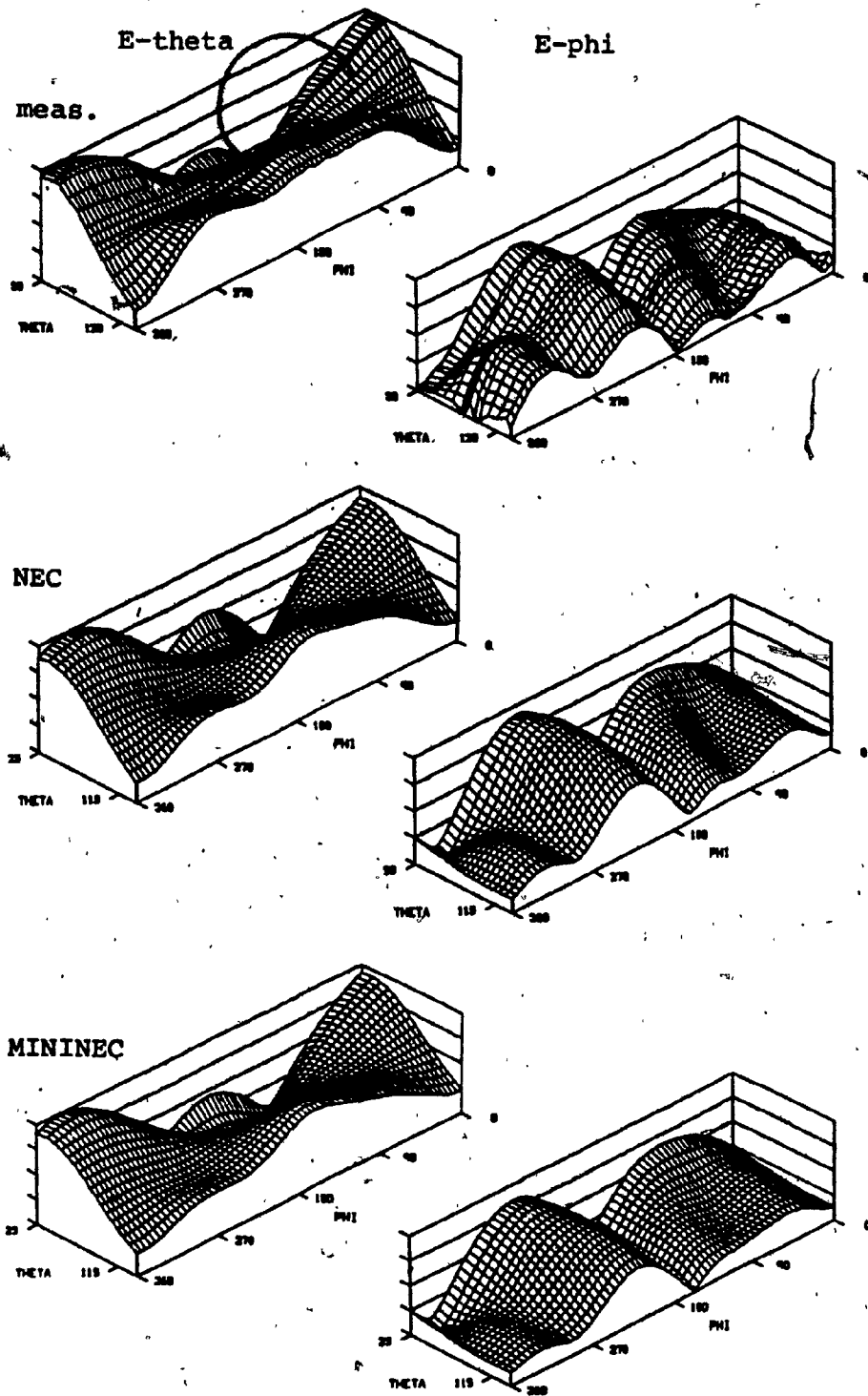


Fig. 74. E-theta and E-phi altitude plots at 6 MHz, starboard antenna, measured and computed from model S with NEC and MININEC

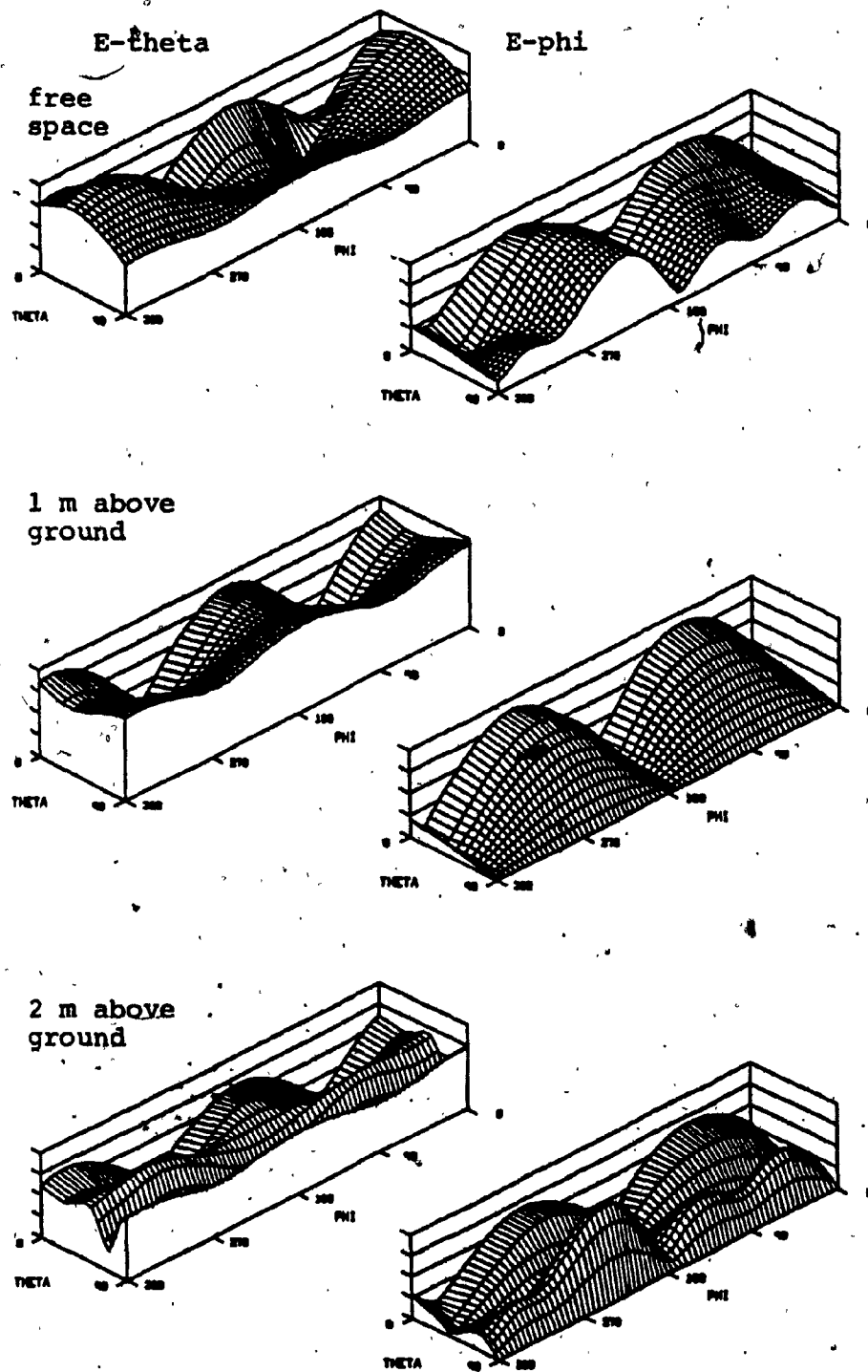


Fig. 75. E-theta and E-phi altitude plots from model S at 6 MHz, starboard antenna, in free space and at 1 m and 30 m above ground

E-theta and Impedance

Figure 76 compares the E-theta values obtained from the frequency sweeps on models S and C with the experimental values. The curves can be misleading due to the sparsity of experimental points, but for both port and starboard antennas, the complex model tracks best the measured curve. This of course reflects the fact that the complex model produces better radiation patterns, but does not in itself constitute a proof as did the equivalent ideal dipole orientations.

Impedance curves computed from model S are compared to the experimental curves in Figure 77. The general variation of amplitude with frequency is reproduced and can be understood by visualizing the antenna and top surface of the fuselage as a section of transmission line terminated in an open circuit. Hence the regularly spaced resonances occurring when the antenna length is a multiple of a half-wavelength. The loss exhibited by the behavior of the resistance curve is characteristic of a moderately lossy transmission line and is due to radiation. "Bumps" in the resistance curves occur in the vicinity of 4 MHz, the first resonant frequency of an anti-symmetric mode of the airframe (Granger and Bolljahn, 1955).

Thus the port antenna, whose true length is 771 inches, is expected to first exhibit resonance at 7.7, 15.3, 23.0, and 30.6 MHz. The starboard antenna, at 508 inches,

is expected to first resonate at 11.6, 23.3, and 34.9 MHz. The measured resistance peaks, which occur at resonance, are seen to be actually lower in frequency than predicted above. The possible causes of this phenomenon and the ways to account for them will be discussed in later paragraphs.

In model S, antenna lengths are slightly above the true values because of various stick model approximations, and effective lengths are further increased by the unusual lengths of the feed elements. Including half of the feed elements brings the antenna lengths to 835 and 556 inches respectively. Hence resonances are expected at 7.1, 14.1, 21.2, and 28.3 MHz for the port antenna, and at 10.6, 21.2, and 31.9 MHz for the starboard antenna. Examination of the computed resistance curves confirms well these values.

One of the objects of stick model optimization was the improvement of input impedance values at 2 MHz. Results from all models are plotted together in Figure 78 on two Argand diagrams, one for each of the port and starboard antennas. The first peculiar characteristic of some impedance values is the negative resistance, which becomes especially large for the starboard antenna. No common characteristic emerges from the models concerned. Closer examination of the plots will permit one to draw conclusions of a general order. As noted before in Chapter V, impedance agreement does not seem to have any relation to pattern agreement, as

the thin model (ST3) produced the best resistance values. Moreover, although it would leave radiation patterns unchanged, increasing the radius of the feed element did affect the input impedance by decreasing the reactance component. This is clear from the SE-SE' and S*-S*' model pairs. Model ST2 produced the overall best impedance agreement. As a final note, model S* and other models optimized along the same lines (those models with the "**") consistently produced the lowest reactance values.

Figure 79 compares the impedance curves obtained from model C with the experimental ones. Antenna lengths on the complex model are closer to reality with 785 and 501 inches respectively, including half of the small 1-foot feed elements. This suggests higher resonant frequencies of 7.5, 15.0, 22.6, and 30.1 MHz for the port antenna, and of 11.8, 23.6, and 35.4 MHz for the starboard antenna. This once again is confirmed by the computed resistance peaks, and increases further the offset from the measured resistance peaks, mysteriously shifted left from the expected positions. Investigation was made to determine if some physical factor had not been accounted for in the wire-grid modelling of the antennas. Indeed several factors were identified that could have brought an additional capacitive effect. Among these was the possible connection of lightning arresters near the feed points, the dielectric coating around the

antennas, and the stand-off insulators that shield the antennas from the surface of the fuselage. To account for the above, correction was brought to the impedances of model C by shunting them with a small capacitance, originally estimated from antenna specifications at several picofarads.

Figure 80 shows the result of shunting port antenna impedances with 15 and 30 pF respectively. Improvement is already apparent with 15 pF, the computed curves shifting to the left. With 30 pF, alignment is close to perfect, but the computed curves suffer from a lack of points, especially in the reactance component. In order to better appreciate the degree of agreement that can be achieved, and to precisely determine the corresponding shunt capacitance, a frequency sweep was made over a limited frequency range. Model CF was chosen for this purpose, and was tested at 16, 17, 18, 19, 19.4, 19.7, 20, 21, and 22 MHz. The results, combined with the earlier ones at 24 MHz, would cover a full impedance cycle for both antennas, and provide the necessary resolution near the resonant frequencies.

Port antenna results appear in Figure 81. In a), a comparison of impedances from models C and CF is shown over the frequency range of the sweep. Very similar results are obtained, the most apparent discrepancies being attributable to the lack of data for model C. In b), impedance curves of model CF over the same frequency range are shunted by 30,

40, 45, and 50 pF respectively and compared with the measured curves. Best agreement seems to occur somewhere between 40 and 45 pF. The equivalent starboard antenna results appear in Figure 82. Models C and CF agree once again very closely, and impedance curves of model CF are seen to match best the measured curves with a shunt capacitance of 45 pF.

Figure 83 compares impedance values obtained at 2 MHz from all complex models. Highly accurate resistance values are obtained compared to stick models, although some values become slightly negative for the port antenna. Hence the reactance component alone is a sufficient indicator of performance. The magnitude of this component is observed once more to be inversely proportional to the radius of the feed element. Indeed, models C and CE, CF and CD, and C' are in increasing order of feed element radius. An observation that can now be made for the first time is that more uniform segment lengths in the source region improve the accuracy of the input impedance (Burke and Poggio, 1980). Hence model CE is superior to model C in terms of impedance. That this is not true for model CD versus model CF may be due to the fact that the segment length discontinuities had already been corrected to a sufficient degree in model CF.

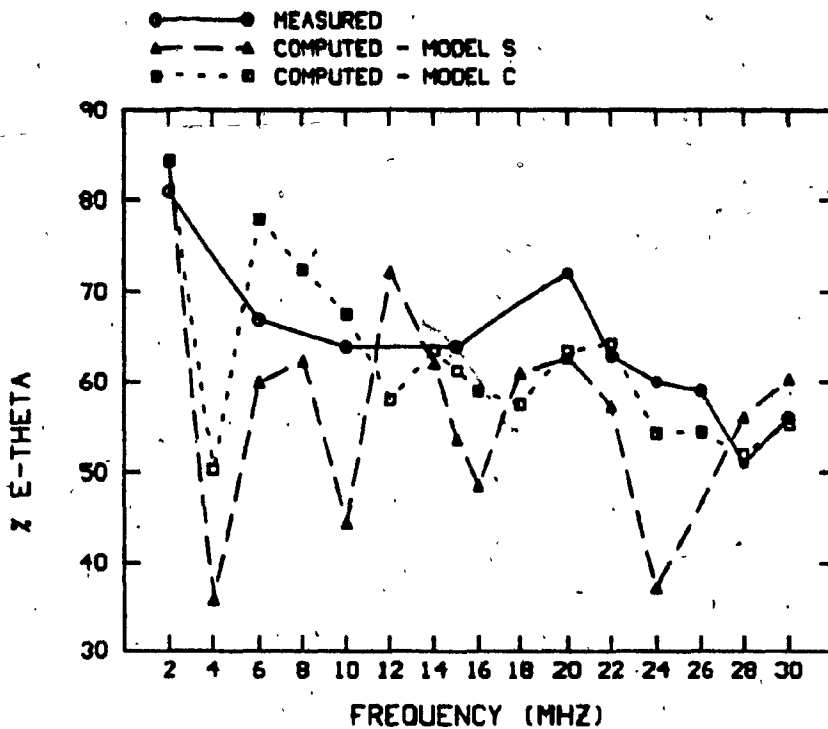
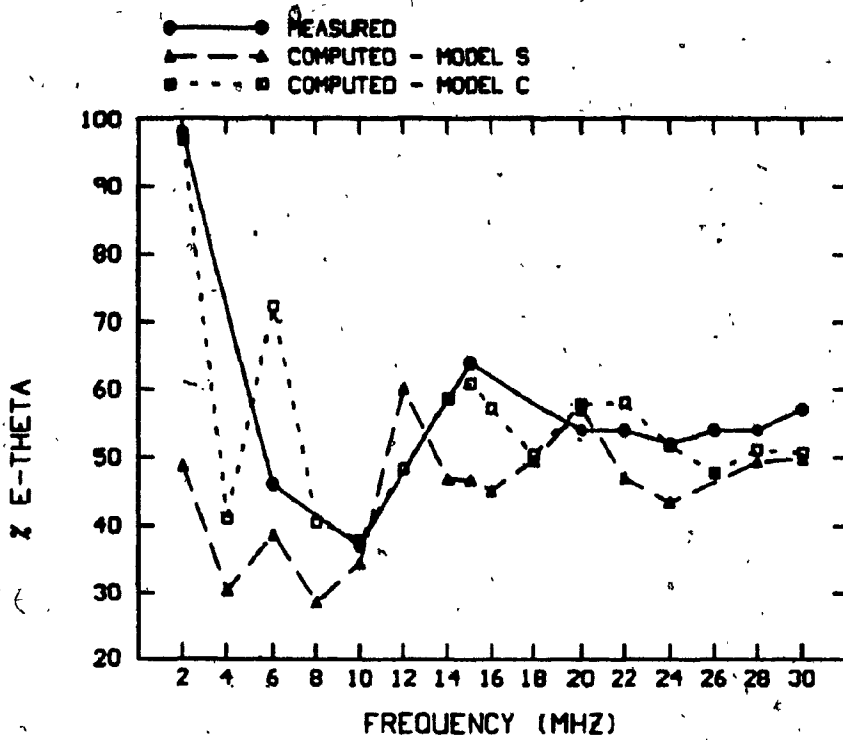


Fig. 76. Comparisons of measured and computed E-theta curves for models S and C, port and starboard antennas

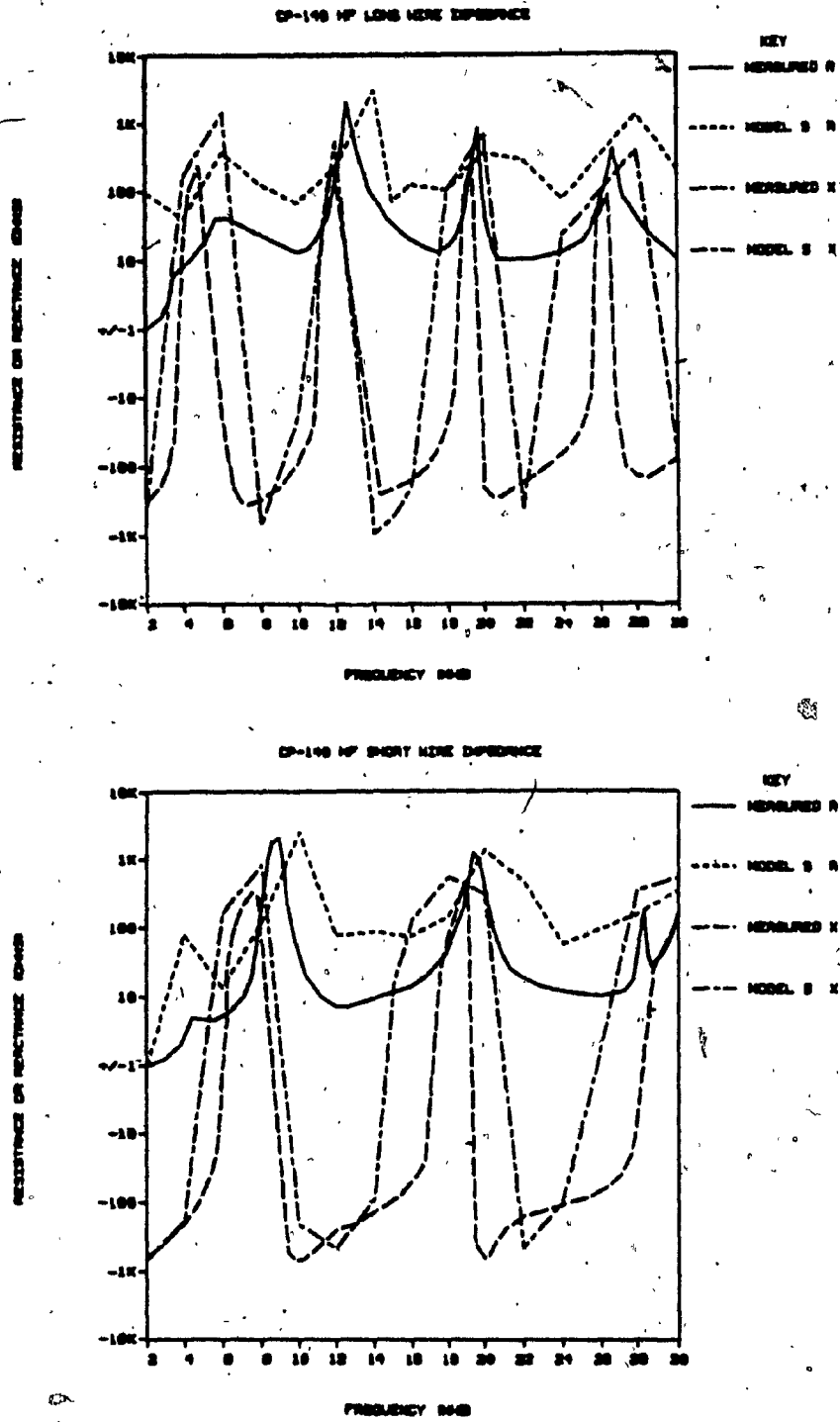


Fig. 77. Comparisons of measured and computed impedance curves for model S, port and starboard antennas

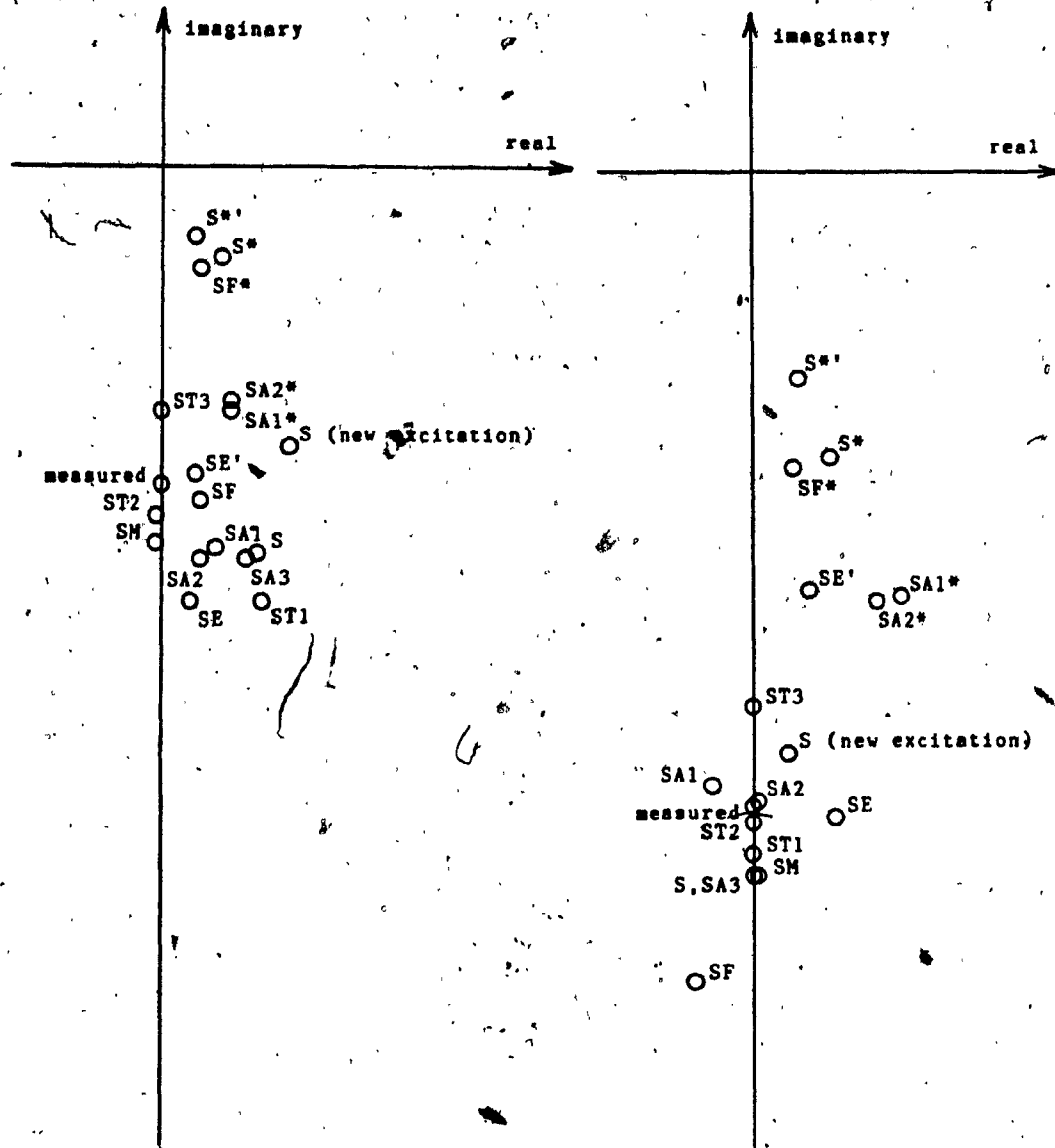


Fig. 78. Impedances of CP-140 stick models at 2 MHz, port and starboard antennas

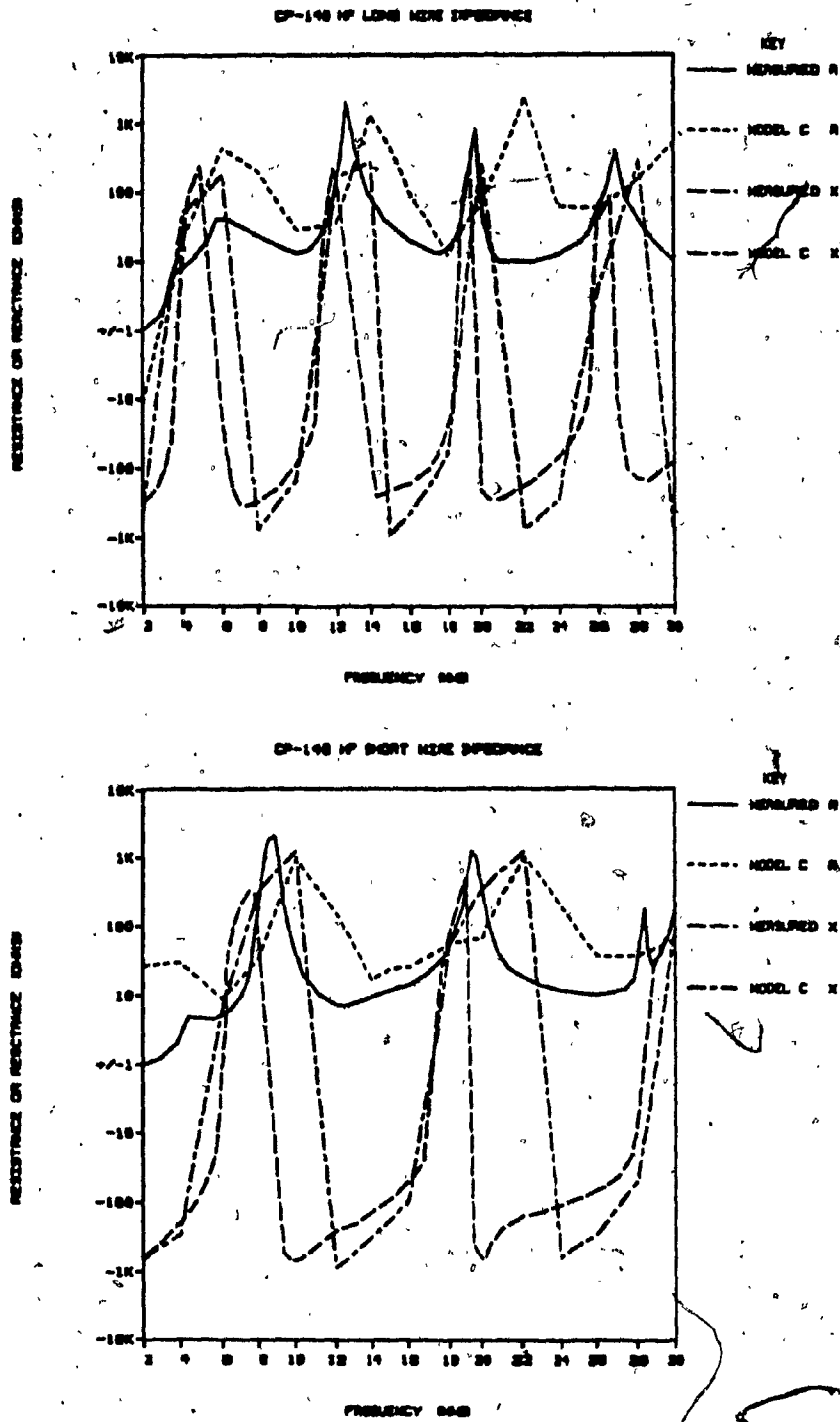


Fig. 79. Comparisons of measured and computed impedance curves for model C, port and starboard antennas

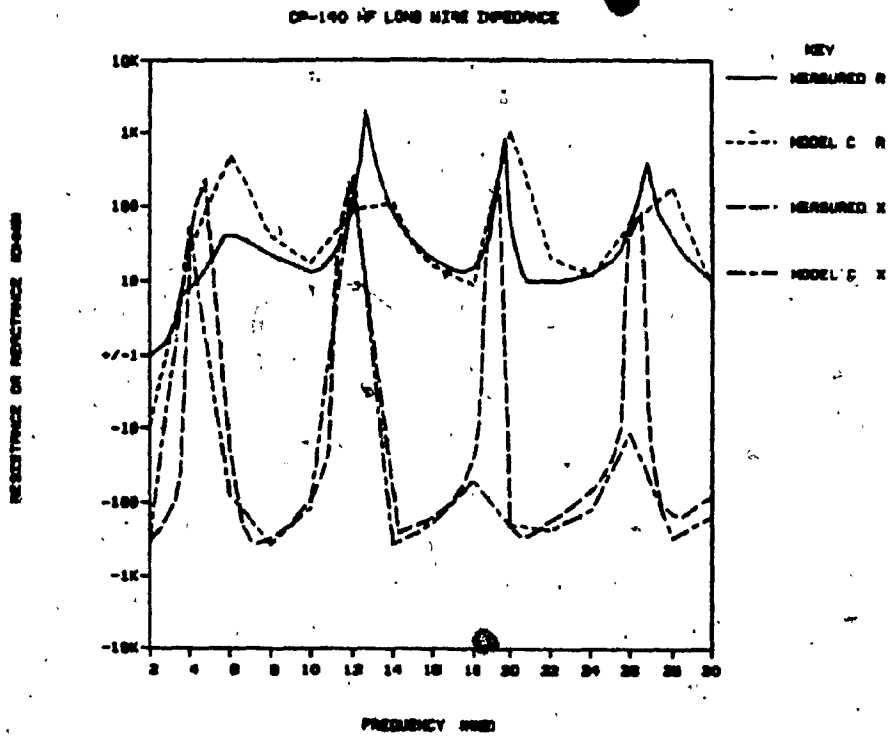
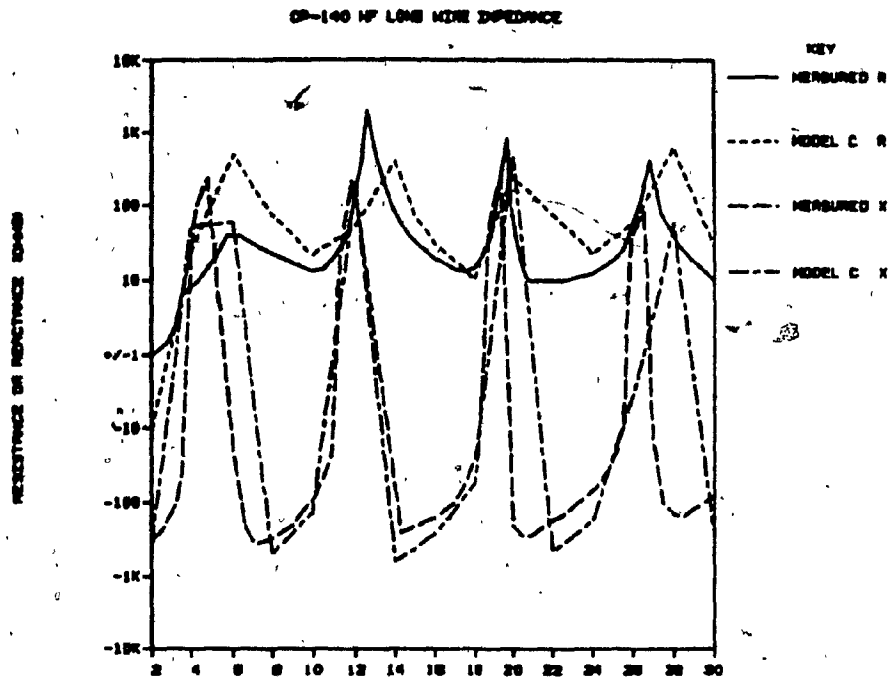


Fig. 80. Comparisons of measured impedance curves, port antenna, with those computed from model C with shunt capacitance of 15 and 30 pF.

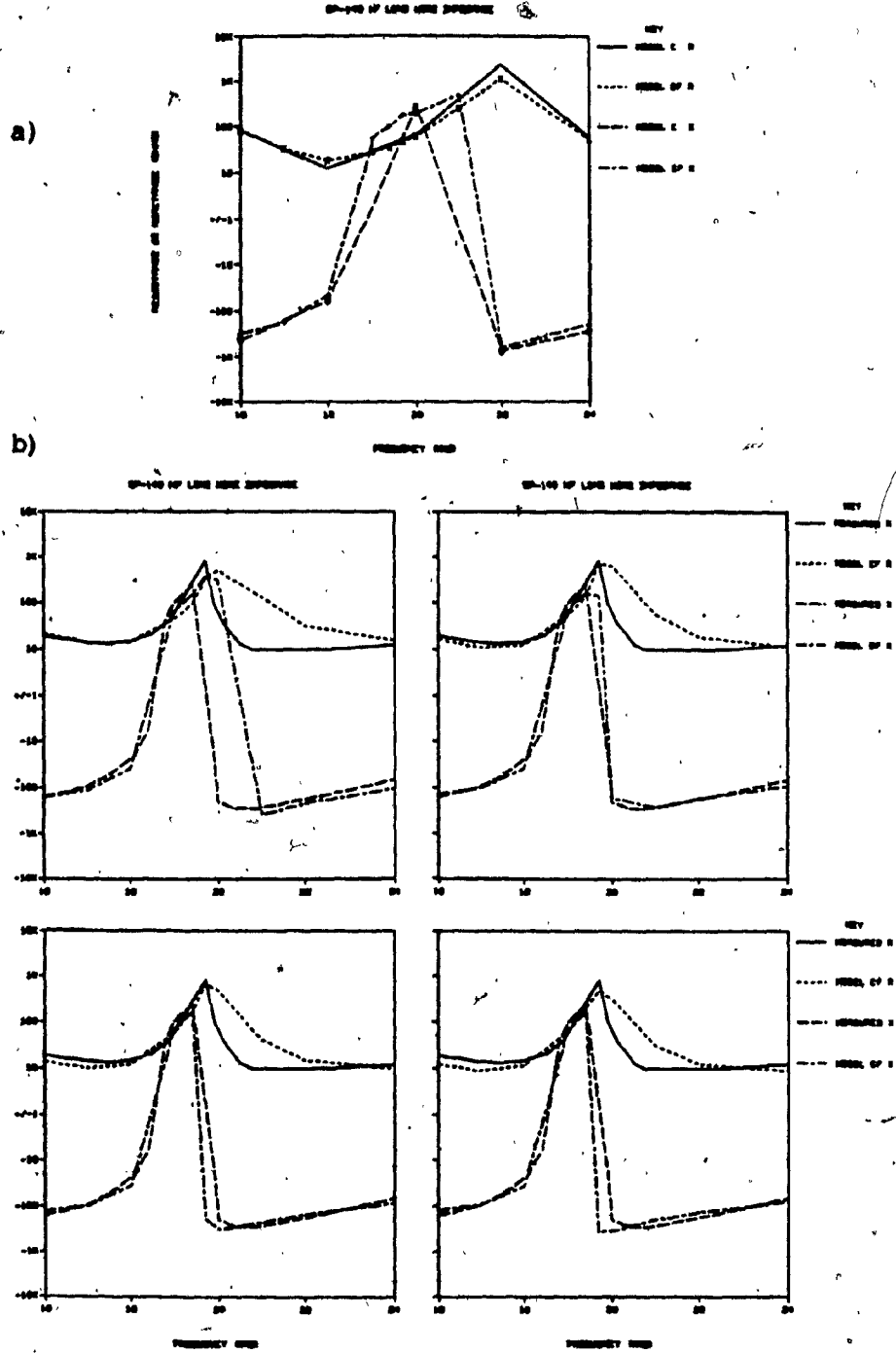


Fig. 81. Impedance curves for poft antenna, 16 to 24 MHz. In a), comparison of models C and CF, and in b), comparison of measurements with model CF shunted with 30, 40, 45, and 50 pF.

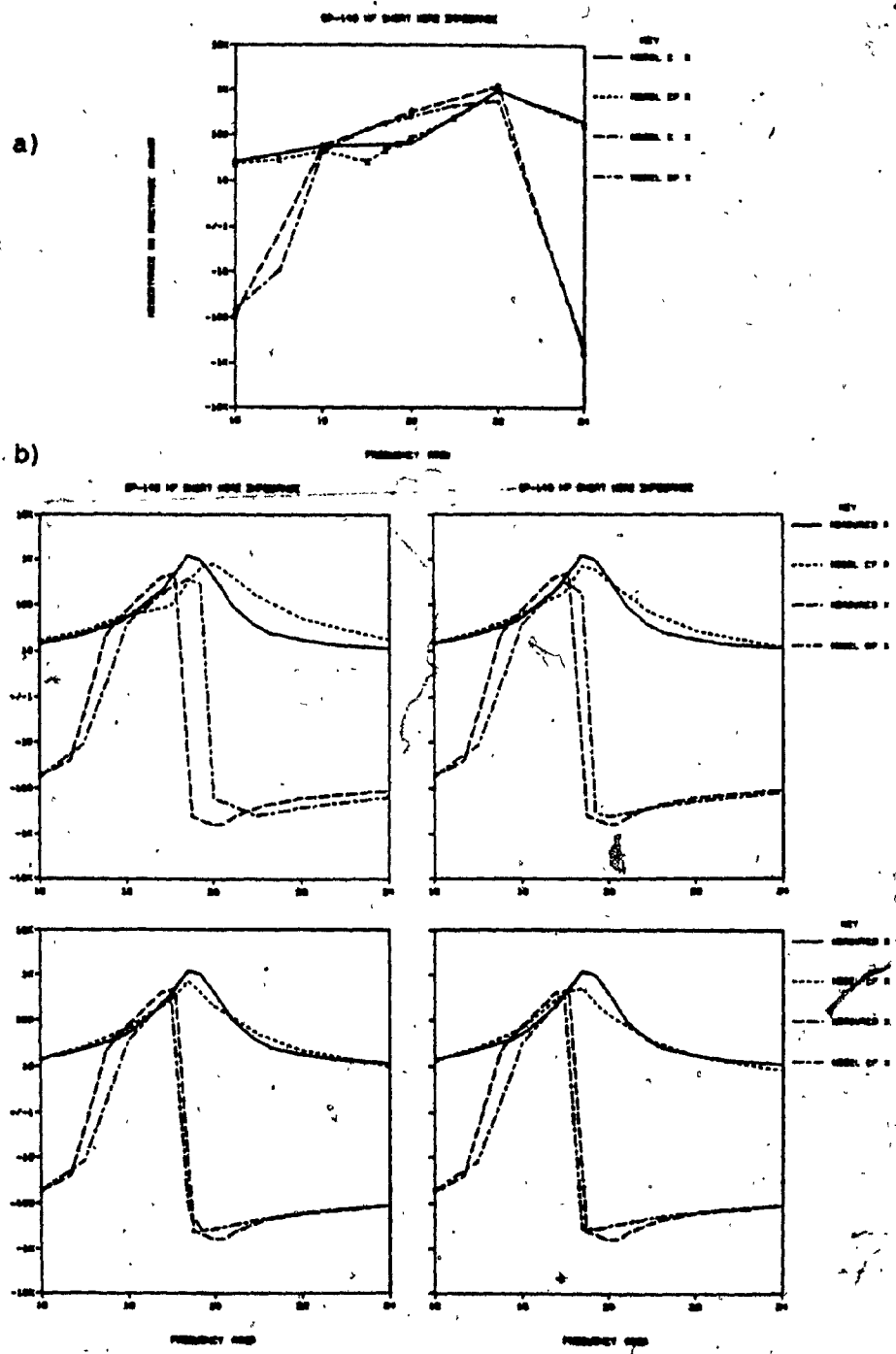


Fig. 82. Impedance curves for starboard antenna, 16 to 24 MHz. In a), comparison of models C and CF, and in b), comparison of measurements with model CF shunted with 30, 40, 45, and 50 pF.

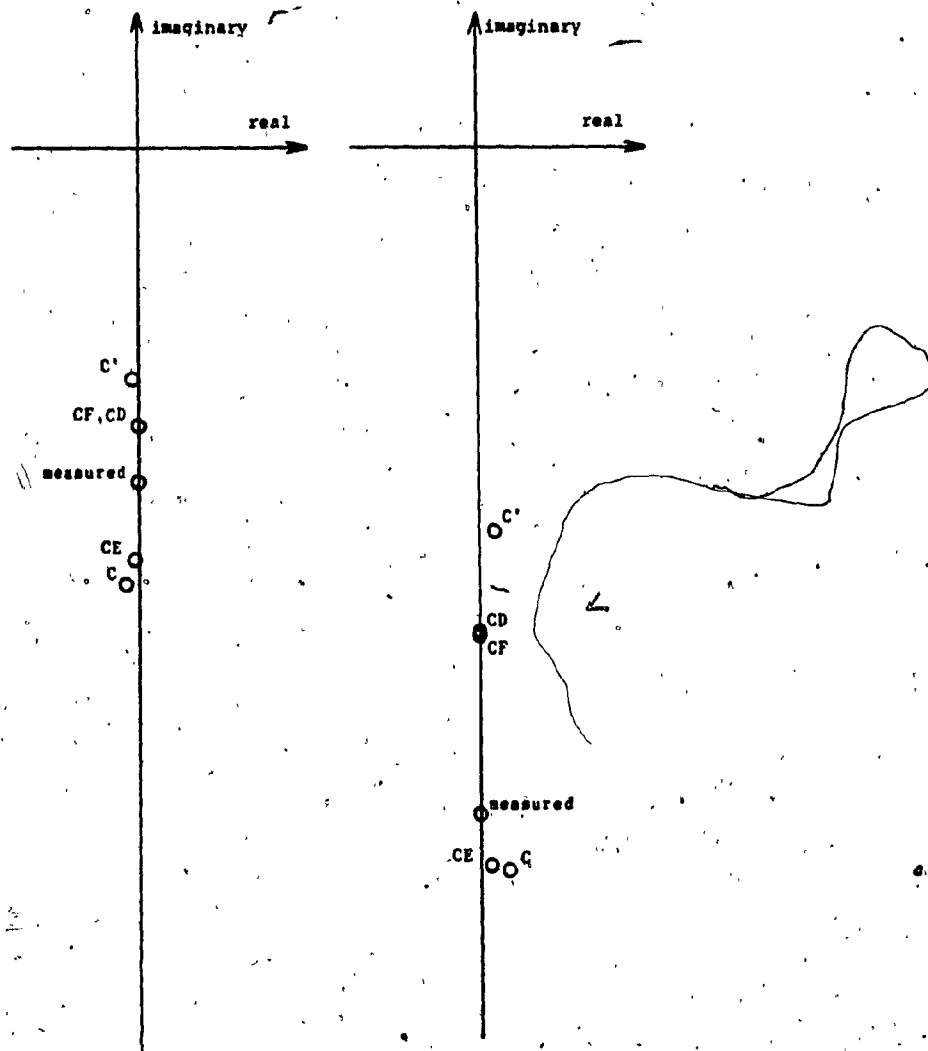


Fig. 83. Impedances of CP-140 complex models at 2 MHz, port and starboard antennas

SUMMARY AND CONCLUSIONS

Successful modelling of HF antennas on the CP-140/Aurora airframe was achieved through the wire-grid modelling technique implemented in the method of moments code NEC. In the process, auxiliary software was created that eases various steps of the modelling and displays electromagnetic quantities in a most meaningful way.

The EMC laboratory's wire-grid modelling program DIDEK was put to test for the first time in the generation of the first complex CP-140 model. Digitization via tablet was a clear improvement over past methods, and simultaneous display showing the progress of the work was particularly helpful. Merging and reflection of geometry files functioned well and saved considerable labor. Being the author's first experience with the program, a few weeks elapsed before the model was completed. Since then, however, experience was gained and other models were generated at a much quicker pace. In the summer of 1984, under the author's supervision, a complex helicopter model was completely digitized in a morning's time (after careful marking of orthographic views). Very convincing use of the program was also made in instances when digitization via the tablet was not desired. DIDEK has therefore imposed itself as the optimum modelling tool. Thought is now being given

to integrating computation of perimeters or areas into DIDEK. This would be of great assistance in the selection of wire radii based on the isoperimetric inequalities.

Program CHECK was written to systematically verify wire-grid models against the established modelling guidelines. This is particularly helpful for the checking of wire junctions, which is impractical manually since the number of checks is approximately equal to the square of the number of wires. The demonstration in this thesis of the critical importance of the modelling guidelines adds further value to the program. Integration of CHECK concepts to DIDEK is being considered as another worthwhile future innovation.

Program MININEC, the mini-computer version of NEC, was fully integrated to the existing laboratory software. This involved BASIC to FORTRAN language conversion, the introduction of file capability, and the creation of input and output format conversion programs. Hence for the first time a method of moments code could be executed on laboratory facilities. A test run was made in parallel with NEC on a CP-140 simple model with rather extreme cases of violation of modelling guidelines, and yet little pattern differences resulted. For ordinary cases, therefore, MININEC is virtually interchangeable with NEC, and the few basic features that it retains of NEC are sufficient in most purposes. The

limited memory available on the present laboratory facilities restrains its range of applications, but expected system upgrade will undoubtedly extend its use. MININEC is especially helpful in the testing of small structures because of the slow turnaround and the exemption from "spooling" in or out to a main-frame computer. These advantages were recently fully exploited in the trial-and-error generation of a TACAN signal.

Advanced graphical methods were exploited to improve the display of impedances, radiated patterns, and induced wire currents. Graphics package DIGPLOT was exploited to produce the desired logarithmic form of impedance plots. Graphics package MOVIE.BYU with Watkin's hidden surface algorithm was exploited to produce the type of radiation pattern display closest to the natural mental image. This type of display has lead the author to greater understanding of radiation pattern fundamentals and has lead him to the concept of equivalent ideal dipole orientation for the lower frequency patterns of this work. Use of color and shading, which is theoretically possible with MOVIE.BYU, is being contemplated to further enhance the plots. Finally, use of color was exploited in the creation of a user-oriented program, SPCTRM, for the display of current magnitude and phase. Difficulties with color reproduction limit for now the usefulness of the method at the EMC laboratory. Use of

the program was nevertheless pioneered on various projects, and already interesting conclusions related to the CP-140 have been reached that could not have been made through other current display programs. These were not discussed in this thesis.

A theoretical description was given of two programs exploiting various numerical methods to extend the usefulness of the antenna analysis codes. The basis behind the choice of the MIL-SPEC angles and HF aircraft assessment parameters was explained as part of the description of ISO-LEV. Program EFAR, which generates the radiation pattern contribution of selected wires, was described next with an account of the critical examination and of the improvements that were made by the author. Work remains to be done on the program to optimize its input and output formats and thus facilitate its use. This program, in conjunction with SPCTRM, would help to extract precious information not yet harvested from the computations of the CP-140 project. EFAR was first used by the author in investigations on a ship model that raised interesting questions.

Until experimental measurements would become available for the present CP-140 HF configuration, preliminary work was done on an old configuration that was called the P3V-1. It featured a dual installation consisting of port and starboard antennas, as is the case today, but of similar

lengths. Stick models with some 70 segments were generated and the port antenna was tested. The starboard antenna was installed and shorted, installed and terminated with 50 ohms, or not installed at all to account for the uncertainty in its state during measurements. This permitted at the same time a study of the coupling phenomenon occurring between the two antennas. Frequencies of test were from 2 to 12 MHz in 2-MHz increment. Execution times were of the order of 50 CPU seconds.

Patterns at 2 and 4 MHz seemed to lead to the conclusion that the starboard antenna had been terminated with 50 ohms during measurements. Changes in impedance or in patterns revealed the inter-antenna coupling to be especially strong at 11 MHz. Thin and fat models were tested, thin models yielding generally superior impedance results but fat models giving superior pattern agreement. Results at 2 MHz were disappointing, and pattern agreement elsewhere did not generally go above reproduction of the lobes and nulls.

In the CP-140 HF configuration, port and starboard antennas were of dissimilar lengths and were therefore both excited in succession at the various test frequencies. As measurements this time specified, the passive antenna was left shorted. Because of the P3V-1 results, only fat models were generated. A first stick model was derived and tested over the HF band (2-30 MHz) in 2-MHz increments. No better

agreement was obtained than for the P3V-1 model, but surprisingly the pattern deterioration expected in the higher frequencies did not occur.

Various optimization attempts were made in order to determine the degree of agreement that can possibly be obtained with the economy associated with stick models. Variations to radii or topology were made, and CHECK errors were removed. The critical frequency of 2 MHz was chosen as a test. Analysis by equivalent ideal dipole orientations at 2 MHz was shown both theoretically and experimentally to be valid and more convenient than pattern comparisons. One particular model with wings slightly moved forward (SF*) emerged as the best model. Apparently contradictory results were sometimes obtained, but in general the removal of CHECK errors appeared as the dominant factor of improvement. Overly sacrificing the realism of the model had the opposite effect.

Therefore the art of the antenna engineer appears as that of identifying schemes that would remove electromagnetic incompatibilities while retaining the integrity of the model. Some experience was gained in this respect, but the utter simplicity of stick models severely restricted the field of action. A worthwhile goal for the future would be the identification of the factors that cause given directions of shift in the equivalent dipole orientation. This

could best be achieved by more gradual changes in modelling parameters in such a way that the movement of the equivalent dipole orientation can be traced, as it was for the S-ST1-ST2-ST3 sequence of models.

A complex model (327 segments) was derived with radii selected in accordance with equality of cross-sectional areas. It was tested in parallel with the original stick model (execution time about 750 CPU seconds), and consistently better pattern agreement was witnessed, in spite of the numerous CHECK errors initially tolerated. The faithful reproduction of pattern details makes the model suitable for system range calculations. A significant exception occurred however at 24 MHz where pattern quality was average. A sequence of optimized complex models was therefore generated and tested at 2 MHz and 24 MHz until removal of all incompatibilities in one model would correct the 24 MHz problem.

The simple model generated impedance curves over the HF band that reproduced the general variation of magnitude with frequency. Resonance peaks were directly related to the length of the excited antenna, but did not correspond to the measured resonance peaks, which were mysteriously shifted to the left of their expected position. The repetition of this phenomenon for the complex model suggested that some physical factor had not been taken into account in the

wire-grid modelling of the antennas. Several factors were indeed identified that could have added a capacitive effect. Complex model impedance values were therefore shunted with different amounts of capacitance until 45 pF would produce an excellent fit with the measured curves. The complex model can therefore, with proper correction, generate impedance values that can be used to assess the tuning of antenna couplers. It will be of interest, in the future, to try to duplicate the phenomenon with the impedances of the stick model.

In the examination of the impedances of the various optimized models at 2 MHz, it was found that superior models in terms of patterns do not necessarily yield the best impedance values, and therefore the two issues must be given independent treatment. An inverse correlation was found between the radius of the feed element and the magnitude of the reactance component, and as expected, continuity of segment length in the source region appeared to improve the impedance value.

It is the author's confidence that the way is well traced for further analysis of results from the CP-140 project, and for efficient treatment of similar problems in the future.

LIST OF REFERENCES

- ANTENNA COMPATIBILITY PLAN. 1975. Lockheed Aircraft Corporation, California Division, Burbank, California, U.S.A, January 10.
- ARCHER, A. M. 1961. Evaluation of the antenna system installed on the P3V-1 aircraft (U), volume III: Final CNI antenna radiation pattern analysis--part II, volume IV: Impedance and design data on the CNI antennas. Report no. LR 13565-III, Lockheed Aircraft Corporation, California Division, Burbank, California, U.S.A, February 22.
- BAHSOUN, Youssef. 1981. Calculation of radiation patterns given the current distribution on wire antenna. Internal Note no. 1, Concordia EMC Laboratory, Faculty of Engineering, Concordia University, 1455 de Maisonneuve Blvd., West, Montreal, Canada, H3G 1M8, March 20.
- _____. 1982. Evaluation of an HF helicopter antenna measurements and numerical techniques. Master's thesis, Faculty of Engineering, Concordia University, Montreal, Quebec, Canada, March.
- BAHSOUN, Y., and KUBINA, S. J. 1981. A digital data base for the numerical calculation of isotropic level and radiated power by an aircraft antenna. Technical Note no. TN-EMC-81-06, Electromagnetics Laboratory, Concordia University, Loyola Campus, 7141 Sherbrooke St. W., Montreal, Quebec, H4B 1R6, August 11.
- BURKE, G. J., and POGGIO, A. J. 1980. Numerical electromagnetic code (NEC)--method of moments, new rev. ed.; part I: Program description--theory, part III: User's guide. Technical Document 116, Naval Ocean Systems Center (NOSC), San Diego, California 92152, January 2.
- BURDEN, Richard L.; FAIRES, J. Douglas; and REYNOLDS, Albert C. 1981. Numerical analysis, 2d ed. Prindel, Weber & Schmidt, Statler Office Building, 20 Providence Street, Boston, Massachusetts 02116.

CHRISTIANSEN, Hank, and STEPHENSON, Mike. 1985. MOVIE.BYU training text, 1985 ed. H. N. Christiansen, Graphics Utah Style, 1980 North 1450 East, Provo, Utah 84604.

GRANGER, J. V. N., and BOLLJAHN, J. T. 1955. Aircraft antennas. PROC. I.R.E., vol. 43, pp.533-550, May.

HARRINGTON, Roger F. 1968. Field computation by moment methods, reprint ed. By the Author, R. D, 2, West Lake Road, Cazenovia, N.Y. 13035.

JAGGARD, D. L. 1979 An application of isoperimetric inequalities to the calculation of equivalent radii. Proceedings of the National Radio Science Meeting, Boulder, Colorado, November.

JASIK, Henry, ed. Antenna engineering handbook, 1st. ed. McGraw-Hill Book Company, New York.

JULIAN, Alfredo J.; LOGAN, James C.; and ROCKWAY, John W. 1982. MININEC: a mini-numerical electromagnetics code. Technical Document 516, Naval Ocean Systems Center (NOSC), San Diego, California 92152, September 6.

KUBINA, S. J. 1983a. Study on electromagnetic analysis techniques for aircraft antennas. Technical Note no. TN-EMC-83-05, final report, 1 May 1982 to 1 June 1984, Concordia University, EMC Laboratory, Loyola campus, 7141 Sherbrooke St. W., Montreal, Quebec, Canada, H4B 1R6.

_____. 1983b. Numerical modelling methods for predicting antenna performance on aircraft. Proceedings of AGARD Lecture Series No. 131: The performance of antennas in their operational environment, AGARD-LS-131, October.

_____. 1985. Study on electromagnetic analysis techniques for aircraft antennas. Technical Note no. TN-EMC-85-02, final report, 1 June 1984 to December 1984, Concordia University, EMC Laboratory, Loyola campus, 7141 Sherbrooke St. W., Montreal, Quebec, Canada, H4B 1R6.

KUBINA, S. J.; CERNY, E.; and GAUDINE, D. 1984. The DIDEC system: a new interactive model building technique. Technical Note no. TN-EMC-84-04, Concordia University, EMC Laboratory, Loyola Campus, 7141 Sherbrooke St. W., Montreal, Quebec, Canada, H4B 1R6.

LAROSE, Colin L. 1982. Computer-aided analysis for HF aircraft antennas. Technical report for ENGR C410, Concordia University, September 27.

_____. 1984. The method of moments. Presentation for Antennas and Propagation, 304-593B, McGill University, April 3.

_____. 1985a. Installation and testing of MININEC. Study on electromagnetic analysis techniques for aircraft antennas, Technical Note no. TM-EMC-85-02, final report, 1 June 1984 to 1 December 1984, Concordia University, EMC Laboratory, Loyola Campus, 7141 Sherbrooke St. W., Montreal, Quebec, Canada, H4B 1R6.

_____. 1985b. Special software development projects. Study on electromagnetic analysis techniques for aircraft antennas, Technical Note no. TM-EMC-85-02, final report, 1 June 1984 to 1 December 1984, Concordia University, EMC Laboratory, Loyola Campus, 7141 Sherbrooke St. W., Montreal, Quebec, Canada, H4B 1R6.

LAROSE, Colin L., and KUBINA, S. J., 1983. Modelling of wire antennas on the CP-140. Study on electromagnetic analysis techniques for aircraft antennas, Technical Note no. TN-EMC-83-05, final report, 1 May 1982 to 1 June 1984, Concordia University, EMC Laboratory, Loyola Campus, 7141 Sherbrooke St. W., Montreal, Quebec, Canada, H4B 1R6.

_____. 1984. "Bugs" in geometry section of MININEC. Technical Note no. TN-EMC-84-02, Electromagnetics Laboratory, Concordia University, Loyola Campus, 7141 Sherbrooke St. W., Montreal, Quebec, Canada, H4B 1R6, 12 March.

_____. 1985. Additional results: modelling of wire antennas on the CP-140. Study on electromagnetic analysis techniques for aircraft antennas, Technical Note no. TM-EMC-85-02, final report, 1 June 1984 to 1 December 1984, Concordia University, EMC Laboratory, Loyola Campus, 7141 Sherbrooke St. W., Montreal, Quebec, Canada, H4B 1R6.

SPIEGEL, Murray R. 1968. Mathematical handbook of formulas and tables. Schaum's Outline Series, McGraw-Hill Book Company, New York.

STUTZMAN, Warren L., and THIELE, Gary A. 1981. Antenna theory and design. New York: John Wiley & Sons.

TRUEMAN, C. W. 1979. Average field matching wire antenna moment method and aircraft HF antenna application. Doctoral thesis, McGill University, Montreal, Quebec, April.

WARNER, James R. 1979. DIGRAF user's guide, version 2.0. Regents of the University of Colorado, 3645 Marine Street, Campus Box B-45, Boulder, Colorado 80309, January.

WU, TAI T., and KING, W. P. Ronald. 1976. The tapered antenna and its application to the junction problem for thin wires. IEEE Trans. Antennas Propagat., vol. AP-24, pp. 42-45, Jan.